



**This electronic thesis or dissertation has been
downloaded from Explore Bristol Research,
<http://research-information.bristol.ac.uk>**

Author:
Nichols, Maddy

Title:
Fabrication of Acoustically Micropatterned Coacervate-Based Hydrogels

General rights

Access to the thesis is subject to the Creative Commons Attribution - NonCommercial-No Derivatives 4.0 International Public License. A copy of this may be found at <https://creativecommons.org/licenses/by-nc-nd/4.0/legalcode>. This license sets out your rights and the restrictions that apply to your access to the thesis so it is important you read this before proceeding.

Take down policy

Some pages of this thesis may have been removed for copyright restrictions prior to having it been deposited in Explore Bristol Research. However, if you have discovered material within the thesis that you consider to be unlawful e.g. breaches of copyright (either yours or that of a third party) or any other law, including but not limited to those relating to patent, trademark, confidentiality, data protection, obscenity, defamation, libel, then please contact collections-metadata@bristol.ac.uk and include the following information in your message:

- Your contact details
- Bibliographic details for the item, including a URL
- An outline nature of the complaint

Your claim will be investigated and, where appropriate, the item in question will be removed from public view as soon as possible.

Fabrication of Acoustically Micropatterned Coacervate-Based Hydrogels

By

MADELEINE KATE NICHOLS



Department of Chemistry
UNIVERSITY OF BRISTOL

A dissertation submitted to the University of Bristol in accordance
with the requirements of the degree of DOCTOR OF PHILOSOPHY in the
Faculty of Science.

AUGUST 2018

Word count: forty three thousand two hundred

ABSTRACT

The central theme of this thesis is to exploit the non-contact technique of acoustic trapping for the manipulation of complex coacervate microdroplets in the construction of micropatterned hydrogels and gelatinous films for biological applications. Recently, the move towards interdisciplinary research has blurred the boundaries between engineering, chemistry, physics and biology. This overlap has created exciting opportunities to combine different expertise in the construction of functional materials for desired applications.

Ordered hydrogels are achieved through in-situ coacervation followed by hydrogel transformation within an acoustic trapping device in the presence of an applied acoustic standing wave field. The higher density of the coacervate droplets compared with their surrounding aqueous phase resulted in the droplets migrating to pressure minima of the acoustic field. Coacervates preferentially sequester guest molecules, such as dyes, enzymes and other biomolecules, on their interiors and this behaviour was exploited to reveal and explore the droplet behaviours within the acoustic field and the spatially organised hydrogel networks formed using fluorescence microscopy. Significantly upon initiating the hydrogelation transformation within an applied acoustic field, the droplets transformed at their trapped positions to form self-supporting hydrogel monoliths, with patterning fixed into the hydrogel network following removal from the acoustic device in both 1D lines and 2D gridded arrays.

The ordered self-supporting hydrogels fabrication process was then adapted to produce gelatinous thin films. Through removal of the unordered material comprising the majority of the hydrogel network, ordered gelatinous thin films in both 1D and 2D were produced. Layering of these films enabled pursuit of higher ordered structures and more complex gel architectures. Significantly, the thin films enabled better site-specific studies of behaviours of transformed coacervate populations with different guest molecules encapsulated within the spatially fixed network, particularly cascades such as the enzymatic reactions of urease and coupled glucose oxidase and horseradish peroxidase. Further, an alternative enzymatically driven hydrogelation route was demonstrated, from the evolution of the acidic product as glucose oxidase breaks down the substrate glucose, and used in achieving more distinct layered thin films. Layering of these enzymatically gelled thin films produced convincing 3D gel structures.

Finally, a coacervate hydrogel system comprising more biologically relevant molecules was developed. Through combining adenosine monophosphate with poly-L-lysine the resulting coacervate system was shown to hydrogelate via metal coordination upon mixing with zinc chloride. For this nucleotide-based coacervate system, trapping of the droplets within the acoustic field was demonstrated and protocols were developed for transformation into both ordered hydrogels and thin films. The successful patterning of this system shows the versatility of the acoustic trapping technique across different coacervate based hydrogel systems for fabrication of micro-patterned, soft viscoelastic materials.

DEDICATION AND ACKNOWLEDGEMENTS

There are a great many people without whom this undertaking would not have been possible. Throughout my PhD, I have been privileged to work alongside a knowledgeable and excellent team of scientists. Firstly, I would like to thank my supervisors; Dr Avinash Patil, Dr Adrian Barnes, Professor Bruce Drinkwater and Professor Stephen Mann for their inspiring discussion, advice, direction, support and challenging me to raise my scientific game.

As a student of the Bristol Centre for Functional Nanomaterials, I would like to thank them for the opportunity to do this PhD and I extend my thanks to the larger network of academics who have been involved with my training and projects along the way too, particularly Dr Annela Seddon, who continues to be utterly fantastic as the head of the BCFN.

A huge thank you to everyone that proof-read my thesis, your support and feedback was instrumental. Thanks must also go to all members of the brilliant research communities of the COMC, UNDT and BCFN past and present. Thank you for your advice, support and friendship, it has been an honour working with you all. I wish you all the luck in the world and look forward to hearing about all your future successes, academic or otherwise.

I am incredibly grateful for the opportunities afforded to me to promote science outside of the lab; visiting primary schools with ChemLabs, running science talks or demos at festivals and discussing science in the Cosmic Shed. Always working alongside some passionate, talented and wonderful teams of people. A special mention must go to the trip to the Paralympics pit lane, seeing where materials expertise could be used to improve prosthetics. To everyone I have met through those things, thank you for being so awesome.

It seems I have also developed a penchant for physical punishment during my time researching, having taken on all manner of personal challenges. My heartfelt thanks and love to everyone that sponsored, enthused about or trained with me for any of these events. And huge respect and admiration for those who were there beside me in the athletic endeavours; ultramarathons, muddy runs, tandem triathlons - we covered a lot!

Researching is not always the most conducive to a social life... To all my friends, I can never express enough gratitude for your support, limitless encouragement and unwavering patience despite my not always deserving it. Times have changed a lot over the last four years, but thank you for the parts you have all played in helping me to this point through thick and thin.

My final thanks must go to my family for their unrelenting support, kindness, wisdom, compassion, cuddles and love. To my sister Izzy, thank you for your incredible insight, keeping me grounded and

your impeccable wit. And my dearest mum, thank you for all your warm words of encouragement and motivation over cups of tea, unending patience and unfaltering belief in me.

- Madeleine Nichols

Every single one of us possesses the strength to attempt something you aren't sure you can accomplish

- Scott Jurek

AUTHOR'S DECLARATION

I declare that the work in this dissertation was carried out in accordance with the requirements of the University's Regulations and Code of Practice for Research Degree Programmes and that it has not been submitted for any other academic award. Except where indicated by specific reference in the text, the work is the candidate's own work. Work done in collaboration with, or with the assistance of, others, is indicated as such. Any views expressed in the dissertation are those of the author.

SIGNED: DATE:

PUBLICATIONS

Publications relating to the work presented in this thesis:

Madeleine K Nichols, Ravinash Krishna Kumar, Philip G Bassindale, Liangfei Tian, Adrian C Barnes, Bruce W Drinkwater, Avinash J Patil, Stephen Mann, 'Fabrication of Micro-patterned Dipeptide Hydrogels by Acoustic Trapping of Stimulus-Responsive Coacervate Droplets', *Small*, vol 14, 1800739

Other publications:

James PK Armstrong, Jennifer L Puetzer, Andrea Serio, Anne Geraldine Guex, Michaella Kapnisi, Alexandre Breant, Yifan Zong, Valentine Assal, Stacey C Skaalure, Oisín King, Tara Murty, Christoph Meinert, Amanda C Franklin, Philip G Bassindale, Madeleine K Nichols, Cesare M Terraciano, Dietmar W Hutmacher, Bruce W Drinkwater, Travis J Klein, Adam W Perriman, Molly M Stevens, 'Engineering Anisotropic Muscle Tissue using Acoustic Cell Patterning', *Advanced Materials* (forthcoming)

TABLE OF CONTENTS

	Page
List of Tables	xvii
List of Figures	xix
List of Equations	xxv
1 Introduction	1
1.1 Thesis overview	3
1.2 The advent of micromanipulation	5
1.3 From micromanipulation to microfabrication	6
1.3.1 Lithography	6
1.3.2 3D printing	8
1.3.3 Electrochemical manipulation	9
1.3.4 Acoustic trapping	9
1.4 Soft matter materials: Hydrogels	12
1.4.1 Hydrogels	12
1.4.2 Molecules	13
1.4.3 Intermolecular interactions	14
1.4.4 Polymer hydrogels	18
1.4.5 Molecular hydrogels	19
1.4.6 Coacervate-based hydrogels	21
1.4.6.1 Complex coacervation	21
1.4.6.2 Coacervate droplet applications	23
1.4.6.3 Specific design of coacervate droplets	24
1.4.7 Hydrogel applications	25
1.5 Microfabrication of hydrogels	27
1.5.1 Water in hydrogels	27
1.5.2 Controlling cross-linking	28
1.5.3 Acoustic patterning of hydrogels	29

2	Materials and Methods	33
2.1	General Techniques	35
2.1.1	Microscopy	35
2.1.2	Dynamic Light Scattering and Zeta Potential	36
2.1.3	Electron microscopy	38
2.1.4	Rheology	38
2.1.5	Ultraviolet-Visible spectroscopy	42
2.1.6	Differential Scanning Calorimetry	43
2.2	Experimental Methods	44
2.2.1	Acoustic trapping devices	44
2.2.1.1	Fabrication	44
2.2.1.2	Impedance analysis	44
2.2.1.3	Acoustic patterning of coacervate droplets	44
2.2.2	General methods	45
2.2.2.1	Lab procedures and data processing	45
2.2.2.2	Slide functionalization	45
2.2.2.3	Zeta potential	46
2.2.2.4	Size distribution of coacervate droplets	46
2.2.2.5	Fluorescent tagging of enzymes	47
2.2.3	Chapter 4 methods	47
2.2.3.1	Fmoc-AA/PDDA Coacervate Preparation	47
2.2.3.2	Coacervate density measurements	47
2.2.3.3	Hydrogelation of coacervate droplets	48
2.2.3.4	Acoustic trapping of coacervate droplets	48
2.2.3.5	Hydrogelation of ordered coacervate droplets	49
2.2.3.6	Scanning Electron Microscopy imaging of coacervate-based hydrogels	49
2.2.3.7	Transmission Electron Microscopy imaging of coacervate-based hydrogels	49
2.2.3.8	Sequestration measurements	50
2.2.3.9	Rheology	50
2.2.4	Chapter 5 methods	51
2.2.4.1	Thin film fabrication protocol	51
2.2.4.2	Thin film one-layer one-step enzymatic cascade reaction	51
2.2.4.3	Thin film one-layer two-step enzymatic cascade reaction	51
2.2.4.4	Enzymatic hydrogelation	52
2.2.4.5	Acoustically patterned thin film enzymatic gelation	52
2.2.4.6	Enzymatically gelled thin film layering	52
2.2.4.7	Enzymatically gelled thin film enzyme reactions	53

2.2.5	Chapter 6 methods	53
2.2.5.1	PLys/AMP Coacervate preparation	53
2.2.5.2	AMP nucleotide gelation	53
2.2.5.3	PLys/AMP coacervate gelation	53
2.2.5.4	Acoustic trapping of PLys/AMP coacervates	53
2.2.5.5	Acoustically patterned PLys/AMP coacervate hydrogels	54
2.2.5.6	Rheology of PLys/AMP coacervate hydrogels	54
2.2.5.7	Differential Scanning Calorimetry	54
3	Theory and Development of Acoustic Trapping Devices	57
3.1	Introduction	59
3.1.1	Origins of the acoustic force	60
3.1.2	Acoustic trapping	61
3.1.2.1	1-dimensional standing wave	62
3.1.2.2	2-dimensional standing wave	64
3.1.3	Acoustic Trapping Devices	66
3.1.3.1	Counter-propagating standing wave devices	67
3.1.3.2	The piezoelectric effect	69
3.1.3.3	Impedance analysis	70
3.1.3.4	Acoustic Streaming	72
3.2	Trapping device fabrication	73
3.2.1	Modelling of the Acoustic Field	74
3.3	Results and Discussion	79
3.3.1	Device design	79
3.3.1.1	Reflections	79
3.3.1.2	Coupling agent	80
3.3.1.3	Device reusability	81
3.3.2	Impedance analysis and driving frequencies	82
3.3.2.1	Matching transducers	82
3.3.2.2	Driving frequencies	84
3.3.3	Model outputs compared with experimental	85
3.4	Conclusions and Future Work	87
4	Fabrication of Micropatterned Hydrogels by Acoustic Trapping of Reconfigurable Polymer/Dipeptide Coacervate Droplets	91
4.1	Introduction	93
4.1.1	A stimulus-responsive coacervate-based hydrogel system	94
4.2	Results and Discussion	96
4.2.1	Coacervation in a 1D acoustic field	96

4.2.1.1	Coalescence in 1D trapping points	100
4.2.1.2	Patterning across the whole device	101
4.2.2	Hydrogelation in a 1D acoustic field	101
4.2.2.1	Hydrogelation transformation	101
4.2.2.2	Hydrogelation in the presence of a 1D acoustic field	103
4.2.2.3	Scanning electron microscopy of 1D patterned hydrogels	104
4.2.2.4	Transmission electron microscopy of 1D patterned hydrogels	108
4.2.3	Chemical communication within hydrogels	108
4.2.3.1	Sequestration of guest molecules	109
4.2.3.2	Ordered hydrogelation in presence of guest molecules	111
4.2.3.3	3D rendering of 1D ordered hydrogels	113
4.2.4	Coacervation in a 2D acoustic field	113
4.2.4.1	Coacervate droplet behaviour in a 2D acoustic field	115
4.2.4.2	Towards one droplet per nodal point	116
4.2.5	Hydrogelation in a 2D acoustic field	119
4.2.5.1	Effect of micropatterning on hydrogel mechanical properties	121
4.3	Conclusions and Future work	122
5	Acoustically Micropatterned Coacervate-Based Gelatinous Thin Films for Chemical Communication and 3D Constructs	129
5.1	Introduction	131
5.1.1	Chemical complexity in hydrogels	132
5.2	Results and Discussion	134
5.2.1	Fabrication routes for micropatterned gelatinous thin films	134
5.2.1.1	Effect of droplet viscosity	135
5.2.1.2	Gelation of 1D patterned droplets	137
5.2.2	Chemical communication within gelatinous thin films	139
5.2.2.1	One step enzymatic cascade reaction in a 1D patterned thin film	139
5.2.2.2	Void morphologies in gelatinous thin films	141
5.2.2.3	Two-step coupled enzymatic cascade reaction in a 1D patterned thin film	142
5.2.3	Layering of thin films for 3D constructs	145
5.2.3.1	Layer distinction through patterning direction	145
5.2.3.2	Layer distinction with different guest molecules	146
5.2.3.3	Two layer two-step coupled enzymatic reaction	148
5.2.4	Enzymatic hydrogelation	150
5.2.4.1	Acoustically patterned enzymatic hydrogelation	152
5.2.4.2	Enzymatically hydrogelated acoustically patterned gelatinous thin films	153

5.2.4.3	Layering of enzymatically hydrogelated thin films	154
5.2.4.4	Higher layering	156
5.2.5	2D patterned thin films	156
5.2.5.1	2D two-step enzymatic cascade reaction	157
5.2.5.2	Effect of enzymes on droplet coalescence in a 2D acoustic field . .	160
5.2.5.3	2D enzymatically hydrogelated films	161
5.3	Conclusions and Future Work	161
5.3.1	Towards enzymatically controllable structures	164
5.3.2	Towards biological relevance	166
6	Development of Acoustically Micropatterned Polypeptide/Nucleotide Coacervate Based Hydrogels	169
6.1	Introduction	171
6.1.1	Biologically relevant building blocks	171
6.1.2	Biologically relevant materials design	172
6.1.2.1	Metal coordination	173
6.1.2.2	A polypeptide/nucleotide coacervate based hydrogel	174
6.2	Results and Discussion	175
6.2.1	AMP gelation	175
6.2.2	PLys/AMP coacervation	178
6.2.2.1	Tailoring coacervate droplet sizes for acoustic trapping	178
6.2.3	PLys/AMP coacervate gelation	180
6.2.4	PLys AMP hydrogel characterisation	181
6.2.4.1	Rheological quantification of gelation time	182
6.2.4.2	Differential Scanning Calorimetry	184
6.2.5	Acoustic patterning of PLys/AMP coacervates in a 2D acoustic field	184
6.2.6	Hydrogelation of PLys/AMP coacervate droplets in an acoustic field	186
6.2.6.1	Hydrogelation of coacervate droplets in a 1D acoustic field	187
6.2.6.2	Micropatterned thin films	188
6.2.6.3	Guest molecules	189
6.3	Conclusions and Future Work	193
7	General Conclusions	197
	Bibliography	207

LIST OF TABLES

TABLE	Page
2.1 Epifluorescence microscopy filters	35
4.1 DLS size measurements of coacervate droplets formed at an equimolar mixing ratio and for varying concentrations of FMOC-AA mixed with PDDA (40 mM)	97
4.2 Table displaying half-wavelength spacings as calculated theoretically and measured from images of ordered coacervate droplets at each of the identified driving frequencies for 1D patterning	98
4.3 Table displaying half-wavelength spacings as calculated theoretically and measured directly from images of ordered coacervate droplets at each of the identified driving frequencies for 2D acoustic patterning	115
6.1 Dynamic light scattering size range measurements of coacervate droplets mixed at different volume ratios from stock solutions of PLys and AMP at 50 mM	179
6.2 Dynamic light scattering size range measurements of coacervate droplets formed at different volume ratios from stock solutions of PLys and AMP at 50 mM	180

LIST OF FIGURES

FIGURE	Page
1.1 The photolithographic process and soft lithographic process of micromolding for the fabrication of microfluidic devices	7
1.2 Some examples of 3D printed structures	8
1.3 Some examples of acoustically patterned arrangements of cells, particles and fibres	11
1.4 Intramolecular interactions: covalent and ionic bonds	15
1.5 Different types of dipole interactions	16
1.6 Different types of intermolecular interactions	17
1.7 Different functionalised-peptide low molecular weight gelators and different self-assembled morphologies	21
1.8 Images of the coacervate phase, coacervation and phase separation	22
2.1 Electric double layer of a particle in solution	37
2.2 Shearing of a solid or fluid between two parallel plates	39
2.3 Rheological response of a sample to an applied oscillating strain	41
2.4 Schematic of glass channel slide preparation	46
3.1 The trapping of dust at half-wavelength spacing within a pipe, known as Kundt's tube	59
3.2 Schematic of the forces within a 1-dimensional acoustic standing wave	63
3.3 Schematic showing the one transducer and reflector setup for a counter-propagating standing wave	67
3.4 Schematic showing the two transducer counter-propagating standing wave	68
3.5 Schematic showing the shape changes within a piezoelectric material under an applied alternating current	70
3.6 Through thickness modes supported within a transducer	71
3.7 Impedance curve for a transducer over 1-12 MHz range	72
3.8 Schematic of the acoustic trapping device including dimensions and the locations of different features	74
3.9 Modelling of the acoustic pressure field within an acoustic trapping device with up to 5 activated transducers	75

3.10	Plane wave modelling of the 1D acoustic pressure field at different driving frequencies within an acoustic trapping device	76
3.11	Modelled 2D plane wave pressure field over a 20 mm square acoustic trapping chamber	77
3.12	Modelled 2D Huygens wave pressure field over a 20 mm square acoustic trapping chamber	78
3.13	Modelled pressure field over the vertical 2mm thickness of the acoustic trapping chamber	78
3.14	Large area view of trapped coacervates in the central area of a trapping device at different times after adherence of transducers using superglue	81
3.15	Impedance analysis of a transducer in different situations	83
3.16	2D (6.7 x 6.69 MHz) trapping of coacervate droplets in an acoustic field driven at different voltages	85
3.17	Plane wave modelled and experimentally observed trapping at different driving frequencies in a 1D acoustic field	86
3.18	Ordered hydrogels patterned at 2.15 MHz (1D) and 2.15 x 2.14 MHz (2D)	87
3.19	Micropatterned hydrogel with the transducers oriented vertically along the 15 mm long edge	88
4.1	Schematic showing the self-assembly of a low molecular weight gelator (LMWG) into a fibrous network and self-supporting hydrogel	94
4.2	Schematic of the pH induced structural reconfiguration of the coacervated Fmoc-AA within an Fmoc-AA/PDDA coacervate droplet	95
4.3	Time-lapse image series every 10 seconds after application of an acoustic field (1D 6.7 MHz) to a sample of coacervate droplets	98
4.4	Modelled pressure fields and experimentally observed 1D patterning of coacervate droplets at different frequencies	99
4.5	Coalescence behaviours of droplets at the nodal points of the acoustic field in 1D	100
4.6	Stitched image of the entire device chamber with coacervate droplets trapped in a 1D (6.7 MHz) acoustic field	102
4.7	Photographs and microscopy images of acoustically micropatterned hydrogels at different frequencies and an unpatterned hydrogel	104
4.8	Scanning electron microscopy images of air dried 1D (6.7 MHz) micropatterned hydrogels	105
4.9	Scanning electron microscopy images of lyophilised 1D (6.7 MHz) micropatterned hydrogels	106
4.10	Scanning electron microscopy images of lyophilised unordered hydrogels	106
4.11	Scanning electron microscopy images of lyophilised 1D (2.15 MHz) micropatterned hydrogels	107
4.12	Drying of 1D (2.15 MHz) micropatterned hydrogels in air and lyophilised	107
4.13	Transmission electron microscopy images of a 1D (6.7 MHz) micropatterned hydrogel .	109
4.14	Unordered coacervate droplet sequestration of guest molecules at maximal loading concentration	109
4.15	Maximal droplet loading concentration using UV Vis spectroscopy	110

4.16	Acoustically patterned coacervate droplets sequestering guest molecules	111
4.17	Acoustically patterned coacervate droplets and corresponding transformed micropatterned hydrogels with guest molecules loaded into the droplets	112
4.18	Fibrils emanating from transformed coacervate droplets loaded with Hoechst dye	113
4.19	3D stack of a 1D (6.7 MHz) acoustically micropatterned hydrogel revealing the nature of the vertical extent of the patterning	114
4.20	Comparison of plane wave modelled and observed trapping in a 2D acoustic field	114
4.21	Coalescence behaviours of droplets at the nodal points of a 2D (6.7 x 6.69 MHz) acoustic field	115
4.22	Disrupted 1:1 ratio Fmoc-AA:PDDA coacervate droplets left to trap for 1 hour in a 2D (6.7 x 6.69 MHz) acoustic field	116
4.23	Zeta potential values for different coacervate droplets for 40 mM solutions of Fmoc-AA and PDDA, at the stated volume ratios	117
4.24	Time-lapse series of 3:7 ratio Fmoc-AA:PDDA coacervate droplets in a 2D (6.7 x 6.69 MHz) acoustic field over 30 minutes with images shown every 5 minutes	117
4.25	Time-lapse series of 5:2 ratio Fmoc-AA:PDDA coacervate droplets in a 2D (6.7 x 6.69 MHz) acoustic field over 30 minutes with images shown every 5 minutes	118
4.26	Whole device patterning for 3:7 ratio Fmoc-AA:PDDA in a 2D (6.7 x 6.69 MHz) acoustic field	119
4.27	Micropatterned hydrogel at 3:7 ratio Fmoc-AA:PDDA in a 2D (6.7 x 6.69 MHz) acoustic field	120
4.28	Strain and frequency sweep rheology data for unordered, 1D (6.7 MHz) and 2D (6.7 x 6.69 MHz) ordered hydrogels	122
4.29	Schematic outlining the whole proposed and implemented acoustic micropatterning of hydrogels process	123
5.1	Two different hydrogel patterning approaches using 3D printing to impart features into a hydrogel matrix	132
5.2	The lock and key model of enzyme reactions	133
5.3	Trapping of preformed coacervate droplets made from different molecular weight PDDA in a 1D (6.7 MHz) acoustic field at a 3:7 Fmoc-AA:PDDA ratio after 30 minutes	136
5.4	Coacervate droplets (3:7 ratio, 400-500 kDa PDDA) remaining on the glass slide following supernatant removal with a paper towel	138
5.5	Fluorescence microscopy images of 1D (6.7 MHz) micropatterned gelatinous thin film fibrils	139
5.6	One step horseradish peroxidase enzymatic reaction scheme	140
5.7	Evolution of 2,3 diaminophenazine observed in the green fluorescence channel as the horseradish peroxidase enzyme reaction occurs in a 1D (6.7 MHz) thin film	141
5.8	Brightfield and fluorescence images of the void morphologies observed in transformed coacervate droplets loaded with Hoechst dye	142

5.9	Coupled enzymatic reaction scheme of glucose oxidase and horseradish peroxidase . . .	143
5.10	Time-lapse series of red, blue and green fluorescence channels during the glucose oxidase and horseradish peroxidase coupled enzymatic reaction in a 1D (6.7 MHz) patterned gelatinous thin film with fluorescently tagged enzymes	144
5.11	Schematic of the desired coupled enzyme reaction within a stacked 2 layer thin film . . .	145
5.12	Bright field images of a two layered orthogonally patterned thin film stack	146
5.13	3D fluorescent image of a two layered orthogonally patterned thin film stack with different fluorescent dyes loaded into each layer	147
5.14	Time-lapse series of red, blue and green fluorescence channels during the glucose oxidase and horseradish peroxidase coupled enzymatic reaction in a 2 layer orthogonally patterned gelatinous thin film stack	149
5.15	pH curves for evolution of gluconic acid from glucose oxidase and substrate glucose . .	151
5.16	Vial inversion test for bulk gelation of coacervate droplets loaded with glucose oxidase mixed with differing volumes of glucose	151
5.17	Enzymatic hydrogelation of the entire volume of acoustically patterned coacervate solution	152
5.18	Enzymatically hydrogelated thin films patterned in 1D (6.7 MHz) loaded with Hoechst dye	153
5.19	Orthogonally patterned 2 layer enzymatically hydrogelated thin film stack with Hoechst dye loaded into layer 1 and rhodamine dye into layer 2	154
5.20	Orthogonally patterned 2 layer enzymatically hydrogelated thin film stack with green fluorescently tagged glucose oxidase loaded into layer 1 and red fluorescently tagged glucose oxidase in layer 2	155
5.21	3 layer enzymatically hydrogelated thin film stack	156
5.22	Gridded array of preformed coacervate droplets at 3:7 Fmoc-AA:PDDA ratio with 400-500 kDa PDDA trapped in a 2D (6.7 x 6.69 MHz) acoustic field for 30 minutes	157
5.23	Time-lapse series of red, blue and green fluorescence channels during the glucose oxidase and horseradish peroxidase coupled enzymatic reaction in a 2D (6.7x6.69 MHz) micropatterned gelatinous thin film with fluorescently tagged enzymes	159
5.24	Trapping behaviours of preformed coacervate droplets (3:7 Fmoc-AA:PDDA, 400-500 kDa PDDA) loaded with glucose oxidase and horesradish peroxidase enzymes in a 2D (6.7x6.69 MHz) acoustic field	160
5.25	Enzymatically hydrogelated thin films patterned in 2D (6.7 x 6.69 MHz) loaded with Hoechst dye	161
5.26	Embedding of micropatterned coacervate thin films into agarose hydrogel	164
5.27	Urease enzyme reaction scheme	164
5.28	Schematic for an on-off enzyme switch to oscillate the coacervate system between droplet and hydrogel phases	165
5.29	Enzymatically controlled disruption of a gelatinous thin film loaded with urease	166
6.1	Naming conventions and structures of different nucleotides	172

6.2	Structures of nucleotide based hydrogels	174
6.3	Vial inversion test for the gelation of adenosine-5'-monphosphate mixed at different concentrations with 50 mM zinc chloride	176
6.4	Vial inversion tests for different volumes of adenosine-5'-monphosphate mixed with 50 mM zinc chloride	177
6.5	Vials inverted at different times following the mixing of adenosine-5'-monphosphate with 50 mM zinc chloride	177
6.6	Comparison of a hydrogelated polylysine/AMP coacervate solution with an AMP-only nucleotide hydrogel	180
6.7	Rheology frequency sweep data for nucleotide-only and coacervate hydrogels	181
6.8	Rheology strain sweep data for nucleotide-only hydrogels at different concentrations and a coacervate hydrogel	182
6.9	Rheological measurements of viscoelastic changes with time upon mixing a coacervate solution with zinc chloride	183
6.10	Differential scanning calorimetry profiles for nucelotide-only and coacervate hydrogels	184
6.11	2D (6.7 x 6.69 MHz) acoustically patterned coacervate droplets formed at 1:4 and 1:10 PLys:AMP volume ratios	185
6.12	2D (6.7 x 6.69 MHz) micropatterned coacervate hydrogel formed at a 1:4 PLys:AMP ratio	186
6.13	1D (6.7 MHz) micropatterned coacervate hydrogel formed at a 1:4 PLys:AMP ratio	187
6.14	2D (6.7 x 6.69 MHz) micropatterned coacervate droplets at a 1:4 PLys:AMP ratio and those same droplets following removal of the supernatant with a paper towel	188
6.15	2D (6.7 x 6.69 MHz) micropatterned coacervate hydrogel thin film formed at a 1:4 PLys:AMP ratio	189
6.16	Images of the different steps of the 1D (6.7 MHz) 1:4 ratio coacervate thin film patterning procedure	190
6.17	Sequestration of Hoechst dye into PLys:AMP coacervate droplets formed at different volume ratios	191
6.18	Sequestration of FITC-Gox and Cy5-ss-DNA within unordered transformed 1:2 PLys:AMP thin film hydrogels	191
6.19	Sequestration of Hoechst within a transformed thin film hydrogel	192
7.1	Micropatterned hydrogel summary	200
7.2	Micropatterned gelatinous thin film summary	202
7.3	Micropatterned polypeptide/nucleotide coacervate hydrogel summary	204

LIST OF EQUATIONS

1.1	Gibbs free energy	22
2.1	Stokes-Einstein equation for hydrodynamic radius of a particle	36
2.2	Henry's equation for zeta potential from electrophoretic mobility	37
2.3	Shear stress in a material	39
2.4	Strain of a material	39
2.5	Strain of a typical Hookean solid	40
2.6	Strain in a Newtonian fluid	40
2.7	Complex modulus of a material	41
2.7	Storage and loss moduli of a material defined by the complex modulus	42
2.8	Beer Lambert law	42
2.11	Mass conservation laws	48
3.1	Gorkov relation of the acoustic force to the acoustic potential	60
3.2	Gorkov potential	60
3.2	Acoustophoretic compressibility and density factors	61
3.3	Incoming pressure of a 1D planar standing wave	62
3.4	Incoming velocity of a 1D planar standing wave	62
3.5	Time averaged acoustic radiation potential	62
3.6	Time averaged acoustic radiation force	62
3.7	Acoustophoretic contrast factor	63
3.8	Acoustic energy density	64
3.9	Gor'kov potential as the sum of two acoustic pressures	64
3.10	Pressure for two incoherent orthogonal standing waves	65
3.11	Velocity for two incoherent orthogonal standing waves	65
3.12	Pressure squared for two incoherent orthogonal standing waves	65
3.13	Pressure squared for two incoherent orthogonal standing waves after sufficient time for mixing terms to decay	65
3.14	Velocity squared for two incoherent orthogonal standing waves after sufficient time for mixing terms to decay	65
3.15	Acoustic radiation force for two temporally uncorrelated orthogonal standing waves	66

CHAPTER



INTRODUCTION

1.1 Thesis overview

The non-contact technique of acoustic trapping was used for the manipulation of complex coacervate microdroplet systems, which could undergo structural reconfiguration into hydrogels. By initiating hydrogelation in the presence of a standing wave acoustic field, micropatterned hydrogels and gelatinous films with both 1D and 2D features were fabricated. Two different coacervate systems were used; the first comprised a cationic polymer and functionalized dipeptide, and self-assembled into a hydrogel network upon reduction of the environmental pH and the second, formed on the mixing of a polypeptide with a nucleotide, self-assembled into a supramolecular hydrogel via metal coordination.

In this introductory chapter, the fundamental background information is given which is key in understanding later results and discussion. The relevant information regarding acoustically patterned hydrogels and how this research has arisen within overarching research fields is presented. An overview of different manipulation techniques and their respective limitations is given first, then the theory of hydrogels from the basics of molecules to the intermolecular interactions and forces within materials is discussed. Some discussion of different hydrogel applications is then given alongside the development of techniques to structure hydrogels, including some brief theory of acoustic patterning and then how the combination of coacervate systems with acoustic patterning could conceivably be utilised in the microfabrication of hydrogels.

In chapter 2, the background to some major techniques used throughout the projects has been provided alongside the experimental methodologies employed. This is so that attention to the results and discussion can be given in the relevant chapters.

The mathematics and theory related to standing wave acoustic fields and the trapping devices used throughout this research is presented in chapter 3. In acoustic trapping, due to differing acoustic properties between particles in suspension and their surrounding fluid, upon exposure to an acoustic field the incoming sound waves will be scattered off the particles. This change in momentum results in an acoustic radiation force, which acts to move the particles towards the pressure minima or maxima of the applied acoustic field. In a standing wave field, as used in this work, these pressure points are stationary and thus ordered patterns of particles will be formed. For the case of coacervate

droplets, the acoustic force will move the droplets to the pressure minima.

Chapter 4 presents the results of acoustically trapping coacervate droplets and the hydrogelation transformation. Ordered hydrogels are obtained through in-situ coacervation followed by hydrogel transformation within an acoustic trapping device in the presence of an applied acoustic standing wave field. The acoustic trapping devices comprised two orthogonal pairs of transducers. Driving a single pair trapped the coacervate droplets into 1D lines while driving both pairs produced a 2D grid-like array, with the microdroplets migrating to the nodal points where the two orthogonally applied fields intersect. Following the hydrogel transformation in the presence of the 1D or 2D field ordered hydrogels with 1D or 2D ordered features retained in the network were produced. Different driving frequencies of the standing wave acoustic field enabled controllable periodicity within the ordered architectures produced. The higher density of the coacervate droplets compared with their surrounding aqueous phase resulted in the droplets migrating to pressure minima of the acoustic field. Coacervates preferentially sequester guest molecules, such as dyes, enzymes and other biomolecules, on their interiors and this property was exploited to reveal and explore the droplet behaviours within the acoustic field and the spatially organised hydrogel networks formed, using fluorescence microscopy. As a result, pH induced self-assembly of the dipeptide molecules while acoustically trapped enabled the spatial isolation of the guest molecules within the micropatterned hydrogel monoliths.

Chapter 5 builds on the previous chapter by presenting an alternative fabrication process to produce gelatinous thin films. For this, excess supernatant phase was removed from the device so that only the patterned bulk coacervate phase remains and undergoes hydrogel transformation to produce ordered gelatinous thin films in both 1D and 2D. Layering of these films enabled pursuit of higher ordered structures and more complex gel architectures. Significantly, the thin films enabled better site-specific studies of behaviours of transformed coacervate populations with different guest molecules encapsulated within the spatially fixed network, particularly cascades such as the enzymatic reactions of urease and coupled glucose oxidase and horseradish peroxidase. Further, an alternative enzymatically driven hydrogelation route was demonstrated, from the evolution of the acidic product as glucose oxidase breaks down the substrate glucose, and used in achieving more distinct layered thin films. Layering of these enzymatically gelled thin films produced convincing

3D gel structures.

Chapter 6 examines the applicability of acoustic patterning another coacervate-based hydrogel system, comprising more biologically relevant molecules. Through combining adenosine monophosphate (AMP), reported as a nucleotide capable of gelation, with poly-L-lysine (PLys) the resulting coacervate system was shown to hydrogelate via metal coordination upon mixing with zinc chloride. For this nucleotide-based coacervate system, it was possible to demonstrate trapping of the droplets within the acoustic field and protocols were developed for transformation into both ordered hydrogels and thin films.

In summary, the above findings clearly demonstrate the versatility of the acoustic trapping technique in the fabrication of micropatterned, soft, viscoelastic materials and micro-array technology.

1.2 The advent of micromanipulation

With the invention of the microscope in the 17th century, resolution of phenomena occurring on length-scales below that which can be seen by our eyes was possible. [1] On the small scale, behaviors could be understood and the fundamentals of matter investigated. This has enabled the understanding of larger-scale behaviours based on a few fundamental interaction forces between the different molecules and atoms they are comprised of.

Naturally, this knowledge created a desire to manipulate molecules to explore and control larger-scale behaviours. Initially, manipulation was done by hand but more accurate and sophisticated micromanipulation techniques have since developed, often based on specific properties of the systems under investigation. These manipulations comprise an important part of microfabrication; designing and building on the small scale, with precise control over the assembly.

Alongside these manipulation methods, different analytical techniques have developed and improved and subsequently molecules and materials have been understood in greater depth. This has given rise to the birth of new areas of research which can no longer be constrained to one particular discipline. The field of soft matter lies at this intersection, with relevance in physics, chemistry, biology and engineering. In certain conditions, based on the interplay of attractive forces between the different molecules (Section 1.4.3), soft matter systems will exhibit spontaneous self-assembled

structures which result in complex macroscopic behaviours. These systems exist naturally but can also be specifically designed from the ‘bottom up’ as smart materials which exhibit particular behaviours. Thus through understanding of molecules on the small scale and through careful selection and sometimes customisation of the building blocks, alongside manipulation techniques, we can construct soft materials from the bottom up for desired applications.

1.3 From micromanipulation to microfabrication

The manipulation of objects enabled understanding of their behaviours but through using different manipulation techniques to organise objects and components within larger scale materials, the resulting properties could be controlled. The size regime of the molecules and the manipulations being in the realm of microns lead to this process being called microfabrication. There are several different processes used in microfabrication, each selected based on the system requirements and properties, and sometimes used in combination, to structure a material.

1.3.1 Lithography

There are several different variants of lithography with photolithography being the most common, due to its extensive use in the fabrication of semiconductors. Moore’s law predicted a doubling in the number of components per integrated circuit every year, which has largely been followed as transistors have become smaller and faster. [2, 3] Producing microchips has required the fabrication methods to keep up.

Photolithography selectively illuminates some areas of a photo-sensitive layer of material, known as a photoresist, with ultraviolet (UV) radiation. Accurate features can be obtained using lasers or masks. Lasers will trace out a pre-programmed pattern over the surface and masks, which are pre-cut stencils, shield some areas of the surface from the light. Irradiated areas will transform chemically and remain fixed in place on the substrate material. Unexposed areas can be removed so that only the patterned features remain as shown in Figure 1.1a. [4]

Optical diffraction limits the achievable size of the patterned features to the UV wavelength. Some variants of lithography exist such as extreme UV, focused ion beam and electron-beam which can

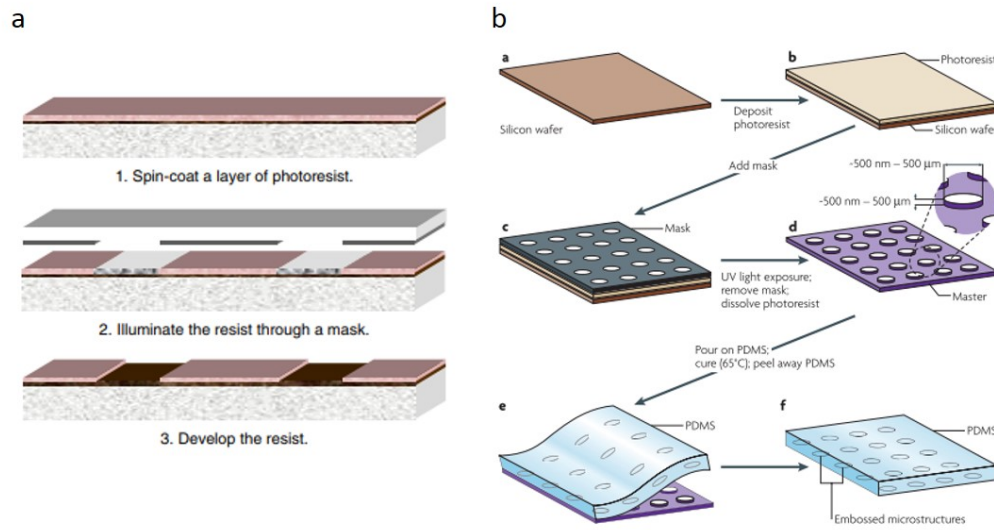


Figure 1.1: a) The photolithographic process. Photoresist material is spun onto a substrate. Certain areas of the resist are exposed to the UV light through the use of a mask. Unexposed areas are then rinsed away to leave the patterned features on the substrate. b) Photolithography can also be used in combination with other fabrication technology in micromoulding, where the photopatterned material is used as a mould to form microstructures in poly(dimethylsiloxane). Taken from references [5] and [6]

achieve nm sized features. [7–9] It is also an expensive method, is unsuitable for non-planar surfaces and only suitable for rigid inorganic materials.

Lithography has also been integrated alongside other fabrication technology and is known as soft lithography. These developments have enabled the micropatterning of more molecules and materials. [10, 11] A specific branch of soft lithography is micromoulding, used in the fabrication of microfluidic devices. Microfluidics is the use of devices, with a 10–100 μm diameter, for the manipulation of liquids and gases. They are an important tool for miniaturised systems, biomedical devices and biochemistry research. [6, 12] The movement towards polymers in the fabrication of these devices made them cheaper, rugged and applicable to more chemical systems.

A 'master' is fabricated first using photolithography. This acts as a mould to cast a polymer in. Channels will be formed within the polymer where there were ridges on the master. In microfluidics poly(dimethylsiloxane) (PDMS) is most commonly used as it provides a hydrophobic surface and can be functionalised or modified to aid in fluid flows (Figure 1.1b).

1.3.2 3D printing

Additive manufacture, also known as 3D printing, is the process of producing a 3D construct by depositing material onto a bed, layer by layer. [13] The computer aided design process has enabled very complex and precise 3D structures to be produced, spanning all size regimes (Figure 1.2).

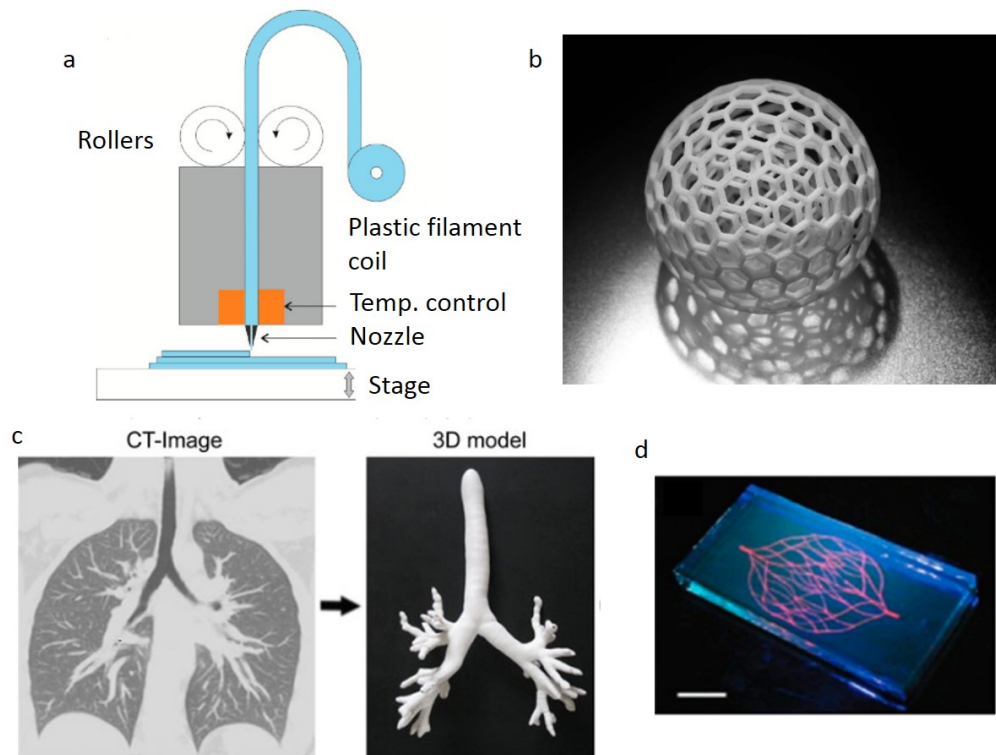


Figure 1.2: a) schematic of a 3D printer. Heated plastic is extruded through the nozzle onto a stage and built up in sequential layers into the pre-programmed design. [13] b) It is possible to print multiple spheres inside of each other through 3D printing. [14] c) medical data can be used to print 3D anatomical models such as this one of the human trachea and bronchial tree. Flow patterns of gases were then studied within the model. [15] d) 3D printing technologies can be used to fabricate microvascular networks. Scale bar 10mm [16]

The most common 3D printer uses a printhead to extrude heated plastic in sequential layers (Figure 1.2a). As it is patterned, the heat will enable fusion with the layer below and, as the whole structure cools, it will harden. It is possible to print with other materials; plastic, metal, ceramics, liquids, powders or even cells, making 3D printing a very versatile technique in many areas. [17] In the medical research field, 3D printing has been used extensively in creating prosthetics, anatomical models, tissue and organ fabrication and in pharmaceutical research such as drug delivery. [18–24]

Limitations arise in the smallest features that can be produced and the extrudability of the materials.

1.3.3 Electrochemical manipulation

The selective manipulation of different molecules is also possible based on their chemical properties. Both magnetic, electric and electromagnetic fields can be used as non-contact manipulation methods. In constant fields, particles will become trapped at particular locations within it and this behaviour can be used within fluidic devices.

Magnetic fields can be used to transport and position both magnetic and non-magnetic objects. [25] The force on a magnetic particle inside a magnetic field depends on size and magnetic susceptibility of solvent and particle. Materials that are repelled are classed as diamagnetic and most materials fall into this category. Paramagnetic materials will experience a small attractive force and align in a magnetic field while ferromagnetic materials are strongly attracted to magnetic fields. Magnetism has been used for the patterning of cells and in the levitation of droplets and even a frog. [26–28] The strongest forces result within ferromagnetic materials and so this has led to the magnetic labelling of molecules in order to use this technique. [29]

The basis of trapping from electric fields follows a similar principle. Electrical forces can be classified by whether they act on a molecule with a fixed or induced electrical charge. [30] In a uniform electric field, charged particles will experience a force and move. Contrastingly uncharged particles will not experience sufficient forces to move. However when uncharged particles are in a non-uniform electric field, they will move because the magnitude of the field is different at each side of the particle. Electric fields have been used in trapping cells. [31, 32] Limitations arise in the specific design and fabrication of the electrodes for the desired operation of these devices.

1.3.4 Acoustic trapping

Acoustic trapping is the immobilisation of micron-sized objects in ultrasonic waves. As a technique, acoustic trapping requires no additional functionalities be implemented into systems, only that a difference in acoustic properties exists between the droplets or particles in suspension and their surrounding solution. This presents many benefits over the other techniques as no additional functionalities need to be incorporated into the system and trapping devices are easier to fabricate.

Acoustic trapping requires molecules in solution to scatter the sound waves as they pass through, something that will be an intrinsic feature of most systems due to the differing material properties of the material and its surrounding media. As acoustic waves pass through a suspension of particles, this scattering results in particles experiencing an acoustic force and moving. More detail regarding the history and theory of the acoustic force can be found in chapter 3.

For acoustic trapping, the density and compressibility properties must differ between the object and the media. [33, 34] In a standing wave acoustic field, the forces will act to move particles towards stationary pressure points of the applied field. The locations of these pressure minima or maxima, known as nodes, are every half-wavelength of the applied sound wave. Acoustic traps were integrated into a micro-fluidic channel for the cleaning of blood through separation of lipids from red blood cells. The different compressibilities and densities between the lipids and blood cells resulted in them moving to different positions in the acoustic trap, thus enabling their separation. [35] Another microfluidic device was used, with acoustic trapping, to position cancer cells around target cells to study the cell-cell interactions. [36] Microfluidic devices integrated with ultrasonic trapping enable positioning of cells and the ability to expose them to continuous flows. This enables the study of cell washing or enrichment. [37–39]

There are two types of acoustic device; surface and bulk wave. Simply, in surface wave devices acoustic waves propagate across the surface of a substrate whereas in bulk devices they propagate through materials. Acoustic trapping can also be used in producing stationary organised patterns of particles with applications in materials design and fabrication and within tissue engineering.

Acoustic patterning in both one and two dimensions of different cells, using standing surface acoustic wave devices has been demonstrated by Shi *et al.* [40] These acoustic capabilities were integrated within micro-fluidic devices but as a consequence did not pattern or trap large numbers of particles in large volumes of fluid. Gesellchen *et al.* used acoustics to pattern Schwann cells at the nodal positions of an acoustic field in several successive layers (Figure 1.3a). Their approach used a heptagonal device which produced nodes at the intersection of the different applied travelling wave fields. This setup enabled controllable nodal positions by adjusting the wave properties and hence location of field intersections. [41] Similarly, adjustable nodal points within a standing wave field, produced using two counter-propagating waves, were demonstrated by Grinenko *et al.* [42] This method was adopted

in a square device comprising two orthogonally oriented counter-propagating standing wave fields and used to demonstrate particle manipulation in two dimensions in an x-y plane. [43] These devices fall under the classification of dynamic field devices and they present the advantage that trapping positions can be at any arbitrary position within the device, rather than at a fixed position. While the patterning of cells has been demonstrated in many studies, the main limitation is that the cells will move from their patterned positions in the absence of an acoustic field. [44] However it is possible to immobilize them within a more rigid material once patterned, so that the patterning is not lost following removal from the acoustic field.

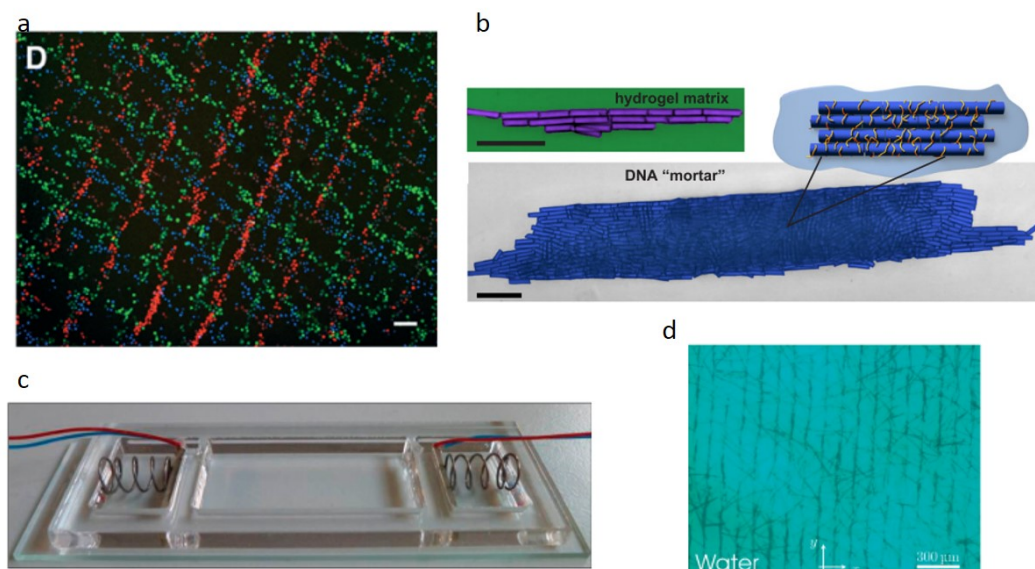


Figure 1.3: a) Patterning of Schwann cells within an acoustic device where each layer of cells was patterned in a different colour to build up the pattern displayed here. Scale bar $100\ \mu\text{m}$ [41] b) The alignments of acoustically trapped anisotropic particles can be fixed into a hydrogel matrix or by using a DNA mortar. Scale bars $100\ \mu\text{m}$ [45] c) photo of an acoustic patterning device used by Scholz *et al.* d) polycrystalline wool fibres acoustically patterned in water in the acoustic device shown in c). Scale bar $300\ \mu\text{m}$ [46]

Immobilisation of ordered particles has formed the basis of some other acoustic patterning research. Collino *et al.* demonstrated the patterning of anisotropic microparticles in an acoustic field with tunable packing. These conformations could be fixed in place and removed from the device by cross-linking a hydrogel matrix, or using a DNA mortar between the different particles (Figure 1.3b). [45] In a similar fashion, acrylic particles have been aligned within polysiloxane resins by first patterning

the particles and then setting the resins. [47] This approach has been adopted for the alignment of nanowires and particles within composite materials (Figure 1.3c & d). [46, 48]

Limitations of this technique arise with the sizes and shapes of the particles that can be trapped. Recent developments have demonstrated trapping of mm sized objects with complex shapes using a lock mechanism. [49] Varying the driving frequency will change the size it is possible to trap within the overall range of μm to mm, as long as the particle radius, a , remains much smaller than the wavelength, λ , of the applied acoustic field ($a \ll \lambda$). [50] The attenuation of the sound waves within the fluid medium is a second limiting factor. However, by increasing the amplitude of the waves to produce sufficient trapping forces, particles or objects will trap in fluid volumes of μLs to litres.

Whilst these different techniques are limited to specific systems, in the field of soft matter they are powerful methods in the fabrication of structured soft materials.

1.4 Soft matter materials: Hydrogels

One of the genres of soft matter materials is hydrogels. The material properties can be understood as the result of the different interactions and forces between the different molecules due to their chemistry. This section will first define a hydrogel and then review the relevant theory underlying hydrogels.

1.4.1 Hydrogels

First documented by Wichterle and Lim in 1960 for use in contact lenses, hydrogels were defined as entangled networks of polymers forming a matrix, which can absorb up to several thousand times their dry weight in water. [51] Flory initially outlined four main types: [52]

- Well-ordered lamellar structures
- Disordered covalent polymeric networks
- Polymer networks through physical aggregation
- Disordered particulate structures

Since this initial observation, the definition of a hydrogel has adapted since they are no longer formed only from polymers. Modern definitions encompass the material properties, with hydrogels defined as soft solid-like materials comprising two or more components, one of which is water present in substantial quantity. The highly hydrated materials exhibit the ability to reversibly swell and will embody solid-like properties, despite consisting of so much liquid, due to the 3D network created through in situ bonds. [53, 54] These in situ bonds are known as cross-links and can arise due to physical or chemical interactions.

The components of the hydrogel contribute towards the overall behaviour, such that the material will exhibit both liquid-like and solid-like properties due to the liquid and cross-linked network respectively. Simply, classification of a material as a gel can be demonstrated by the vial inversion test. When the vial is inverted, if the material formed at the bottom of the vial does not flow and can support its own weight, then it is a gel. [55, 56]

Quantitatively, the material behaviour can be characterised through rheology; the study of deformations and flow of matter. [57] The elastic or storage modulus G' and viscous or loss modulus G'' describe the solid and liquid contributions respectively. Where an elastic response to deformation is exhibited by the material over extended timescales (G' plateau or moduli independence from forces applied at different frequencies with $G' > G''$), this implies the presence of a network that can store the deformation energy rather than dissipating it by flowing, as a solid would. Rheologically, a gel will not relax or flow like a liquid, since the network structure will not relax.

To understand hydrogels as materials, it is important to know how the smaller scale behaviours contribute to the material properties.

1.4.2 Molecules

Materials are comprised of different 'building blocks' known as molecules. Molecules are discrete, spatially ordered, heterogeneous groups of atoms.

In the design of materials, the different properties and capabilities of the molecules included are important. The functionality of a given molecule depends on the elemental composition in combination with the arrangement and connectivity of the component atoms. The connectivity arises through the sharing of electrons between atoms in covalent bonds, which hold all the atoms together

as a molecule. This sharing blurs the distinction of atoms as individuals so that they become part of a larger species. Of particular importance are functional groups which are responsible for specific functions exhibited by a range of molecules. These recurring molecular groups can exist in different charged states, due to the presence or absence of electrons, based on the environmental conditions (pH, salinity, temperature etc.) the molecule is subjected to.

The pH scale is a logarithmic scale concerning the amount of H_3O^+ compared to OH^- present in solution, where $pH = -\log[H_3O^+]$. These both form as a result of proton (H^+) association or dissociation from functional groups when in solution. Given the pH of solution, the charge on the functional group can be known from the acid dissociation constant; $pK_a = -\log[K_a]$ where K_a is a constant for chemical dissociation. At a pH less than the pKa, the functional group will be protonated but at pH greater than the pKa, the group will be de-protonated. [58] Thus the charges on functional groups can be changed by altering the pH of the solution and this is one way that different molecular and intermolecular behaviours can be controlled.

1.4.3 Intermolecular interactions

Fundamental in the design of materials is the different forces existing between different molecules and macromolecules, which act to hold the materials together. With understanding of these different forces, molecules can be designed to utilise particular interactions in the formation of superstructures. [59]

Forces between different molecules arise due to the distribution of electrons within them. As a standard reference for gauging the strength of the different forces, the thermal energy $\approx \frac{3}{2}kT$, can be used where $kT = 2.5 \text{ kJmol}^{-1}$ at standard conditions. A summary of the different interactions is given in Figure 1.6.

Chemical bonds exist between the atoms comprising molecules and can be classified as intramolecular bonds (Figure 1.4). There are two types; covalent and ionic. In covalent bonds the electron density is redistributed between two neighbouring atoms. Covalent interactions are short range and very strong ($\gg kT$). An ionic bond is due to the attraction between two oppositely charged species. Between two atoms, the electrons transfer from one atom to another resulting in two ions and hence a cohesive force holds them together. [60]

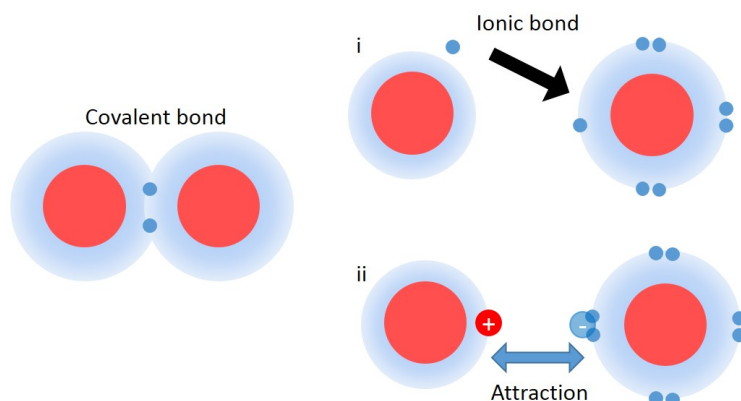


Figure 1.4: Covalent and ionic bonds. Covalent bonds share electrons and ionic bonds rearrange the electrons between the two atoms resulting in ions which then are electrostatically attracted to each other.

Charged species also interact with polar molecules. These molecules have a slight charge, known as a dipole moment, due to the anisotropic electron density distribution over the whole or part of the molecule. The orientation of the dipole is important, and in some molecules it will be permanent but in others it can be freely rotating. Consequently the freely rotating dipoles have weaker interactions. Molecules with a dipole moment of any type can induce the polarisation of other neutrally charged molecules, which don't have a dipole by distorting the electron distribution of that molecule. [61] Cohesive Van der Waals interactions exist between neutral molecules, based on the polarisability of the molecules. A dipole can spontaneously be formed within a molecule due to the random fluctuations in the position of the electrons or the electron distribution can be induced by the charge from a nearby dipole. There are 3 main forms of interaction (Figure 1.5):

- between permanent dipoles
- between dipoles and induced dipoles
- between non-polar molecules due to the fluctuations in electron distribution

The strength of these interactions decays rapidly with increasing interatomic spacing.

Hydrogen bonding and hydrophobic interactions are particularly relevant to water and so are of primary interest with regard to hydrogels. In hydrogen bonding a strong highly-directional bond exists between a hydrogen atom, attached to an electronegative atom and a lone pair bearing

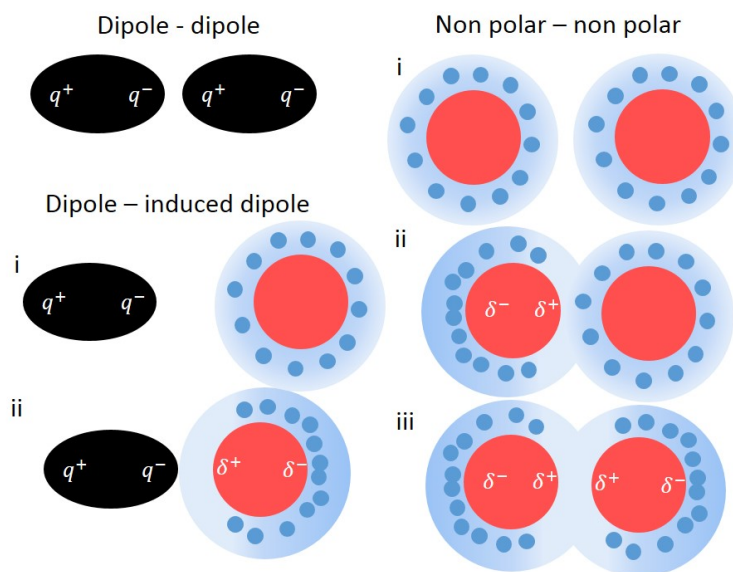


Figure 1.5: Different types of dipole interactions. Dipole - dipole. These interactions exist between permanently polarised molecules. The slight charge is denoted by q . Dipole - induced dipole. A dipole can induce a redistribution of the electrons within a non polar molecule and induce a dipole within it. Induced dipoles are denoted by δ . Non polar - non polar. Dipole interactions can also exist between non polar molecules due to random fluctuations in the electron distribution.

electronegative atom denoted $X-H \cdots Y$, where X and Y are oxygen, nitrogen or fluorine. This hydrogen bond can be considered similar to a charge-dipole interaction. [62]

The differing behaviour of molecules in water is due to their charge compared to the slight charge on the water molecules. Water molecules orient themselves into a framework of H-bonds. When non-polar molecules are added into water, they are initially 'caged' within this water framework and are hence surrounded by water molecules. Non-polar molecules tend to associate with one another and will thus rearrange into aggregates without interference from the polar water molecules. The H-bond framework of water in the presence of these poorly hydrated or hydrophobic chemical groups dynamically rearranges to minimise the overall loss in entropy. This rearrangement releases the water molecules surrounding the non-polar molecules, increasing the entropy of the system. Additionally the rearrangement facilitates the reduction of hydrophobic surface area in aqueous solution, forcing the hydrophobic groups together. These hydrophobic interactions are the driving forces in the formation of micelles from amphiphilic molecules. The hydrophobic sections cluster together to inhibit being 'caged' by the water molecules. Simultaneously the hydrophilic sections

orient to surround the cluster and interact favourably with the polar water molecule framework.

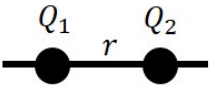
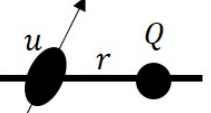
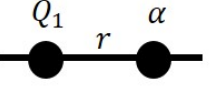
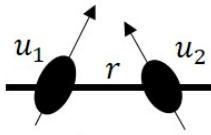
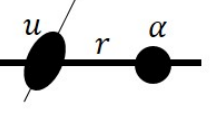
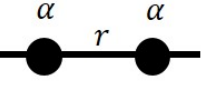
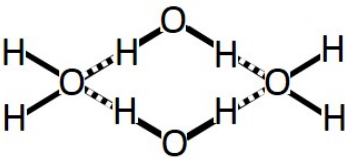
<u>Interaction</u>	<u>Interaction Energy</u>
Covalent	Many
Electrostatic	 $w(r) \propto \frac{1}{r}$
Charge - dipole	
Charge - non polar	 $w(r) \propto \frac{1}{r^4}$
Van der Waals	
Dipole - dipole	 $w(r) \propto \frac{1}{r^6}$ (free dipole) $w(r) \propto \frac{1}{r^3}$ (fixed dipole)
Dipole - non polar	
Non polar - non polar	 $w(r) \propto \frac{1}{r^6}$
Hydrogen-bond	 <p>Complicated form: $r_{OH}(\text{intra}) = 0.1 \text{ nm}$ $r_{OH}(\text{inter}) = 0.18 \text{ nm}$</p>

Figure 1.6: Different types of intermolecular interactions and how they scale with molecular separation. Q is the electric charge, r is the separation of the molecules, u is the induced dipole moment and α is the polarisability of the molecule. Adapted from reference [62]

All these different interactions are important in the formation of large-scale structures. Hydrogels rely particularly on the balance of cohesive forces. They can be broadly classified into two types due to the nature of the bonds holding the 3D network together; physically (H-bonds etc.) or chemically (covalent) cross-linked networks.

1.4.4 Polymer hydrogels

Macromolecules are a single molecule consisting of a chain of repeating smaller units known as monomers. When macromolecules are covalently bound together in a linear sequence through a process known as polymerisation, the resulting molecule is known as a polymer.

The behaviour of these polymer chains is dictated by the inter-chain interactions and the entanglement. Both of which are dependent on three main factors:

- Degree of polymerisation

This defines the number of monomer segments in the chain

- Chemical composition of the monomers

The structure and stereochemistry of each monomer unit

- Monomer distribution

Where polymers are formed from combinations of different monomers, such as copolymers, the distribution can be random, block or branched in different arrangements

When polymers are in solution, the overall behaviour of the chain as a whole within the fluid medium is important, as well as the interactions between the polymer chains and those between the solvent molecules. Different system changes within the polymer solution will serve to encourage or inhibit different interactions. This influence on the interplay of the differing interactions within the solution will govern the interactions between the different polymer chains and resulting solution properties. Where there are very strong interactions between the polymer chains, they can become physically cross-linked into a solid matrix and this material is known as a hydrogel.

There are a variety of different polymer types which can be classified by the behaviour of the monomer units, such as polyelectrolytes which possess charges along the chain which can be permanent or pH dependent. Polymers occur naturally and have also been produced synthetically over the last \approx 150 years. Biopolymers are key components in biological systems and can be classified into 3 groups: polysaccharides, polynucleotides and proteins.

Polysaccharides, otherwise known as carbohydrates, consist of repeating monosaccharides, or sugar units, connected to a hydroxyl group by a glycosidic bond. [63, 64]

Polynucleotides, known as nucleic acids, are the basis for all life as the constituents of both DNA and RNA. There are five different nucleobases; adenine, guanine, cytosine, uracil and thymine which, along with a backbone, comprise a nucleic acid. [65, 66]

Proteins provide the control over the functions within a living organism and are responsible for forming structures, directing biological reactions, the storage and transport of chemicals and to catalyse different reactions. They consist of one or more chains of amino acids held together by peptide bonds, which are a type of covalent bond. [67]

1.4.5 Molecular hydrogels

An alternative process for hydrogel preparation is through the self-assembly of small molecules. [68–70] Molecular self-assembly is ubiquitous across biology and underlies the formation of more complex systems. [71] Fundamentally, molecular self-assembly is the spontaneous arrangement of disordered molecules into a structure based on local non-covalent intermolecular interactions. Since the process occurs at the molecular level, this is an example of a 'bottom-up' process. For molecules to self-assemble without the influence of any external forces, there must be a reduction in the Gibbs free energy such that the thermodynamic stability of the assembled structure is higher than that of the disorganised molecular components. Distinctive features of self-assembly are the increase in order, weak 'non-covalent' interactions and that the ordering can occur between different molecular groups and nanoscale building blocks not exclusively atoms and molecules.

Stable aggregates can be formed through the spontaneous association of molecules under equilibrium conditions, joined by non-covalent bonds. Non-covalent interactions mean that the gelation is reversible. These small molecules, known as low molecular weight gelators (LMWG), self-assemble into one dimensional nanofibril structures, which then bundle and entangle into a fibrogenic matrix through non-covalent interactions. [72] This entangled nanostructured matrix provides the scaffold for gelation, rather than covalent or physical cross-linking as with polymer hydrogels, immobilising water through surface tension and capillary forces. [73]

Many different molecules are documented as LMWG, resulting in a diverse range of structures which will self-assemble into hydrogels. [68–70, 74] Generally, there are hydrophobic and hydrophilic regions of the molecule which ensure compatibility with water and self-assembly. A trigger is required

to initiate the self-assembly and focuses on the interplay of the solubility of the LMWG in two different states of the system. A range of methods can be used to self-assemble the molecules such as heat-cool cycles, cleavage of bonds, solvents or changing pH. [75–78]

Molecules in solution have complex interaction potentials due to the different attractive and repulsive interactions of various strength over varied distances. The added interactions of the solute-solute and solute-solvent must be considered too. When the molecular interactions drive self-assembly a network will be formed. One dimensional structures will assemble through the non-covalent interactions of H-bonding and π -stacking upon environmental triggers. These nanofilaments then bundle into a fibrogenic matrix through further non-covalent interactions (hydrophobic attraction, electrostatics, H-bonding and π - π stacking) between the different assembled components. Cross-links arise from entanglement or branching of these fibres.

A special case of non-covalent interaction between aromatic rings is π - π stacking. These rings contain π bonds which are a particular type of covalent bond where the electron orbitals overlap. In this electrostatic interaction positive point charges are assigned to the carbon atoms in the ring and negative half-charges assigned to the π system above and below the plane. [79, 80] The strength of this interaction is $<20kT$ and widely utilised in the design of soft materials.

A suitable series of gelators are amino acids, often in the form of di- or tri- peptides functionalised with chemical groups at the N-terminus. Chemical groups are usually a large aromatic group, such as fluorenylmethoxycarbonyl (Fmoc), naphthalene or pyrenes. Zhao *et al.* first reported the formation of a supramolecular hydrogel, from the enzymatic transformation of hydrophilic Fmoc-Tyrosine-O-Phosphate to the fibrogenic state of Fmoc-Tyrosine. [81] Since then Fmoc-functionalised peptides have been identified as effective LMWG (Figure 1.7). [77] Further tailoring of the peptide sequences results in different self-assembled morphologies such as tapes, ribbons and tubes. [82]

Where different self-assembly routes can be used on the same LMWG, this will also influence the structures formed. Fmoc-diphenylalanine will gelate through changes in pH or solvent and these different routes will result in a hydrogel with varying mechanical properties. [78] As with polymer hydrogels, there is interest in controlling the hydrogel matrix of molecular hydrogels towards improving the mechanical properties.

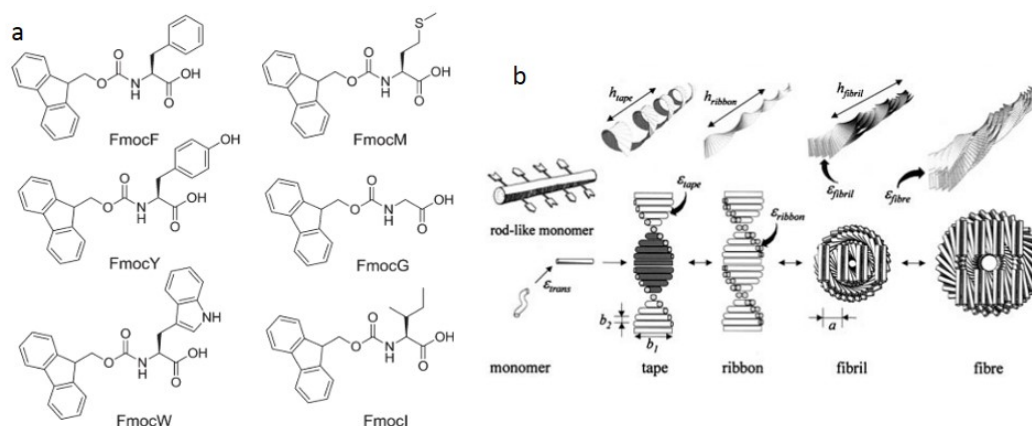


Figure 1.7: a) different low molecular weight gelators from Fmoc-functionalised peptides. FMOCF - Fmoc-phenylalanine, FMOCY - Fmoc-tyrosine, FMOCW - Fmoc-tryptophan, FMOCM - Fmoc-methionine, FMOCG - Fmoc-glycine, FMOCI - Fmoc-isoleucine b) different morphologies possible through tailoring the peptide sequences. Taken from references [77] and [82]

1.4.6 Coacervate-based hydrogels

Of particular note for this thesis are hydrogels formed through the environmentally induced hydrogelation transformation of reconfigurable coacervate droplets. Coacervate droplets based on the complexation of small molecules provide a unique opportunity to use LMWG, which then enables structural reconfiguration into a hydrogel.

Coacervation was first investigated by Bungenburg de Jong in 1929 when he reported the formation of spherical microdroplets in solution upon mixing. [83] Since then, there has been much research into the specific design of coacervate systems and the mechanisms of their spontaneous formation.

1.4.6.1 Complex coacervation

Fundamental in the formation of coacervate droplets is the process of complex coacervation which is the spontaneous structural reorganisation process upon the mixing of two or more oppositely charged macromolecules or polymers due to their associative interactions, into a liquid-liquid phase separation. [84] These two liquid phases; one polymer rich, viscous bulk phase of spherical microdroplets and a polymer sparse supernatant phase, co-exist in thermodynamic equilibrium with the solvent. [85]

The rapid spontaneous formation of coacervate droplets is a delicate balance of forces. The key factors in coacervation are the interaction potential between molecular species, solubility of the free molecular species compared to bound in a complex/aggregate, complex/aggregate size relating to solubility, interactions between solvent and organic molecules and the hydrophobic effect. It is now largely agreed that coacervation proceeds in two steps; first the formation of the droplets and second the phase separation. [86] The enthalpic and entropic contributions can be described by the Gibbs free energy:

$$(1.1) \quad \Delta G = \Delta H_m - T\Delta S_m$$

Droplet formation is driven by the electrostatic interactions towards selective charge neutralization. There must exist sufficient charges for significant electrostatic interactions but not so strong that it causes precipitation (a solid-liquid phase separation). The liquid-liquid phase separation from a homogeneous polyelectrolytic solution into a dense polymer rich coacervate phase and dilute supernatant phase leads to a gain in entropy due to the configurational rearrangements of the phase separation. The molecules assemble into droplets and consequently the interactions between these droplets and the molecules remaining in the other liquid phase are altered, leading to a redistribution of the droplets within it.

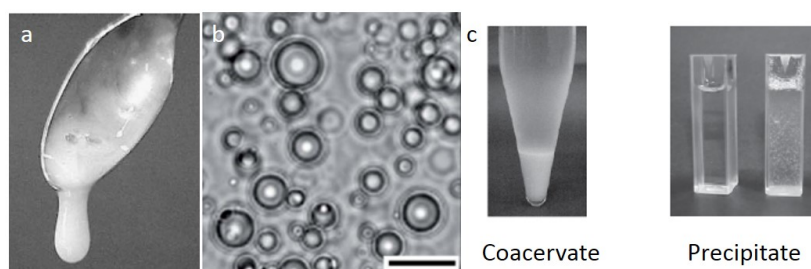


Figure 1.8: a) The coacervate bulk phase is extremely viscous b) coacervate microdroplets as viewed under a microscope. Scale bar 25 μm c) solution undergoing coacervation compared to a solution undergoing phase separation. Images taken from references [87, 88]

The kinetics of the phase separation has been shown to mimic a spinodal decay process (unmixing of one phase to form two distinct phases); from the formation of the micro-droplets at the phase

separation threshold randomly throughout the solution to settling of the bulk phase at the bottom of the vial. Phase separation is driven by electrostatic and solute-solvent interactions. When two oppositely charged segments join, there is some amount of counter ions released into the solvent, increasing the entropy. [89] Further mathematical derivations of the process can be found in reference [86]

1.4.6.2 Coacervate droplet applications

A diverse variety of materials have been shown to undergo coacervation; polyelectrolytes, polysaccharides, proteins and nucleic acids. [87, 90–92] This extensive variety has led to suitability of the droplets in different applications. The exploitation of the droplet behaviours is key in their use across many areas.

The variety of different properties of the coacervate phase from free-flowing liquids to viscous gel-like materials has led to coacervate based food additives to modify the viscosity, foaming ability, interfacial stability or improving flavour. [93–95] Coacervation has also been observed in nature resulting in complex coacervate systems being selected for research into biological areas, including protolife. [96, 97]

Protolife is the area of investigation into the very basic reactions and processes that have evolved into life as we know it. It has been proposed that life developed from non-living molecules through a spontaneous and gradual build up of molecular complexity. [98] The key aspects for any given system to be considered living are the processes of:

- Homeostasis - maintaining of conditions such as salinity, temperature, acidity, etc. to prevent deviation from the chemical functions and processes of the system.
- Replication - the system must be able to replicate itself so that more successful systems can be produced.
- Metabolism - the process of using different molecular species as fuel in maintaining the system.
- Compartmentalization - distinction between the system and its surrounding environment, usually with some kind of barrier or membrane.

Chemical systems which embody some or all of these characteristics are defined as protocells. [99] Further to these characteristics a protocell must form spontaneously, this is another caveat in the emergence of life where the first step would be the self-ordering of molecules into a cell-like structure. [100]

Coacervates are used as protocells, which are cell-like prototypes that embody basic cellular functionalities and behaviours. The molecularly crowded droplet interiors mimic the molecular crowding within real cells. [101] Despite having no explicit membrane, the difference between the coacervate interior and exterior results in the sequestration of various different guest molecules such as dyes, proteins or nanoparticles on the droplet interior. [102, 103] Loading of multiple guest molecules has enabled the droplets to be used as micro-reaction vessels for nanoparticle enzyme catalysis and *in vitro* gene expression. [104–107]

Further to this, coacervates comprising proteins and polyelectrolytes result in bound protein concentrations much higher than that sustainable in aqueous solution with protein functionality retained [108–110] Seonghye *et al.* have demonstrated that coacervation of mussel adhesive proteins results in droplets with increased adhesive properties. [111] The retention of activity of molecules both comprising the droplets and loaded on the interior has been used in drug delivery. [112] For example Macewan *et al.* showed that polymers based on human elastin will undergo a temperature induced reversible phase-transition between solution and coacervate phase, which can be used for release of encapsulated drugs. [113]

1.4.6.3 Specific design of coacervate droplets

To understand the dynamic and adaptive behaviors of living systems requires chemical analogues capable of emulating the processes. In order to study this, reconfigurable systems that sense and respond to external stimuli are fundamental. Structural and functional response are essential for regenerative medicine, actuated materials, dynamic polymer systems and extending protolife research. [114–116]

Through careful selection of chemical components, coacervate droplets can be tailored to exhibit specific functionalities based on the molecules undergoing coacervation. It has already been shown that coacervated molecules retain their functionalities. One system has even been shown to gelate

on the interior of the droplet to form a population of coacervate microgelled droplets. [117]

Reconfigurable coacervate systems are largely unexplored but coacervates comprising polymer/small molecules are promising options. Compared to other coacervate systems, their relatively weak electrostatic interactions increases the potential for manipulation of the droplets through environmentally triggered processes such as pH, salt or temperature induced self transformations. Such systems could be used in reconfigurable ensembles for environmental sensing, biologically inspired materials development, integration of protocells with cells and for storage and release technologies. [118]

1.4.7 Hydrogel applications

The broad range of different materials, both natural and synthetic, that can be used in hydrogels makes them extremely versatile for application in many different areas such as food, agriculture, biomedicine and soft robotics. [119–122]

The range of polymers that can be used, the physical form of the hydrogels, and the differing responses to environmental changes, make hydrogels particularly relevant for imitation of biological structures and processes. [123, 124] Even the cytoplasm comprising the majority of the cell interior exhibits the characteristics of a sol-gel. [125] The similarities between gel materials and living matter have led to substantial improvements and widespread use of viscoelastic materials, particularly in biological research areas. [126–138]

Tissue engineering is the growth of tissues in vitro, supported on a scaffold material, which can then be used in transplantation. To aid in biological integration, biopolymers such as collagen, chitosan or cellulose are often used as scaffold materials. [135] The different metabolic processes of the cells must be maintained throughout and so adequate movement of nutrients and waste products into and out of the cells and the scaffold is important. [137] Diffusion is the primary transport mechanism within a hydrogel scaffold and molecular size, as well as hydrogel properties, will govern the diffusion rate. For example, small molecules such as oxygen or glucose diffuse freely through an alginate hydrogel, however the rate of diffusion of larger molecules, such as proteins, is slower due to the polymer size, cross-linking concentration and pore size. [139, 140]

The diffusion of water into and out of hydrogel materials can also be used in controlling hydrogel behaviour. As a hydrogel swells, the absorption of water can induce macroscopic shape changes.

Bashir *et al.* designed a pH responsive mechanical cantilever based on polymer swelling. As the poly(methacrylic acid) (PMAA) polymer hydrogel expanded in different pH conditions it would bend the attached cantilever to differing extents. [141] Specific stimuli-responses to various environmental conditions, such as temperature, pH or salinity, can be tuned by controlling the functional groups present in the molecules. [142–144]

The extent of swelling within a hydrogel network is important biologically and the hydrogel structure will determine how the water behaves within it. [145, 146] In drug delivery, hydrogel swelling is used for controlled release. As physiological conditions change this will result in differential swelling and the drugs will be released as a direct response to this absorption of water. [131, 147] This approach allows real-time monitoring and delivery of drugs exactly when they are required. [123] For example, the swelling of glucose sensitive hydrogels will trigger the release of insulin for control of blood sugars. [148] Thermosensitive hydrogels such as poly(N-iso-propylacrylamide) will release drugs upon temperature changes and have been used as an on-off switch for drug release in response to temperature changes. [149] Chen *et al.* showed that micelles, loaded with drugs on the interior, can be dispersed within chitosan hydrogels. The micelles act to limit and sustain the rate of diffusion of the drug into the hydrogel matrix and in this way poorly soluble drugs can also be delivered. [130]

For regenerative medicine, the properties must be adapted for stable attachment or integration with the body. [132] This can be achieved by the addition of bioactive components to aid in maintaining cell viability. Biopolymer hydrogels have been used to encapsulate cells producing therapeutic proteins. The hydrogels allow diffusion of metabolic products and substrates but prevent an immune reaction. [138, 150] Copolymerising or functionalising with another molecule can aid in biological processes too. When a methacrylate group is added to poly(vinyl alcohol) (PVA), it allows non-toxic photocross-linking of the hydrogel, so that cells can be seeded prior to cross-linking. [151, 152]

In some cases, the desired properties are unachievable through chemical changes to the structure of the molecules. In these instances multiple hydrogel systems can be combined to enhance the overall properties. Polymer hydrogels based on a combination of both ionic and covalently cross-linked networks have shown improved stretchability, up to 20x their original length compared with some hydrogels that rupture at 1.2x their length. [153] These and other highly stretchable hydrogel materials have even enabled integration of hydrogels with electronics into wearable biological devices. [154]

Further developments in improving hydrogel properties have been the advent of double network hydrogels; a hydrogel composed of two polymers where each contributes different network properties resulting in vastly improved mechanical toughness. [155, 156] In order to select the best materials for the application, an understanding of how the hydrogel structure can influence the overall behaviours and properties is important.

1.5 Microfabrication of hydrogels

This tailoring of hydrogel properties through molecular modifications, or addition of other molecules into the network, can prove successful for desired applications. However, there is evidence to suggest that mechanical properties can be improved by introducing ordered features into the hydrogel networks. [156] For biological hydrogel applications, the diffusion properties must also be considered and are governed by the water content alongside other features of the hydrogel network such as pore size, distribution and interconnectivity. [139] These features are hard to control within the network and are largely dictated by the location of the cross-links. In response to this challenge, hydrogels have been micropatterned in attempts to control the structure of the cross-linked networks.

As the understanding of the molecular interactions has improved, the importance of the arrangement of the 3D network on the overall material properties has been found. Hydrogel swelling and location of cross-links influences the shape, volume, pore size and resulting mechanical or optical properties. The behaviour of water as it enters or leaves the hydrogel network during swelling is largely governed by the location of the cross-links. Thus by imparting order into the cross-linked networks, better control over the swelling of the material is achieved.

1.5.1 Water in hydrogels

To understand the behaviour of water within the hydrogel matrix, it helps to consider the hydration process of a dry hydrogel. The first water molecules to enter the matrix will hydrate the most polar, hydrophilic groups. The network swells as these groups become hydrated, exposing hydrophobic groups which the water will also interact with and become hydrophobically-bound. This water is collectively known as bound water. Once all the polar and hydrophobic sites have bound water

molecules, additional water entering the network due to osmosis is opposed by the cross-links, resulting in an elastic network retraction force. Thus the swelling of a hydrogel has a limit and will reach an equilibrium. This additional water is known as free water and it is assumed that it fills the space between polymer chains, pores and voids within the network. [157]

1.5.2 Controlling cross-linking

In attempts to control cross-linking and the swelling behaviours of hydrogels, a variety of microfabrication techniques have been used as well as combinations of them.

Photolithography has been used in imparting features into hydrogels. Hahn *et al.* demonstrated a variety of patterning with variable periodicity within hydrogels from functionalised poly(ethylene glycol). [158] Patterning was extended to 3D shapes using laser-based lithography by Applegate *et al.* in silk-based hydrogels, with controlled features, demonstrated in 1 cm thick samples. [159] While Wang *et al.* demonstrated the cooperative deformations possible in a composite patterned gel due to the differential swelling in neighbouring regions of material. [160] Guvendiren *et al.* patterned the surface of hydrogels constraining high cross-linking density in particular areas of the material. This was found to control the osmotic pressure and swelling of the hydrogel into different conformations and hence the overall material modulus. [161]

3D printing of hydrogels is mainly performed with temperature cross-linked systems. [162] There are some critical parameters with this technique, such as material temperature for extrusion, and feature retention and temperature difference to drive the speed of gelation. 3D structures are particularly important for scaffold design in tissue engineering and hydrogel based bio-inks are of great interest. These are gel-precursor solutions, extruded alongside cells such that they become embedded within the hydrogel. [22, 163]

Moulds have also been produced using 3D printing. One hydrogel is used as a sacrificial template which a second hydrogel can form around. Once the hydrogel is set, the template can be dissolved leaving a 3D self-supporting structure behind. Bertassoni *et al.* printed agarose gels which were then used as casts for other hydrogel materials to form microchannels. [164] Colloidal crystal templates can be prepared using polymer microspheres, which can then be dissolved once the hydrogel has set around them. [165]

Recently the technique of ionoprinting was used to electrically embed ions into a polyelectrolyte hydrogel by applying a current through it. These ions formed robust cross-links in the hydrogel network, stiffening the hydrogel in those regions. [166] Magnetic particles have also been added into hydrogels, not to aid with their fabrication but to enhance directional properties. [167, 168]

Microfluidic devices have been used alongside photopolymerisation in producing gradient hydrogels. By using a carefully designed inlet, Burdick *et al.* demonstrated controlled concentration gradients can be introduced to the hydrogel by adjusting the flow rate of the precursor solution. [169] In solution, the shape conformation of polymers depends on various solute and solvent interactions. [170] Individual molecules in solution are much smaller in size and form less complicated shapes than polymers, and the electrical or chemical properties of these molecules can be used in manipulation on the nanoscale. [171] Recently an electro-microfluidic device was designed by Chiang *et al.* to pattern a variety of hydrogel precursors based on their differing properties in an electric field. [172] This technique used programmable microgels and other complexes to facilitate in the manipulations. Microgels are cross-linked building blocks containing reconfigurable objects or molecules. Other properties can be introduced by embedding different particles on their interior too, such as magnetite for magnetic properties. [173, 174]

Loading molecular hydrogel components into precursory containers presents larger sized objects that can be manipulated more easily than individual polymer chains/molecules. Introducing particles into hydrogels is a promising approach to advance functionality and improve properties. [175, 176] Dehne *et al.* loaded colloids into hydrogels to influence the elasticity of the hydrogel. [177] The larger sizes of these objects would make them suitable for acoustic trapping, which has been under-utilised in hydrogel patterning. The use of programmable precursory droplets presents an ideal opportunity to combine reconfigurable coacervate droplets with the technique of acoustic trapping in producing patterned hydrogels.

1.5.3 Acoustic patterning of hydrogels

Hydrogels have been used to preserve organised patterns in the absence of an applied acoustic field. The hydrogel matrix acts to immobilize movement of objects away from the trapped locations when the field is removed, which would otherwise occur in aqueous solution. Cells have been patterned

and then fixed into collagen hydrogels to study the effect of controlling extracellular organization. Importantly the cell viability was not affected by exposure to the acoustic field and proliferation of the patterned cells within the hydrogel was increased. [178] Other cells have also been embedded into gels in this manner such as yeast and red blood cells within polyacrylamide, alginate and agar. [179]

Acoustic trapping no doubt provides a powerful tool for fixing ordered objects into hydrogel networks. However, an acoustic field does not affect the hydrogel directly. Manipulation is not possible due to size and insufficient acoustic contrast. [179, 180] Since the gel structure itself can not be manipulated directly, this has limited the use of acoustics in directly patterning hydrogels. Size and shape limitations further hinder use of the technique in direct patterning of both the polymer and molecular hydrogel components themselves. However, acoustic patterning of appropriately sized objects in the form of programmable precursory hydrogel compartments, such as microgels, is a viable route to utilise acoustic patterning in hydrogel fabrication.

Across chemistry there are a variety of different compartment structures, known as vesicles, available which vary in size, composition and materials. In the area of protolife there exist several other cell-like compartments; proteinosomes, colloidosomes, polymersomes and lipid-based vesicles. [181–184] Recently the acoustic patterning of coacervate droplets into 2 dimensional arrays was documented. [185] Coacervate droplets are micron-sized and can be formed from a variety of different combinations of molecules and polymers. Further, through careful selection of the components, comprising LMWG, coacervate droplets have been shown to transform into a hydrogel. [118] This presents an ideal opportunity to combine reconfigurable coacervate droplets with the technique of acoustic trapping in producing patterned hydrogels. It is conceivable that initiating the hydrogel transformation and self-assembly process of such coacervate droplets, while they were held at the pressure minima of a standing wave acoustic field, could impart ordered structures into the final hydrogel network. The work presented herein describes the investigations to fabricate an ordered hydrogel material using coacervate droplets, comprised from a LMWG and polymer, and the technique of acoustic trapping.

CHAPTER

2

MATERIALS AND METHODS

2.1 General Techniques

The information provided in this chapter covers the foundations of the techniques used throughout this thesis, followed by the details regarding experimental methods and procedures.

2.1.1 Microscopy

Optical microscopy in bright-field and epifluorescence mode was performed using a Leica DMI 6000 inverted microscope with 2.5x, 4x, 10x, 20x and 40x dry magnification objective lenses. The fluorescence filters available are displayed in Table 2.1.

Value	Fluorescence	Excitation / nm	Emission cutoff / nm
I3	blue	450-490	510
N2.1	green	515-560	580
D	Violet	355-435	455
A	UV	340-380	400

Table 2.1: Fluorescence filters available in optical epifluorescence microscopy.

The fluorescence phenomenon occurs when a photon of light is emitted from a molecule upon the transition of an excited electron to a lower energy state. Fluorescence microscopy selectively irradiates samples with light in a specific wavelength band. If this matches the absorption wavelength for a specific fluorescent species, electrons will be excited. In samples prepared with fluorescent species, the photons emitted from these chemical species are detected and when compared to the non-emitting background can be used to provide information on structure and behaviour of systems which conventional microscopy can not. [186]

In confocal microscopy a pinhole suppresses out of focus light so only the plane of focus is observed, resulting in a controlled depth of focus into a sample, which optical microscopy can not provide.

In confocal laser scanning microscopy, lasers are used to initiate electronic transitions of electrons to higher energy states. When these electrons return to a lower energy state they will emit photons of light. These are detected by different detector channels in the microscope and used in presenting an image to the user. The controllable depth of focus enables optical sectioning such that detailed 3D renderings of image stacks of fluorescently prepared samples can be produced.

The selective irradiation of fluorescent chemical species at specific wavelengths using lasers enables

multiple fluorophores to be imaged within the same sample. In cases where one laser can induce electron transitions within multiple fluorescent species, a sequential scan can be used to isolate different fluorophores. Several sequential layers can be used. The different detector channels can be assigned specific detection wavelength ranges so that the emission spectra can be tailored to the fluorophore of interest. For every layer of the scan different lasers are activated, thus enabling specific excitation and detection of photons within an energy region of interest.

All fluorescent confocal images were acquired using a Leica SP5-II confocal laser scanning microscope attached to a Leica DMI 6000 inverted epifluorescence microscope equipped with a 150mW Ar laser (458, 476, 488, 514 nm lines), 20mW solid state yellow laser (561 nm), 20mW Red/HeNe diode laser (633 nm) and 50mW 405nm laser with 10x, 20x dry and 40x, 63x oil immersion lenses. Images were acquired using Leica LAS X Acquisition software.

Many different samples prepared with a variety of different fluorophores were investigated throughout the course of this work. The specific experimental set-ups are detailed within the relevant chapters and discussions and experimental methods.

2.1.2 Dynamic Light Scattering and Zeta Potential

In dynamic light scattering (DLS) the hydrodynamic radius, D_H , of a particle is calculated. This is the size of the particles when they are hydrated and includes any adsorbed molecules and surrounding ions. Particles in solution will scatter light and there will be fluctuations in the intensity of the light signal due to their Brownian motion. From this, an autocorrelation function is found and used in extracting the diffusion coefficient, D_t . This is related to the hydrodynamic radius of a particle through the Stokes-Einstein equation: [187]

$$(2.1) \quad D_H = \frac{k_B T}{3\pi\eta D_t}$$

where k_B is the Boltzmann constant, T is the temperature of the sample and η is the viscosity.

While this technique was developed for monodisperse particle sizing, it can be extended to that of polydisperse solutions, such as coacervates, with an average population size being returned.

Charged particles will attract a layer of strongly bound counter-ions, known as the Stern layer. Consequently this layer of counter-ions will attract ions which surround the particle in a layer known as the diffuse layer. Ions here are less associated to the particle such that as the particle moves, some of these electrons will remain in the dispersant as opposed to moving and remaining as a stable part of the ions and particles entity. The zeta potential, ζ , is the charge at the boundary of this double layer.

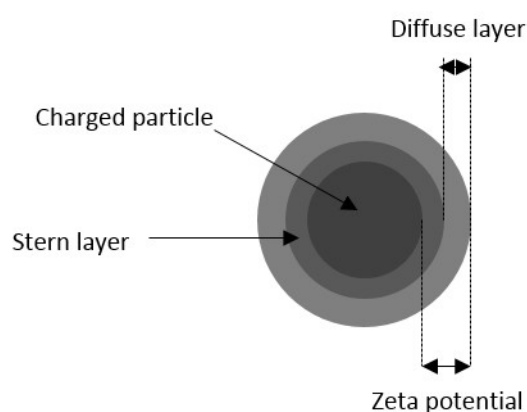


Figure 2.1: Electric double layer of a particle in solution. The double layer consisting of the Stern layer and diffuse layer and the definition of the zeta potential of the particle. [188]

Measurements of the zeta potential are found through analysing the electrophoresis of the charged particles. A capillary cell is used to apply an electric field to the sample under analysis. Under illumination, as the particles move in solution under the applied field, their motion will result in fluctuations in light intensity reaching the detector which is proportional to their speed of movement. From this an electrophoretic mobility, U_E , can be calculated and relates to the zeta potential, ζ , through Henry's equation: [188]

$$(2.2) \quad U_E = \frac{2\epsilon\zeta f(\kappa a)}{2\eta}$$

where ϵ is the dielectric constant, $f(\kappa a)$ is Henry's function and η is the viscosity.

A Malvern Zetasizer Nano ZS machine was used to perform both DLS measurements of the hydrodynamic radii and to find the zeta potential of various coacervate samples. For both set-ups a

He-Ne laser (633 nm) illuminated samples loaded in a cuvette and light scattering was detected by a backscatter detector at 173°. Further information regarding the measurements taken can be found in the relevant experimental methods.

2.1.3 Electron microscopy

High energy electrons are produced via thermionic emission from a tungsten filament. These beams of electrons are accelerated towards samples mounted on a stage, passing through a series of different apertures and focused by electromagnetic lenses. The different interactions of these electrons with the sample are used in creating images. The wave particle duality of electrons states that their wavelength, λ , is proportional to their momentum, p , ($\lambda = \frac{h}{p}$ where h is Planck's constant), typically 12pm for SEM and 2.5pm for TEM, enabling much greater resolution than optical microscopy. [189] In the case of scanning electron microscopy (SEM) upon reaching the sample, different interactions with the surface of the sample can occur producing secondary and backscattered electrons or even X-rays. The electron beam is rastered over the surface of the sample while backscattered electrons are detected and used in producing an image. To improve imaging contrast through sample electron interactions, samples are often sputter coated in an electron dense material such as gold, prior to imaging.

With transmission electron microscopy (TEM) the electrons pass straight through the sample. The resulting absorption or scattering of these electrons are used in producing an image on a fluorescent screen. Samples investigated by TEM are generally thin (100 μm or less) or dilute suspensions dried onto grids. Selective deposition of electron dense atoms around features of interest, through sample staining, enhances the electron sample interaction to aid in better imaging contrast. SEM electrons generally have lower energies than those used in TEM to limit the depth of penetration into samples. Images were acquired using a Jeol IT300 SEM and a Jeol 1400 TEM. Specific sample preparation is outlined in the relevant experimental methods.

2.1.4 Rheology

One of the aims of the work in this thesis was to characterise the effects of introducing order into hydrogels. Hydrogels are interesting materials in that they are neither crystalline solids or free flowing

liquids, but exhibit behaviour somewhere between the two. Several techniques were used when analysing the material behaviour of these soft matter systems, with the technique of rheology used to study the specific response of materials to applied forces. [190]

When a shear stress, σ , is applied, a material will deform in response (Figure 2.2) with the relative deformation of the material known as the strain γ .

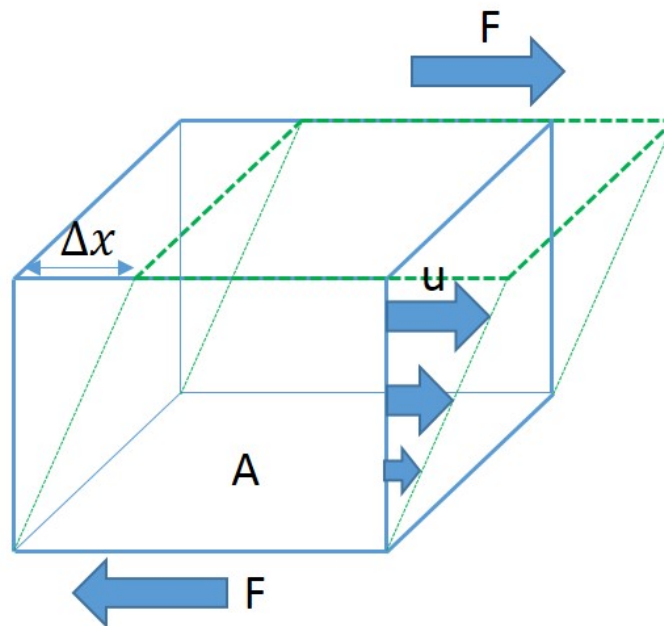


Figure 2.2: Shearing of a solid or fluid between two parallel plates. F is the shear force applied over an area, A , inducing a displacement Δx . In the case of fluids there is a velocity gradient u between the top and bottom plate. For the fluid to move at constant velocity, a constant shear stress must be applied. Across the gap between the two plates, that velocity change must be continuous resulting in a constant strain rate $\dot{\gamma}$.

$$(2.3) \quad \sigma = \frac{F}{A}$$

$$(2.4) \quad \gamma = \frac{\Delta x}{y}$$

where F is the force applied over an area A . Typically, solid materials store transferred energy and resist deformation, while liquids dissipate this energy through flowing. The intermolecular forces between the atoms comprising the material will govern the nature and timeframe of the response due to energy transfer into the material. Hence, the structure of any given material will dictate its behaviour.

A typical Hookean solid will exhibit linear behaviour, with stress proportional to strain, as defined by a constant of proportionality, G , known as the shear modulus

$$(2.5) \quad \sigma = G\gamma = \frac{d\sigma}{d\gamma}\gamma$$

The shape of these materials is always recovered.

Regarding fluids, upon application of a stress the fluid will move until the stress is no longer applied. In a parallel plate setup (Figure 2.2), when the stress is applied to the top of the fluid, the fluid will move at a constant velocity, provided the force is constant. As the two plates are moved there must be a continuous change in velocity across the gap and hence a strain rate, $\dot{\gamma}$, can be calculated. Newtonian fluids have a linear relationship between shear stress and shear rate related by a constant of proportionality, η , known as the viscosity.

$$(2.6) \quad \sigma = \frac{du}{dt}\dot{\gamma} = \eta\dot{\gamma}$$

In the case of soft matter the overall response will be a combination of Hookean and Newtonian behaviour, often varying with time. The material's behaviour can be accounted for by ascertaining the solid-like (elastic) behaviour alongside the fluid-like (viscous) behaviour. Materials embodying both elastic and viscous responses are known as viscoelastic. [55]

For a constrained sample, an oscillating strain can be applied at a defined frequency, f , to study the resulting deformation. The applied oscillating strain develops a time-dependent oscillating stress response within the material. If the strain is oscillating with time, then so must the stress response, as shown in Figure 2.3.

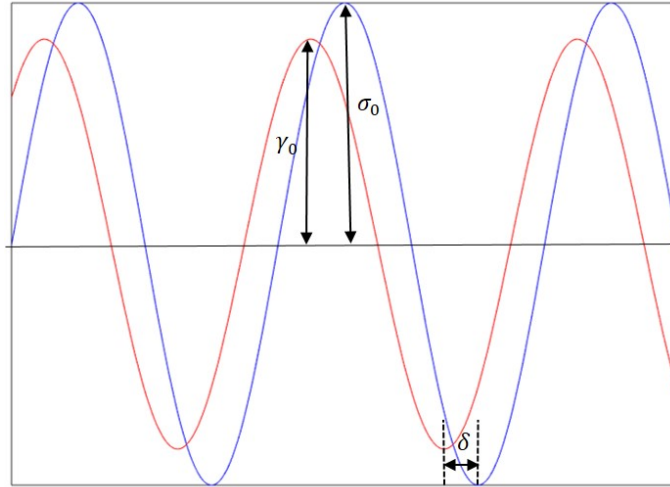


Figure 2.3: The oscillating stress response (blue) to an applied oscillating strain (red). σ_0 is the maximum stress and γ_0 the maximum strain with a phase difference, δ , between the oscillatory strain and stress.

For a given frequency, f , the angular frequency $\omega = 2\pi f$, and the ratio of the maximum stress, σ_0 , and maximum strain, γ_0 is constant and defined by the complex modulus, G^* .

$$(2.7) \quad G^*(\omega) = \frac{\sigma_0}{\gamma_0}$$

The other constant is the phase difference, δ , between the maximum stress and the maximum strain. Stress is proportional to strain in perfect solids and thus solids will respond directly in phase. For perfect fluids, stress is proportional to the rate of strain and a phase difference of $\frac{\pi}{2}$ results. The phase difference for viscoelastic materials will reside between these two extremes ($0 < \delta < \frac{\pi}{2}$), with the elastic energy stored and the viscous energy dissipated described by the phase difference to the applied oscillating stress. Together, δ and G^* , characterise a material's mechanical properties. [190]

G^* can be rearranged to be described by two separate moduli representing the elastic and viscous contributions to the overall material response. In a rheological context, they are known as the storage (G') and loss (G'') moduli respectively.

$$G^* = G'(\omega) + iG''(\omega)$$

$$G'(\omega) = G^*(\omega) \cos(\delta)$$

$$G''(\omega) = G^*(\omega) \sin(\delta)$$

Experiments were performed using a Malvern Kinexus pro rheometer with samples constrained between a base plate and a 20 mm diameter parallel plate geometry at a constant temperature of 25° C. Further details regarding experiments are detailed in the relevant methods later.

2.1.5 Ultraviolet-Visible spectroscopy

In ultraviolet-visible spectroscopy (UV-Vis) different wavelengths of light are passed through a chemical sample. The absorbance of any of this light provides information about optically active species within the sample. When a photon from light of a specific wavelength matches the energy gap required to move an electron from the highest occupied molecular orbital (HOMO) to the lowest unoccupied molecular orbital (LUMO) the energy is absorbed and the electron transitions. Provided this energy gap falls within the range of 190-800 nm, the transition will be observed using UV-Vis.[191] The difference between the intensity of the light incident on the sample, I_0 , and light transmitted, I_t , provides information on the absorbance, A , of the sample which can be found using Beer-Lambert law:

$$(2.8) \quad A = \log_{10} \frac{I_0}{I_t} = \epsilon Cl$$

where ϵ is the extinction coefficient, C is the concentration of the sample and l is the path length that the light travels. Extinction coefficient is the likelihood of energy absorption at a given wavelength, specific to a given chemical species. From this relation, the absorbance of a sample at a given wavelength is directly proportional to the concentration of a chemical species in the sample.

A Perkin Elmer Lambda 750 with a 100mm InGaAs Int. Sphere was used in combination with a Grant LT EcoCool system and a Perkin Elmer Peltier Temperature Programmer 1 to take absorbance

measurements at 25° C in the range of 190-800 nm. Further details can be found in the relevant chapters and discussion sections and experimental methods.

2.1.6 Differential Scanning Calorimetry

Differential scanning calorimetry (DSC) is a thermoanalytical technique used to identify phase transitions and thermodynamic mechanisms. The amount of heat required to raise a sample and a reference sample to a given temperature, as a function of temperature, is found and compared. A sample will require more or less heat flow in a state of transformation compared to the unchanging reference. [192]

Experimental setup consists of two different sealed pans, one containing the sample and the other the reference of air, both within a sealed environment. As the temperature of the whole system changes the difference in heat flow to the sample and reference will describe the different transitions occurring within the sample. An endothermic melting transition from solid to liquid within the sample would be seen as an increase in heat flow to the sample, to continue raising its temperature at the same rate as the reference.

A TA Instruments DSC was used to monitor gel-sol transitions of different hydrogels produced in this work.

2.2 Experimental Methods

All the different methods and protocols concerning the entirety of the work performed in this thesis can be found here arranged by the chapter they were relevant to, so that full attention can be given to the results and discussion sections in the experimental chapters.

2.2.1 Acoustic trapping devices

2.2.1.1 Fabrication

Devices were designed in AUTOCAD and cut out into acrylic using a laser cutter (Trotec Speedy 100). The devices comprised a central 20 mm square cavity, surrounded by 4 orthogonally arranged transducers (Noliac, NCE51 WAE 15 x 2 x 1 mm), attached to the device using superglue. Oppositely sited transducers were wired in parallel into two pairs.

2.2.1.2 Impedance analysis

Impedance outputs of the transducers were analyzed from 1 - 12 MHz using a Trewmac Analyser. These served to identify the driving frequencies and transducers to drive as a matched pair (Section 3.1.3.3).

2.2.1.3 Acoustic patterning of coacervate droplets

Functionalised glass slides (48x64mm Agar Scientific) were attached to the base of the device using Fixogum adhesive. Water wells behind the transducers were filled prior to all trapping experiments. To achieve patterning in 1D, one pair of transducers was driven at a driving frequency, determined through impedance analysis, of 2.15, 6.7 or 11.3 MHz at 10 volts peak to peak (V_{pp}) by a signal generator (Keysight 33220A 20 MHz Waveform generator). For 2D trapping, both pairs were driven, each with a separate signal generator, at 2.15/2.14, 6.7/6.69 MHz, 11.3/11.29 or the frequencies stated.

2.2.2 General methods

2.2.2.1 Lab procedures and data processing

Several routine laboratory techniques were regularly performed. These included use of purified water (Millipore, 18.2 M Ω cm), vortex mixing (Biocote Vortex Mixer SA8), pH measurements (Mettler Toledo pH/ion meter S220), centrifugation (Heraeus Biofuge Primo and Eppendorf Centrifuge S424) and freeze drying (Labconco Freezone 1). Samples were weighed out to an appropriate level of accuracy (± 0.1 mg, Sartorius CP124S).

Images were processed using FIJI (Fiji is just ImageJ, V6.1). Measurements were taken directly from calibrated scale images. 3D confocal image stacks were processed using Volocity (V6.3 Visualisation Package).

Data was processed in both Excel (2016) and MATLAB (R2015a).

2.2.2.2 Slide functionalization

Functionalization of borosilicate glass microscopy slides was required because coacervates wetted out on the surface, due to the negative charge from the silica oxide groups. Functionalization of the surface by addition of side groups from 2-[Methoxy (polyethyleneoxy) propyl] trimethoxysilane, (ABCR GmbH), or hexadecyl trimethoxysilane, (Fluka) to the slide, increased the hydrophobicity by neutralising the surface charge, thus preventing coacervate wetting. To do so the 48x64mm glass slides (Agar Scientific) were sonicated (VWR Ultrasonic Bath) in a beaker containing ethanol to remove surface dirt and expose hydroxyl groups. The rinse was repeated again in ethanol and then MilliQ water. Slides were then dried using compressed air and placed into a 2% PEG/Silane toluene solution and left to incubate overnight at room temperature. After this, slides were rinsed in ethanol twice and again dried with compressed air.

To image coacervate samples, channel glass slides were prepared as shown in Figure 2.4. 22x22mm square coverglasses were functionalized following the protocol above and then adhered onto microscopy glass slides using UV curing optical glue no. 81 (Norland). The glue was set by UV exposure over 20 minutes at 365 nm. A top layer of coverglass was affixed to create two channels using optical glue no. 63 (Norland), again UV cured as before. Channels had a volume capacity of $\approx 10 \mu\text{L}$.

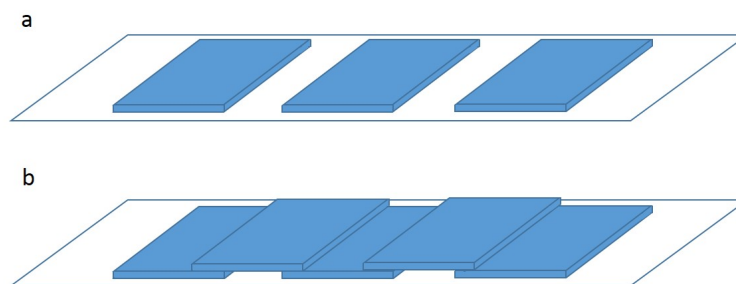


Figure 2.4: Schematic of glass channel slide preparation. a) A first layer of three functionalised coverglass slides were adhered onto the microscopy slide using UV-curing glue. A gap between each is necessary. b) After curing, a second layer of two functionalised coverglass slides were adhered using UV-curing glue such that a channel is formed where the gaps were between the slides on the first layer.

2.2.2.3 Zeta potential

Coacervate samples were prepared at ratios and concentrations of interest. 800 μL of coacervate solution was pipetted into the electrode capillary cell for electrophoresis measurements. Samples were equilibrated for 2 minutes and then 5 measurements of zeta potential were collected. Any data with a large discrepancy was ignored in finding the average values. Between measurements, the capillary cell was washed sequentially with ethanol and MilliQ water and then dried with a compressed air gun.

2.2.2.4 Size distribution of coacervate droplets

Coacervate droplets were prepared at the desired concentration and ratio and subsequently added into a microscope channel slide (Section 2.2.2.2) or observed within the trapping device mounted onto a microscope. Droplet sizes could be directly observed using optical microscopy with images acquired at varying magnifications. Images of the resulting droplets in several areas of the sample were acquired over varying time-frames. Diameter measurements were then taken from these images in FIJI and processed in Excel.

For DLS measurements, coacervates were prepared at the desired concentration and ratio and then loaded into a disposable cuvette with path length 1 cm. Measurements were performed at 25° C following a 1 minute equilibration time.

2.2.2.5 Fluorescent tagging of enzymes

10 mg enzyme was dissolved in 4 mL of a pH 8.5 sodium carbonate buffer (100 mM). 100 μ L of the desired fluorescent tag dissolved in dimethyl sulfoxide (DMSO) (1 mg/mL) was added dropwise to the enzyme solution. This mixture was left to stir at room temperature for 5 hrs in the dark. The solution was then dialysed several times against solutions of pH 7 buffer using dialysis tubing (Medicell membranes 12-14 kDa). Lastly, it was dialysed against MilliQ water for 2 hrs. The tagged protein sample was then aliquoted into eppendorf tubes, flash frozen in liquid nitrogen, and immediately lyophilised for 2 days. The product was stored in the freezer and stocks were made up by dissolving a small amount of product in MilliQ water. Concentrations were found using UV Vis spectra.

2.2.3 Chapter 4 methods

2.2.3.1 FMOC-AA/PDDA Coacervate Preparation

N-fluorenylmethoxycarbonyl di-alanine-OH, (FMOC-AA, BAChem) and poly(diallyldimethylammonium) chloride, (PDDA, Sigma Aldrich, 100-200 kDa) were used as received to produce 40 mM aqueous solutions. The concentration of PDDA was equated with respect to the monomer (M_w (monomer) = 161.7 Da). FMOC-AA required stepwise additions of sodium hydroxide, (NaOH, 1 M) to drive the pH of solution to 8.5 to aid dissolution in water. This solution was then filtered with a 200 μ m filter and used without further purification. PDDA and FMOC-AA solutions were stored at room temperature and used within 3-5 days. For coacervation, first PDDA and then FMOC-AA were mixed directly at the required ratios. In the case of introducing guest molecules into the coacervates they were added to the PDDA at the desired concentration prior to FMOC-AA addition so they were present during coacervation.

2.2.3.2 Coacervate density measurements

Three samples of coacervates were prepared at a 1:1 molar ratio, total volume of 1.5 mL, in eppendorf tubes. Every mass measurement was performed in triplicate for each of the 3 samples. These tubes were all weighed prior to and after addition of coacervate solutions. The measurements were used to acquire the mass of coacervate solution. Each sample was then centrifuged for 15 mins at 5000 rpm

to separate out the bulk and supernatant phases. All of the supernatant was carefully extracted from each tube and stored for later measurements. The mass of the remaining bulk within each eppendorf tube was calculated. A fixed volume of each of the 3 supernatant solutions was also weighed. Through mass conservation laws and the known volumes and masses, a density value was obtained.

$$(2.9) \quad M = M_c + M_{SN}$$

$$(2.10) \quad M = \rho V$$

$$(2.11) \quad \rho = f\rho_c + (1 - f)\rho_{SN}$$

where M is the total mass, ρ the density, V the volume and the subscripts C and SN are parameter values of the coacervate bulk and supernatant phases respectively. f is the volume fraction.

2.2.3.3 Hydrogelation of coacervate droplets

Initiation of the hydrogelation process required lowering the pH of the coacervate solution to initiate supramolecular self-assembly of Fmoc-AA. A small aliquot of coacervate solution was removed, mixed with glucono- δ -lactone (GDL, Sigma Aldrich) powders and then replaced back into the coacervate solution, to final concentration of 20 mM. The slow hydrolysis lowered the pH to a value of 4.5 and transformed the solution into a bulk hydrogel. Samples remained in a humid environment overnight throughout the transformation.

2.2.3.4 Acoustic trapping of coacervate droplets

Coacervate droplets were formed in situ in an acoustic trapping device comprising 4 orthogonally placed transducers surrounding a central square cavity. The transducers were wired in parallel as two pairs. To achieve patterning in 1D, one pair of transducers was driven at the desired driving frequency of 2.15, 6.7 or 11.3 MHz at 10 volts peak to peak (V_{pp}) by a signal generator (Keysight 33220A 20 MHz Waveform generator). For 2D trapping, both pairs were driven, each with a separate signal generator, at 2.15/2.14, 6.7/6.69 MHz, 11.3/11.29 or the frequencies stated. Functionalised coverglass was adhered to the base of the device and the water backing wells sited behind the transducers were

filled with water. In an applied acoustic field, first PDDA, then Fmoc-AA were added at the desired ratio.

2.2.3.5 Hydrogelation of ordered coacervate droplets

Following in situ preparation of coacervate droplets within an applied acoustic field (Section 2.2.3.4), the sample was left to experience the acoustic force for 5 minutes, enabling droplet migration to trapping points. An aliquot of solution (200 μL) was carefully removed, mixed with GDL powder (final concentration 20 mM) and then carefully replaced back to minimise patterning disruption and to mix with the rest of the coacervate solution and lower the pH of the whole volume. Samples again remained in a humid environment overnight, with the acoustic field applied throughout the transformation.

2.2.3.6 Scanning Electron Microscopy imaging of coacervate-based hydrogels

Hydrogel samples were first frozen in liquid nitrogen, with the samples remaining on the glass coverslip throughout freezing. For consistency, unordered gel samples were prepared in moulds that were the same size as the ordered gels formed in the trapping device sample cavity (20 x 20 x 2 mm). Following freezing, all samples were immediately lyophilised for 2 days. Small pieces of the sample were then mounted onto an SEM stub topped with an adhesive carbon pad. Prior to imaging samples were sputter coated in gold to enhance contrast.

2.2.3.7 Transmission Electron Microscopy imaging of coacervate-based hydrogels

5 μL of hydrogel sample, that had previously been sonicated and diluted to expose the fibrils, was mounted onto carbon coated TEM grids. The grids were then rinsed, with MilliQ water, to remove excess hydrogel and then excess solution was wicked away with filter paper. Nanofilaments were negatively stained to improve imaging contrast through addition of 5 μL aqueous uranyl acetate. Excess acetate solution was wicked away and then the samples were left to dry overnight at room temperature.

Carbon coating was achieved by sputtering carbon films onto freshly cleaved mica (Agar Scientific). These carbon films were then floated on to a water filled Buchner filter with copper grids (Agar

Scientific) arranged on the base. Gravimetric filtering resulted in removal of the water and the lowering of the hydrated carbon films over the positioned copper grids. Once dry, the grids were carbon coated.

2.2.3.8 Sequestration measurements

Coacervate samples were prepared in the presence of guest molecules, including a control sample with no guests sequestered. All samples were centrifuged for 15 mins at 5000 rpm to separate out the bulk and supernatant phases. UV-Vis spectra of the supernatant were acquired for each sample. Comparison of the absorption at the characteristic wavelengths for each guest molecule enables quantification of guest molecules remaining in the supernatant and hence concentration of guest molecules residing within the coacervate droplets.

In finding the maximal loading capacity of the coacervate droplets, sequential volumes of the guest molecule were added into coacervate samples. Following separation of the supernatant and bulk via centrifugation, the spectra of the supernatants were analysed. The first sample for which there appeared a noticeable absorbance (≥ 0.1 AU) is the threshold concentration for maximal loading of the guest molecule within the bulk phase.

2.2.3.9 Rheology

Rheological experiments were performed to analyse the properties of ordered and unordered hydrogels. Both ordered and unordered hydrogel samples were prepared to a size of 20x20x2mm. These samples were carefully removed from the trapping device and placed onto the baseplate of the rheometer as self-supporting gels. A 20 mm parallel plate geometry, at a 1.5 mm working distance, was used to perform strain amplitude and frequency sweeps for unordered, 1D (6.7 MHz) and 2D (6.7x6.69 MHz) ordered gels after a 5 minute relaxation time at 25°C. 1D ordered samples were all oriented with the patterning in the same direction on the base plate. All measurements were performed in triplicate and each sample was used for one measurement. Small amplitude oscillatory shear (SAOS) strain sweeps were applied from 0.01-100 % at a frequency of 1 Hz. Frequency sweeps were from 0.1 to 10 Hz at a strain within the linear viscoelastic region for each gel sample. Samples were aged for 2-3 days prior to measurement.

2.2.4 Chapter 5 methods

2.2.4.1 Thin film fabrication protocol

Coacervates were formed in an Eppendorf tube to 1 mL at a 3:7 Fmoc(40 mM):PDDA(40 mM) ratio using 400-500 kDa PDDA. Any guest molecules were added to the PDDA prior to mixing with Fmoc-AA solution. The prepared coacervate solution was added into the trapping device with the acoustic field applied and left to trap for 1 hr (1D) or 30 mins (2D). After this time, the supernatant was removed by the capillary action of dipping a piece of paper towel into a corner of the device. It was held there for a further 10 seconds beyond when the majority of the fluid appeared to have been removed. Following supernatant removal, 1 mL of aqueous GDL (20 mM) was added to replace it within the sample cavity. Samples were then left to gelate overnight in a humid environment in the presence of the applied acoustic field. After this time, the acoustic field was removed and the remaining GDL solution was removed, again via capillary action with paper towel, and the thin film left to air dry.

2.2.4.2 Thin film one-layer one-step enzymatic cascade reaction

Thin films containing horseradish peroxidase (HRP, Peroxidase from Horseradish, Sigma) were prepared as outlined in section 2.2.4.1 with coacervation occurring in the presence of HRP. A reaction mixture of o-phenylenediamine, o-PD, (20 μ L, 50 mM) and hydrogen peroxide, H_2O_2 , (20 μ L, 50 mM) was added to the thin film. Reaction progression was monitored using the evolution of fluorescent product as there was enzyme mediated conversion of non-fluorescent o-phenylenediamine (o-PD) to fluorescent 2,3-diaminophenazine (2,3-DAP), detected using fluorescence microscopy ($\lambda_{ex} = 355 - 425nm, \lambda_{em} = 455nm$).

2.2.4.3 Thin film one-layer two-step enzymatic cascade reaction

Glucose oxidase, (GOx, Glucose Oxidase from *aspergillus niger*, Sigma Aldrich) and HRP were used as received in the enzyme tagging protocol (Section 2.2.2.5) to add tags of rhodamine isothiocyanate (RITC) and dylight-405 respectively. Following the thin film protocol with supernatant removal (Section 2.2.4.1), coacervates were prepared in the presence of RITC tagged Glucose Oxidase (RITC-

GOx, 5 μL , 1 mg/mL) and dylight 405 tagged Horse Radish peroxidase, (dylight-HRP, 40 μL , 1 mg/mL) GOx and HRP form a coupled enzymatic reaction following the addition of GOx substrate glucose ($\beta - D -$ glucose, Sigma Aldrich).

The reaction was again monitored by observing the enzyme mediated conversion of non-fluorescent o-PD to fluorescent 2,3-DAP. Following preparation of the thin film containing both enzymes, fluorescence microscopy was used to monitor the evolution of the fluorescent product as the reaction progressed. A SP5-II confocal laser scanning microscope sequential scan was used with the following settings to monitor each fluorophore; dylight-405 ($\lambda_{ex} = 405 \text{ nm}$, $\lambda_{em} = 410 - 450 \text{ nm}$), RITC, ($\lambda_{ex} = 561 \text{ nm}$, $\lambda_{em} = 570 - 630 \text{ nm}$) and 2,3-DAP ($\lambda_{ex} = 458 \text{ nm}$, $\lambda_{em} = 470 - 520 \text{ nm}$). Green channel fluorescence was monitored to observe the progression of the reaction within the thin film. A reaction mixture of o-PD (20 μL , 50 mM) and glucose (20 μL , 300 mM) was added to the film and the acquired time-lapse images over 1 hr were analysed for fluorescence intensity using FIJI.

2.2.4.4 Enzymatic hydrogelation

Coacervates (400-500 kDa PDDA 3:7 Fmoc-AA:PDDA ratio) were preformed with guest molecule GOx (20 μL , 1 mg/mL) and mixed with 100 μL glucose and left overnight to gelate.

2.2.4.5 Acoustically patterned thin film enzymatic gelation

Coacervates were prepared following the thin film protocol (Section 2.2.4.1) in the presence of GOx (20 μL , 1 mg/mL). Before addition into the trapping device, glucose (100 μL , 300 mM) was mixed into the coacervate solution. After 1 hour of trapping, the excess supernatant solution was wicked away with a paper towel. No solutions were added to replace the removed fluid. Samples were left to gelate overnight in a humid environment with the acoustic field applied throughout.

2.2.4.6 Enzymatically gelated thin film layering

The first layer of 1D patterned enzymatically gelated thin film was produced following Section 2.2.4.5. A second layer was patterned 24 hours later in 1D following the same protocol and using the orthogonally oriented transducer pair.

2.2.4.7 Enzymatically gelled thin film enzyme reactions

Layer 1, patterned in 1D, contained RITC-GOx (20 μ L, 1 mg/mL) and the 1D orthogonally patterned layer 2 contained dylight-HRP (40 μ L, 1 mg/mL) and untagged GOx (20 μ L, 1 mg/mL). Addition of a reaction mixture of o-PD and glucose again enabled monitoring of the progression of the GOx/HRP coupled enzymatic cascade reaction through fluorescence microscopy as detailed in Section 2.2.4.3.

2.2.5 Chapter 6 methods

2.2.5.1 PLys/AMP Coacervate preparation

Poly-L-Lysine (PLys, poly-L-Lysine hydrochloride salt 15-30k, Sigma Aldrich) was used as received to prepare a 50 mM aqueous solution at pH 8. Adenosine-5'-monophosphate (AMP, adenosine 5'-monophosphate monohydrate, Sigma Aldrich) was used as received to prepare a 50 mM aqueous solution in HEPES buffer (pH 7.4, 10 mM).

2.2.5.2 AMP nucleotide gelation

Following the protocols provided by Liang *et al.* the AMP did gelate. Zinc chloride ($ZnCl_2$), (Sigma Aldrich) was used as received to prepare 100 mM aqueous solutions. Mixing with $ZnCl_2$ at varying volumes and concentrations resulted in hydrogelation.

2.2.5.3 PLys/AMP coacervate gelation

Coacervates were prepared at the desired molar ratio and concentration using 50 mM PLys and AMP solutions and then diluted using HEPES buffer (pH 7.4 10 mM). Further addition of $ZnCl_2$ (varying concentrations and volumes) induced gelation.

2.2.5.4 Acoustic trapping of PLys/AMP coacervates

Coacervates were prepared at the desired ratio to total volume 200 μ L using 50 mM PLys and AMP in an eppendorf tube. Addition of 800 μ L HEPES (pH 7.4 10 mM) diluted the coacervates to a suitable trapping volume. The coacervate solution was then added directly into the sample chamber in the presence of an acoustic field.

2.2.5.5 Acoustically patterned PLys/AMP coacervate hydrogels

Following the protocol for acoustic trapping of coacervates (Section 2.2.1.3), after 1 hr in the applied field, 400 μL ZnCl_2 was added to produce a bulk ordered hydrogel. For thin films, the supernatant was removed using paper towel as previously (Section 2.2.4.1). The removed solution was replaced by 1 mL ZnCl_2 (50 mM) which rapidly transformed the patterned coacervates. Followed by removal of aqueous ZnCl_2 after 5 minutes.

2.2.5.6 Rheology of PLys/AMP coacervate hydrogels

Unordered samples were prepared at the desired AMP concentration or coacervate ratio (PLys:AMP to 200 μL then diluted with 800 μL HEPES buffer) to total 1 mL. 400 μL 50 mM ZnCl_2 was added. Samples were loaded onto the baseplate of a 20 mm circular parallel plate geometry using a spatula. Excess liquid was wicked away with paper towel upon lowering the geometry to a working distance of 1.5 mm. Samples were left for 5 minutes and then sequences run at 25 °C. Strain sweeps were acquired at a frequency of 1 Hz from 0.1 - 100 % strain. Frequency sweeps were acquired at a constant strain of 1% from 0.1 - 100 Hz. Each sample was used for one measurement and then disposed of, with data averaged in triplicate.

For viscoelastic changes with time, measurements were acquired every 10 minutes. Sample hydration was maintained by the presence of water containers.

2.2.5.7 Differential Scanning Calorimetry

Samples were prepared at the desired AMP concentration or coacervate ratio (PLys:AMP to 200 μL then diluted with 800 μL HEPES buffer) to total 1 mL. 400 μL 50 mM ZnCl_2 was added. Samples were then left overnight.

20-30 mg of gel sample was carefully placed into an aluminium hemetic pan which was then sealed. A reference pan of air was used. Runs from 10 to 90 °C at a ramp rate of 2 °C/min were acquired in triplicate for each sample.

CHAPTER

3

THEORY AND DEVELOPMENT OF ACOUSTIC TRAPPING DEVICES

Chapter overview

This chapter focuses on the theoretical analysis of the acoustic trapping phenomena and introduces the design and development of the acoustic trapping devices used for acoustic patterning in this thesis. Some discussion regarding the device design is then given.

3.1 Introduction

Particle trapping with sound was first documented by Faraday in 1831 where he observed patterns in sand on the surface of a Chladni plate, resulting from the vibrations of acoustic waves. [193] These sand patterns varied as a function of the mode shape, due to the vibrational modes of the plate.

Kundt later observed acoustic trapping in a fluid. In 1868, he observed that dust collected at specific intervals along a pipe connected to a vibrating metal rod. The dust piles were shown to coincide with the nodal positions of the acoustic standing wave within the pipe, appearing at every half-wavelength distance (Figure 3.1). [194, 195] Through the relationship of the half-wavelength spacing and the medium of propagation, Kundt was able to measure the speed of sound in a number of different gases. Since then interest has shifted to the behaviours of the particles within the waves, into a research field now known as acoustic trapping.

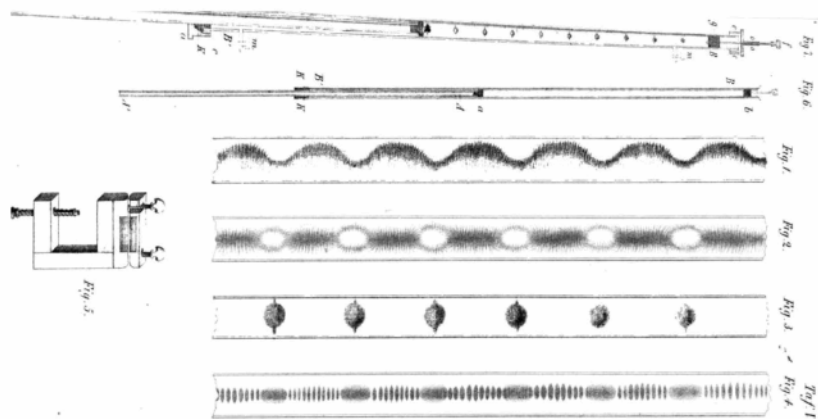


Figure 3.1: The trapping of dust at half-wavelength spacing within a pipe, known as Kundt's tube. Reproduced from reference [195]

King was the first to calculate forces from acoustic fields acting on incompressible spherical particles within an inviscid fluid in 1934. [196] It was shown that the forces experienced by the particles originate from scattering of the waves off the surface of the particles and the non-linear response of the fluid. Yosioka and Kawasima extended this analysis for compressible particles in 1955. [197] Later, Gor'Kov eloquently demonstrated that the acoustic force can be derived from the derivative of an energy potential, calculated from the linear terms of the wave equation. This is the approach that is used for modelling and deriving forces today. [198]

3.1.1 Origins of the acoustic force

When an acoustic wave propagates through a medium, it will be scattered by any particles held in suspension. As a result, these particles experience an acoustic force and consequently they will move, with their motion known as acoustophoresis. [199]

Several scientists observed and mathematically described the acoustic force with the most concise description provided by Gor'kov in 1962 defining acoustic force, F^{rad} , as the gradient of a potential, U^{rad} : [198]

$$(3.1) \quad F^{rad} = -\nabla U^{rad}$$

$$(3.2) \quad U^{rad} = \frac{4\pi a^3}{3} \nabla \left\{ \frac{1}{2} f_1 \kappa_0 \langle p_{in}^2 \rangle - \frac{3}{4} f_2 \rho_0 \langle v_{in}^2 \rangle \right\}$$

with U^{rad} defined for a spherical particle with radius, a , bulk modulus κ_0 , $\langle p_{in}^2 \rangle$ and $\langle v_{in}^2 \rangle$ the time averaged squared sound pressure and velocity respectively. Factors f_1 and f_2 are constants relating the compressibilities of the particle, κ_p , and fluid, κ_0 , and the densities of the particle, ρ_p and fluid, ρ_0 , respectively.

$$f_1 = 1 - \frac{\kappa_p}{\kappa_0}$$

$$f_2 = \frac{2(\rho_p - \rho_0)}{2\rho_p + \rho_0}$$

The above equations hold for particles which act as weak point scatterers of acoustic waves and are much smaller (radius, a) than the acoustic wavelength, λ , ($a \ll \lambda$). The terms relate to the first order scattering coefficients for a multipole expansion, arising from the scattered mass of fluid and motion of the particles. A more detailed derivation of this equation is eloquently presented by Bruus in the Acoustofluidics series. [200]

The acoustic radiation force will arise from the differing compressibility or density between the particles and the host fluid. [201] It is worth mentioning the effect of the secondary radiation force which arises from the interactions between compressible particles moving in an acoustic field. Oscillating pressure changes from the acoustic field induce volume changes of the particles in solution which results in net forces. These forces, known as Bjerknes forces, are attractive resulting in the particles joining together and behaving as a single entity. As they then move towards the trapping points, they can form several lines of sub-wavelength spaced structures perpendicular to the direction of the applied field. There are attractive forces between the different particles within the line but repulsive forces between each line resulting in a fixed separation between the lines. [202] This distance can be used in determining the compressibility of the particles if their density and the properties of the fluid are known.

3.1.2 Acoustic trapping

Acoustophoresis is exhibited by particles suspended in a fluid in the presence of both progressive and standing waves. Progressive waves are singular and propagate through a medium while standing waves are a combination of wave forms resulting in stationary nodal and anti-nodal positions. Shaping an acoustic field to limit the particle movement to a given position forms an acoustic trap. [203] Trapping is the fundamental purpose for use of acoustic devices within this work. The acoustic force is derived for a 1-dimensional standing wave and then extended to that of 2-dimensional

standing waves as these are representative of the experiments presented and discussed later in this thesis.

3.1.2.1 1-dimensional standing wave

A 1D planar, half-wavelength, standing wave in a channel of width w can be described as $p_1(z) = p_a \cos(kz)$ where $k = \frac{\pi}{w}$ and $\frac{\lambda}{2} = w$. Analyzing the radiation force from such a field, the first order incoming pressure $p_{in}(z, t)$ and velocity $v_{in}(z, t)$ fields, at time t and spatial coordinate, z , in a 1-dimensional acoustic standing wave are:

$$(3.3) \quad p_{in}(z, t) = p_a \cos(kz) \sin(\omega t)$$

$$(3.4) \quad v_{in}(z, t) = -\frac{p_a}{\rho_0 c_0} \sin(kz) \cos(\omega t) \mathbf{e}_z$$

with p_a the pressure amplitude, wavenumber, $k = \frac{\omega}{c}$ and angular frequency, ω . Substituting the time averaged pressure and velocity into Equation 3.2, (where $\cos^2(\omega t) = \sin^2(\omega t) = \frac{1}{2}$), the time averaged acoustic radiation potential is thus:

$$(3.5) \quad U^{rad} = \left\{ \frac{f_1}{3} \cos^2(kz) - \frac{f_2}{2} \sin^2(kz) \right\} * \pi a^3 \kappa_0 p_0^2$$

which differentiated to give the acoustic force yields:

$$(3.6) \quad F_z^{rad} = 4\pi A_c k a^3 E_{ac} \sin(2kz)$$

where A_c is the acoustophoretic contrast factor:

$$(3.7) \quad A_c = \frac{f_1}{3} + \frac{f_2}{2}$$

A_c serves to identify the pressure positions in the standing wave field where the particles will trap. For $A_c > 0$, particles denser but less compressible than their surrounding fluid will be trapped at pressure nodes while for $A_c < 0$, where the particles are less dense and more compressible than the surrounding media, particles will trap at pressure antinodes. The $\sin(2kz)$ factor in F_z^{rad} results in the acoustic force oscillating at twice the frequency of the applied acoustic field and phase shifted with respect to it, resulting in stationary trapping points at half-wavelength spacing (Figure 3.2). [200]

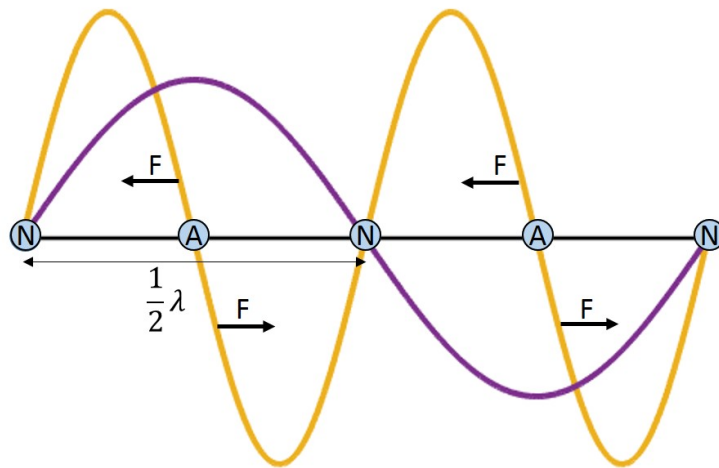


Figure 3.2: Schematic of the forces within a 1-dimensional acoustic standing wave. The purple line shows the acoustic pressure which generates an acoustic force, F , along the axis of propagation at twice the acoustic driving frequency (yellow line). The nodes and antinodes of this profile are shown denoted by N and A respectively. Arrows show the direction of the acoustic force acting on the particles, here towards the nodal positions, as is the case for particles denser than their surrounding media ($A_c > 0$).

and E_{ac} is the acoustic energy density:

$$(3.8) \quad E_{ac} = \frac{p_a^2}{4\rho_0 c_0^2}$$

The acoustic energy density can be viewed as a parameter that characterises the performance of an acoustic device, since the acoustic forces vary with the energy imparted into the fluid. Values of the energy density are hard to estimate, since it is limited by the coupling of acoustic energy from the transducer and the energy dissipated before entering the fluid. Values of E_{ac} for low voltage transducers driven at low MHz frequencies are believed to be $\approx 10 - 100 \text{ J m}^{-3}$. [200]

3.1.2.2 2-dimensional standing wave

Later, it was shown that the Gor'kov potential could be defined using acoustic pressure. [204] This step enabled a much simplified calculation of the acoustic force from the pressure field. The different contributions from fields applied in two directions can be further simplified if they are driven at two different frequencies to minimise the wave interference. This independence can be assumed for the scenarios where any interference between the two wave fields averages to zero within a time frame much less than the response times of the particles. For example a frequency difference of 10 kHz takes 10 ms for 100 cycles of averaging which would be sufficient to have averaged interference to zero. Compared with a particle response time to the field of seconds or minutes, 10 ms would be significantly less and so the independence of the two fields can be assumed.

Continuing from the 1-dimensional analysis, with the pressure given by $p = p_0 \cos(kx) \sin(\omega t)$ based on a plane wave assumption, a second field established in an orthogonal direction to the first results in a total acoustic radiation force, F^{rad} of:

$$(3.9) \quad F^{rad}(x, y) = F_x \sin(2k_x x) \mathbf{e}_x + F_y \sin(2k_y y) \mathbf{e}_y$$

where \mathbf{e}_x and \mathbf{e}_y are directional vectors and k_x and k_y are the wavenumbers in x and y directions respectively.

This can be further extended to obtain the acoustic force from a transducer using the Huygen's construction of superposed linear wave theory (Section 3.2.1). The 4 transducer trapping device arrangement is the most interesting in terms of the field properties. In these devices, assuming the

waves are orthogonal but with different angular frequencies and phases such that they are incoherent the expressions for pressure, p , and velocity, v , are given by:

$$(3.10) \quad p = A \sin k_1(x - x_0) \sin(\omega_1 t + \phi_1) + B \sin k_2(y - y_0) \sin(\omega_2 t + \phi_2)$$

$$(3.11) \quad v = \frac{A}{c_0 \rho_0} \cos k_1(x - x_0) \cos(\omega_1 t + \phi_1) \mathbf{e}_x + \frac{B}{c_0 \rho_0} \cos k_2(y - y_0) \cos(\omega_2 t + \phi_2) \mathbf{e}_y$$

where A and B are amplitudes in x and y, k is the wavenumber with 1 and 2 subscripts denoting x and y respectively, ω is angular velocity, x, y and x_0 , y_0 the positions and offsets after time, t with phase of wave ϕ and direction vectors \mathbf{e}_x and \mathbf{e}_y . Squaring both these terms with $\sin^2(x) = \cos^2(x) = \frac{1}{2}$ results in:

$$(3.12) \quad \langle |p^2| \rangle = \frac{1}{2} A^2 \sin^2 k_1(x - x_0) + \frac{1}{2} B^2 \sin^2 k_2(y - y_0) + \frac{1}{2} AB [\cos(k_1 x - k_2 y) - \cos(k_1 x + k_2 y)] \cdot \langle \cos(\omega_1 - \omega_2) t - \cos(\omega_1 + \omega_2) t \rangle$$

The mixing term decays at a rate $\frac{1}{T(\omega_1 - \omega_2)}$ where T is the time over which the averaging occurs. A similar term is found in the expression for $\langle |v^2| \rangle$. Over sufficient time for these mixing terms to decay, the time dependent phase and positional offsets of the two wave fields can also be neglected leaving:

$$(3.13) \quad \langle |p^2| \rangle = \frac{1}{4} A^2 (1 - \cos 2k_1(x - x_0)) + \frac{1}{4} B^2 (1 - \cos 2k_2(y - y_0))$$

$$(3.14) \quad \langle |v^2| \rangle = \frac{A^2}{4(c_0 \rho_0)} (1 + \cos 2k_1(x - x_0)) + \frac{B^2}{4(c_0 \rho_0)} (1 + \cos 2k_2(y - y_0))$$

following trigonometric simplifications, taking gradients and substituting into Equation 3.2 yields:

$$(3.15) \quad F^{rad} = -4\pi a^3 \left[\frac{1}{3} f_1 + \frac{1}{2} f_2 \right] \{ E_{ac}^x k_1 \sin 2k_1(x - x_0) \mathbf{e}_x + E_{ac}^y k_2 \sin 2k_2(y - y_0) \mathbf{e}_y \}$$

Consequently the force due to two orthogonal standing waves can be written as the superposition of the forces from the two waves. This will only hold for situations where the mixing terms have time to decay to zero.

3.1.3 Acoustic Trapping Devices

The mathematical descriptions of acoustic fields given here describe static acoustic fields, where the fields are fixed by the device geometry and resonant modes. These trapping devices largely fall into two categories; surface acoustic wave (SAW) devices and bulk acoustic waves (BAW) devices. Surface waves are typically generated using a series of electrodes, prepared lithographically, on a piezoelectric material. [205] The electrode spacing matches the acoustic wavelength of the surface wave at the desired driving frequency. When the electrode is driven, a SAW is generated which propagates in either direction within the acoustic material. This excitation wave only propagates in 2D due to the fact it is constrained to the solid surface and will penetrate less than one wavelength deep into that solid. [206]

In contrast to SAW, bulk waves are generated from piezoelectric materials and propagate through the bulk of the fluid. They can further be classified into two groups; propagating or counter-propagating wave devices. Propagating waves pass in only one direction while counter-propagating waves are two wave-forms interacting with each other.

In the case of propagating waves, the refraction of acoustic beams passing through particles produces sufficient forces for acoustic trapping. This behaviour is the basis of acoustic tweezers and single-beam acoustic levitators. [207–209] Counter-propagating wave devices are described in more detail as they are relevant for the devices used in this thesis.

3.1.3.1 Counter-propagating standing wave devices

Acoustic fields are produced by driving piezoelectric transducers. A description of the piezoelectric effect is given in Section 3.1.3.2. A standing wave can be generated as a superposition of two counter-propagating acoustic waves. This results in stable pressure gradients with sufficient acoustic forces to trap particles in suspension.

The simplest counter-propagating setup is that comprising one transducer and a strongly reflecting boundary as shown in Figure 3.3. The transducer is attached to one side of a fluid filled cavity. Upon excitation, the transducer vibrates and emits acoustic energy into the fluid. This outgoing wave propagates through the fluid to the other side of the cavity where it is then reflected by the sound hard boundary. This reflected wave, travelling in the opposite direction, acts as the counter-propagating wave and interacts with the outgoing wave to form a standing wave. The driving frequency of the transducer is chosen so that it corresponds to the cavity resonance, such that an integer number of half-wavelengths is supported, resulting in a standing wave with stable acoustic traps. [33, 210, 211]

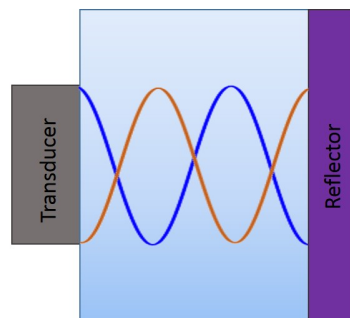


Figure 3.3: Schematic showing the one transducer counter-propagating standing wave. The transducer (grey) is excited at a resonant frequency, here the 3rd cavity resonance, generating a bulk acoustic wave (blue wave). This wave propagates through the fluid until it reflects off the sound hard boundary (purple), reflecting the sound wave back towards the transducer (orange wave) and setting up a standing wave which can be used for acoustic trapping.

Further modifications can be made to maximise the acoustic forces within the device. When driven at their resonance, transducers will impart larger mechanical forces and greater acoustic energy. Dimensions of the transducers can be selected with respect to the cavity dimensions so that the driving frequency corresponds to the cavity resonant frequency. Exciting at the cavity resonance will trap the wave within the cavity, reflecting back and forth and further increasing the amplitude

of the standing wave, and hence acoustic trapping forces, with every pass. Stronger fields will also be achieved where the reflection coefficients within the device are high, including reflection off the surface of the transducer, as the number of passes of the wave across the cavity can be increased through multiple reflections. [212]

Where the manipulation capability of a trapping device is required, a standing wave can be formed from two separate transducers so that the trapping positions within the cavity can be altered. Each transducer is sited either side of the cavity, as shown in Figure 3.4, and driven at the same frequency. The resulting counter-propagating waves set up a standing wave within the device and stable trapping positions at half-wavelength spacing. Through changing the phase difference between the two waves, the trapping positions can be altered. [212]

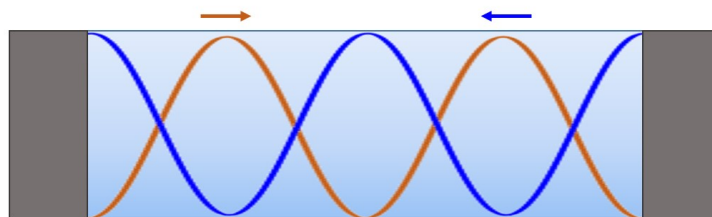


Figure 3.4: Schematic showing the two transducer counter-propagating standing wave. Transducers are grey blocks and the different coloured waves show that they originate from different sources with direction of propagation shown by the correspondingly coloured arrows, assuming no reflection of the waves off the surface of the oppositely sited transducers. Stable trapping points are located at half-wavelength spacing where the two waves intersect.

Minimisation of reflections of the acoustic waves off any boundaries within the setup is crucial. Initially, the use of absorbent backing and matching layers were introduced to the devices to reduce reflections and improve the efficiency of energy transfer from the transducer to the fluid respectively. [212] However, modelling revealed that the acoustic reflection coefficient becomes zero when a transducer is driven at resonance. Hence, they are effectively acoustically transparent and incoming waves will pass straight through, negating the need for backing or matching layers and instantly simplifying the manufacture of these devices. [42]

While devices can be driven at any frequency, transducers do not behave uniformly across them all. Maximum energy from the transducers is achieved at resonant frequencies. Driving them at other frequencies results in substantially smaller amplitudes, but also increases their reflection coefficient.

In some cases, the reflected waves will superpose to amplitudes that compensate for the drop in amplitude of the initial wave, leading to strong enough fields to trap particles. As such the amplitude of the standing wave in the device is a result of the cavity reflections alongside the output from the transducer. [213]

When driven at resonant frequency, both variations of the counter-propagating wave devices have the capacity for particle manipulation due to the possibility of dynamic field reconfigurations enabling varying pressure fields and hence trapping points with time. While the manipulation capabilities were not utilised in any experiments performed in the work presented in this thesis, the expertise in the fabrication of these counter-propagating devices was used in designing the trapping devices for the coacervate systems.

3.1.3.2 The piezoelectric effect

In 1880 Pierre and Jacques Curie observed generation of electrical charges through applying pressure to quartz. This phenomena is now well known as the piezoelectric effect and can be observed in some natural and man-made materials. [214] Application of electrical charges will also generate mechanical deformations within the materials, in the reverse piezoelectric effect. A summary of the role of the piezoelectric effect in producing acoustic fields is given below.

The most commonly used single crystal piezoelectric material is that of lithium niobate. At temperatures less than the Curie Temperature, T_C , there is distortion of the unit cell resulting in an asymmetry in the location of the central ion, thus polarising the unit cell. Upon application of pressure, the unit cell will distort further, moving the central ion off axis and generating charge within the material; the piezoelectric effect. Conversely, applying an external electric field will move the central ion, distorting the shape of the unit cell. For an individual unit cell this deformation is tiny but within larger materials, with many aligned unit cells exhibiting the same behaviour, the mechanical displacements can be large.

The acoustic fields in trapping devices are largely produced using piezoelectric transducers; piezoelectrics coated with conducting materials to act as electrodes. Application of an external electric field induces shape changes within the piezoelectric (Figure 3.5). Polar domains will align in the applied electric field in the direction of current flow. If an alternating current is applied than the

change in alignment direction of the crystals in the piezoelectric oscillates at the frequency of the applied alternating current. Consequently a periodic shape change is set up. Vibrations, due to these rapid shape changes coinciding with the alternating electric field, impart mechanical energy into the acoustic chamber, thus generating the acoustic fields. [214, 215]

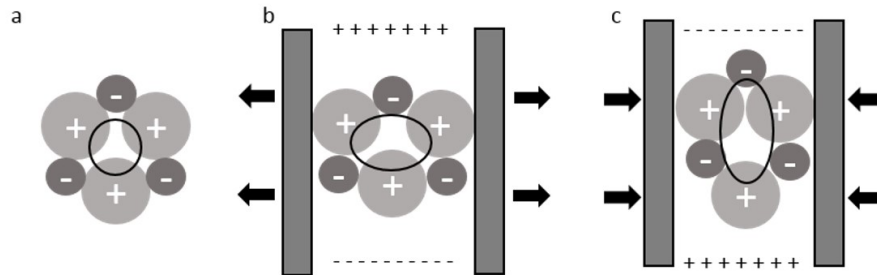


Figure 3.5: Schematic showing the shape changes within a piezoelectric material under an applied alternating current. Transducer faces are represented by the grey rectangles with overall shape displacement indicated by the arrows a) the shape of the unit cell within the piezoelectric b) upon application of the field in the first direction, the unit cell becomes deformed and changes the shape of the transducer as indicated by the arrows. c) reversing the direction of the field, results in material deformation in the other direction. As the current continues to oscillate the periodic deformations impart acoustic energy into the surrounding materials.

Since the acoustic energy from the transducers relies on the mechanical deformations of the crystal, they are narrow band emitters, which must be driven at specific driving frequencies for highest efficiency.

3.1.3.3 Impedance analysis

The largest mechanical output from the transducers will impart the strongest acoustic forces within a trapping device. These strong vibrations will occur at particular frequencies based on the resonance of the transducer. Resonant frequencies can be identified by ascertaining at which frequency the largest mechanical output is seen compared with other frequencies, for the same applied voltage. While the 2 transducer devices can be driven at any frequency, this requires a lot more power to be supplied to increase the vibrations enough to achieve sufficient trapping forces. So transducers tend to be driven at their resonant frequencies to minimise the voltages that must be applied.] [216]

The resonant frequencies are dictated by the material thickness and how the internal vibrations behave within it. Assuming the faces of an unconstrained transducer behave like parallel plates, they

will move uniformly and freely such that they behave like an open pipe. When vibrated at specific standing wave frequencies, known as modes, the waves travel within the transducer as shown in Figure 3.6.

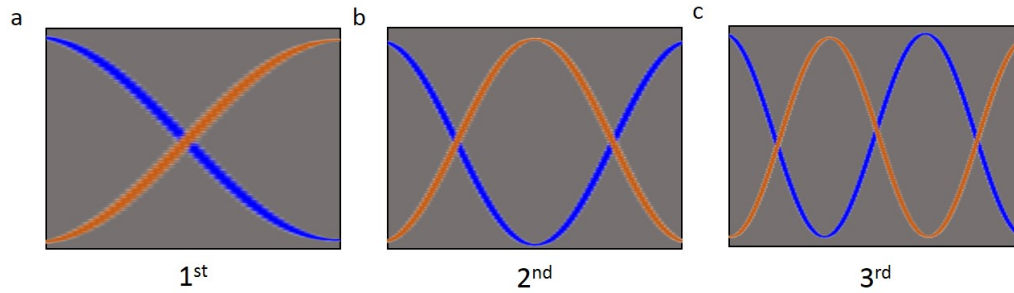


Figure 3.6: 1st, 2nd and 3rd through thickness modes supported within a transducer. Experimentally the 2nd mode is not observed.

The 1st, 2nd and 3rd through thickness modes are supported within the transducer, however the 2nd mode does not exist because the plates would have to be moving in the same direction. Practically only the 1st and 3rd modes are observed and can be used to produce the strongest acoustic forces within a trapping device compared with other frequencies.

The resonant frequencies of transducers can be tested through impedance analysis whereby the transducer is subjected to alternating electric fields at different frequencies and the resonance behaviour monitored. The output enables identification of the fundamental through thickness resonant frequency and subsequent harmonics. A typical impedance plot for transducers used throughout this thesis is shown in Figure 3.7.

For the maximal output and highest acoustic forces within the device, the driving frequency of the transducers must be carefully identified. When driven at resonance, a transducer is effectively acoustically transparent so that there are no reflections. Using multiple transducers, such as in the 2 transducer counter-propagating standing wave setup (Section 3.1.3.1) and utilised for the work here, it is important to match the individual transducer outputs so that the resonant frequencies match. This minimises wave reflections within the device occurring due to the partial reflection of one transducer in the pair not being driven at the resonant frequency. [42] The trapping device was driven at one of the frequencies identified at the minima of these impedance outputs to provide the maximal mechanical outputs.

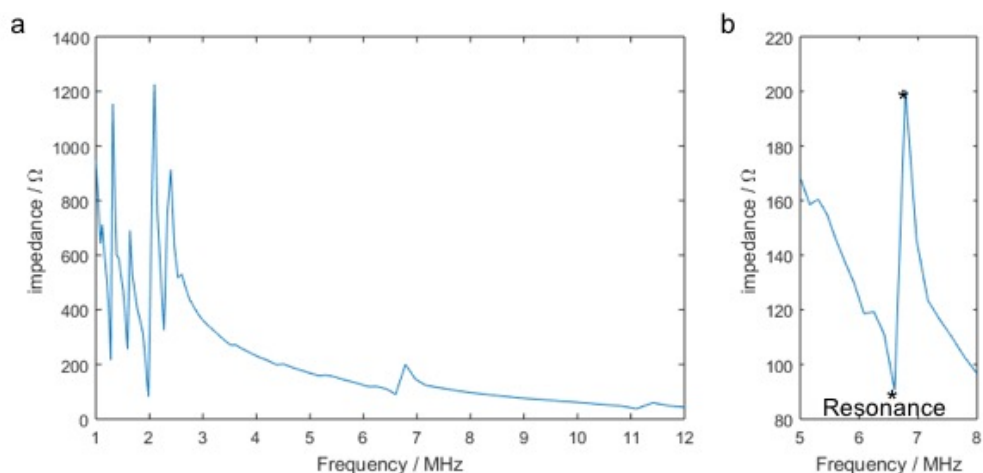


Figure 3.7: a) The typical impedance output for the transducers used in the work presented in the thesis is shown over the whole 1-12 MHz range. b) A more detailed region of interest shows the behaviour at the resonant and anti-resonant frequencies.

3.1.3.4 Acoustic Streaming

When trapping particles in a liquid further forces, other than the acoustic force, can be experienced. Acoustic streaming is a secondary steady flow that is generated due to attenuation of a primary oscillatory acoustic wave by the fluid. [30] In acoustic trapping the motion of the particles suspended in the fluid is the main interest, but water molecules will also be perturbed from their positions by an incoming acoustic wave. The time-averaged displacements from these positions will be zero in an ideal fluid. Alas in real fluids, the viscous attenuation of the acoustic waves results in some deviation and displacement of water molecules from their original positions. [217] Occurring at multiple instances throughout the volume of fluid, this results in a global formation of streaming flows. Experimentally this is observed as particles moving around higher up in the fluid and not settling into any of the trapping points. Forces from these flows can be stronger than that of the acoustic radiation force and so the particles will not be trapped within the applied acoustic field and instead will move around within the streaming flow. [218, 219]

As devices are driven at higher voltages, streaming can become more problematic where trapping is desired. [220] However there are some applications where streaming is used as a beneficial effect. Fluid streaming flows were used in enhancing immunoassays by sweeping fluids across trapped

beads. [221] While Bengtsson *et al.* used streaming for fluid mixing to increase enzyme reaction rates in specifically designed channels in microfluidic devices. [222] The forces from microfluidic flows on cellular membranes have also been shown to increase cell metabolism and encourage cell membrane processes. [217, 223, 224] These serve as a few examples that demonstrate through implementing careful control over the streaming, it can be used beneficially.

3.2 Trapping device fabrication

For particle manipulation, a counter-propagating wave device was developed to produce a standing wave within a fluid filled cavity. [43] A controllable phase difference between the two transducers enabled the position of the nodal points to be changed. The design of such a device required acoustic matching of the transducers with the fluid by use of matching and backing layers around the transducer. The thickness of these layers was chosen to minimise the reflection at the transducer face, achieved when the thickness is $3/4$ of the wavelength within it.

The later revelation of transparency of transducers when driven at resonance resulted in the matching layers no longer being required, rapidly simplifying device manufacture.

Based on this counter-propagating device developed by Courtney *et al.*, a new device was developed. [43] The acoustic trapping device comprised a central square cavity surrounded by 4 orthogonally arranged transducers, each with a water backing well (Figure 3.8). A periphery edge of plastic around the cavity separated the transducers from being directly in contact with the sample. This was an important step to integrate the device with chemical systems. When the transducers were directly in contact with the fluid there were electric field interactions between the chemicals and the electrodes which were stronger than the acoustic field interactions. Further to this it increased the likelihood of chemical contamination within the sample and between different samples. Introduction of the plastic edge prevented these undesired interactions.

Within this trapping setup some acoustic considerations must be mentioned. The transducers were not in direct contact with the fluid and while there have been no detailed investigations into how these adaptations affect the device operation, it is accepted that the complexity of the device is increased. While these device developments may pose a concern for understanding the exact

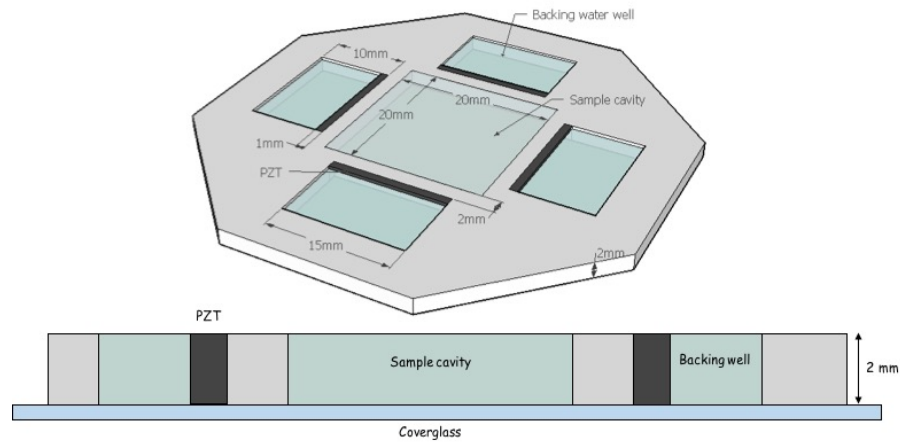


Figure 3.8: Schematic of the acoustic trapping device including dimensions and the locations of different features. The width of the coverglass adhered to the base of the device has been exaggerated for illustration since it was only 0.1 mm thick.

acoustics behaviour, successful trapping was demonstrated with devices largely behaving as expected. Future considerations of these effects may be required but they were not explored as part of the work in this thesis.

Directly opposing transducers were wired as pairs in parallel. 1D trapping used 1 signal generator to drive the transducers at the resonant frequency. 2D trapping used a separate signal generator per pair to drive the transducers at two different frequencies. A frequency difference of 10 kHz was introduced in this case so that the two fields were temporally uncorrelated.

Devices were designed in AUTOCAD and cut out into plastic using a laser cutter (Trotec Speedy 100). The impedance of all transducers (Noliac NCE 51 WAE 15x2x1mm) was analysed from 1-12 MHz using a Trewmac Analyser. The output curves from these tests were carefully analysed to find matching pairs at the specific desired driving frequency. Transducers were adhered to the device using superglue. Prior to addition of fluid samples into the sample cavity, a glass slide (48x64 mm, Agar Scientific) was affixed onto the base of the device using Fixogum flexible adhesive.

3.2.1 Modelling of the Acoustic Field

The acoustic radiation force is non-linear and so exact magnitudes of forces are not obtainable purely through modelling. However based on material properties, the Gor'kov description enables positions

of the minima and maxima of the resulting pressure field to be found, alongside the directions that the forces act.

A MATLAB code was developed by Prof. B Drinkwater which calculated the pressure fields for trapping in an x-y plane for a variety of different device conformations involving 1-5 transducers using the Gor'kov potential. The underlying assumptions of this model were that the length of the transducers, d , were large ($d \gg \lambda$) and therefore emitted plane waves and that all the transducers were driven in phase but acted independently of each other with no reflections in the device. Directional forces were added together to equate the total force as detailed in Section 3.1.2.2. The pressure fields, over a central 5 mm region, for 6 different trapping device conformations at a driving frequency of 1 MHz are shown in Figure 3.9. Transducer size was set at 15 mm which for a driving frequency of 1 MHz satisfies $d \gg \lambda$.

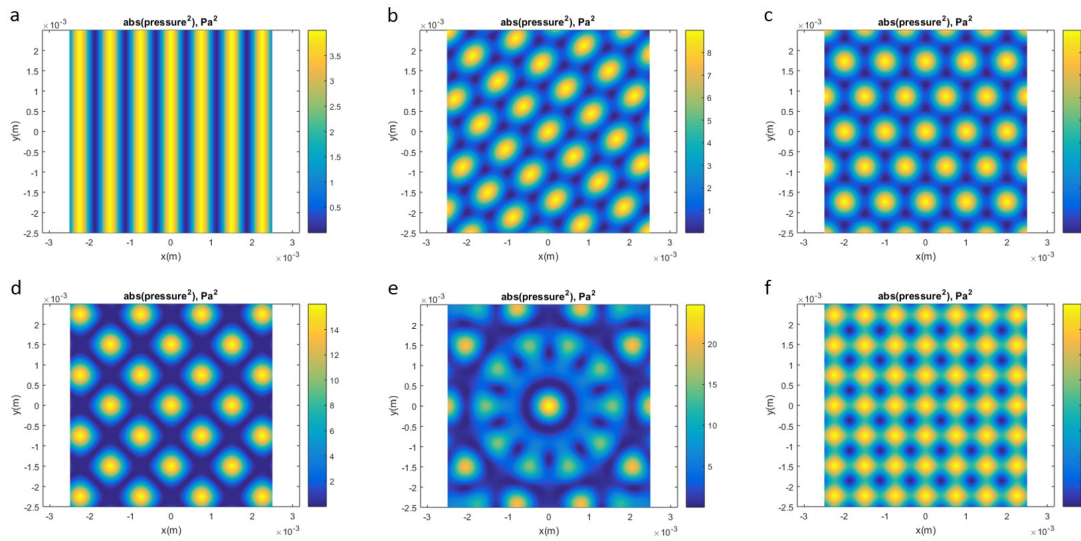


Figure 3.9: Modelling of acoustic pressure field in different geometries within an acoustic trapping device. The pressures are shown for devices with different numbers of transducers over a 5 mm central area driven at 1 MHz. a) 2 as an opposed pair b) 3 in an equilateral triangle c) 4 as 2 opposed pairs with $\frac{\pi}{2}$ phase difference d) 4 as 2 opposed pairs with no phase difference e) 5 arranged in a pentagon f) 4 as 2 opposed pairs driven at two different frequencies (1 and 1.01 MHz) Scale bars show the different pressures within the cavity.

Introducing a slight difference in driving frequency for the two orthogonal pairs leads to the same grid pattern as driving at the same frequency with a $\frac{\pi}{2}$ phase difference. When the two pairs are driven in phase the grid is rotated through 45° , presenting a diamond grid relative to the square shape of the

device.

The driving frequency, f , and speed of wave propagation within the fluid, v , dictate the half-wavelength spacing as governed by $v = f\lambda$. The effect of driving the transducers at different frequencies on the pressure field can be seen in Figure 3.10 which shows pressure fields for 1, 3 and 5 MHz. Based on a wave propagation speed of 1500 m/s, the theoretical half-wavelength spacing would be 0.75, 0.25 and 0.15 mm respectively. Increasing the frequency, decreases the half-wavelength spacing, increasing the number of trapping points within the same area and steepening the pressure gradient. At lower frequencies the width of the trapping points, located at the pressure minima and maxima, is also increased.

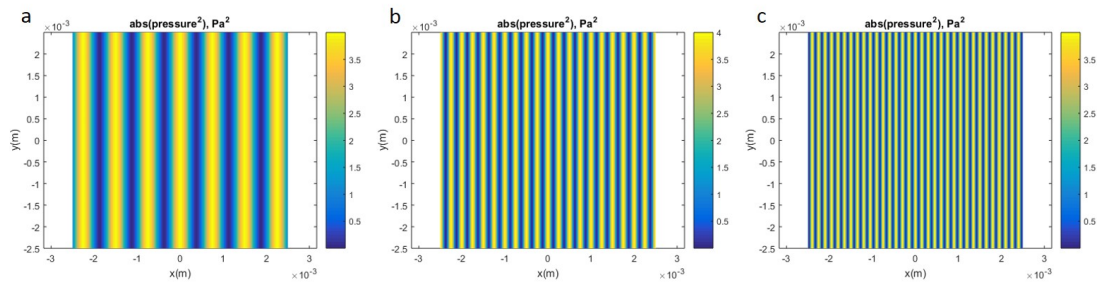


Figure 3.10: Plane wave modelling of the 1D acoustic pressure field at different driving frequencies within a 5 mm central area of an acoustic trapping device a) 1 MHz b) 3 MHz c) 5 MHz. As the driving frequency increases, the half-wavelength spacing decreases and the number of nodal positions in the same area increases

Inputs can be varied to represent the different properties of the fluid and media. However absolute force patterns are based purely on the wave propagation through the host media and hence are dictated by the fluid and driving frequency only. It is the direction of the acoustic radiation forces that will change based on the density of the particles in suspension with respect to the fluid density, $A_C > 0$ or $A_C < 0$. Particle size, a , will further affect the magnitudes of the force and pressures experienced since acoustic force $\propto a^3$.

The assumptions in the plane wave model provide very uniform field outputs extending over the entirety of the device as shown for a 2D acoustic field in Figure 3.11. For this case, an area of 20 mm square is presented which is representative of the dimensions of the acoustic trapping devices used throughout this work. This device cavity is much larger than the transducers (15 mm), which are located in the centre of each edge (Figure 3.11).

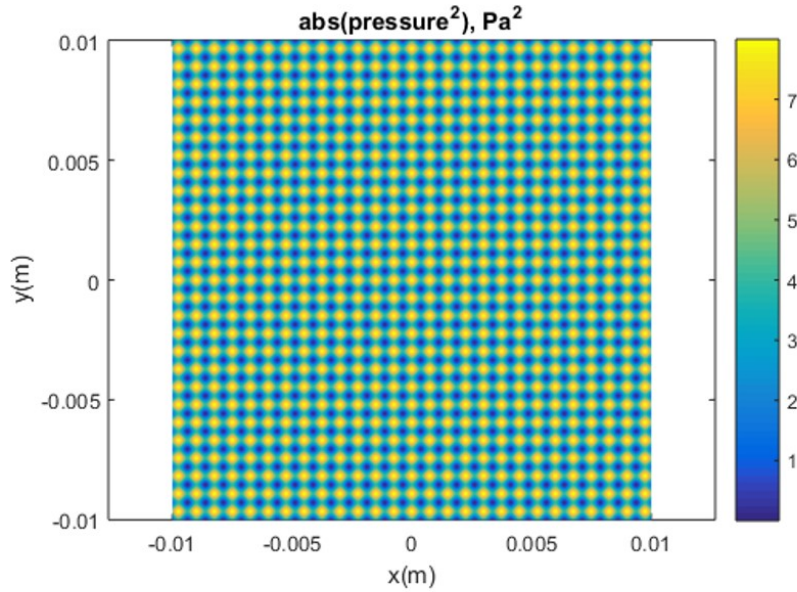


Figure 3.11: Modelled 2D plane wave pressure field over a 20 mm square acoustic trapping chamber

The force variation across the device can be better approximated by adopting the Huygens approach which accounts for the length of the transducer. This adaptation incorporates the length of the transducer actually in contact with the device, and hence emitting energy into it. The total length is divided into smaller sections or elements. Each element is treated as a point source and the acoustic field at each is calculated. The total field is the sum of the different pressures from each point source. Using this regime, the model revealed the variations in the patterning present within the sample cavity of the device shown in Figure 3.12. The strongest patterning can be observed in the centre of the device and along the edges the patterning tends to 1D as there is no overlap with the field produced by the other transducer pair. This output was a better match to experimentally observed trapping.

For the case of 1D field models, again the Huygen's model was a better match for the experimentally observed patterning where the patterning extended across the central area of the device that matched the dimensions of the transducers.

Finite element modelling of trapping devices was also performed using COMSOL Multiphysics software. [46] This provided a more realistic model of the device accounting for interactions of the

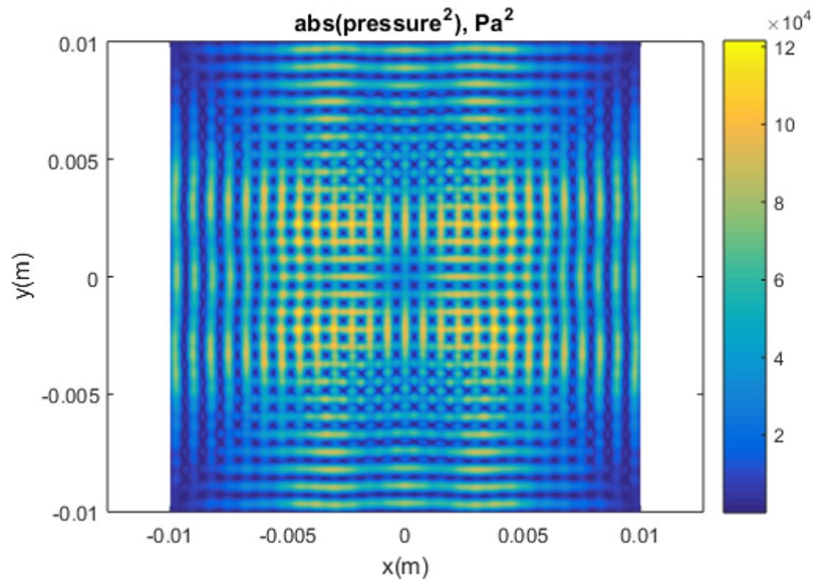


Figure 3.12: Modelled 2D Huygens wave pressure field over a 20 mm square acoustic trapping chamber with 15 mm transducers. While clear gridded patterns can be observed in the centre region of the device, towards the edges the trapping appears 1D.

field with different boundary layers and specific material properties of the device, transducers, fluid and particles beyond that adopted within the MATLAB model. Adopting a similar birds eye view (x-y plane) provided similar field outputs, however using a cut-through slice of the device revealed the acoustic field from a different perspective (x-z plane). Here modelling revealed that the extent of the field over 2mm vertically from the bottom coverglass to the surface of the fluid was minimal with the strongest forces across the base and diminishing as you increased in distance from there (Figure 3.13).

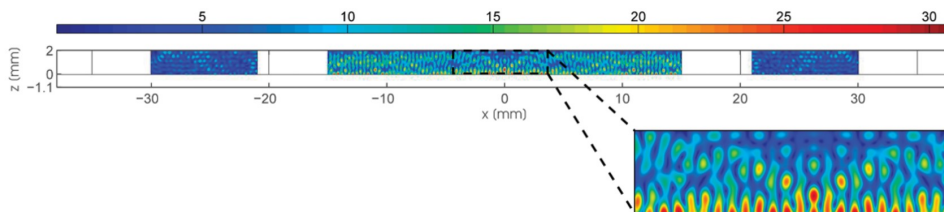


Figure 3.13: Modelled pressure field over the vertical 2 mm thickness of the square acoustic trapping chamber. Taken from reference [46]

These results showed that patterning within these devices was limited to the 2D x-y plane across the bottom of the device, rather than 3D patterning in x-y-z.

3.3 Results and Discussion

The following discussion points pertain specifically to the acoustic trapping device and acoustic related phenomena. Discussion and details of specific experimental results can be found in the relevant experimental chapters following this one.

3.3.1 Device design

Further to the introduction of the periphery edge between the sample chamber and the transducers, little further adaptations were made to the device design over the course of the work. Minor adaptations to the overall size of the device were made so that the device could comfortably be mounted onto microscope stages and to aid in removal of samples. However some discussion regarding design considerations is given.

3.3.1.1 Reflections

The oscillations of the transducer would emit wave fronts in two directions. The ones that were emitted from the back of the transducer, away from the central cavity, were damped as far as possible by filling the wells with water. This had the added benefit of cooling the transducers when the devices were left on for a long time. The plastic edges of the backing wells could act as reflectors and send the wave back towards the transducer which could then pass into the cavity since the transducers are driven at resonance and are effectively acoustically transparent. Device alterations could have been implemented to reduce these potential sources of interference; roughening the edges of the water wells would have minimised the possible reflections by attenuating the wave.

The plastic layer between the transducers and sample cavity would increase the complexity of the acoustics due to the introduction of coupling agents as well as more surfaces for the wave to pass through. The different material behaviour of these surfaces was not investigated but there could have been wave reflections occurring within the 2 mm thick edge and different reflection

behaviour due to varying coefficients at the different surfaces. Particularly partial mirroring between the decoupled back edge of the transducer that was not glued to the plastic, and the edge of the backing well from the sound hard boundary. Any reflections off plastic boundaries could also have been used advantageously through implementing a single transducer propagating wave within the device. Indeed some experiments which were later found to have been performed with only one transducer activated in the pair revealed that there was still strong trapping possible with patterning occurring across the whole cavity. If reflections did arise, they did not act to disrupt the coacervate patterning process as in many samples the expected patterning was always observed as predicted by the modelling, consistent with wave propagation in water.

3.3.1.2 Coupling agent

Mechanical energy transferred from the transducer into the device depends on the coupling of the transducer to the device. Strong coupling will result in maximum energy transfer and the strongest fields. Transducers were adhered to the plastic device using superglue. Over time, this coupling would be weakened by the vibrational energy breaking the hardened glue and the efficiency of acoustic energy transfer drops. Experimentally, soon after adherence the patterned lines were very distinctive (Figure 3.14a) but after some time, as the coupling weakened, the patterned lines and trapping were less resolvable due to the weaker acoustic trapping forces (Figure 3.14b). To address this reduced efficiency the adherence of the transducers to the device was checked every few days. On many occasions throughout their lifetime, the transducers were re-adhered onto the plastic using superglue.

The likelihood of bubbles forming upon extrusion of the glue is quite high and this would prevent efficient transmission of the mechanical vibrations from the transducers into the plastic, due to the reduced contact between the two materials. As far as possible this was minimised by applying the superglue with a spatula so that bubbles could be popped or smoothed before hardening.

Epoxy resin was explored as an alternative means for coupling the transducers to the trapping device. The drying time of this adhesive was much longer than superglue which enabled fine tuning of exact orientation of adherence and the removal of bubbles. In terms of trapping observed, there was no significant improvement in a new device, but as the devices aged and were used a lot, the resin

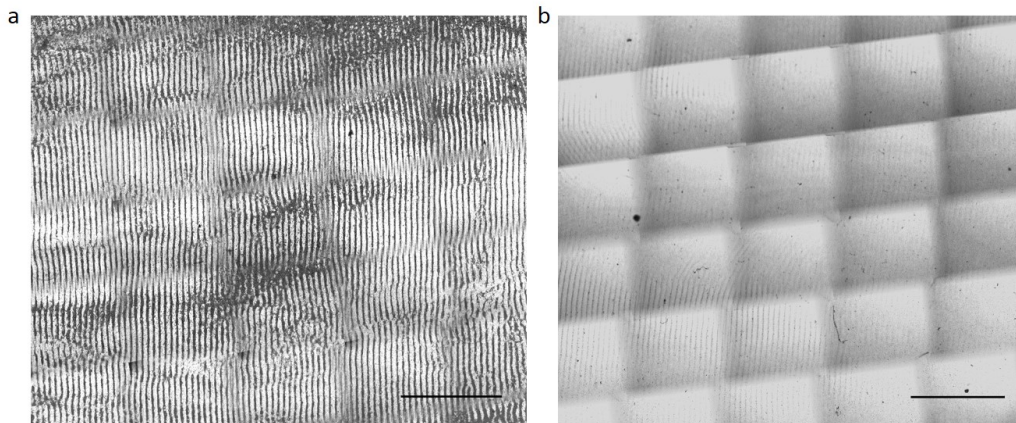


Figure 3.14: Stitched image of large area view of trapped coacervates within a central area of trapping device at different times after transducer adherence with superglue a) freshly adhered transducers have very clearly defined lines extending across the central area shown while b) shows the same device at a later date when the coupling is not as strong since the lines are less resolvable within the sample. Scale bars 2 mm

adhered devices tended to maintain stronger fields within the device longer than those produced with superglue. Future work utilising these devices should use epoxy resin to adhere the transducers.

3.3.1.3 Device reusability

Over the course of the work carried out in this thesis, many devices were produced for simultaneous sample preparation and to replace old ones.

Removal of the coverslip from the device along with any sample of interest to keep, left behind small pieces of glass and dried out Fixogum on the base. These were removed as best as possible using ethanol and mechanical force, possibly damaging the device surface or weakening the coupling between transducer and plastic by dissolving the superglue. Further, any residual glass pieces and dried glue could have introduced strains and stresses into the next coverglass attached to the base, possibly influencing the field shape within the device. Thorough device checking and constant production of new ones addressed these issues as far as possible.

The volume of Fixogum glue used to adhere the glass slide to the device was also not controlled with differing amounts used each time. As such, there would have been different volumes of it seeping into the device cavity and potentially affecting the wave propagation within it. Upon hardening, the wave propagation would be different than through water. On occasions where there was too much,

it was carefully removed using the end of a spatula. When too little adhesive was used, there was leaking of the sample solution into the water backing wells as the seal between device and glass slide was not water tight preventing effective trapping.

3.3.2 Impedance analysis and driving frequencies

3.3.2.1 Matching transducers

In early stages of the work, the importance of transducer matching was neglected. Instead transducers were directly adhered to the device without any investigations into their individual properties and driven at 6.7 MHz or 6.7 x 6.69 MHz in the case of 2-dimensional trapping. There will be some variation in the exact driving frequencies within a population of manufactured transducers. This lead to some interesting trapping results with coacervate droplets, discussed specifically in the relevant experimental chapters. The variability in the trapping between different devices was noticeable through microscopy observations which implied that greater care in transducer pairing was required. Due to mismatching of exact resonant frequencies, within a transducer pair there would be three potential outcomes:

1. The ideal case of transducers matched and driven at their resonant frequency.
2. One transducer in the pair driven at resonance while the other was not. The resulting waves would present a directional imbalance with stronger vibrations and acoustic energy output from one side and then partial reflections of the wave from the surface of the other transducer, leading to wave interference and unstable trapping points.
3. Neither of the transducers were driven at resonance. Acoustic waves produced at 6.7 MHz would be reflected due to the non-zero reflection coefficients of the transducer when driven off resonance. The resulting acoustic forces within the device would be weaker.

Better control over this trapping variability between different samples was found when transducer pairs were matched through impedance analysis and driven at the identified driving frequencies. This was done by directly comparing the impedance curves for every transducer with other ones available and pairing the two that overlapped best at the frequency of interest. However, exact matching at one

frequency did not necessarily mean that there was good matching at the other through thickness mode driving frequencies.

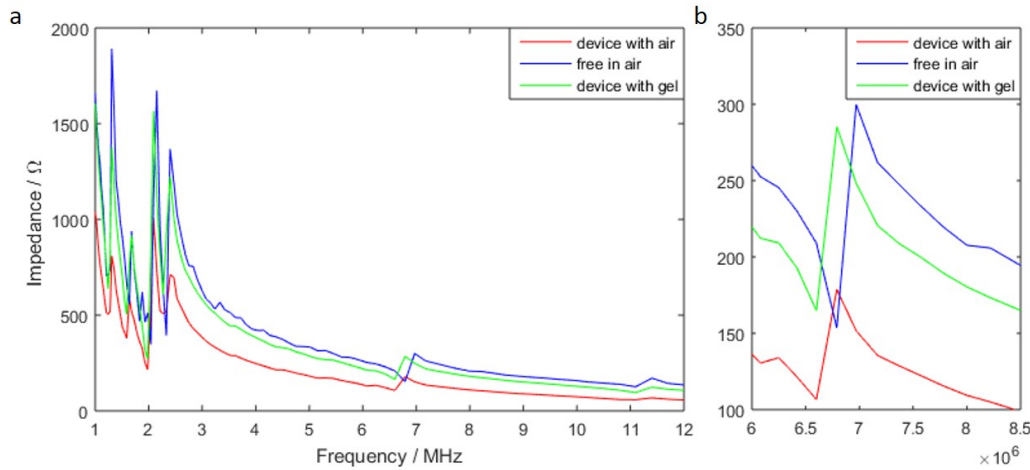


Figure 3.15: Impedance analysis of a transducer in different situations. The red line shows the transducer adhered to the device with superglue with nothing in the sample cavity, blue the transducer free in air unattached and green the transducer adhered to the device with gel in the cavity for a) whole 1-12 MHz output curve and b) through thickness mode around 6.7 MHz region of interest

The device has a 2 mm plastic periphery surrounding the sample cavity. Waves produced from the transducers would have to propagate through the plastic before reaching this central cavity. The symmetry in the device would mean that theoretically whatever effects this has on the resulting wave would happen to both waves from both transducers in the pair. The adherence and resulting constraint of vibrations of the transducer were investigated by analysing the impedance output of a transducer free in air, and attached to the device in different circumstances (empty and with a gel filled cavity) as shown in Figure 3.15a with the blue, red and green curves respectively. Surprisingly there appears to be no huge effect on the transducer output. The resonances shift slightly lower when attached to the device compared to free in air as elucidated by the larger detail image of the 6.7 MHz resonance region (Figure 3.15b). The impedance values are highest for the unconstrained transducer in air and lowest for the transducer constrained to a device with an empty cavity.

These impedance outputs do not demonstrate resonance characteristics due to the absorbing power of the device, implying a highly damped system. Consequently this lead to the conclusion that any undesired reflections within the device were damped before having any adverse effects on the

trapping.

3.3.2.2 Driving frequencies

For the transducers used throughout this work the driving frequencies were identified as 2.15, 6.7 and 11.3 MHz corresponding to half-wavelength spacing of 330, 110 and 63 μm respectively. Between different transducers there was found to be some variation from these exact stated values (± 0.15 MHz). The exact frequency to use was identified from the specific impedance output curve for that transducer.

Due to the discretized nature of the impedance sweep over 1-12 MHz, the exact resonant frequency would not necessarily have been explicitly identified. Experimentally, the trapping of coacervate droplets in solution was observed visually by changing the driving frequency around this value between the neighbouring impedance measurement points. Upon observing the strongest trapping, this frequency was noted and used in all subsequent experiments.

Assuming linearity, pressure is proportional to the voltage applied. For stronger forces the transducers could be driven at higher voltages. An investigation into how the applied voltage affects the trapping was implemented. Changing the forces, resulted in increased or decreased streaming of coacervates. For this work, the polydisperse nature of the coacervates presents an additional problem since the acoustic force experienced by a particle is proportional to the radius (a^3) and when the droplets are trapped there is enhanced coalescence to larger sizes (Sections 4.2.1.1 & 4.2.4.1) but the smallest particles would experience streaming effects. Fortunately the density of the coacervate phase exceeds that of water, so as they coalesced there was gravity driven sedimentation to the base of the device so that most droplets would experience the acoustic force towards the base of the device, where it was strongest (Section 3.2.1 Figure 3.13).

Figure 3.16 shows 2D trapping, with both transducer pairs driven from one signal generator, within a central area of the same device for 1:1 40mM coacervates added into a 6.7 MHz field at different peak to peak voltages (V_{pp}). The wave interference from driving both transducer pairs at the same frequency results in the slightly curved nature of the lines as opposed to clearly distinct lines or grid patterning. 7 V_{pp} (Figure 3.16a) displays a more 1D nature and the lines are not particularly defined. At 8 V_{pp} (Figure 3.16b) the 2D nature of the field can be observed but there is still a lot of material

located between trapping points. $9 V_{pp}$ (Figure 3.16c) is much more distinct. $10 V_{pp}$ gives the clearest patterning with coacervate material accumulating at nodal positions of the field to produce a grid like pattern despite the wave interference, increasing the strength of the field enough for strong trapping patterns but not so much that streaming dominated the movement of the coacervates.

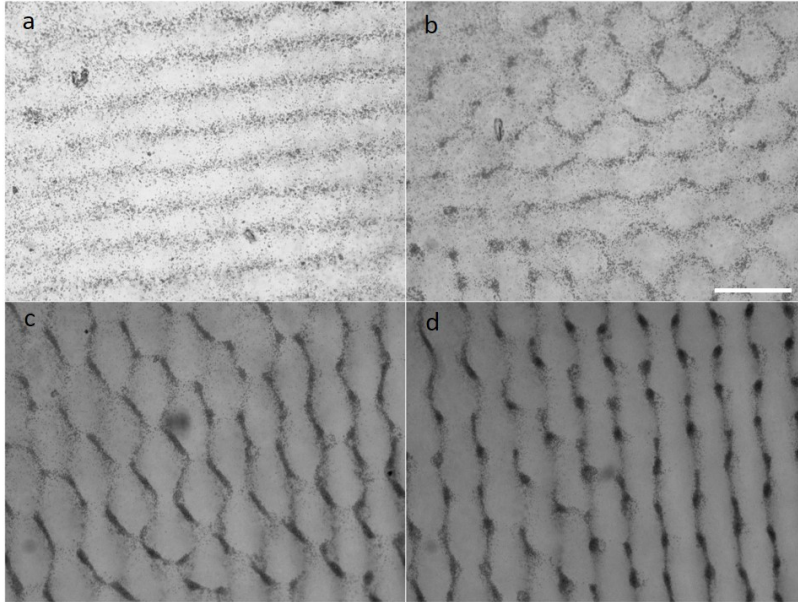


Figure 3.16: 2D (6.7 x 6.69 MHz) trapping of coacervate droplets in an acoustic field driven at different peak to peak voltages, V_{pp} . a) $7 V_{pp}$ displays 1D lines b) at $8 V_{pp}$ the 2D nature of the field is visible but not clear c) $9 V_{pp}$ is much more distinct but d) $10 V_{pp}$ provided the clearest and most reliable trapping results. Scale bar $200 \mu\text{m}$

3.3.3 Model outputs compared with experimental

There are some device variations that can be implemented to improve the vertical field strength such as using a lid on top of the fluid to act as a hard boundary. However, for the work presented here, direct access to the sample cavity was required for extraction/addition of different chemicals. As such, removal and replacement of a lid, however delicately, could perturb the patterning of the droplets.

The acoustic force gradient varies between the different driving frequencies as shown in Figure 3.17a-c. Lower frequencies have larger half-wavelength spacing so fewer nodal positions in a given area and wider pressure points for the particles to migrate towards. Assuming a similar number of

coacervate droplets form at a given concentration and ratio of mixing, this means that there will be more coacervates within each trapping point at lower frequency as the same number of droplets is spread over fewer trapping points, and fewer droplets in each trapping point at higher frequencies where there are more trapping points within the sample cavity. While plane wave model outputs served as a good indicator for the trapping observed experimentally (Figure 3.17d-f), they don't account for polydispersity in size of the coacervate droplets being trapped and their coalescence within the field. However for the purposes of identifying the spacing and expected patterns, the model provides a reasonable approximation.

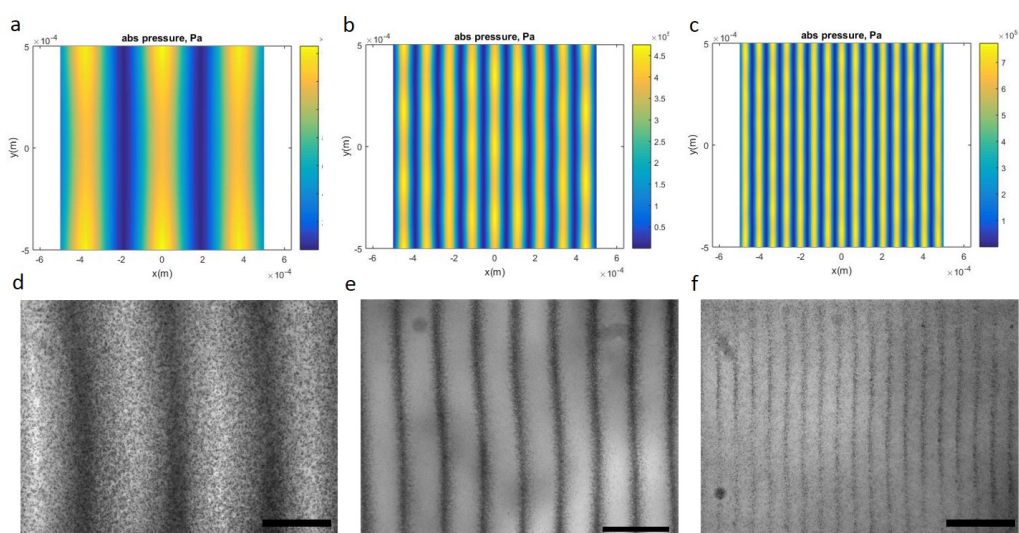


Figure 3.17: Plane wave modelled and experimentally observed trapping at different driving frequencies in a 1D acoustic field. All model outputs show a 1 mm square central area of the field based on a Huygens approximation with the corresponding experimentally observed trapping of coacervates shown below at a) & d) 2.15 MHz b) & e) 6.7 MHz c) & f) 11.3 MHz. Scale bars 200 μm

For trapping of coacervates, at low frequency the force experienced doesn't encourage as much coalescence of the droplets to larger sizes and patterns were harder to resolve at higher magnifications. Fortuitously the half-wavelength spacing of 330 μm for ordered hydrogels at 2.15 MHz can be resolved by eye in the patterned hydrogels as shown in Figure 3.18. Patterning can be seen to extend across the whole of the 20 mm square gel.

The Huygens model was in better agreement with the 2D trapping that was observed experimentally as seen comparing the pressure field and patterned features in Figures 3.12 & 3.18b, where regions of

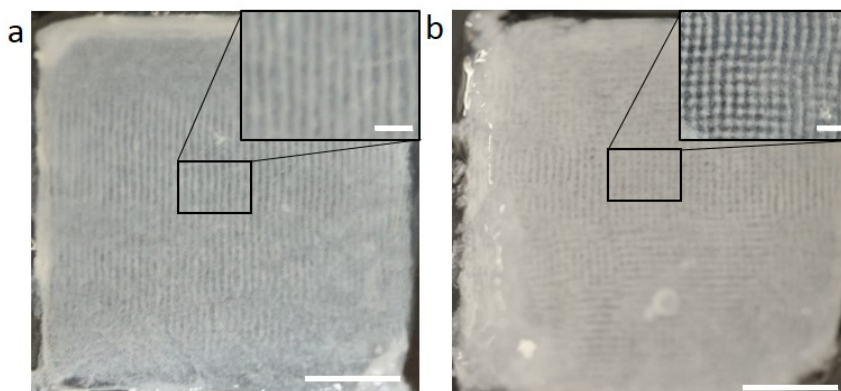


Figure 3.18: Hydrogels patterned at a frequency resolvable by eye a) 2.15 MHz has a half-wavelength spacing of $330 \mu\text{m}$ b) 2.15×2.14 MHz. Scale bars 5 mm and insets 1 mm

2D patterning can be observed but there are also patterned areas within the sample that look 1D.

Experimentally, the 6.7 MHz frequency provided the best properties for the chemical system, as the number of wavelengths in the cavity and size of the pressure points was appropriate for better resolution of the ordering occurring and for interesting behaviors of the droplets within those trapping points. As such, the majority of the investigations were performed at this frequency.

3.4 Conclusions and Future Work

The 2-transducer counter-propagating wave trapping devices detailed here have been used to successfully pattern coacervate droplets into lines and grid-like arrays. Further exploration and optimisation of the acoustic behaviours within these devices has yielded more reliable patterned features within these hydrogels. Particularly, the identification and matching of the driving frequency within a transducer pair is critical. Models based on the Gor'kov potential and a Huygens approach have provided a good match with the trapping behaviours observed experimentally. Several device specific developments and adaptations have been identified for future endeavours.

The capacity for improved vertical ordering with the in plane device could be further developed. For microscopical observation, installing a pair of transducers in a 3rd orthogonal direction is not an option. However, there is evidence to suggest that using larger transducers results in an improved field strength from the bottom of the device. Some preliminary work where the orientation of the

transducers was rotated so that the 15 mm side extended vertically and submerging the device entirely in water resulted in lines of coacervates within the gelled product extending to ≈ 3 mm (Figure 3.19).

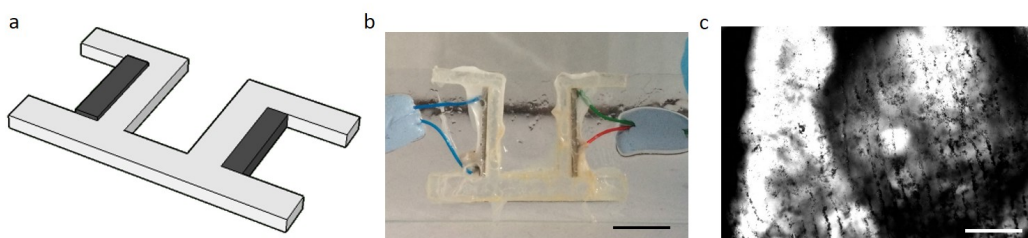


Figure 3.19: Micropatterned hydrogel with the transducers oriented vertically along the 15 mm long edge. a) schematic to show the device design with the transducers represented by the dark grey rectangles and the plastic by the light grey b) shows the device set-up and vertical orientation of the transducers along their longest edge (15 mm). c) acoustically patterned hydrogel, removed from the acoustic field, with lines extending vertically across the image to 3 mm. Scale bars 10 mm and 500 μm

Another possibility would be having stacks of transducers to effectively form a higher extending transducer. Activating them in sequence, or driving the higher ones at higher voltages to better trap streaming particles, could provide an alternative route towards 3 dimensional trapping within this in-plane trapping device. Additionally the plausibility of using a 1-transducer counter-propagating device could be further investigated. Some results where one of the transducers in the pair was not driven during the trapping showed that sample patterning was still obtained. The field could be further strengthened by use of reflectors or the cavity resonance.

Introduction of a lid to the setup could be performed alongside integration of these devices with microfluidic flow channels and inlets. This has been utilised for filtering and directing the separation of different particles with different acoustic properties. The device could consist of an entirely sealed cavity thus strengthening the cavity resonance between the base and the lid without compromising the introduction of different chemicals into the device. Reactions could still be initiated without any human mechanical handling and subsequent perturbations to the device.

Enlarging the device cavity, results in larger areas where the trapping might not be so good due to limited field overlap, as elucidated by Huygens modelling results. Thus a central isolation of sample solutions using cling film located through the centre of the device would provide a possible option,

such as that demonstrated by Caleap *et al.* [225] The remaining cavity was filled with water and trapping was demonstrated in 3D.

The plastic edging was introduced to the device to prevent the migration of coacervate droplets to the electrode surfaces. These could be removed if the cling film setup was adopted which would assist in stronger fields for the same applied voltage since less energy is dissipated into the plastic. This could also aid in reducing the sample variability within the same device. Further, this edge has added complexity to the acoustics within the device and future consideration of the exact impact of these effects may be required.

There were no firm conclusions regarding the comparison of epoxy resin or superglue as a coupling agent. However for consistent fields across multiple samples produced within the same device strong coupling is required. This factor could be implemented in modelling so that the acoustic energy imparted is accounted for based on the quality of the coupling between the transducer and plastic. Understanding of the consequences of the plastic edge on the acoustics within the device could be further ascertained by developing and extending the current models. Modelling revealed the potential for using more transducers in combination for patterning. Different geometries or transducer combinations could be utilised in producing more complex patterns. Of particular interest, would be equidistantly arranged trapping points for the better observation of chemical reaction wavefronts and propagations of reactions through coacervate populations both aqueous and gelled.

Finally, there are many acoustic effects that could be used within the trapping device, such as manipulation of the droplets in solution prior to hydrogelation or in initiating behaviours after hydrogelation. Miller *et al.* demonstrated ultrasonic sonoporation of cells, where the changed membrane permeability enabled the uptake of larger molecules. [224] This could be beneficial within a hydrogel to aid in the movement of molecules through densely cross-linked areas into different pores or inside the coacervate droplets. Ultrasonic pulses have also been shown to release drugs within hydrogel matrices, thus providing a possible mechanism for release of different reactants within the hydrogel network. [226]

CHAPTER

4

**FABRICATION OF MICROPATTERNED HYDROGELS BY ACOUSTIC TRAPPING
OF RECONFIGURABLE POLYMER/DIPEPTIDE COACERVATE DROPLETS**

Chapter overview

In this chapter the fabrication process for micropatterned hydrogels by the acoustic trapping of stimulus-responsive coacervate microdroplets is presented. Coacervate droplets were formed in situ in an applied acoustic field in an acoustic trapping device comprising four orthogonally arranged transducers connected into two counter-propagating standing wave pairs. Driving one pair resulted in 1D lines of droplets extending across the sample cavity and driving both pairs resulted in a 2D grid-like array of droplets. The hydrogel transformation was initiated through addition of glucono- δ -lactone powders into the coacervate solution and following removal from the acoustic device micropatterned features remained within the hydrogel network. Further, loading the coacervate droplets with various guest molecules prior to hydrogelation enabled the spatial immobilisation of the molecules within the aqueous hydrogel network.

4.1 Introduction

Recently the acoustic patterning of coacervate droplets from adenosine 5'-triphosphate (ATP) and poly (diallyldimethylammonium) chloride (PDDA) into 2D grid-like arrays was reported. [185] The spherical ATP/PDDA coacervate microdroplet phase had a different density and compressibility compared to the surrounding aqueous supernatant phase and so was suitable for acoustic trapping. Acoustic trapping is the movement of particles in solution to specific positions within an acoustic field. As acoustic waves pass through the particles, the different compressibility and density compared to the fluid, scatters the waves resulting in an acoustic force. The acoustic force acts to move particles towards pressure minima or maxima. For the case of coacervates, which are denser than their surrounding fluid media, they will move towards pressure minima. In a standing wave counter-propagating acoustic field, such as those employed here, these positions are stationary and spaced by half the acoustic wavelength (λ). Acoustic fields are produced by driving piezoelectric transducers. More information on acoustic trapping and the devices used in this thesis can be found in Chapter 3. There is an extensive coacervate library, all of which have a bulk phase of coacervate microdroplets with a different density and compressibility compared to the surrounding solvent phase. These properties are the minimum requirements for acoustic trapping to be plausible with the system. The

patterning of coacervate droplets using acoustic trapping by Tian *et al.* serves as a proof of concept and it is proposed that this methodology could be extended to the patterning of other coacervate systems. [185]

4.1.1 A stimulus-responsive coacervate-based hydrogel system

The variety of different molecules that can undergo coacervation is broad. Interest has now developed in designing droplets from components that offer additional functionality. Coacervated proteins have demonstrated retention of their activity however the coacervation of other molecules capable of different functions has been underused. [107] A recently documented stimulus-responsive coacervate-based hydrogel system comprising a polymer with a small molecule was shown to exhibit reconfigurable transformation between coacervate droplets and a hydrogel state through response to an environmental change. The system comprised the cationic polymer (PDDA) and deprotonated N-(fluorenyl-9-methoxy-carbonyl)di-alanine (Fmoc-AA) and was selected for this work. [118]

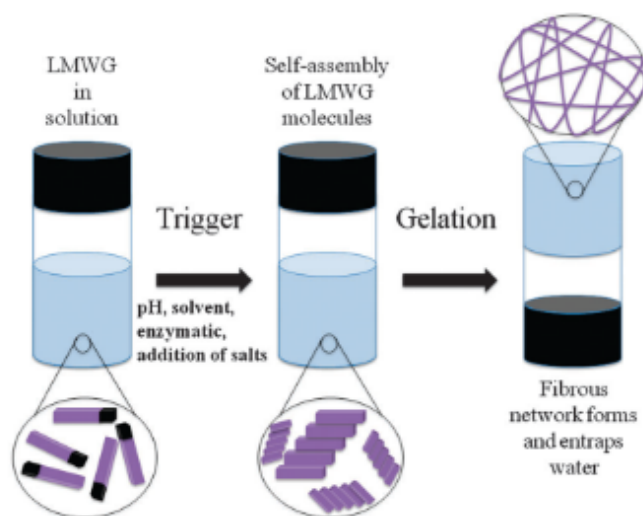


Figure 4.1: Schematic showing the self-assembly of a low molecular weight gelator (LMWG) into a fibrous network and self-supporting hydrogel. [75]

Amino acids in the form of di- or tri-peptides, functionalised at the N-terminus with groups such as fluorenylmethylcarbonyl (Fmoc), naphthalene or tert-butyloxycarbonyl, have been identified as a new class of low molecular weight gelators (Section 1.4.5). Under the right conditions these molecules will self-assemble into nanofilaments which then bundle into a fibrogenic hydrogel matrix

(Figure 4.1). More information on molecular hydrogels can be found in Section 1.4.5.

Upon decrease of the pH Fmoc-functionalised dialanine (Fmoc-AA) readily self-assembles into a supramolecular hydrogel due to protonation of the carboxylic acid group. [227] When Fmoc-AA is in a coacervate microdroplet with PDDA, the coacervate microdroplets undergo structural reconfiguration and transform into a hydrogel network with fibrils comprised from superhelical arrangements of alanine and fluorenyl residues which π - π stack and then emanate out from the droplet into aster-like structures (Figure 4.2). As these fibrils grow and interconnect with those from neighbouring droplets which have also transformed, a 3D coacervate-based hydrogel network is formed.

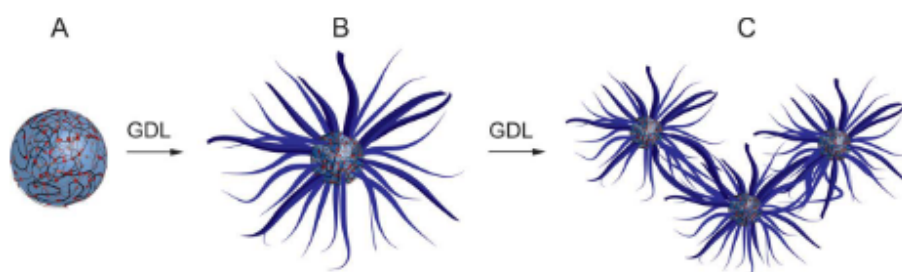


Figure 4.2: Schematic of the pH induced structural reconfiguration of the coacervated Fmoc-AA within an Fmoc-AA/PDDA coacervate droplet. A) the coacervate droplets spontaneously form upon mixing of Fmoc-AA (red spheres) with PDDA (black lines) B) following addition of GDL to lower the pH of the solution through hydrolysis there is supramolecular self-assembly of the Fmoc-AA molecules into fibrils which emanate out from the surface of the droplets C) as the self-assembly occurs throughout the solution of coacervates the fibrils interconnect and form a hydrogel network. Figure reproduced from reference [118]

The nature of the bonding with the π - π stacked structures comprising the fibrils emanating out from the droplets is reversible. Upon increasing the pH the resulting deprotonation of the Fmoc-AA re-introduces electrostatic interactions between the Fmoc-AA and PDDA and coacervate droplets are recovered. More information on the different intermolecular interactions and the coacervation process can be found in Sections 1.4.3 and 1.4.6.1 respectively.

This reconfigurable system presented the ideal opportunity for combination with the technique of acoustic trapping for the investigation into the possibility of utilising acoustic patterning in micropatterned hydrogel fabrication. Acoustic trapping devices had four orthogonally placed transducers surrounding a central square cavity. There was a 2 mm plastic periphery between the transducers

and cavity. It was conceivable that by first patterning the coacervate droplets in an acoustic field and then initiating the hydrogel transformation they would form a hydrogel network with the coacervate droplets remaining as ordered features within it. By driving 1 or 2 pairs of transducers to produce standing waves fields in 1D or 2D respectively, ordered lines or grid-like arrays of coacervate droplets were produced following similar protocols as with the aqueous arrays of ATP/PDDA droplets. The Fmoc-AA/PDDA system was then optimised for transformation into both 1D and 2D micropatterned hydrogels.

4.2 Results and Discussion

4.2.1 Coacervation in a 1D acoustic field

For the purpose of acoustic trapping, much higher concentrations than those previously investigated were of interest. At a 40 mM equimolar ratio, microscopical images revealed abundant spherical droplets in solution with an average size of $3.2 \pm 0.7 \mu\text{m}$ 5 minutes after mixing. Droplet size increases due to the coalescence of the droplets as they move under Brownian motion and collide. When left for some time, there is little increase in average size of the droplets. Most collisions will not be strong enough to overcome the surface repulsion between the two like charged droplets ($\zeta = -4 \pm 0.3 \text{ mV}$) however when concentrations and droplet numbers are higher, there are greater levels of coalescence. Dynamic light scattering (DLS) size measurements of droplets formed at different equimolar concentrations show that droplets remain smaller at lower concentrations due to the increased inter-droplet spacing and fewer collisions leading to coalescence. Size measurements of coacervate droplets formed with 40 mM PDDA and varying concentrations of Fmoc-AA is also shown (Table 4.1). At low concentrations the droplets are $< 1 \mu\text{m}$ in size. For acoustic trapping of droplets, the initial size in free solution should be as large as possible for most of the droplets to be large enough to experience the acoustic force.

When left for some time, many of the coacervate droplets will sediment onto the surface of the glass channel slides (Section 2.2.2.2). Retention of the spherical shape is due to the functionalised surface of the glass. This gravity driven sedimentation is due to the higher density of the bulk droplet phase ($\rho_{coac} = 1.8 \text{ g cm}^{-3}$) compared with the surrounding aqueous supernatant phase ($\rho_{SN} = 0.98 \text{ g cm}^{-3}$).

Equimolar concentration / mM	Size / μm	Concentration FMOC-AA/ mM	Size / μm
40	3.0 ± 0.1	40	3.0 ± 0.1
20	2.2 ± 0.3	20	1.4 ± 0.3
10	1.3 ± 0.1	10	0.8 ± 0.01
5	1.3 ± 0.1	5	0.3 ± 0.02

Table 4.1: DLS size measurements of coacervate droplets formed at an equimolar mixing ratio and for varying concentrations of FMOC-AA mixed with PDDA (40 mM)

When left for several hours, the bulk and supernatant phases will separate out under gravity leaving a denser region (bulk phase) and translucent upper solution (supernatant phase) above it. This density difference is important for the technique of acoustic trapping.

It was conceivable that the difference in density between the bulk and supernatant phases ($\rho_{coac} > \rho_{SN}$) would provide sufficient acoustophoretic contrast for droplets to experience the acoustic force and migrate to the nodal positions of an acoustic standing wave. (Section 3.1.2).

Coacervate droplets were formed in situ within an acoustic trapping device comprising four orthogonally arranged transducers surrounding a central 20 mm square sample well. One pair of transducers was driven at 6.7 MHz (Section 3.2). Following the trapping protocol (Section 2.2.1.3) first PDDA, and then FMOC-AA solutions were added into the device so that coacervation occurred in the presence of a 1D acoustic standing wave field. Over the course of 30 seconds, as droplets migrated to the pressure minima of the field, clearly distinct periodically arranged lines became visible across the sample cavity (Figure 4.3).

From impedance analysis, three different driving frequencies for the strongest acoustic forces were identified at 2.15, 6.7 and 11.3 MHz (± 0.15 MHz). Coacervate droplets (1:1 molar ratio, 40 mM) were formed in situ in an applied field at each of these frequencies. As predicted, coacervate droplets experienced the acoustic force and migrated towards the nodal points of the applied field. At each frequency the trapping positions were resolvable with steeper pressure gradients at higher frequency (Figure 4.4). Assuming the same number of coacervate droplets within each sample, more trapping points in the cavity means fewer droplets in each. The narrower and more numerous trapping points at higher frequencies (Figure 4.4b & d) hold the droplets in very close proximity leading to increased coalescence. However highest frequencies have more nodal points across the same area so fewer droplets in each and the coalescence was limited by the number of droplets within each point. At

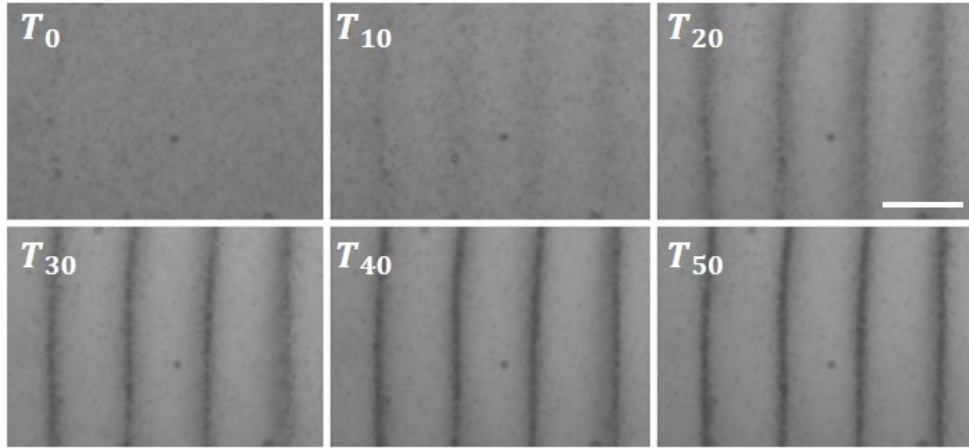


Figure 4.3: Time-lapse image series every 10 seconds after application of an acoustic field (1D 6.7 MHz) to a sample of coacervate droplets. After 30 seconds clearly ordered lines vertically across the field of view can be seen. Scale bar 100 μm

lower frequency, the wider trapping points exhibit less coalescence with groups of coacervate droplets locating there but not forced close enough to all coalesce with another (Figure 4.4c). However the highest frequency of 11.3 MHz and lowest frequency of 2.15 MHz exhibited trapping that was not as clear as the driving frequency of 6.7 MHz (Figure 4.4d). As such 6.7 MHz was used for the majority of the work as it provided the best resolution of trapped coacervate droplets and the nodal point width encouraged the most interesting droplet behaviours within the pressure minima points.

Comparing the line spacing measurements in images of patterned coacervate droplets with that of the modelled nodal spacing, there is good agreement with the lines of coacervate droplets displaying similar values to the expected half-wavelength spacings at the 3 different frequencies. (Figure 4.4 and Table 4.2).

Frequency / MHz	Theoretical $\frac{\lambda}{2}$ spacing / μm	Measured $\frac{\lambda}{2}$ spacing / μm
2.14	343	$356 \pm 8 \%$
6.7	110	$114 \pm 5 \%$
11.3	65	$66 \pm 10 \%$

Table 4.2: Table displaying half-wavelength spacings as calculated theoretically and measured from images of ordered coacervate droplets at each of the identified driving frequencies for 1D patterning

The assumptions made for the modelling were that the fluid medium was water and the specific values presented in Table 4.2 were obtained using the equation ($v = f\lambda$) relating velocity of ultrasound

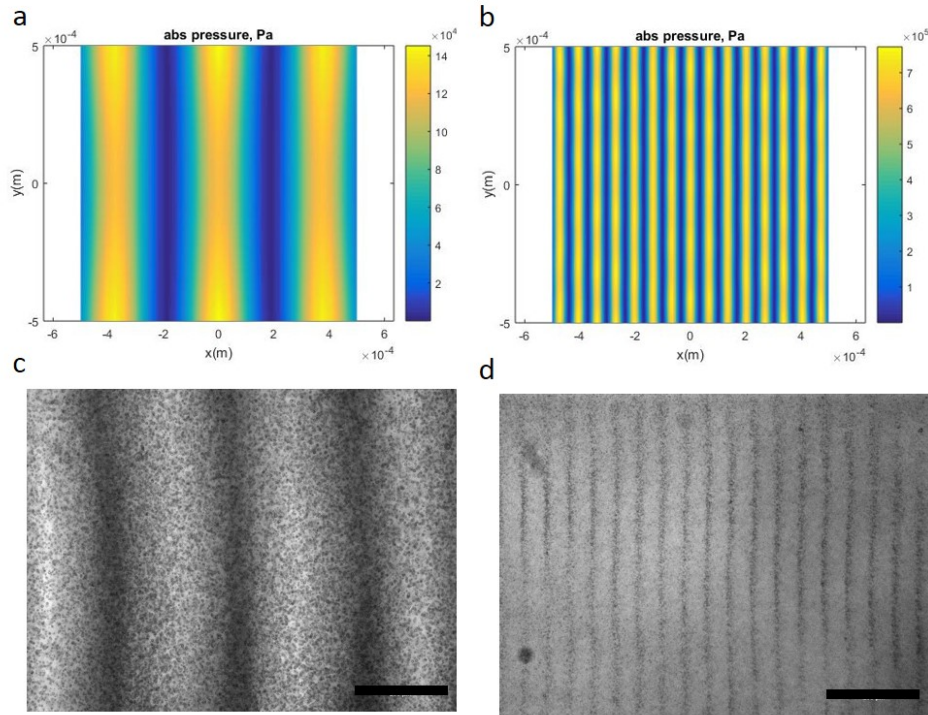


Figure 4.4: Modelled pressure fields and experimentally observed 1D patterning of coacervate droplets at different frequencies. a) lowest frequency 2.15 MHz model and c) corresponding trapped coacervate droplets migrate to the wide nodal regions of pressure minima. b) & d) modelled and trapped coacervate droplets at 11.3 MHz. The steep pressure gradients at the highest pressure result in less distinct lines of trapped coacervate droplets. Scale bars 200 μm

in the medium, v , frequency of the ultrasound, f and the resulting wavelength, λ . Here a value of 1500 m s^{-1} was used for v . Measurements of the spacing in the samples of acoustically trapped droplets were taken manually. Many images of the trapped lines of material in the central area of the device were acquired. These images were then analysed in FIJI where straight lines were drawn by hand between the midpoints of two adjacent lines of coacervate droplets to obtain a node to node measurement. To statistically minimise the error from human judgement of the line midpoint, 300 or more measurements were acquired at each trapping frequency and averaged with a standard deviation also presented in Table 4.2. The variation of the measured spacing from that of the theoretical arises due to the system assumptions in the model regarding the density differences between the droplets and the water phase and that the density of the supernatant phase will be different from that of water.

Coacervate droplets formed in situ in an applied acoustic field at the critical coacervation concentration (4 mM) did not produce any images with clearly defined trapping points. The small numbers of droplets within the volume of solution resulted in limited coalescence so that the droplets would have been too small to experience the acoustic force. Further, the limited numbers would obscure identification of any trapped particles since there were no reference points to distinguish the droplet locations with respect to other trapping points. As such the higher concentrations of coacervate constituents Fmoc-AA and PDDA were used at 40 mM. Coacervation at this concentration yielded an abundance of droplets, such that the trapping points were clearly resolvable and identifiable. In light of these observations this concentration was used throughout the work.

4.2.1.1 Coalescence in 1D trapping points

Coacervate droplets were formed in situ in the acoustic trapping device, in a 1D (6.7 MHz) applied field and left to trap for 30 minutes. Over this time as the droplets were held in close proximity within the trapped lines, there was increased coalescence (Figure 4.5a).

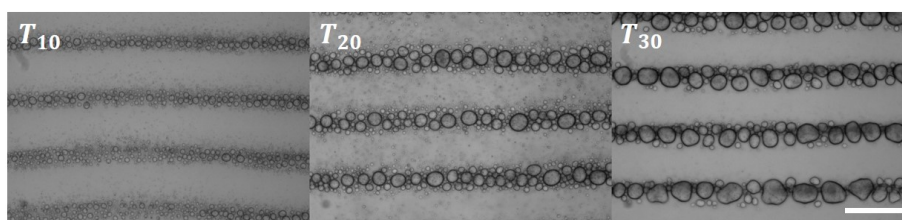


Figure 4.5: Coalescence behaviours of droplets at the nodal points of a 6.7 MHz 1D acoustic field with time in minutes. Scale bar 100 μm

If droplets had been loaded with fluorescent dyes and time lapse image series acquired then the growth in size of the droplets as they coalesced could be quantified from fluorescence analysis. This method would also serve to identify the settling of new coacervate droplets at the trapping site. With this understanding of the droplet behaviours in the trapping points, the loading concentrations of guest molecules within the droplets could be done very specifically.

4.2.1.2 Patterning across the whole device

Multiple images were stitched together to observe the trapping across the whole 20 mm square device (Figure 4.6). Significantly, samples trapped in a 1D (6.7 MHz) acoustic field showed that the patterned lines extended across the entire width of the trapping device. It can also be seen that the trapping varies across the device. Particularly in the case of this sample, there is strong vertically patterned lines of coacervate material across the centre of the device but this varies towards the top area of the device particularly. The strongest and most clearly defined trapping can be observed across the centre of the device between the pair of activated transducers. Towards the top and bottom edges the trapping is less distinct and the sample appears 'cloudy'. At these positions within the device the forces are much weaker and streaming flows more dominant. This is experimental evidence of the better approximation of the acoustic field within the device from the Huygens model, due to the inclusion of the transducer length (Section 3.2.1).

4.2.2 Hydrogelation in a 1D acoustic field

4.2.2.1 Hydrogelation transformation

Solutions of Fmoc-AA were pH-driven to deprotonate the molecule and aid the dissolution in water. The self-assembly of the molecules into a supramolecular hydrogel relied upon the protonation of the Fmoc-AA molecules and so the pH of solution had to be reduced. As the pH of the coacervate solution drops below the pKa of the carboxyl group, it becomes protonated, inducing π - π stacking and supramolecular self-assembly into a hydrogel of supramolecular nanofibrils (Section 1.4.2). The coacervated Fmoc-AA molecules stack within their coacervated position, with surrounding uncoacervated Fmoc-AA in the supernatant and other nearby molecules into the nanofibrils. Within the droplets there was surface specific reconfiguration of Fmoc-AA held within the coacervate droplet matrix, resulting in slightly contracted droplet cores with fibrils emanating from the surface in all directions.

The slow hydrolysis of glucono- δ -lactone (GDL) into gluconic acid was used to initiate the hydrogelation of the Fmoc-AA/PDDA coacervate system. A small aliquot of coacervate solution was removed, mixed with GDL powder (20 mM final concentration) and replaced back into the bulk solution (Sec-

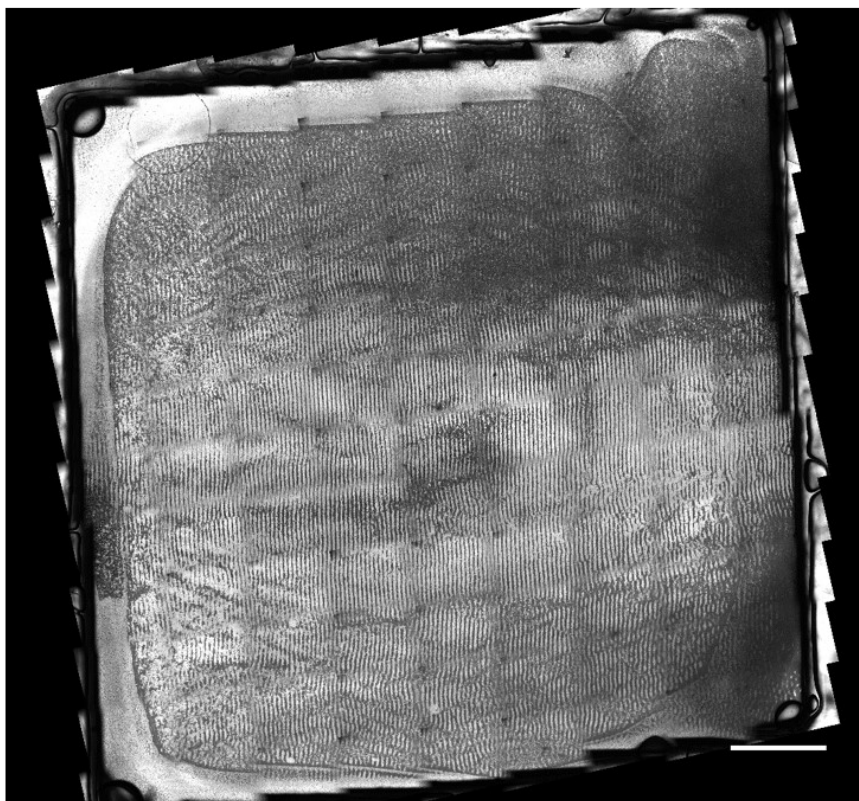


Figure 4.6: Stitched image of the entire device chamber with coacervate droplets trapped in a 1D (6.7 MHz) acoustic field. Lines of patterned coacervate droplets extend vertically across the cavity but towards the top and bottom the trapping is less distinct. Scale bar 2.5 mm

tion 2.2.3.3). Samples were left overnight for the diffusion of the acid throughout the volume to lower the pH homogeneously and for total gelation transformation of the sample, with the acoustic field applied throughout. Uncoacervated Fmoc-AA present in the supernatant phase of the solution also self-associated into fibrils such that the entire volume of solution transformed during hydrogelation.

Several alternative acids (hydrogen chloride, gluconic acid, acetic acid) were briefly explored to initiate hydrogelation. However the rapid reduction in pH often meant that any viscous turbulence introduced to the system upon addition of the acid was contained within the rapidly transformed gel network. Diffusion of these acids across the coacervate volume occurred too slowly, so there was localised inhomogeneous gelation at the site of addition that did not propagate across the whole sample. Consequently addition of GDL powders was used throughout all experiments performed.

4.2.2.2 Hydrogelation in the presence of a 1D acoustic field

Coacervate droplets were left to trap in the acoustic field for 5 minutes before the addition of GDL by removal of a small aliquot from one corner of the device, and careful replacement after mixing with GDL (Section 2.2.3.5). The associated fluid flows in these steps, would partially disrupt trapped coacervate material. This was minimised as far as possible by careful pipette extraction and replacement of fluids slowly out of and into the device. Some investigations into the possibility of introducing GDL into the coacervate solution prior to addition into the trapping device were performed however the resulting hydrogels did not exhibit features like those produced with the GDL added at a later time after they had been left to trap.

The slow hydrolysis of GDL and hence reduction in the pH over 10s of minutes enabled the recovery of any droplets perturbed from their trapped positions during mixing to migrate back to the trapping points of the acoustic field before becoming immobilized in the network as the droplets transformed. The diffusion of the GDL resulted in full transformation of the whole coacervate solution. The droplets transformed at their trapped locations within the acoustic field to produce ordered features within it. Transforming hydrogel samples were left overnight in the presence of an acoustic field contained in a humid environment so that the hydrogel networks did not dehydrate.

Acoustically patterned hydrogels could be removed from the trapping device and retained the ordered features as shown in Figure 4.7. When patterned at the lowest identified driving frequency (2.15 MHz) in 1D the half-wavelength spacing of $\approx 350 \mu\text{m}$ enabled resolution of the patterning across the hydrogel by eye (Figure 4.7a). The patterning had been fixed within the transformed hydrogel network and lines can be seen to extend across the whole sample. As with the trapped lines of coacervate droplets, the transformed lines are present vertically, between the activated pair of transducers, across the whole sample. Their extent vertically across the sample is limited to about the length of the transducer ($\approx 15\text{mm}$). Towards the top and bottom edges it is harder to elucidate the lines. The cavity is longer than the transducers coupled to it and again, as with the trapped coacervates, this is where the relevance of adopting the Huygens approach when modelling the fields is relevant (Section 3.2.1). The half-wavelength spacing for 6.7 MHz patterned gels can not be resolved by eye and appears unordered on the macroscale (Figure 4.7b). However microscopy reveals the ordered features within these hydrogels (Figure 4.7c). Again they were present at the expected half-wavelength spacing. The

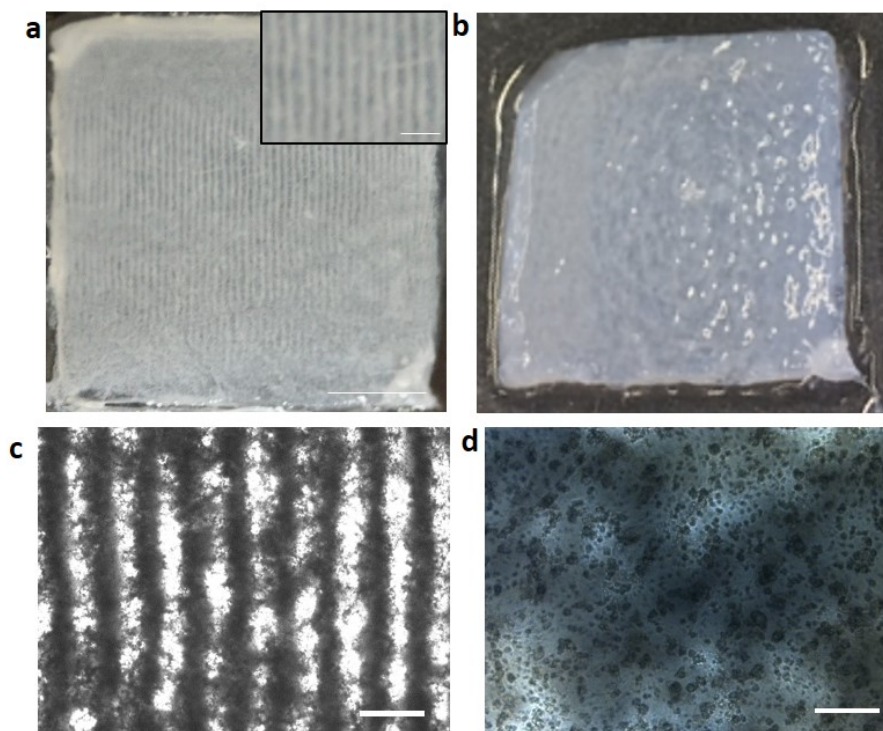


Figure 4.7: Photographs and microscopy images of acoustically micropatterned hydrogels at different frequencies and an unpatterned hydrogel a) 1D 2.15 MHz b) macroscale image of 1D 6.7 MHz patterned gel with half-wavelength spacing of $110\ \mu\text{m}$ not resolvable without magnification c) magnified 6.7 MHz 1D patterned sample reveals patterned lines extending vertically across the hydrogel sample from the transformation of ordered coacervate droplets at the nodal points d) unpatterned hydrogel sample shows no features like those seen in the ordered hydrogels. Scale bars a & b 5 mm and insets 1 mm, c & d $100\ \mu\text{m}$

acoustic field is imparting these ordered features into the hydrogels since hydrogels formed in the absence of an acoustic field do not display any similar features (Figure 4.7d).

4.2.2.3 Scanning electron microscopy of 1D patterned hydrogels

Ordered and unpatterned gel samples were imaged using scanning electron microscopy (SEM), following hydrogel preparation techniques (Section 2.2.3.6). Prior to imaging small pieces of the gels were transferred onto carbon sticky pads on SEM stubs and sputter coated in gold to enhance imaging contrast.

Firstly, patterned hydrogels were left to air dry and dehydrate over several days. Upon return film

structures remained that appeared slightly contracted in size around the edges of the gel. If samples were removed from the trapping device and left to air dry on Teflon tape then these films could be removed from the surface. Upon immersion in water for several days there was no rehydration of these dried down hydrogels.

Interestingly any contraction was not evident upon measuring the spacing of ordered features within air dried 1D patterned 6.7 MHz gels both microscopically and using SEM with half-wavelength measurements ($101 \pm 15 \mu\text{m}$) within error of those measured using optical microscopy ($114 \pm 6 \mu\text{m}$, measurements acquired by same process as outlined in Section 4.2.1) prior to drying. The decrease in the average spacing of the patterned features is attributed to shrinkage during drying, however no specific weight or volume loss measurements were acquired. The gelled features within these samples that are not in the direction of acoustic alignment were a result of higher up fibrils collapsing down on top of the ordered features as the water evaporated (Figure 4.8).

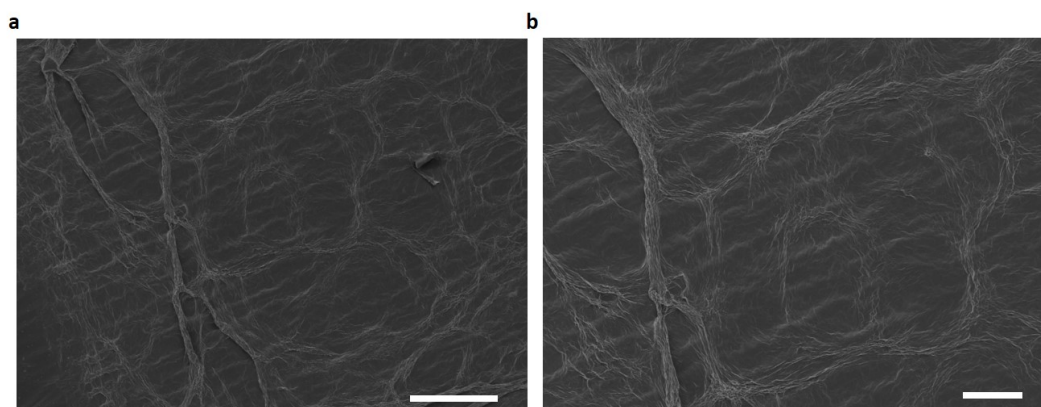


Figure 4.8: SEM images of air dried 6.7 MHz 1D hydrogels. Scale bars a) 500 and b) 200 μm

Hydrated samples were then flash frozen and immediately lyophilised whole on the glass slide (Section 2.2.3.6). Interestingly, periodic structures observed within the ordered gel samples were not at the expected half-wavelength spacing for the frequency they were patterned at, instead they were observed on the order of $\approx 10 \mu\text{m}$ (Figure 4.9). While features of this periodicity were not observed in trapping aqueous samples, the presence of sub wavelength structures has been observed with trapped micro-bubbles as a result of the forces due to their volume changes as they move through regions of different pressure in the acoustic field (Section 3.1.1). [228] While these were not visible

using optical microscopy, it is possible they may have been present within the sample and acted to template the growth of the ice crystals and produce these features. Different angles revealed that these sheets appeared to extend deep into the interior of the piece of hydrogel, interconnected by fibrillar structures.

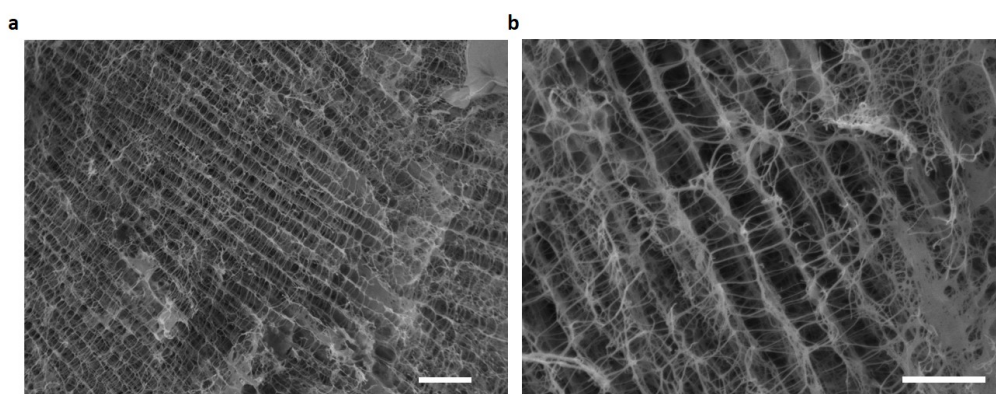


Figure 4.9: SEM images of lyophilised 6.7 MHz 1D hydrogels. Scale bars a) 10 and b) 20 μm

Compared with unordered hydrogels, prepared for SEM following the exact same method, there were no ordered periodic structures within the hydrogel arranged into organised layered sheets (Figure 4.10).

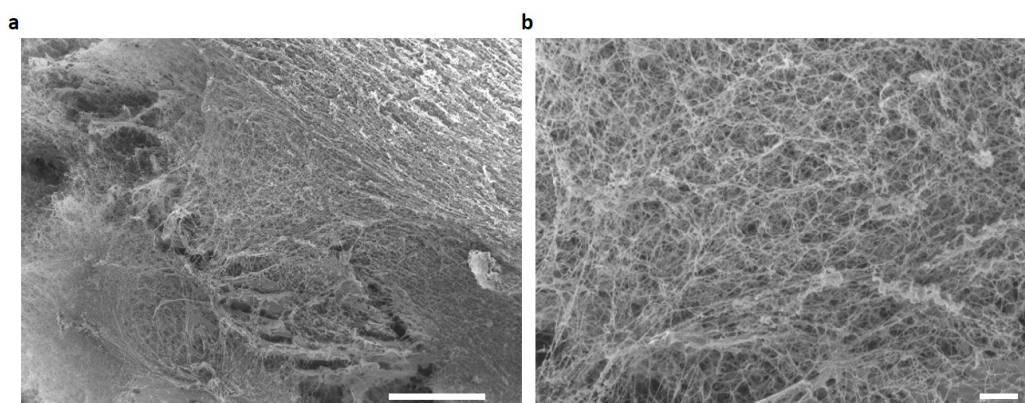


Figure 4.10: SEM images of lyophilised unordered hydrogels. Scale bars a) 100 and b) 10 μm

Similar SEM investigations with samples patterned at 2.15 MHz revealed periodic features again spaced at $\approx 10 \mu\text{m}$, however this time there were no interconnecting fibril structures between the lamellae (Figure 4.11).

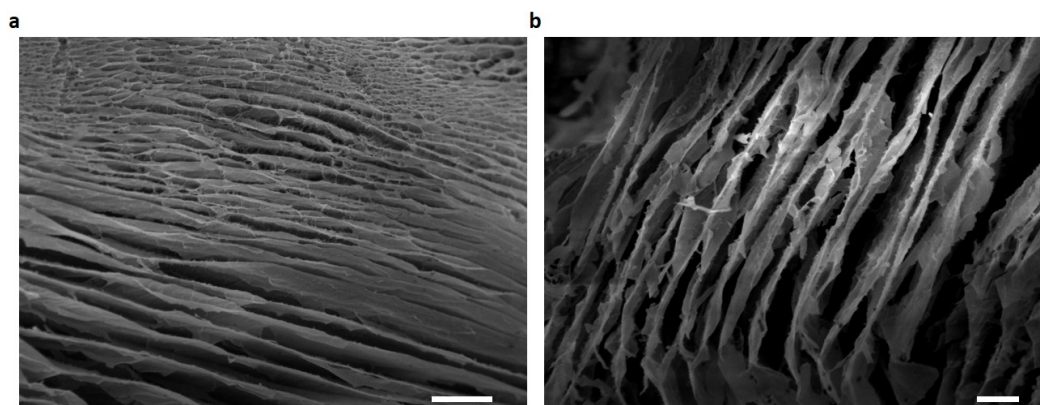


Figure 4.11: SEM images of lyophilised 2.15 MHz 1D hydrogels. Scale bars a) 50 and b) 20 μm

Since the periodicity of the 2.15 MHz patterned gels could be seen by eye, two 1D patterned samples were prepared with one left to air dry and the other lyophilised. (Figure 4.12) Fractured lyophilised samples patterned at 2.15 MHz revealed no contraction of the gels as there was retention of the half-wavelength spacing with ordered features clearly visible by eye (Figure 4.12b & c).

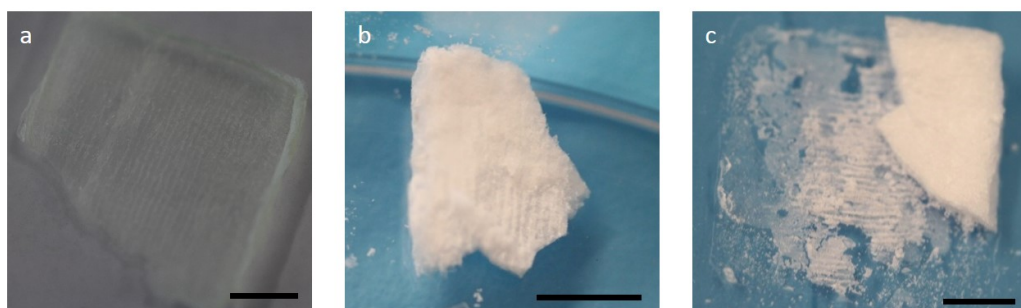


Figure 4.12: Drying of 1D patterned hydrogels at 2.15 MHz a) air-dried onto Teflon tape and then removed b) fractured piece of lyophilised hydrogel, ordered features can still be resolved by eye c) corresponding remaining sample of b) where the ordered features have remained on the surface of the glass. Scale bars 5 mm.

With the evidence of retention of the patterned half-wavelength spacing from direct observation of the lyophilised 2.15 MHz gels (Figure 4.12), the apparent decrease in periodicity observed in both 2.15 and 6.7 MHz (Figures 4.11 and 4.9 respectively) patterned samples could not be attributed to the structures becoming compacted during ice crystal formation in the lyophilisation process. It was speculated that the handling of the aerogel sample when it was transferred onto the stub, using tweezers, could have crushed the structures. However later experiments where pieces of gel were

lyophilised directly on the SEM stub revealed similar periodic features with reduced periodicity. These periodic features were never observed within unordered gel samples (Figure 4.10), prepared following exactly the same procedures as the ordered gels so their presence is attributed to the acoustically patterned structures however the mechanism of this reduced spacing is not yet fully understood.

Further information regarding these features within the hydrogel and the nature of the fibres could have been obtained from atomic force microscopy (AFM), where a probe is rastered over the surface of the sample and the different interactions between the sample and the tip are used to build a map of the surface. This technique requires no sample processing or staining and generates high resolution images. The self-supporting gels were too thick to be imaged directly and the half-wavelength spacings of dried down films were too large for the scanning area of an AFM, at distances of 60 μm or more. When measurements were attempted on small regions of the sample the tip became stuck within the coacervate material. Another option would have been high speed AFM, which can be used to image larger areas and can interact with the sample surface without compromising it.

4.2.2.4 Transmission electron microscopy of 1D patterned hydrogels

Hydrogel samples were also investigated using transmission electron microscopy (TEM). The preparation procedure for these samples disrupted any ordered features present in the hydrogel (Section 2.2.3.7). These investigations revealed the presence of nanofibrils bundled together into thicker fibril structures (Figure 4.13a). Dense approximately spherical droplet structures were also visible with fibrils emanating out from them in a variety of thicknesses (Figure 4.13b) supporting the contracted cores theory. Some areas of the TEM grid revealed large regions of intertwined fibrils (Figure 4.13c). Further information on the structure of the fibrils could have been obtained using small angle scattering techniques which would provide information on the structures across nm to μm sizes.

4.2.3 Chemical communication within hydrogels

The sequestration properties of coacervate droplets are well documented and have been exploited for gene expression and protein folding as well as to deliver biomolecular payloads to cells. [107, 229–231] Here the sequestration was used to investigate the behaviours of the droplets in the acoustic

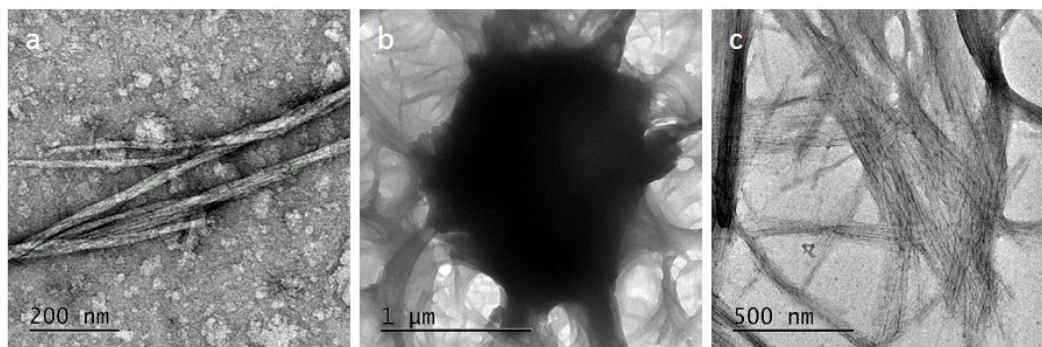


Figure 4.13: Transmission electron microscopy images of hydrogel material. Scale bars as stated

field and to increase the complexity of chemical reactions possible within the coacervate system. Use of fluorescent or fluorescently tagged molecules was particularly key for investigating the 3D nature of the system using confocal fluorescence microscopy.

4.2.3.1 Sequestration of guest molecules

Fluorescent guest molecules were added into the PDDA before mixing with FMOc-AA so they were present in solution for coacervation (Section 2.2.3.1). The different guest species readily sequestered on the droplet interiors as revealed by confocal microscopy images (Figure 4.14). The dark background shows that there was a very low concentration of the guest in the supernatant phase and that the coacervate droplets will sequester dyes (Hoechst Figure 4.14a), enzymes (tagged glucose oxidase Figure 4.14b) and biomolecules (tagged single-stranded DNA Figure 4.14c).

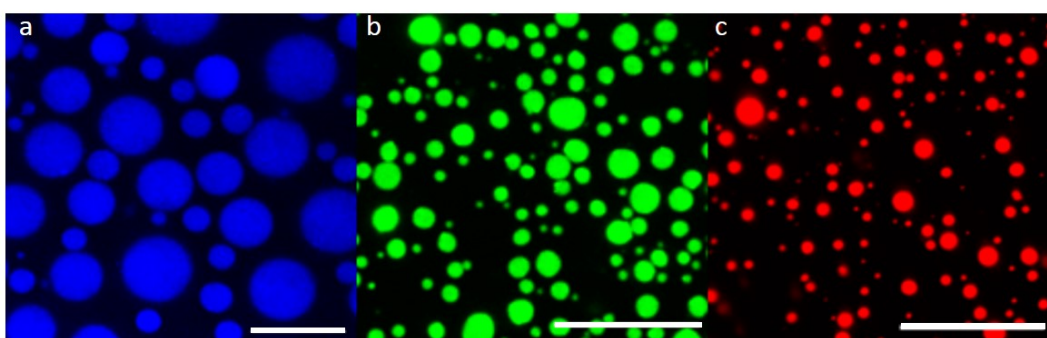


Figure 4.14: Unordered coacervate droplets containing a) Hoechst 33258 b) FITC tagged glucose oxidase and c) Cy5 tagged single stranded DNA at maximal loading concentration. Scale bars 10 μm

The sequestration of the guest molecules on the droplet interior is an equilibrium with the concen-

tration of guest molecule remaining in the supernatant phase. Molecules preferentially locate on the droplet interior. [232] For fluorescence microscopy it was important to optimise the volume of addition so that there was a strong enough signal from the droplet interior for observation but not to add so much that the background fluorescence increased. Maximal droplet loading investigations were performed with UV-Vis (Section 2.2.3.8 Figure 4.15).

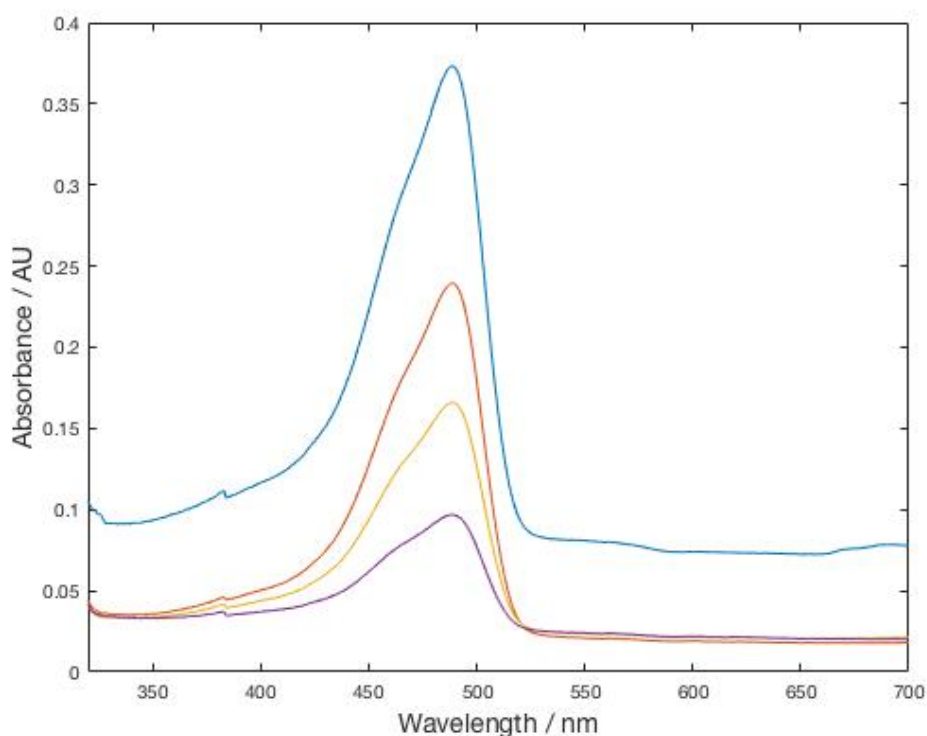


Figure 4.15: Maximal droplet loading concentration using UV Vis spectroscopy. The absorbance values shown here are for the supernatant phase when loaded with different concentrations of dye. As the concentration of dye added into the coacervate solution is reduced, so is the absorbance value at 490 nm. The highest concentration added is shown by the blue line and the lowest concentration added by the purple with others in between. In this way, the maximal loading concentration of a dye to the coacervate droplets, for the majority of the dye to be sequestered on the droplet interiors and not be present in the supernatant phase, was found.

The loading concentration for which there was an appreciable signal within the supernatant phase following separation from the bulk was the maximum volume to add to resolve droplets using fluorescence. Further addition of higher volumes of guest would not be partitioned inside the droplets but remain in the supernatant thus increasing the background signals. Due to this equilibrium,

addition of guest molecules after coacervation was also possible.

Upon ascertaining the maximal loading concentrations for the three different guest molecules they were loaded into coacervate droplets formed in situ in the acoustic trapping device. As demonstrated earlier, after 1 minute lines of ordered coacervate material could be observed with the guest molecules on the interior of the droplets (Figure 4.16). In this way the acoustic field could be used to produce ordered patterns of coacervate droplets in water, loaded with different molecules which could be used in subsequent reactions. This spatial positioning that the acoustic trapping provides enables further study into reaction propagation and chemical communication across coacervate populations.

[185]

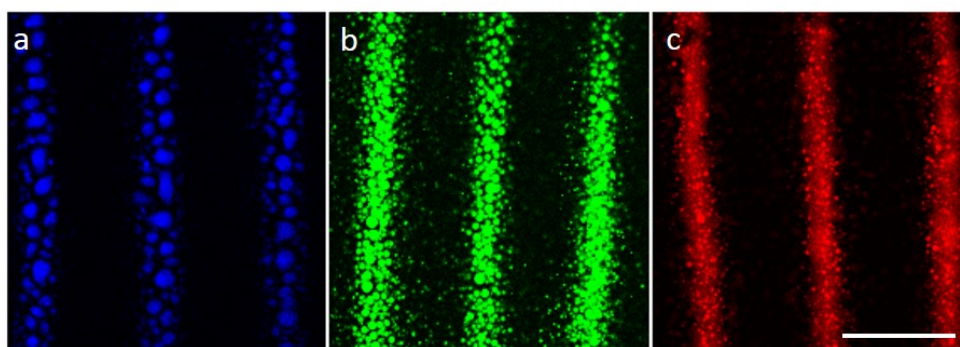


Figure 4.16: 1D (6.7 MHz) acoustically patterned coacervate droplets containing a) Hoechst 33258 b) FITC tagged glucose oxidase and c) Cy5 tagged single stranded DNA. Scale bars 100 μm

The guest molecules were chosen to highlight the potential for loading other similar molecules within the droplets. The loading of glucose oxidase and single stranded DNA within the droplets demonstrates the potential for producing ordered patterns of enzymes which can be utilised in chemical reactions and biomolecules such as DNA which can be utilised in the transfer of information.

4.2.3.2 Ordered hydrogelation in presence of guest molecules

Coacervate droplets loaded with guest molecules were trapped in an acoustic field and transformed into ordered hydrogels via addition of GDL to the solution (Section 2.2.3.5). The droplets transformed at their trapped locations thus retaining the ordered features in the resulting hydrogel network as shown in Section 4.2.2.2. As observed in unordered hydrogels, the guest molecules were retained on the interior of the contracted droplet cores (Figure 4.17), thus immobilizing the guest molecules

within the spatially ordered hydrogel network.

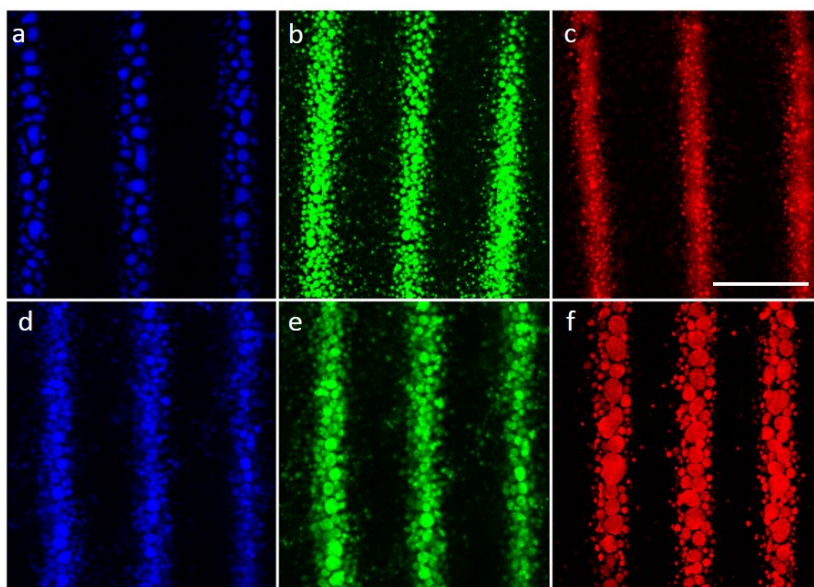


Figure 4.17: Acoustically patterned coacervate droplets containing a) Hoechst 33258 b) FITC tagged glucose oxidase and c) Cy5 tagged single stranded DNA and d-f) the corresponding ordered hydrogels containing the same guest molecules. Scale bar 100 μm

Initiating the hydrogelation transformation within the system while the coacervate droplets were trapped at the pressure minima resulted in the retention of the ordering within the resulting hydrogel network. Any guest molecules remain within the transformed droplets and were thus spatially distributed within the hydrogel network even following removal of the applied acoustic field. Thus the transformed hydrogels could be removed from the trapping device with ordering and spatial positioning of guest molecules retained enabling more complex studies in different environments, without requiring an acoustic field to maintain positioning.

As observed with guest molecules within the unordered hydrogels, there was no leaching of molecules outside of the droplets or loss of ordered features after several days, demonstrating the immobilization of guest molecules within an ordered hydrogel matrix. The main difference between the ordered droplets and ordered hydrogel are the contracted cores of the coacervate droplets, due to the surface specific reconfiguration in fibril formation. However, the spherical coacervate structures retained within the hydrogel network may not appear contracted due to the increased sizes from the field induced coalescence over the course of the hydrogel transformation (Section 4.2.1.1).

Within the patterned hydrogels, elucidation of the fibril network was easier to resolve. The guest molecule Hoechst dye binds directly to π -stacked structures enabling resolution of the fibrils forming the hydrogel network directly (Figure 4.18).

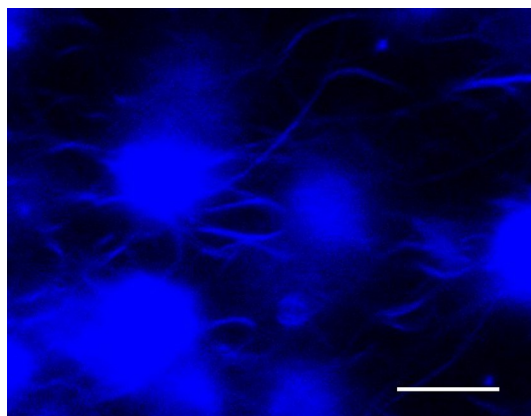


Figure 4.18: Fibrils emanating from transformed coacervate droplets loaded with Hoechst dye. The dye elucidates the nanofibrils. Scale bar 5 μm

4.2.3.3 3D rendering of 1D ordered hydrogels

Addition of the fluorescent guest molecules enabled collection of confocal microscopy z-stacks which revealed the nature of the patterning in the z-plane as opposed to previously observed bright-field x-y plane images (Figure 4.19). This was performed for both ordered droplets and micropatterned hydrogels. These data revealed that the vertical extent of the patterning was limited to $\approx 70 \mu\text{m}$. As identified by the modelling mentioned in Section 3.2.1. The acoustic forces were too low, higher up from the base of the device to trap coacervate droplets at these locations in solution. Consequently, while the ordered features could be resolved by eye at 2.15 MHz and verified by microscopy at higher frequencies, they did not extend throughout the entirety of the 2 mm thick gel and thus the micropatterned coacervate droplets produced only partially ordered hydrogel monoliths.

4.2.4 Coacervation in a 2D acoustic field

The previous sections described investigations regarding the 1D patterning of coacervate droplets. The results presented could also be replicated for the instance of 2D trapping since the trapping

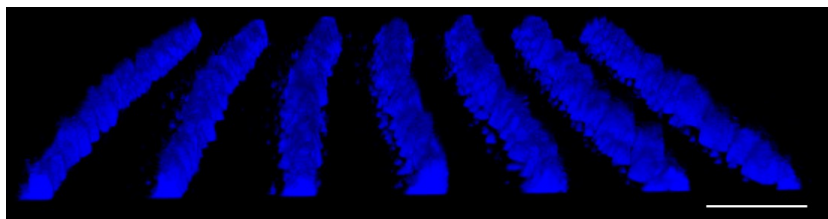


Figure 4.19: 3D stack of a 1D (6.7 MHz) acoustically micropatterned hydrogel revealing the nature of the vertical extent of the patterning. Coacervate droplets were loaded with Hoechst dye to acquire the image stack sequence. Scale bar 160 μm

devices used in this work comprise two pairs of transducers. As such, patterning was also possible in a 2D grid-like array by driving both pairs of transducers respectively (Section 2.2.1.3).

Coacervate droplets were formed in situ in the trapping device, as for 1D, however this time with both pairs of transducers activated in a temporally uncorrelated 2D (6.7 x 6.69 MHz) applied acoustic field. The 10 kHz difference in driving frequency between the orthogonally applied fields ensured any field interference averages to zero after 10 ms, so with response times of the coacervate droplets in the acoustic field on the order of a minute, the acoustic field modelling assumptions hold (Section 3.2.1). Similarly to the measurements acquired for the 1D trapped droplets, measurements of the spacing of the droplets were found as outlined in Section 4.2.1 for both the horizontal and vertical spacing between the trapping points.

Coacervate droplets formed in situ at 40 mM equimolar ratio trapped in a 2D (6.7 x 6.69 MHz) field are displayed in Figure 4.20b after 5 minutes in the acoustic field. The droplets migrated to the pressure minima of the applied acoustic field with clusters of droplets arranged in a grid like pattern.

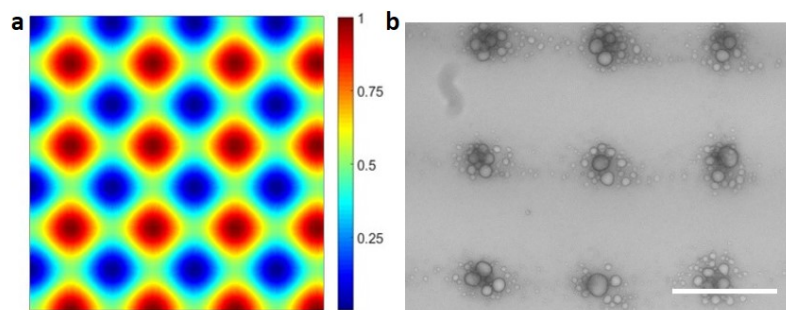


Figure 4.20: Comparison of plane wave modelled and observed trapping in a 2D acoustic field. a) and b) show 2D (6.7 x 6.69 MHz) modelled and experimental trapping respectively Scale bar 100 μm

Frequency / MHz	Theoretical $\frac{\lambda}{2}$ spacing / μm	Measured $\frac{\lambda}{2}$ spacing / μm
2.15 x 2.14	325 x 343	$345 \pm 9\%$ x $358 \pm 10\%$
6.7 x 6.69	110 x 110	$111 \pm 6\%$ x $112 \pm 6\%$
11.3 x 11.31	65 x 65	$67 \pm 6\%$ x $68 \pm 6\%$

Table 4.3: Table displaying half-wavelength spacings as calculated theoretically and measured directly from images of ordered coacervate droplets at each of the identified driving frequencies for 2D acoustic patterning

The half-wavelength spacings measured from optical micrographs at the three different driving frequency combinations in 2D were in good agreement with the theoretical ones (Table 4.3).

4.2.4.1 Coacervate droplet behaviour in a 2D acoustic field

When the droplets were left in an acoustic field for some time, the droplets tended to coalesce to much larger sizes than they would in free solution. It can clearly be seen that at the nodal points of the 2D field the droplets have coalesced, with some very large droplets present amongst the clusters of droplets (Figure 4.20b). They were held in close enough proximity by the acoustic force to overcome like charge repulsion and for coalescence to occur. Time-lapse image series revealed the coalescence of the droplets at the nodal points of a 2D applied field (Figure 4.21a).

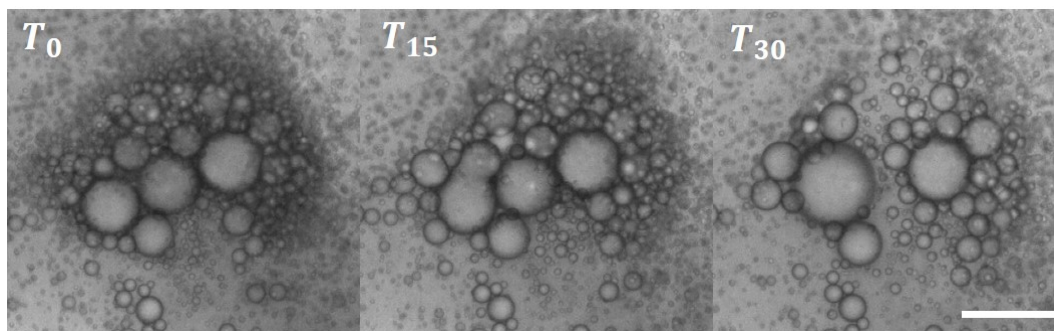


Figure 4.21: Coalescence behaviours of droplets within a nodal point of a 6.7 x 6.69 MHz 2D with time in seconds. After 30 seconds the droplets present in the nodal point at $T=0$ have coalesced into larger ones. Scale bar 10 μm

The recent report on the acoustic patterning of a PDDA/ATP coacervate system demonstrated that the droplets within each nodal point had coalesced into one large droplet per nodal point when left in a 2D acoustic field for up to 1 hour. This was attempted with the FMOC-AA/PDDA coacervate droplets at 1:1 40 mM ratio. However, after this time frame, the droplets were disrupted. Figure 4.22

shows the coalescence of coacervate material at the nodal positions of the applied 2D field until they have disrupted. New droplets have trapped over the top of the wetted out coacervate material.

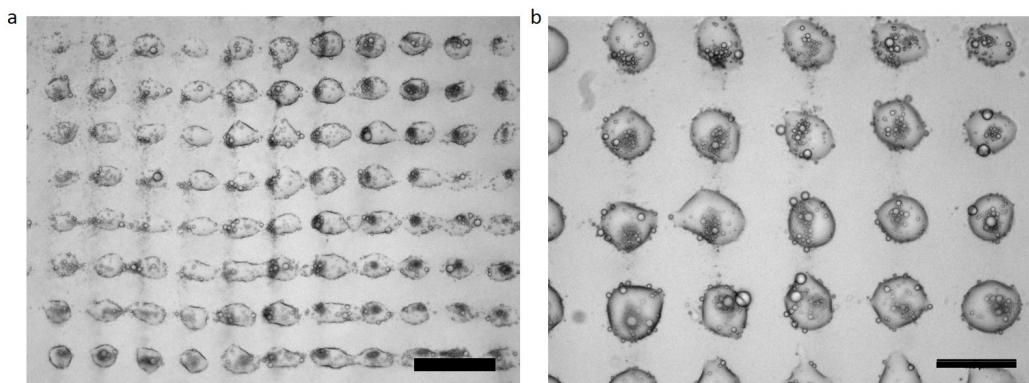


Figure 4.22: Disrupted 1:1 ratio Fmoc-AA:PDDA coacervate droplets left to trap for 1 hour in a 2D (6.7 x 6.69 MHz) acoustic field. Scale bars a) 200 and b) 100 μm

This disruption is attributed to the higher density of the Fmoc-AA/PDDA coacervate droplets compared with PDDA/ATP. The interiors of these droplets are more crowded and thus more viscous so that at larger sizes the behaviours of the polymer chains in the densely packed interiors disrupt the droplets.

4.2.4.2 Towards one droplet per nodal point

It is well documented that coacervate behaviour is known to vary with the stoichiometry of addition as this affects the zeta potential (ZP) and thus inter-droplet behaviours and coalescence. [233–235] The coalescence can be controlled by altering the surface charge of the droplets to electrostatically hinder or encourage the coalescence. The ZP of droplets formed at different volume ratios of Fmoc-AA:PDDA was found (Figure 4.23).

Coacervate droplets were formed at the volume ratios that varied the most in ZP compared to the 1:1 ratio. These were the very low and very high ratios. Based on the coalescence behaviours of the droplets formed at these ratios in an applied 2D acoustic field (6.7 x 6.69 MHz) after 10 minutes the volume ratios of 2.5 (5:2 Fmoc-AA:PDDA) and 0.42 (3:7 Fmoc-AA:PDDA) were selected for further investigation. Coacervate droplets were again formed in situ in the trapping device and left to trap in a 2D (6.7 x 6.69 MHz) acoustic field for 30 minutes. The resulting arrays of droplets were not disrupted

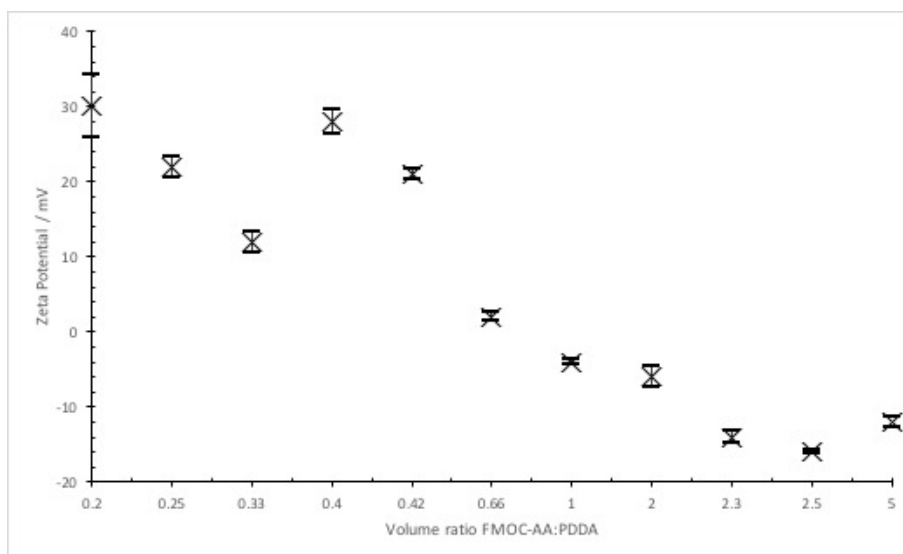


Figure 4.23: Zeta potential values for different coacervate droplets for 40 mM solutions of FMOc-AA and PDDA, at the stated volume ratios.

with the largest droplets in the nodal positions remaining intact and spherical (Figures 4.24 and 4.25). The coalescence can be observed as the time progresses with clusters of droplets at 5 and 10 minutes in the field and larger droplets surrounded by some smaller ones at 30 minutes. Both ratios exhibited large spherical droplets at the nodal points, indicating that the different ZP lead to more favourable droplet interactions and stable large droplets compared with the equimolar ratio.

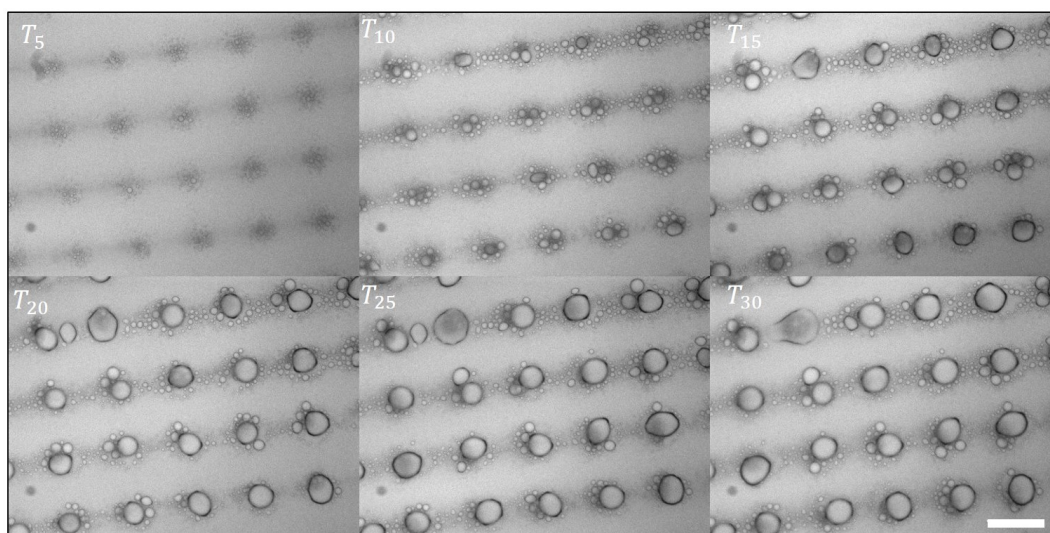


Figure 4.24: Time-lapse series of 3:7 FMOc-AA:PDDA coacervate solution ratio over 30 minutes with images shown every 5 minutes. Scale bar 100 μm

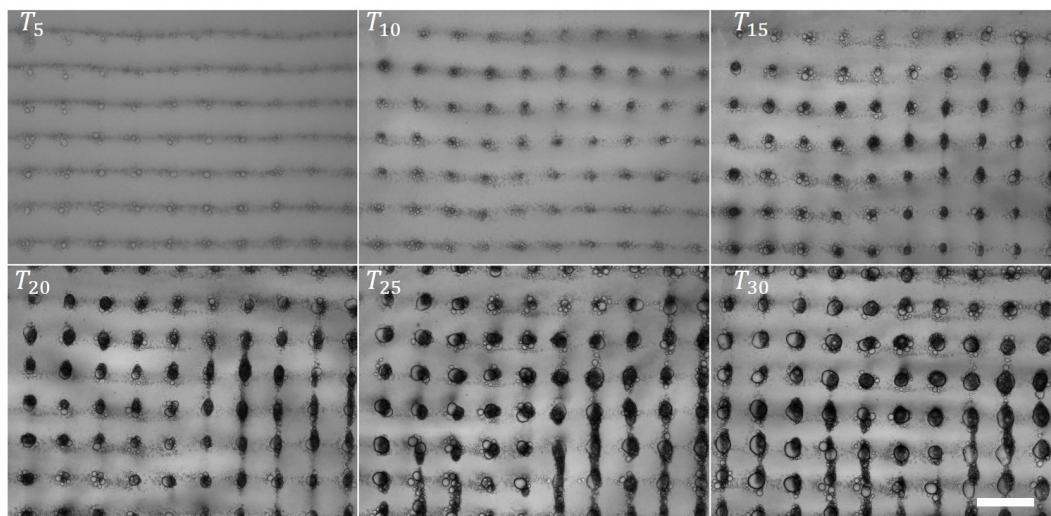


Figure 4.25: Time-lapse series of 5:2 Fmoc-AA:PDDA coacervate solution ratio over 30 minutes with images shown every 5 minutes. Scale bar 100 μm

Different coalescence behaviours can clearly be observed with the 3:7 providing the best route to 1 droplet per node (Figure 4.24). The darker regions within the trapping points at the 5:2 ratio (Figure 4.25) which start to appear at 15 minutes are clusters of coacervate droplets that are not stably trapped at one nodal point. Their movement between nodal points can be seen comparing the images at 20 and 25 minutes, where they start distributed between two nodal points at the top of the field of view and then have moved further down in the latter one.

Compared with the disrupted droplets observed for 1:1 ratio (Figure 4.22) at these ratios the coacervate droplets were coalescing at the nodal points and remaining as half-domes on the glass surface, not wetting out into non-spherical shapes.

The promising coalescence of the coacervate droplets formed at a 3:7 (Fmoc-AA:PDDA) ratio, to sizes of $48 \pm 6.2 \mu\text{m}$ after 30 minutes, was further investigated to see if singular droplets within each trapping point could be produced. After 1 hour of trapping, the array of droplets shown in Figure 4.26 was produced. Across a large area of the device, a singular, spatially isolated droplet within each trapping point was observed. Right in the centre of this image, distinct droplets can be seen but moving away from there, towards the edges of the field of view, while there are still large droplets within the 2D nodal points, there are more coacervate droplets between them as the trapping tends towards 1D at the point where the 2 orthogonal fields no longer intersect. As with previous trapping

observations, the Huygens model presented a more accurate model of the trapping within the device (Section 3.3.3).

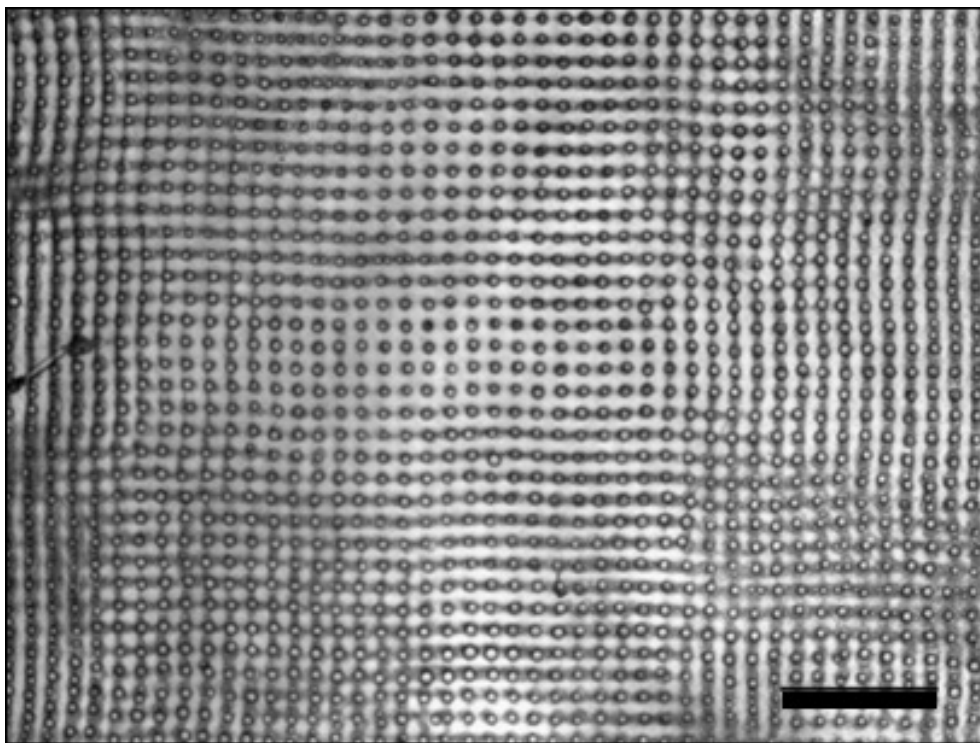


Figure 4.26: Optimised ratio of 3:7 FMOC-AA:PDDA whole device patterning in a 2D acoustic field (6.7 x 6.69 MHz). After 1 hour the clusters of droplets at the nodal points have coalesced into one large droplet per node across a large area of the trapping device. Scale bar 500 μm

4.2.5 Hydrogelation in a 2D acoustic field

Having found the best ratio of addition for 1 droplet per node in 2D trapping, the coacervate droplets were formed at this ratio (3:7 FMOC-AA:PDDA volume ratio) and left to trap for 1 hour to form the large isolated droplets at each trapping point, before initiating hydrogelation. The resulting hydrogels had multiple spatially distinct single droplets in the transformed 2D array (Figure 4.27). Droplets were loaded with Hoechst dye for fluorescence microscopy to investigate the structures. There was no vertical improvement in the vertical extent of the patterning with features again persisting to $\approx 70 \mu\text{m}$.

In the low frequency 2D trapped sample it can be seen that the patterning transformed into the hydrogel network is a little more interesting (Figure 4.27b). There are areas of the gel where the grid-

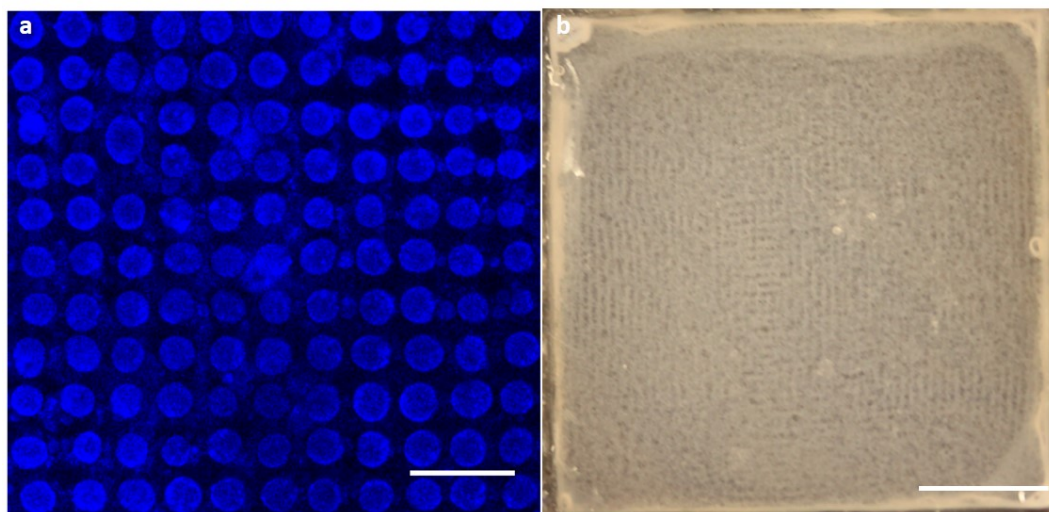


Figure 4.27: Optimised ratio of 3:7 Fmoc-AA:PDDA 2D patterned hydrogels. a) central region of 6.7 x 6.69 MHz field with droplets loaded with Hoechst dye reveals that one droplet per node has been retained within the transformed hydrogel. b) 2.15 x 2.14 MHz field shows spacing resolvable by eye. Scale bar a) 250 μm b) 5 mm

like array of nodal points can be clearly observed but towards the edge of the sample the ordering appears to be 1D lines. The expected uniformity in the 2D patterning as predicted by the plane wave model is not observed and is in better agreement with the Huygens model. This is again due to the size of the transducer with respect to the sample cavity of the trapping device and the limited region of overlap between the two acoustic fields when both pairs of transducers are activated. In this case, the two different standing waves and the summation of their contributions are more dependent on the size of the transducers than the 1D case because the region in which they overlap will only be right at the centre of the device. In light of these observations, the most appropriate modelling of the expected patterning observed is from the Huygens model. A further contribution to the variation in expected patterning within the device will arise from the polydispersity in size of the coacervate droplets. In the acoustic field they coalesce to greater sizes at the nodal points but there are also still plentiful smaller sized droplets present.

The size polydispersity of the coacervate droplets may also affect the acoustic trapping. Larger ones will experience a stronger acoustic force while very small coacervate droplets ($< 500 \text{ nm}$) will experience a smaller one if they experience it at all ($F^{rad} \propto a^3$). Alongside the slight variation in pressures, this will result in different numbers of droplets accumulating at each trapping point

in the 2D field. Further the smaller ones present in solution will continue to trap and migrate to the trapping points over the course of the experiment, such that there is a constant supply of new coacervate droplets arriving at the trapping points. Streaming of droplets higher up in the device was also observed. This would affect the migration of those droplets to the trapping points since depending on their size the streaming forces would dominate over gravity and the acoustic force.

4.2.5.1 Effect of micropatterning on hydrogel mechanical properties

The effect of introducing order into the hydrogels was explored further using rheology. As outlined in Section 2.2.3.9, 20 mm square unordered, 1D (6.7 MHz) and 2D (6.7 x 6.69 MHz) ordered samples were loaded onto a parallel plate geometry for small amplitude oscillatory strain and frequency sweeps (Figure 4.28). For the strain sweeps the elastic moduli were higher than the viscous moduli for all samples, as is characteristic for a viscoelastic material. The linear viscoelastic region (LVE) persisted up to 5, 8 and 4 % shear strain for unordered, 1D and 2D ordered gels respectively. The G' ($22 * 10^3$ Pa) and G'' ($4 * 10^3$ Pa) values of the 1D ordered hydrogels were similar to those obtained for the unordered gels without an applied acoustic field; G' ($25 * 10^3$ Pa) and G'' ($5 * 10^3$ Pa). The 2D ordered hydrogels had lower moduli; G' ($8.8 * 10^3$ Pa) and G'' ($1.7 * 10^3$ Pa) implying that the 2D patterned hydrogels were less solid-like than the other gels. Frequency sweeps at 1 Hz revealed negligible difference between the three different hydrogels implying similar deformation properties and LVE behaviours.

The negligible difference between the moduli and LVE between the different ordered and unordered hydrogels implied that the ordering had no effect on the resulting mechanical properties. This was due to the fact that the micropatterned hydrogels were only partially ordered with the patterned features localized towards the bottom of the sample. This is a known limitation within the acoustic device (Section 3.2.1) and was further investigated using confocal fluorescence microscopy which revealed the ordered features within the hydrogel only extend to $\approx 70 \mu\text{m}$ vertically. This vertical limitation is thought to be the main reason why there were no differences in the mechanical properties from rheological investigations.

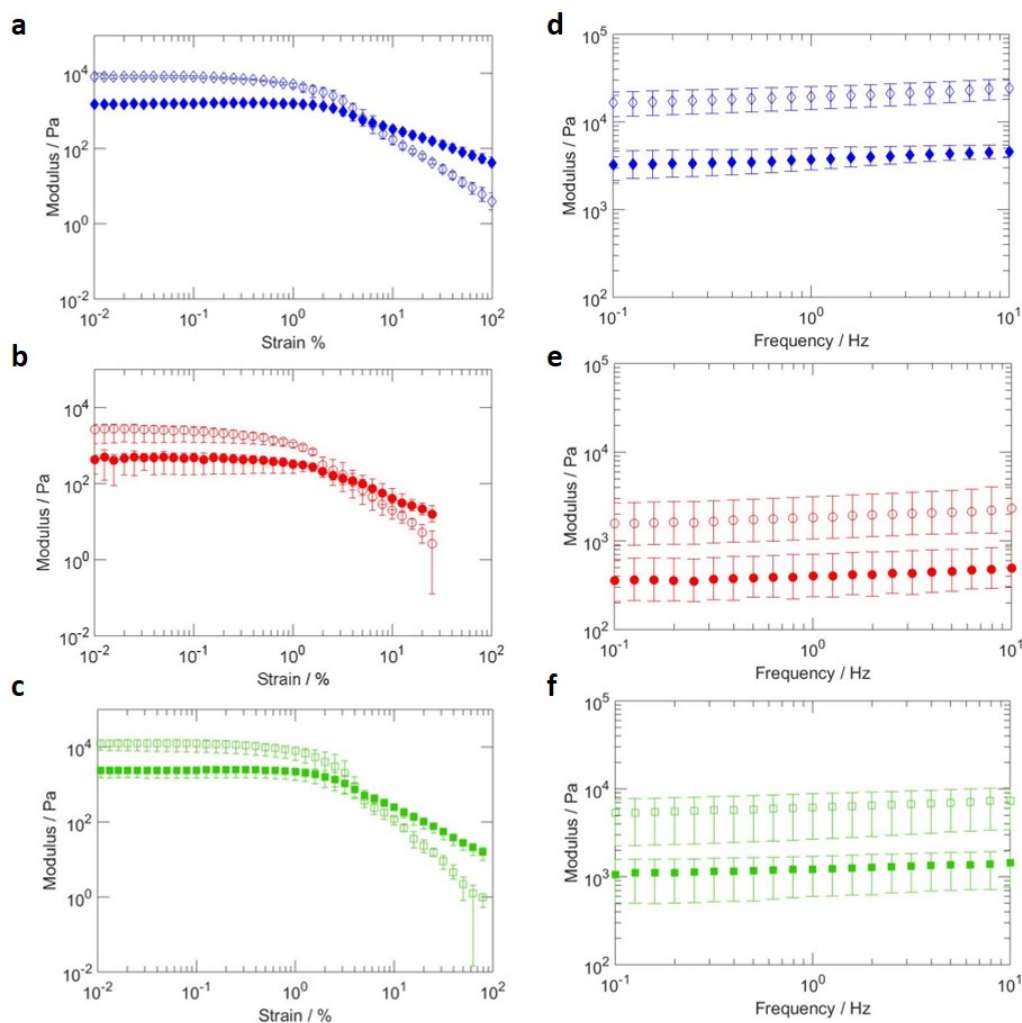


Figure 4.28: Strain and frequency sweep rheology data for unordered, 1D and 2D ordered hydrogels. All gels were produced at 40 mM equimolar ratio. All datasets have hollow symbols representing the elastic modulus (G') and filled circles the viscous modulus (G'') a) unordered gel strain sweep b) corresponding frequency sweep c) 1D 6.7 MHz ordered gel strain sweep d) corresponding frequency sweep e) 2D 6.7x6.69 MHz ordered gel strain sweep f) corresponding frequency sweep. Samples were used once for each test and then disposed and all data is averaged in triplicate.

4.3 Conclusions and Future work

The non-contact technique of acoustic trapping has been used to pattern Fmoc-AA/PDDA coacervate droplets, formed in situ, into 1D lines and 2D grid-like arrays. Initiation of the pH induced transformation of coacervate droplets while trapped at the pressure minima of a standing wave acoustic field resulted in the formation of patterned hydrogels retaining the 1D or 2D ordered fea-

tures within the hydrogel network following removal from the acoustic field and trapping device (Figure 4.29). The periodicity of the spacing within the network could be altered through changing the driving frequency of the counter-propagating standing wave transducer pair. However the pressure gradient of the acoustic fields driven at different frequencies and number of nodal points within the cavity are important to facilitate the clearest ordered structures within the hydrogel. For this work, 6.7 MHz was the optimum frequency and used for the majority of investigations.

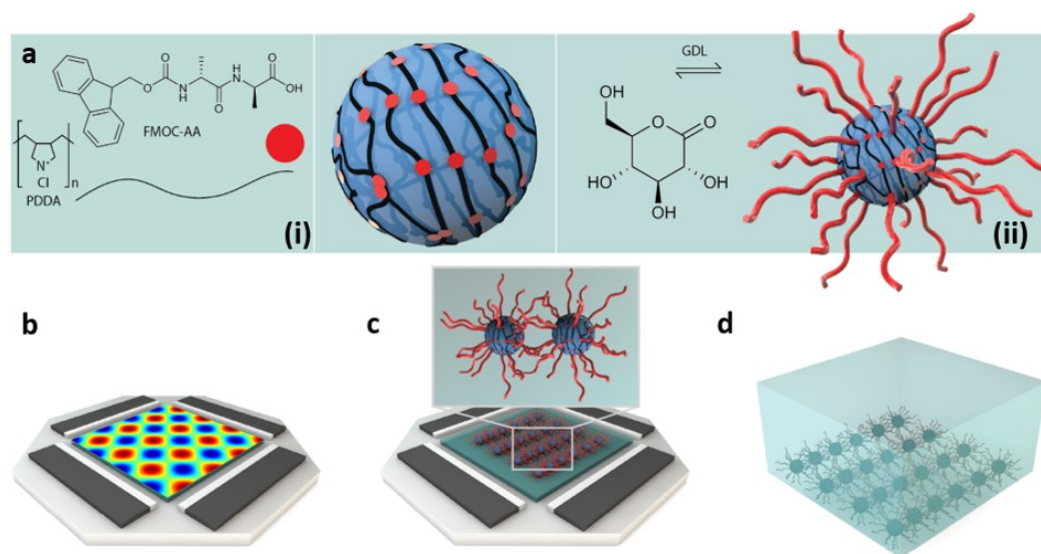


Figure 4.29: Schematic outlining the whole proposed and implemented acoustic patterning of hydrogels process. a) mixing of Fmoc-AA with PDDA results in spontaneous formation of coacervate droplets which are responsive to changes in pH and will structurally reconfigure upon reduction of the pH which was implemented using glucono- δ -lactone powders b) pressure field of a 2D acoustic field from driving both pairs of transducers. c) coacervate droplets formed in situ in the presence of an acoustic field migrated to the pressure minima of the field to form a grid-like array. Initiation of hydrogelation while the droplets were trapped resulted in transformation of the droplets into a hydrogel at their trapped locations d) the resulting hydrogel could be removed from the acoustic field with the micropatterned features retained in the network

Coacervate droplets were loaded with different guest molecules (dyes, enzymes and biomolecules) to observe their behaviour within the transformed patterned hydrogel network. They remained localised within the interiors of the transformed coacervate droplets and thus isolated within the 1D or 2D patterned hydrogel networks, presenting the opportunity for spatial control and immobilisation of guest molecules into a periodic array. Loading of the coacervate droplets with enzymes and single stranded-DNA serves as a representative example of the potential to pattern a broad

variety of different molecules within the network by loading them into the coacervate droplets prior to transformation. A major benefit of the patterned hydrogels is the aqueous hydrogel network enables further investigations to be performed without an acoustic field to maintain the ordering. Significantly, the sequestered guest molecules also revealed that the micropatterned hydrogels were only partially ordered up to $\approx 70 \mu\text{m}$ vertically through fluorescence microscopy, accounting for the negligible difference in mechanical properties between ordered and unordered hydrogels.

Finally, the coacervate mixing ratio was optimised to encourage coalescence of the droplets over long time frames at the nodal points of a 2D acoustic field into one droplet per node. Studies into the coacervate behaviours over prolonged exposure to the acoustic field were further enabled through fluorescence microscopy. A ratio of 3:7 (Fmoc-AA:PDDA) was found to be the best to produce one large coacervate droplet per node when left to trap in the acoustic field for 30 minutes or longer. This patterning was also over much larger areas of the sample than observed in initial investigations. This optimization enabled large spatially isolated single droplets at the nodal points of a 2D acoustic field to be transformed within the hydrogel network.

The observed patterning of the coacervates within the acoustic trapping device was in best agreement with the Huygens model of the acoustic field. Particularly in the 2D trapping case, where the effects of the transducer size dictated where the fields would overlap and result in 2D rather than 1D trapping. There are some other variables, such as polydispersity of droplet size, that should be considered when modelling the trapping of these aqueous systems alongside the device adaptations and in future this may require more extensive understanding and investigation. A lot of the earlier trapping experiments were performed without dedicated matching of the transducers during device fabrication. This could result in directional imbalance between the two transducers or any of the other situations outlined in Section 3.1.3.3. Ordered hydrogels produced using acoustic trapping devices fabricated with optimised transducer pairings, still exhibited the same ordered features, producing patterned features also in best agreement with outputs from the Huygens rather than plane wave model.

The acoustic trapping device utilised in this work serves to illustrate that patterning and transformation of the patterned droplets into ordered 1D lines and 2D gridded arrays. Further geometries and hence patterning arrangements would be possible. Adding another standing wave transducer

pair would enable a hexagonal device, with all nodal points equidistant from their neighbours, which would be useful in observing propagation of reaction fronts through the hydrogel. Use of a ring transducer enables patterning of the droplets into concentric rings which again would be useful for observing how reactions propagate outwards from the centre. Further, in pursuit of stronger and higher trapping of coacervate droplets across the height of the gels, a 3rd pair of transducers could be introduced to trap material in the z-direction in addition to x-y. Where specific half-wavelength separations are desired the driving frequency can be altered through the choice of transducer, since driving frequencies are size dependent. Larger transducers with respect to the size of the cavity would also improve the size of the area of field overlap and improve the extent of the patterning, enabling larger areas of hydrogel to be usefully patterned. These implementations may alter the mechanical properties significantly for rheological differences to be observed.

The patterning fixed into hydrogels already transformed should not be affected by a further applied field. In this way, the acoustic field could be used as a tool to achieve other acoustic phenomena within the hydrogel. These devices have already been utilised in particle manipulation. Enzyme substrates or other guest molecules could be introduced and moved through the hydrogel network using this manipulation capability. Beyond this, cavitation might be a potential option for chemical release within the hydrogel network. [226]

Patterning of different ratios of coacervate droplets could be explored in 1D or 2D to see if their differing behaviours might result in any interesting hydrogel structures following transformation. The studies presented here only looked at droplet behaviours in the field up to one hour. Beyond this point there may be some phenomena of note and benefit for spatially organised studies.

There are a variety of other protocellular systems that theoretically exhibit the desired size and density properties for acoustic manipulation such as proteinosomes (1s - 100s μm) and colloidosomes (10s - 100s μm). [183, 236] These could be patterned alongside the coacervate droplets and used in population communication studies or as reaction compartments and vessels to introduce different chemicals into the hydrogel network. Proteinosomes have fixed size porous membranes and so no leaching of specific guest molecules occurs. [183] Encapsulating other protocells in an ordered manner could introduce responses to other stimuli within the micropatterned hydrogel, such as controlled directional swelling, leading to more complex and controllable behaviours.

The results presented here suggest that acoustic patterning offers the potential for construction of micropatterned viscoelastic soft materials for use in tissue engineering, micro-array technologies and cell biology. The extension of this microfabrication route could facilitate the production of more complex architectures and behaviours within the spatially controlled hydrogel networks.

CHAPTER

5

**ACOUSTICALLY MICROPATTERNED COACERVATE-BASED GELATINOUS THIN
FILMS FOR CHEMICAL COMMUNICATION AND 3D CONSTRUCTS**

Chapter overview

In this chapter a protocol was developed to fabricate gelatinous thin film hydrogel constructs, removing the majority of the supernatant without disruption of the patterned coacervate droplets in both 1D and 2D such that only the ordered droplets comprised the hydrogel films. The sequestration properties of the droplets were exploited to prepare thin films containing enzymes to observe both one and two step cascades to demonstrate the retention of functionality within the film constructs. The acidic product from the breaking down of glucose by glucose oxidase was then used for hydrogelation of the films, negating the need for any fluid mixing compared to the previous gelation route with glucono- δ -lactone powders. The morphologies of the enzymatically hydrogelated 1D micropatterned thin films were continuously connected, extending across the width of the films. These films were then stacked sequentially, following a layering procedure, to produce convincing 3D hydrogel architectures.

5.1 Introduction

The large volumes of water retained within the 3D networks of hydrogels makes them extremely biologically relevant materials. This high water content and physical similarity to biological tissues has made them promising in the area of tissue engineering. [137, 237–244] In both these applications, the motion of molecules within the hydrogels is critical for cellular metabolism processes. [245, 246] However in the presence of a 3D cross-linked network, with which the molecules can interact and become obstructed by, the diffusion becomes a little more complicated (Section 1.5.1). As such structuring the hydrogel into a 3D supportive scaffold is of great importance. [137, 247]

Large scale control over the ordering of the network is particularly difficult within 3D materials but through adopting a layering approach, a variety of different structures can be produced. Lee *et al.* have used gelatin as a sacrificial hydrogel to embed channels into collagen through 3D printing (Figure 5.1a). [248] While Hong *et al.* fabricated a bilayer from 3D printed sequential layers of PEG-alginate hydrogel lines arranged orthogonally to produce a cross-hatched arrangement. (Figure 5.1b) In this way the stretchy hydrogels could be constrained. This technique can be used with more layers to produce a mesh structure and produced in smaller dimensions. (Figure 5.1c) [249]

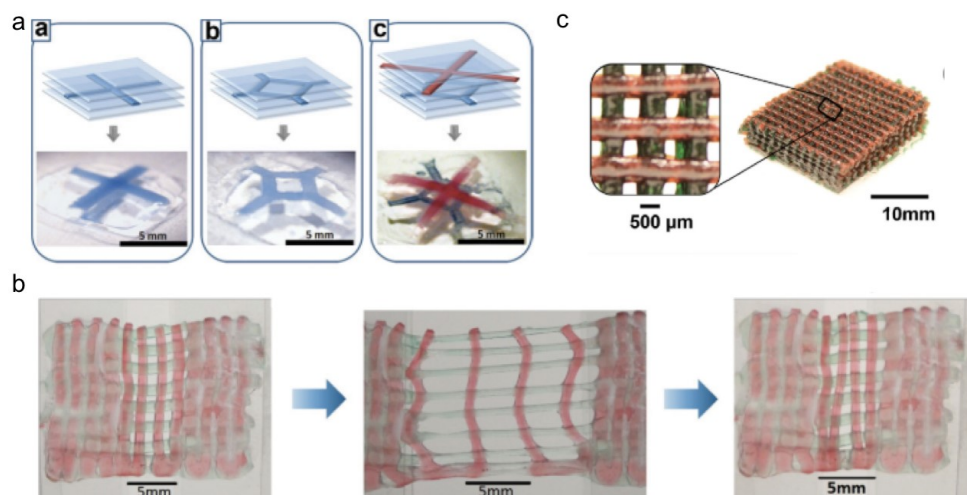


Figure 5.1: Different 3D printing hydrogel patterning approaches a) the layering technique utilising patterned gelatin as a sacrificial feature to create the channels within the collagen hydrogel b) layering of lines of gel material, with each layer elucidated by a different colour, to form a cross hatched arrangement with a highly elastic hydrogel c) the layering of many more layers in a similar process to that shown in b). Figures reproduced from [248, 249].

Some advances in hydrogel fabrication have been that of thin films, which exhibit the same functionality as their thicker counterparts, such as stimuli-response, but minimise the materials required. [250–252] In the fabrication of the acoustically micropatterned hydrogels (Chapter 4), the functionalised dipeptide within the entire sample, in both the bulk and supernatant phases, transformed into fibrils upon lowering of the pH of the entire solution. Unordered and uncoacervated material was also transformed into the hydrogel such that the ordered coacervate features imparted into the hydrogel network extended $\approx 70 \mu\text{m}$ and comprised $\approx 5\%$ of the total vertical gel height of $\approx 2 \text{ mm}$. Thus, the potential to remove the unordered gelled material comprising the bulk of the hydrogel to produce gelatinous thin films comprised of only the ordered transformed bulk phase was explored. Further, these thin films could conceivably be sequentially layered towards higher vertically-extending ordered structures.

5.1.1 Chemical complexity in hydrogels

In addition to 3D structuring, the movement of different molecules within the hydrogel is important in maintaining cell viability and responding to environmental cues. [253, 254] Where the organisation

of different molecules within the hydrogel is important, chemical compartments can be used. They can lend themselves to manipulation more easily than the hydrogel molecules themselves and so can be arranged within the hydrogel (Section 1.5.2). Different vesicles have been used for isolation of chemical reactions, such as enzyme cascades. Enzymes are globular proteins residing within cells, which convert a specific substrate into products. Their specificity is often described using a lock and key model with the lock representing the enzyme and the key the substrate. Only the correct key will fit inside the lock and then be converted into products, which are then released from the enzyme. (Figure 5.2).

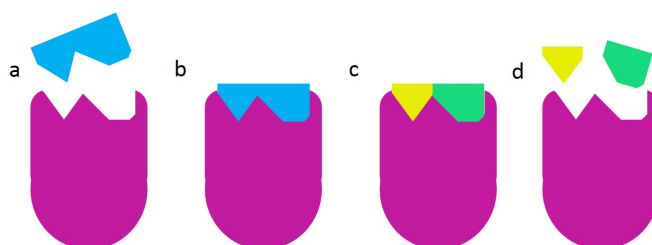


Figure 5.2: The lock and key model of enzyme reactions. a) the substrate (blue molecule) is the only molecule that will fit into the active site of the enzyme (purple) b) when the substrate enters the active site of the enzyme it is known as an enzyme/substrate complex c) the substrate is converted into products (yellow and green molecules) to form an enzyme/products complex d) products are released from the active site.

In some cases, coupled enzymatic reactions are required to provide useful products. Here, a product from the breaking down of the first substrate by the first enzyme acts as the substrate for the second enzyme. A commonly used coupled enzymatic reaction is that of glucose oxidase with horseradish peroxidase. Upon addition of glucose, the substrate for glucose oxidase, the hydrogen peroxide product formed then acts as the substrate for the horseradish peroxidase. [255] While both the enzymes produce the products rapidly, the diffusion of the substrates from one enzyme to the next is another important factor in the rate of reaction. By loading enzymes into compartments within layered hydrogel constructs, the localisation of the reaction substrates and products within the compartment would enhance the rate of reaction, enabling delivery of chemicals within specific areas of the hydrogel to any cells loaded within it or to facilitate in programmed release of particular molecules into the network.

Van Dongen *et al.* demonstrated the successful immobilization of a three enzyme cascade, with the

enzymes loaded into different layers of a polymersome vesicle. [256] Work by Linko *et al.* demonstrated increased reaction rates for a coupled enzymatic cascade occurring within compartments assembled through DNA-origami. [257] Coacervate droplets loaded with actinorhodin polyketide synthase were found to stabilise the reaction and even demonstrated an increased yield of product. [258] The enzymatic activity was facilitated by the compartmentalization and through using these compartments it should be possible to distribute and then monitor enzyme reactions within a hydrogel.

In the previous chapter it was demonstrated that the acoustic patterning of stimulus-responsive coacervate droplets could be used in producing micropatterned hydrogels with intact coacervate droplets retained and periodically arranged within the network. It was further demonstrated that the coacervate droplets retain sequestered enzymes following hydrogel transformation. Through fabricating a thin film hydrogel containing enzymes the reactions could proceed with less unorderd hydrogel for the substrate to diffuse through. It is also conceivable that through introducing patterned features into hydrogels such as the continuous lines formed in 1D patterned hydrogels, they could also act as diffusion pathways. Thus it is proposed that a polymer/dipeptide coacervate thin film system could also be used for the study of enzymatic reactions occurring within micropatterned hydrogel constructs.

5.2 Results and Discussion

5.2.1 Fabrication routes for micropatterned gelatinous thin films

The immediate choice for removal of unorderd gel was directly slicing off the unorderd section of gel. This could be done manually or through microtoming. Both were decided against since manual precision would not be attainable for the final width of $\approx 70 \mu\text{m}$ without any disruption of the ordered features present and microtoming required sample processing prior to slicing. This could impact on the behaviours of any sequestered guest molecules and perhaps disrupt the ordering imparted within the hydrogel matrix.

Earlier studies had shown that addition of other fluids or reaction mixtures into aqueous arrays in an applied acoustic field did not disrupt the patterning. [185] Thus, it was believed that extraction

of some supernatant to then be replaced with water as a diluent would be achievable without any impact on the ordered droplets. Consequently, many investigations into different methods of removing most of the supernatant as a fluid prior to gelation were investigated. Here the majority of material that would gelate would be present within the bulk phase of ordered coacervate droplets and the surrounding supernatant phase would be too dilute to entirely transform. After gelation of only the ordered material, the remaining ungelated fluid could be extracted.

After being left to trap in the acoustic field, preliminary investigations revealed that removal and replacement of fluids into the cavity disrupted the trapping sufficiently by introducing streaming flows and other undesirable effects which acted to perturb droplets from their trapped locations. Upon removal of the fluid the directional motion of the supernatant 'pulled' droplets away from their trapped location. After 1 minute this partially recovered but large areas remained disordered compared with the initial trapping. Leaving the system to recover the original trapping for up to one hour, did not result in the same trapping.

Further, upon replacing the volume of supernatant extracted with an equivalent volume of water, the forces from the fluid as it entered the device when ejected from the pipette were strong enough to disrupt the trapped droplets in that location. Further away from this entry location, while the trapping was not perturbed as noticeably, the movement of smaller coacervates in fluid flows introduced could be seen. As an alternative to pipettes, wider nozzled syringes were used to try and lessen the force impacts upon entry of the fluid into the device. While this lessened the entry forces, similar mixing fronts were still observed.

5.2.1.1 Effect of droplet viscosity

Results indicated that trapped droplets within the device were slightly perturbed from their location to varying extents based on their proximity to the site of fluid extraction or addition into the acoustic device. Consequently, different molecular weight (M_w) PDDA chains were investigated to increase the viscosity of the coacervate droplets and aid in minimising their perturbation from trapped locations due to fluid movements.

Varying M_w PDDA solutions of 8.5, 200-350 and 400-500 kDa were made at 40 mM monomer concentration and mixed with 40 mM Fmoc-AA solutions (3:7 Fmoc-AA:PDDA) and then added into

a 1D (6.7 MHz) acoustic field. Coacervates were preformed in an eppendorf tube prior to addition into the acoustic field to see if larger droplets, and hence a stronger surface interaction with the glass, could be achieved by encouragement of coacervation prior to addition into the acoustic field. After 30 minutes in the applied field, there was coalescence of the droplets into larger droplets, and in some cases tube-like features, at all the different Mw PDDA (Figure 5.3).

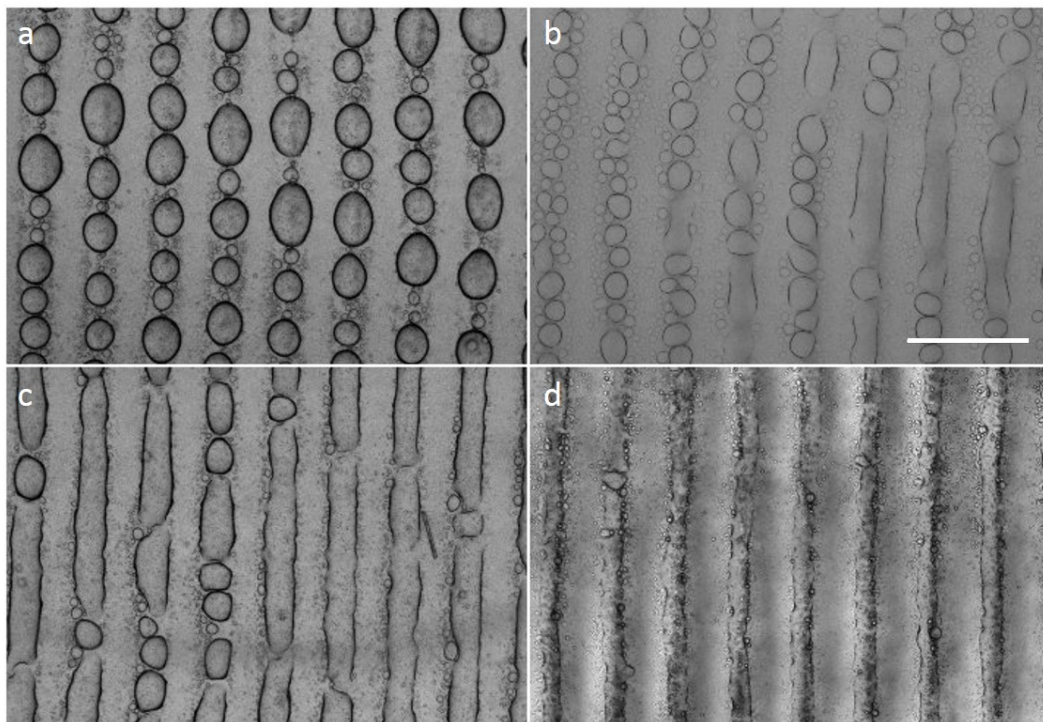


Figure 5.3: Trapping of preformed coacervate droplets made from different molecular weight PDDA in a 1D (6.7 MHz) acoustic field at a 3:7 Fmoc-AA:PDDA ratio after 30 minutes a) 8.5 kDa PDDA coacervate droplets have coalesced into large droplets within each nodal point, but they still remain distinct from each other b) 100-200 kDa form the large droplets which have coalesced into longer tube structures in some areas of the nodal point but smaller droplets also remain surrounding them c) 200-350 kDa PDDA droplets now coalesce to larger droplets which then merge into tube shapes within several nodal points d) 400-500 kDa PDDA coacervates readily coalesce within the trapping points into connected tubes within every nodal points and very few smaller coacervates can be found unlike with the droplets formed from other Mw PDDA. All of these samples were trapped within the same trapping device. Scale bar 200 μm

For comparison, the same trapping device and viewing area (\approx central) was used for all samples with the images shown acquired after 30 minutes of trapping in the acoustic field. The 8.5 kDa coacervate droplets formed large droplets within the node (Figure 5.3a). The 100-200 kDa coacervate droplets form large droplets within each node with some of them merging into tubes of material (Figure 5.3b).

Droplets formed with 200-350 kDa PDPA display more extensive merging of the droplets within each trapped line however some regions still display distinct droplets (Figure 5.3c). Finally, the 400-500 kDa droplets formed connected tubes of coacervate material within and along each nodal point (Figure 5.3d). The increased viscosity of the longer chain would result in slower recovery of a spherical shape during the coalescence and so the droplets instead connect into a tube. These connected structures would form different hydrogel morphologies and could serve to act as diffusion channels within the hydrogel.

Repeating the supernatant removal with a pipette, still resulted in the perturbation of these droplets and the insertion forces continued to dislodge droplets from the surface when fluids were replaced. In the samples with connected tube features, the distinction between neighbouring tubes was lost upon fluid reinsertion. As a consequence, alternative calmer total fluid extraction methods were explored. The capillary action from wicking of solution using a paper towel dipped into one corner of the device was found to be the most effective in removing all excess liquid without disrupting the ordered coacervates from their nodal locations in the field, leaving all the features unperturbed on the surface of the glass slide (Figure 5.4). This figure also reveals the variability in the formation of tubes or connected lines of coacervate material, across the trapping device.

5.2.1.2 Gelation of 1D patterned droplets

The patterned droplets left behind on the surface of the glass slide were then immersed in a GDL solution (1 mL, 20 mM), pipetted into the device slowly in one corner, and left to hydrogelate overnight in the presence of the acoustic field. Supernatant removal was performed both in the presence and absence of the acoustic field to ascertain if the surface interaction was strong enough for patterning to be retained during the hydrogelation transformation. While ordered features were observed in both samples, the droplet patterning was retained much better with the field applied throughout and so the field was left applied throughout the whole process, from addition of coacervates into the cavity through to removal of the gelated sample from the device. The field applied throughout enabled further field-induced coalescence before droplet transformation.

To verify transformation into a gel, coacervates were loaded with Hoechst dye prior to 1D (6.7 MHz) patterning to resolve fibrils in any hydrogel network formed. Upon removal of the GDL solution,

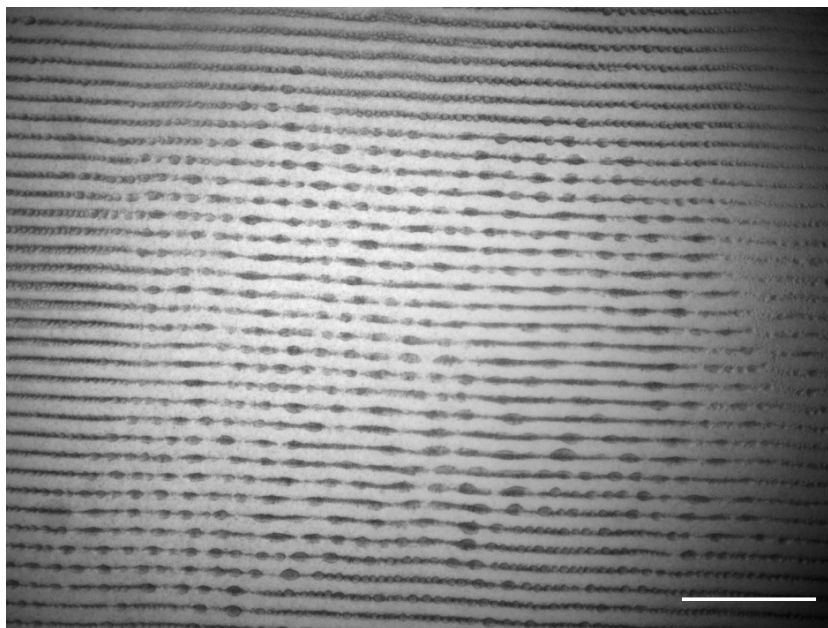


Figure 5.4: Coacervate droplets (3:7 ratio 400-500 kDa PDDA) remaining on the glass slide following supernatant removal with a paper towel. The large area view of the sample following SN removal shows the majority of droplets and tube features remain intact and within their trapped locations. Scale bars 800 μm

again using a paper towel, confocal microscopy revealed the presence of Hoechst stained fibrils emanating from droplets and thus verified that there was gelation of the bulk coacervate phase across the surface of the glass into a thin film hydrogel construct. At low magnification the ordered lines of transformed coacervate droplets appear to have remained as spherical and distinct droplets on the surface of the glass (Figure 5.5a). However, higher magnification within a nodal point, reveals the fibrils present due to the droplets which have transformed (Figure 5.5b).

The ordered features had been retained on the glass surface to form micropatterned gelatinous thin films with no surrounding unordered gel matrix. 3D imaging revealed that this patterning extended $\approx 40 \mu\text{m}$ high. Compared with the ordered features within the monolith gels, which extend to $\approx 70 \mu\text{m}$ high, there has been some loss in the vertical extent of the patterning. This reduction in the height is believed to be primarily due to the transformation of more Fmoc-AA held in coacervate droplets into the fibrils rather than free Fmoc-AA molecules within the supernatant. Since the supernatant phase was removed, all the fibrils must comprise of Fmoc-AA contained within the bulk phase droplets. This results in more coacervate droplets fully transforming and the reduced height of the structures

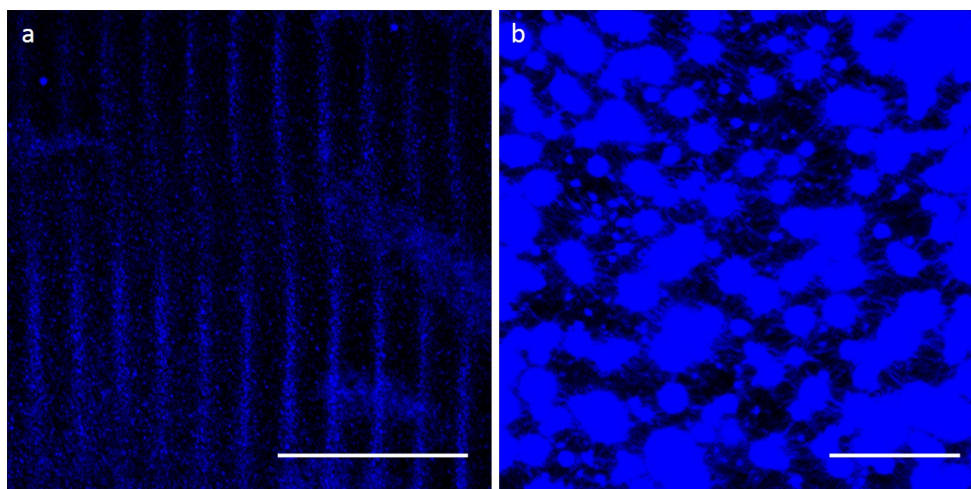


Figure 5.5: Fluorescence microscopy images of a transformed 1D (6.7 MHz) patterned gelatinous thin film a) ordered lines of transformed coacervate droplets on the surface of the glass b) using Hoechst dye, fibrils can be resolved emanating out from the droplets verifying gelation into a thin film. Scale bars a) 500 μm b) 20 μm

formed.

In light of the improved patterning achieved with the higher Mw 400-500 kDa PDDA at the 3:7 ratio, all gelatinous thin films were produced under these conditions at 40 mM concentration.

5.2.2 Chemical communication within gelatinous thin films

As shown in Section 4.2.3.1 the sequestration properties of the coacervate droplets could be exploited in producing spatially organised networks of immobilised guest molecules. This would also be the case for the gelatinous thin films. Reaction substrates added to the thin films would not have to diffuse through inhomogeneous unordered gel material, as with the monolith gels, before encountering the enzyme containing droplets in the thin film, thus addressing some of the diffusion limitations with hydrogels.

5.2.2.1 One step enzymatic cascade reaction in a 1D patterned thin film

Initially a one step cascade reaction was performed in a 1D (6.7 MHz) thin film. The enzyme horseradish peroxidase (HRP) converts the substrate hydrogen peroxide, (H_2O_2) into water and converts a non-fluorescent product (o-phenylenediamine, o-PD) into a fluorescent one (2,3 di-

aminophenazine, 2,3-DAP), which enables fluorescent monitoring of the progression of the reaction using confocal fluorescence microscopy (Figure 5.6).

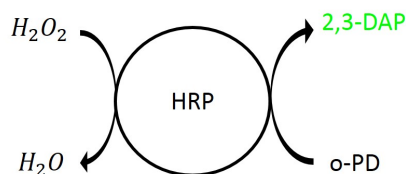


Figure 5.6: One step horseradish peroxidase enzymatic reaction scheme. Upon addition of the reaction mixture of hydrogen peroxide (H_2O_2) and o-phenylenediamine (o-PD), the substrate H_2O_2 is broken down into water (H_2O) and there is an enzyme mediated conversion of the non fluorescent o-PD to green fluorescent 2,3-diaminophenazine (2,3-DAP) which can be detected using fluorescence microscopy.

The coacervate droplets were loaded with HRP (5 μ L, 2 mg/mL) (Section 2.2.4.2). Addition of a reaction mixture of H_2O_2 (20 μ L, 50 mM) and o-PD (20 μ L, 25 mM) to the surface of the gelatinous thin film initiated the reaction which could be monitored by the HRP-mediated conversion of o-PD to 2,3-DAP. Fluorescence microscopy ($\lambda_{ex} = 355\text{-}435$ nm, $\lambda_{em} = 455$ nm) was used to monitor the progression of the reaction as the fluorescent product evolved.

The reaction mixture of H_2O_2 and o-PD was added just outside the field of view directly onto the thin film, such that the molecules would need to diffuse into the gelled features and move through the network before the fluorescence would be seen. Time-lapse images revealed that 30 seconds after addition of the reaction mixture, fluorescence could be observed in the green channel, which implied that the enzymatic reaction had occurred. (Figure 5.7). As more product was evolved and the fluorescence increased it can be seen that the fluorescence signals originated within the gelled features. When left longer, the diffusion of the reactants throughout the gel resulted in all hydrogelled features turning green. The lack of fluorescent signal from the background implied there was no movement of the product outside of these hydrogelled features. This suggested that the reaction and products were constrained within the gelled features where the enzymes were located, demonstrating the potential to use the transformed coacervate droplets as reaction compartments.

Over time o-PD slowly oxidises and will change from a transparent solution to a dark red colour. Fresh o-PD stocks were used for every experiment but to verify that the increase in fluorescence within the green channel was purely due to the cascade reaction, control experiments were performed on the

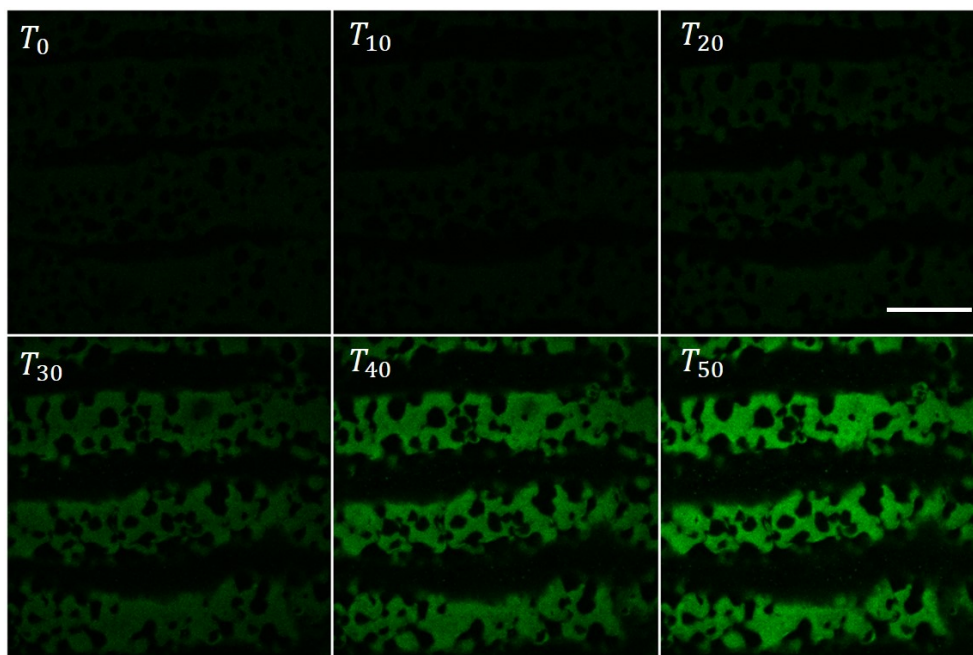


Figure 5.7: Evolution of 2,3 diaminophenazine observed in the green fluorescence channel as the horseradish peroxidase enzyme reaction occurs in a 1D (6.7 MHz) thin film. Time is given in seconds following addition of the reaction mixture of o-PD and H_2O_2 to the thin film, outside the field of view. Scale bar 100 μm

thin films with results confirming that the fluorescent product was only evolved over the course of seconds or minutes when all the required chemical substrates were added to the film.

5.2.2.2 Void morphologies in gelatinous thin films

Within the micropatterned film presented in Figure 5.7, where there are transformed connected tube features, voids can be observed. These are believed to form as a consequence of full transformation of coacervate droplets entirely into fibrils. One node of a 2D patterned thin film is shown in Figure 5.8.

The nodal points of the acoustic field are packed with trapped coacervate droplets. As outlined in section 4.2.1.1 this encourages coalescence of the droplets to much larger sizes than in free solution. In chapter 4 during hydrogelation, the droplets contract in size as some of the FMOC-AA contained in the droplets alongside FMOC-AA in the supernatant transforms into the fibrils which emanate out from the droplets in all directions as aster-like structures. However in the case of thin films, where the supernatant phase has been removed, the only source of FMOC-AA resides within the coacervate

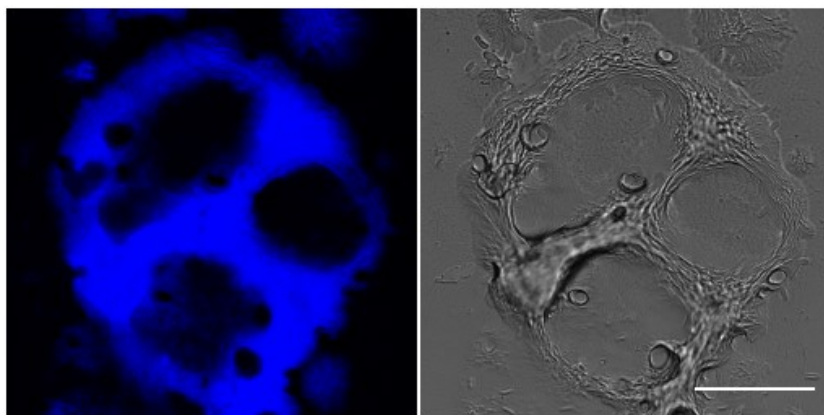


Figure 5.8: Brightfield and fluorescence image of the void morphologies observed in transformed coacervate droplets loaded with Hoechst dye. Scale bar 25 μm

droplets. Thus, it is proposed that more of the droplets within the nodal points must fully transform into fibrils around other droplets present in the trapping point. As these other droplets then also transform it leaves behind spherical voids in the fibril networks formed (Figure 5.8).

5.2.2.3 Two-step coupled enzymatic cascade reaction in a 1D patterned thin film

To explore more complex reactions within the thin films, a two-step coupled enzymatic cascade was also performed. Glucose oxidase (GOx) will evolve H_2O_2 and gluconic acid upon addition of the substrate glucose. The H_2O_2 then acts as the substrate for HRP and again the reaction can be monitored by the evolution of green fluorescence as o-PD is enzymatically converted to fluorescent 2,3-DAP by the HRP (Figure 5.9).

To better elucidate the behaviour of all the guest molecules involved, the enzymes were tagged (Section 2.2.2.5) with rhodamine isothiocyanate on GOx (RITC-GOx, $\lambda_{ex} = 544 \text{ nm}$, $\lambda_{em} = 576 \text{ nm}$) and dylight-405 on HRP (dylight-HRP, $\lambda_{ex} = 400 \text{ nm}$, $\lambda_{em} = 420 \text{ nm}$). These tags were chosen due to their difference in excitation and emission wavelengths from the green region so that they could be monitored outside of the fluorescence window for the evolution of 2,3-DAP as part of a sequential scan on the confocal microscope (Section 2.2.4.3). A 1D (6.7 MHz) thin film was formed from coacervate droplets sequestering both RITC-GOx (5 μL , 1 mg/mL) and HRP-dylight (40 μL , 1 mg/mL).

As previously demonstrated with the one step enzymatic reaction (Section 5.2.2.1) the evolved

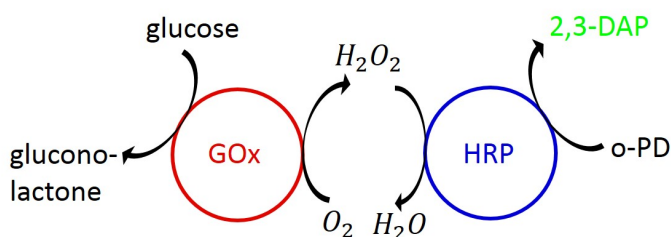


Figure 5.9: Coupled enzymatic reaction scheme of glucose oxidase (GOx) and horseradish peroxidase (HRP). Following addition of the substrate glucose, glucono lactone and H_2O_2 are the enzymatic reaction products with GOx. The evolved H_2O_2 acts as the substrate for HRP which evolves H_2O as a reaction product and also converts non-fluorescent o-PD to fluorescent 2,3-DAP. The different colours shown here depict the different colours of the fluorescent tags on the two enzymes and the green fluorescence of the 2,3-DAP.

product remains within the gelled lines of the 1D patterned thin film (Figure 5.10a & b). Fluorescence analysis was performed on the time-lapse data series to show the changes in fluorescence with time in the different fluorescence channels (Figure 5.10c). The reduction in the red and blue channels, for RITC-GOx and dylight-HRP respectively is due to photo-bleaching of the tag during the image acquisition (every 30 seconds over 30 minutes). The increase in fluorescence in the green channel can clearly be seen as time progresses, which again demonstrated the reaction was occurring within the hydrogelled features.

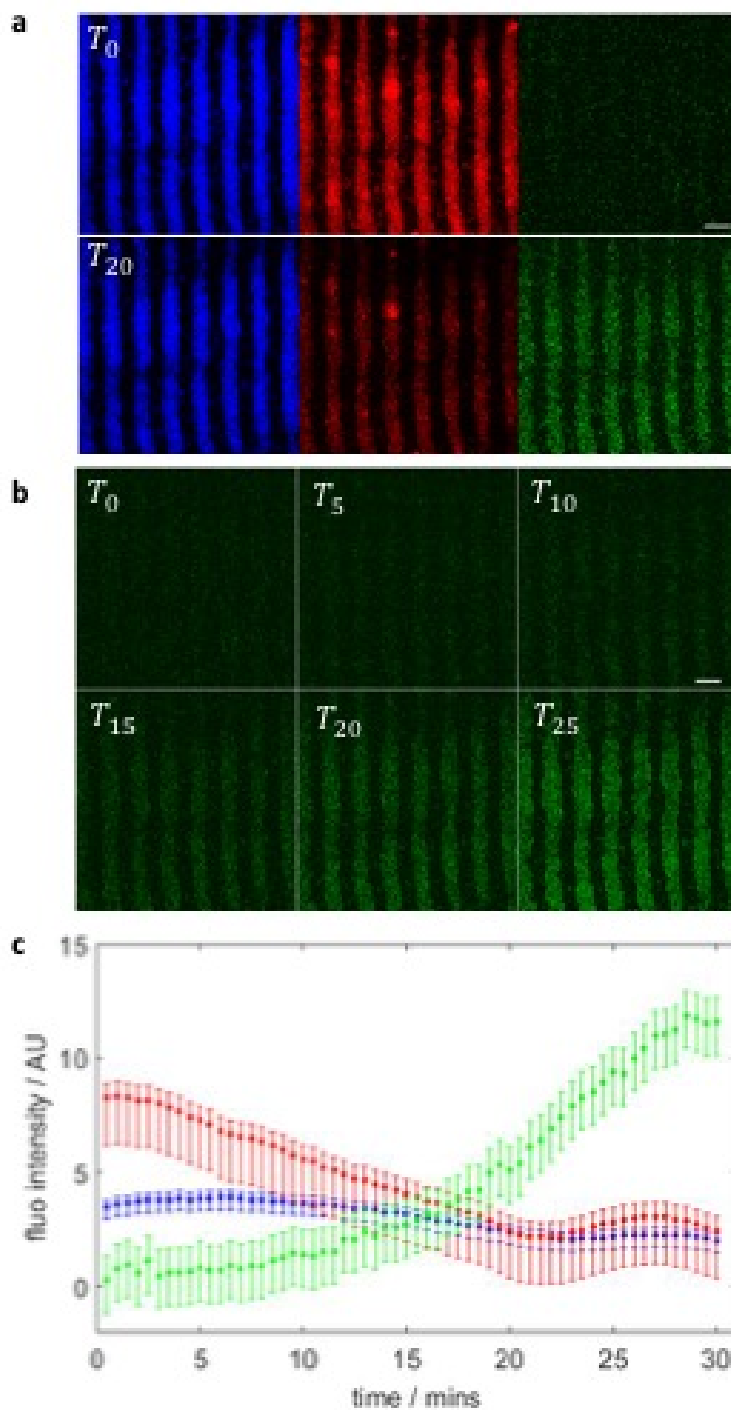


Figure 5.10: Evolution of 2,3-DAP observed in green fluorescence channel as the GOx/HRP coupled enzymatic reaction occurs in a 1D (6.7 MHz) patterned gelatinous thin film. Time is given in minutes following addition of the reaction mixture of o-PD and glucose to the thin film. a) all 3 fluorescence channels showing the two tagged enzymes and the evolution of the fluorescent product in the green channel. The blue and red channels in the images show the location of the fluorescently tagged enzymes dylightHRP and RITC-GOx respectively. b) Green channel fluorescence on a finer time scale c) fluorescence analysis of the different fluorescence channels over the course of image acquisition. Green fluorescence can be seen to increase. Scale bars $100 \mu\text{m}$

5.2.3 Layering of thin films for 3D constructs

Presently, there is a limitation on the extent of patterning vertically within the trapping device (Section 3.2.1). While this limitation was due to the constraints of the acoustic field strength within the trapping device, it was believed that sequential layers of thin films might be a viable route towards achieving higher ordered hydrogels without major redesigning of the trapping device.

Further, layering offers the potential for having spatially distinct enzymes or guest molecules separated from each other within each layer. It was hypothesised that the layer distinction of different guest molecules loaded into two different orthogonally patterned layers could result in interesting behaviours or reaction initiation at the sites where the two layers intersected in the cross-hatch pattern (Figure 5.11).

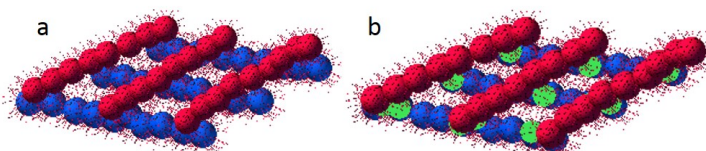


Figure 5.11: Layer 1 patterned in 1D with HRP (blue) then layer 2 patterned orthogonally on top with GOx (red). Following addition of the reaction mixture of o-PD and glucose the reaction can be monitored by the production of 2,3-DAP and fluorescence signal in the green region (green). Where the two layers intersect is hypothesised to be where the reaction, and hence fluorescent signal, originates from.

5.2.3.1 Layer distinction through patterning direction

Initially, a 2 layer gel was investigated. In order to elucidate the success, the gel was formed of two orthogonally arranged 1D patterned layers. Layer 1 was patterned and gelled in 1D, then left for 24 hrs before layer 2 was formed directly on top. The preformed coacervate droplets presented the additional benefit that the different components were already coacervated which would have minimised their permeation into the gelled features already present on the bottom of the device. Brightfield microscopy revealed orthogonally patterned lines had been produced. Adjusting the focal plane revealed that the different layers were in focus at different heights, which implied this layering approach had been successful (Figure 5.12).

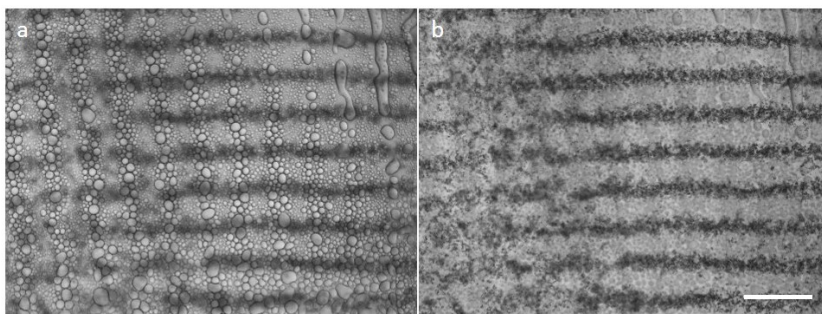


Figure 5.12: Bright field images of a two layered orthogonally patterned thin film stack. a) lower height plane of focus shows the vertical lines of patterned material with some horizontal features across them b) higher height plane of focus shows the horizontal lines in focus and the vertical ones out of focus. Scale bar 200 μm

5.2.3.2 Layer distinction with different guest molecules

Different layers of the thin film stack were then loaded with different dyes, in attempts to further investigate the layered structures through fluorescence microscopy. Layer 1 was patterned in 1D (6.7 MHz) with guest molecule of rhodamine dye followed by layer 2 patterned orthogonally, loaded with Hoechst dye (Section 5.2.3.1).

Here the different diffusion properties of the loaded guest molecules within the coacervates did not serve to distinguish the different layers by remaining separately within each one, rather they had diffused into both layers of the stacked layered construct.

Upon the mixing of different coacervate populations prepared separately with each sequestering a different guest molecule, the coacervates find an equilibrium with the guests sequestered within all the droplets. This equilibria nature is also exhibited between hydrogel and coacervate droplets in solution since there is movement of sequestered dyes between the two layers. There is movement of the dyes from the transformed coacervate network into the aqueous droplets and vice versa as demonstrated by the fluorescent signals observed in both layers of the stacked films.

While the sample produced had displayed movement of the dyes into both patterned layers, there was some encouragement that distinction might be possible with layer 2 blue fluorescence extending a little higher compared with the layer 1 red fluorescence (Figure 5.13a & b).

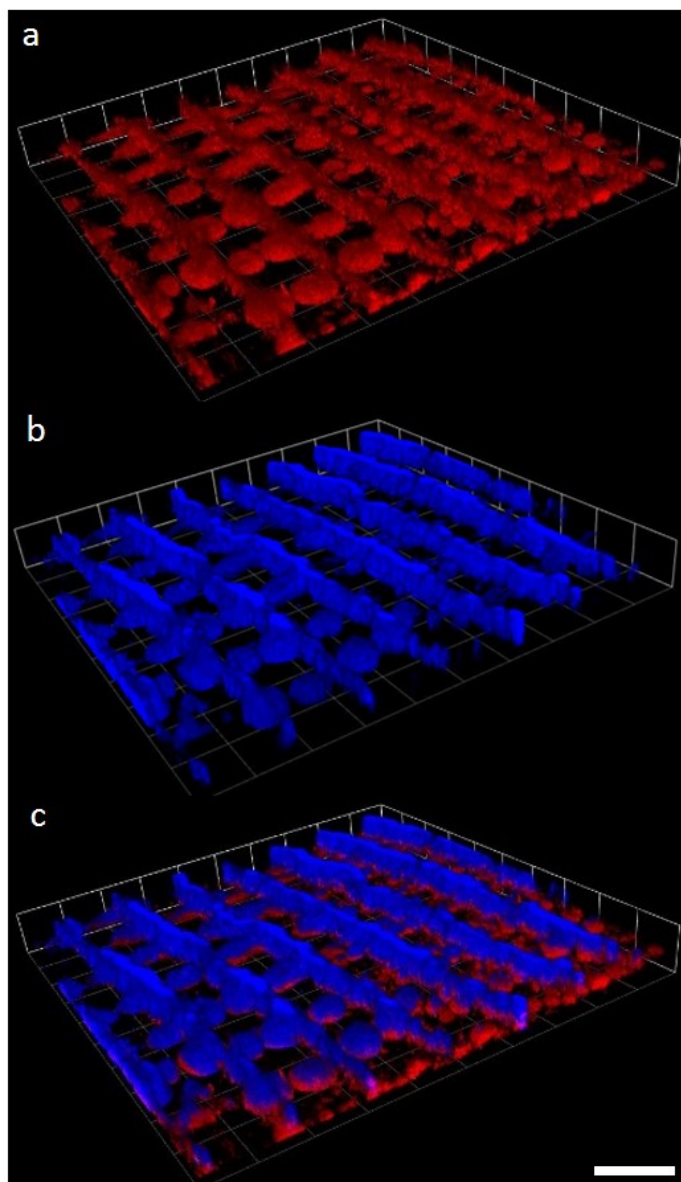


Figure 5.13: 3D fluorescent image of a two layered orthogonally patterned thin film stack with different fluorescent dyes loaded into each layer. a) Layer 1 was patterned with guest molecule rhodamine shown in red and b) layer 2 was patterned with guest molecule Hoechst shown in blue. Fluorescent signals are detected for both colours in both layers of the structure. c) shows the overlaid fluorescence signals from both layers Scale bar $140\ \mu\text{m}$

In attempts to better contain loaded guest molecules within their specific layer, the layer 1 films were left to dehydrate for varying amounts of time before the next layer was added. Films were left for 24, 48 or 72 hrs between patterning layer 2. This extra time for drying was to inhibit the permeation based on the lack of swelling exhibited when similar experiments were performed on the dried down films

of monolith hydrogel (Section 4.2.2.3). However, this route did not serve to minimise the movement of the dyes between the different layers.

5.2.3.3 Two layer two-step coupled enzymatic reaction

It was believed that sequestering other guest molecules such as enzymes or other biomolecules could facilitate the layer distinction since they would be more strongly retained on the droplet interiors than the dyes.

Two layer stacked thin films were formed. The first layer was patterned in 1D (6.7 MHz) loaded with guest molecule of RITC-GOx (5 μ L, 1 mg/mL). The second layer was then patterned orthogonally 24 hours later in 1D (6.7 MHz) using the other transducer pair of the trapping device, and coacervate droplets loaded with dylight-HRP (40 μ L, 1 mg/mL).

Despite being patterned into two different layers, there was movement of both fluorescently tagged enzymes into all gelled features within the layered film (Figure 5.14). A reaction mixture of o-PD (20 μ L, 50mM) and glucose (20 μ L, 300 mM) was added directly onto the surface of the gel thin film, again outside the field of view, and time-lapse images acquired show the evolution of the fluorescence in the green channel as the substrate diffused into the gelled features and the reaction progressed. As the reaction progressed, again there was an increase in green fluorescence as 2,3-DAP was evolved as a reaction product which remained localised within the hydrogel features where the enzymes had been isolated. The apparent decrease in fluorescence in the blue and red channels, for the dylight-HRP and RITC-GOx respectively, was again due to photobleaching from exposure to the lasers during image acquisition.

The presence of the different enzymes within both layers of the patterned hydrogel films presents two possibilities. Firstly, that at this concentration of addition within the second population of droplets, there is sufficient guest molecule remaining within the supernatant to be sequestered in the layer below. This could easily be verified by acquiring fluorescence images of the layer 2 droplets trapped over layer 1. Alternatively, upon transformation of the droplets, the droplets are disassembling as the Fmoc-AA molecules stack into fibrils and hence some of their sequestered guest molecules are released into the network where they become sequestered within both layers. For the latter theory, the movement of molecules from the first layer into the second layer would arise due to the

unbound released guest molecules during the transformation of layer 1 residing until they can be sequestered by the population of droplets in the second layer. The fluorescence intensities within these different time series images could be used to ascertain the kinetics of the enzymatic movement and subsequent reaction which would be beneficial for better control over the propagation of the reaction through the network of gelled droplets.

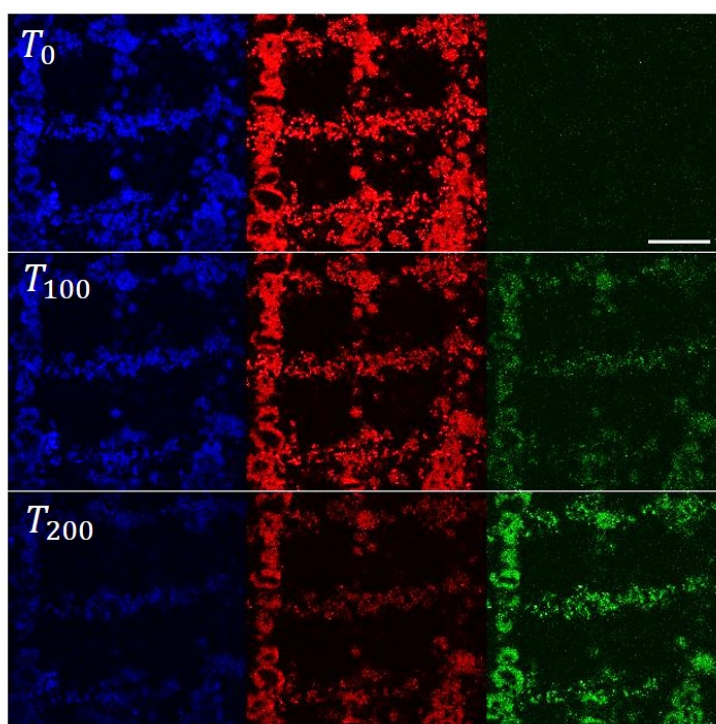


Figure 5.14: Evolution of 2,3-DAP observed in green fluorescence channel as coupled enzymatic reaction occurs in a 2 layer orthogonally patterned gelatinous thin film. Time is given in seconds following addition of the reaction mixture of o-PD and glucose to the thin film. The blue and red channels in the images show the location of the fluorescently tagged enzymes dylightHRP and RITC-GOx respectively. Scale bar 100 μm

While this structure did not demonstrate the cascade reaction originating at the points of intersection between the two thin films as hoped for (Figure 5.11), the square patterning provides interesting structures for hydrogel design.

5.2.4 Enzymatic hydrogelation

The evolution of gluconic acid as a product of the GOx/glucose enzymatic reaction was utilised in initiating the hydrogelation of the Fmoc-AA/PDDA coacervates. Where gluconic acid was evolved in sufficient quantities this would slowly lower the pH of the environment and might conceivably initiate the stimulus-response of the coacervate droplets to transform into a hydrogel. This would serve as a better route than using GDL powders as no solution needed to be removed/replaced for the pH reduction and it would occur naturally as the cascade reaction progressed requiring no further disturbance of the fluids. The minimisation of any fluid movements within the sample cavity would be beneficial in limiting any perturbation of droplets from their trapped locations.

Homogeneous pH reduction over the whole volume of solution was the ideal for the transformation of the coacervate droplets into a hydrogel. In order to ensure that the enzymes were predominantly located within the coacervate droplets and minimised within the supernatant phase, the maximal loading of the enzymes within the coacervate droplets (400-500 kDa PDDA at 3:7 Fmoc-AA:PDDA molar ratio) was investigated with UV - Vis (Section 2.2.3.8). Coacervate solutions were prepared with varying volumes (5, 10 and 20 μL in 1 mL coacervate solution) of tagged GOx. The bulk and supernatant phases were separated out and the UV-Vis spectra of the supernatant phases acquired. Compared with the spectra for a high concentration of tagged enzyme, there were no characteristic peaks with an absorbance above 0.1 AU, thus implying there were no traceable amounts of tagged enzyme within the supernatant phase. The maximum volume of GOx added into samples was fixed at 20 μL . pH curves were acquired for the GOx/glucose reaction and optimised to follow a similar route to the pH reduction with GDL (Figure 5.15). pH was monitored in solution for 20 μL GOx in water mixed with differing volumes of glucose. The more glucose added, the steeper the initial decrease in pH. Compared to the pH reduction curve for the hydrolysis of GDL (blue line) the pH decrease for addition of different volumes of glucose looked promising, if somewhat slower than the hydrolysis of GDL.

Vial inversion tests further verified that the resulting pH reduction from these volumes of GOx and varying volumes of glucose (300 mM) would transform a coacervate solution into a hydrogel (Figure 5.16). No flow was seen in the inverted vials confirming that hydrogels were formed for all of the samples mixed with glucose. However when these vials were shaken, the samples with higher

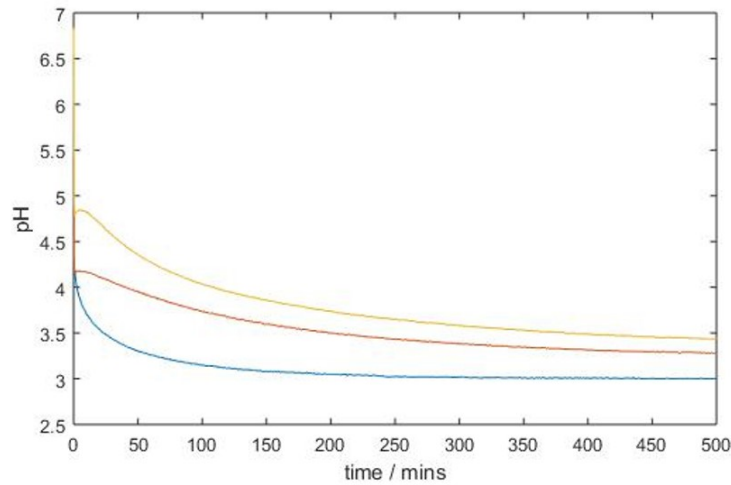


Figure 5.15: pH curves for glucose oxidase evolution of gluconic acid. Reaction mixtures contained 20 μL GOx in water with different volumes of 300 mM glucose added. Blue line shows the equivalent GDL reaction (20 mM), red line shows 100 μL glucose added and yellow line shows 25 μL glucose added to 1 mL of water with 20 μL GOx

volumes of glucose were disrupted presumably due to the extra liquids inhibiting stronger cohesive forces in the gel network. The lower volumes of glucose (50 and 100 μL) had formed self-supporting hydrogels. The vial inversion test does not explicitly verify a hydrogel has been formed but due to time constraints and the promising vial inversion results after 2 days, this served as a quick verification.

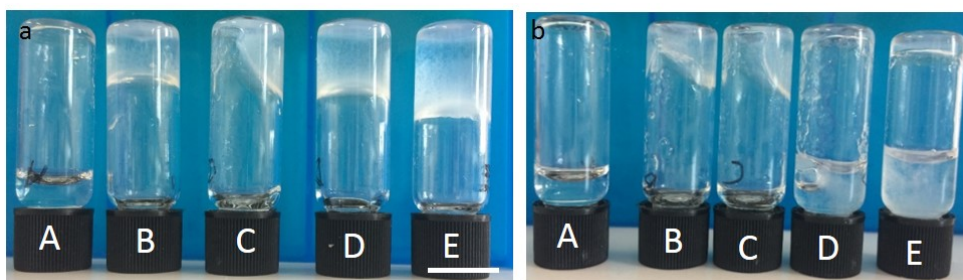


Figure 5.16: Vial inversion test for bulk gelation of coacervate droplets loaded with GOx mixed with differing volumes of glucose (300 mM). Left to right A 0, B 50, C 100, D 150, E 200 μL glucose added and left to gelate for 2 hours prior to vial inversion a) 2 days after inverting the vials there is some evidence of flow down the side of the vial for the 100 μL glucose gel and b) after shaking the vials shown in a) there is some disruption of the gels with the 50 and 100 μL glucose samples remaining predominantly gelled at the bottom of the vial but the higher volume glucose samples have fallen down due to the large volumes of liquid remaining. Scale bar 10 mm

5.2.4.1 Acoustically patterned enzymatic hydrogelation

Coacervates were preformed (3:7 Fmoc-AA:PDDA 400-500 kDa), mixed with 100 μL of glucose and then added into an applied acoustic field. The pH reduction from the enzymatic evolution of acid resulted in a rate of gelation slow enough that there was still time for the droplets to trap before immobilisation in the gel network. Introducing the glucose alongside the coacervates further prevented any disruption of the patterning by fluid addition later on compared with the GDL route. However the full transformation of the entire volume of solution within an acoustic field via the enzymatic hydrogelation route was not possible. Despite trapping droplets with the maximal loading of GOx sequestered on the interior, following the same procedures as the experiments performed in vials, the whole samples were not gelating. Addition of further glucose did not yield full gelation of the whole volume. Only partial gelation of the volume was visible (Figure 5.17). The disordered structures on top of the ordered lines seen vertically across the images were due to the collapse of unordered gelated material which could not be supported due to the lack of an extensive 3D network throughout the volume of solution.

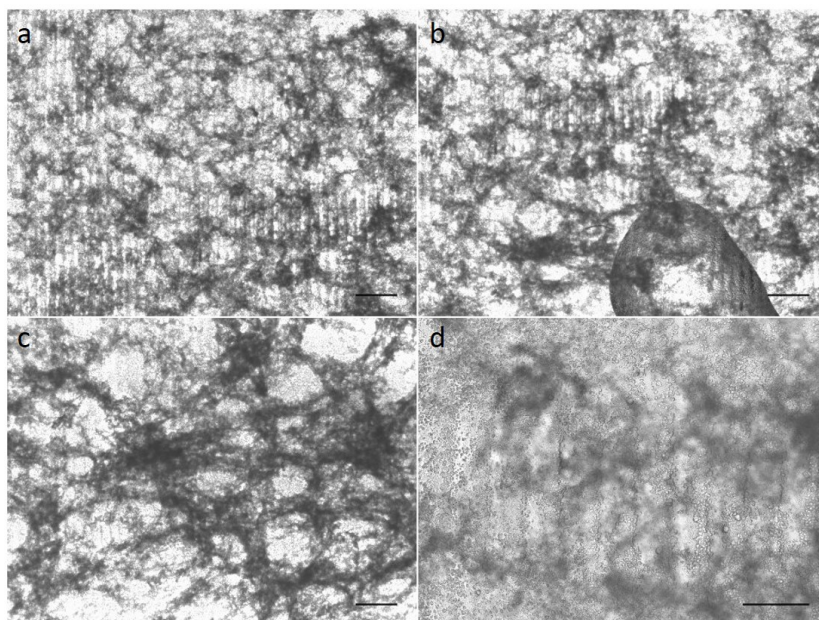


Figure 5.17: Enzymatic hydrogelation of the entire volume of acoustically patterned coacervate solution. The 1D lines imparted by the acoustic field (6.7 MHz) can be seen to extend vertically across the images however there was a lot of unordered transformed material collapsed on top which obscured this patterning. Scale bar 500 μm

5.2.4.2 Enzymatically hydrogelated acoustically patterned gelatinous thin films

Subsequently, the experiment was repeated following the exact same methodology however after 1 hour the supernatant was removed using paper towel and the sample then left in the presence of the acoustic field to trap. This step removed the messy gelled features that were settling atop the ordered ones (Figure 5.17) and produced a gelatinous thin film, as verified by loading coacervates with Hoechst dye and resolving the fibrils of the hydrogel network (Figure 5.18).

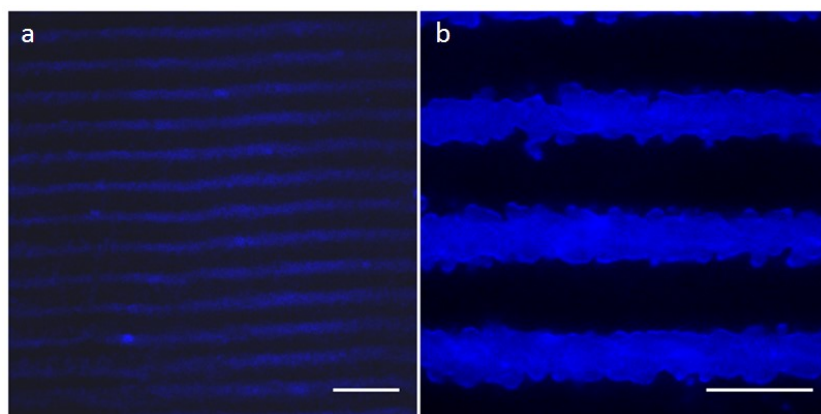


Figure 5.18: Enzymatically hydrogelated thin films loaded with Hoechst dye. a) & b) both show the continuous lines of gelated coacervate droplets patterned in 1D (6.7 MHz). Scale bars a) 200 μm and b) 100 μm

In 1D, distinct continuous lines with minimal coacervate material located between the trapping points were observed (Figure 5.18b). Rather than retaining the spherical appearance of transformed droplets side by side, the closely packed droplets in the nodal points were transforming cohesively into connected structures.

While gluconic acid was free to diffuse within the solution the different connected morphologies were believed to arise from the localisation of the enzyme reaction and products formed within the coacervate microcompartments. This localised pH reduction was sufficient to transform the ordered droplets at the trapping points and retain ordered features within the transformed network. The pH will lower on the droplet interior due to the formation of the acidic product, resulting in fibrils forming from the interior of the droplet, rather than the exterior. This is believed to constrain the fibrils within the droplets, resulting in no voidal features, like those from the GDL thin film route (Figure 5.8). The heights of these thin films were $\approx 40 \mu\text{m}$.

These continuous connected lines of material, extending across very large areas of the film, looked more likely to be structurally resilient to layers patterned and transformed on top of them and perhaps could isolate guest molecules more successfully.

5.2.4.3 Layering of enzymatically hydrogelated thin films

The enzymatically hydrogelated thin films that exhibited continuously connected lines in 1D were utilised in stacking towards 3D constructs. Layered gels were produced with layer 1 patterned in 1D loaded with Hoechst dye, then layer 2 loaded with rhodamine was patterned orthogonally 24 hours later (Section 2.2.4.6). These layered thin films provided much neater transformed gel features and more distinct patterns extending over larger areas of the film (Figure 5.19).

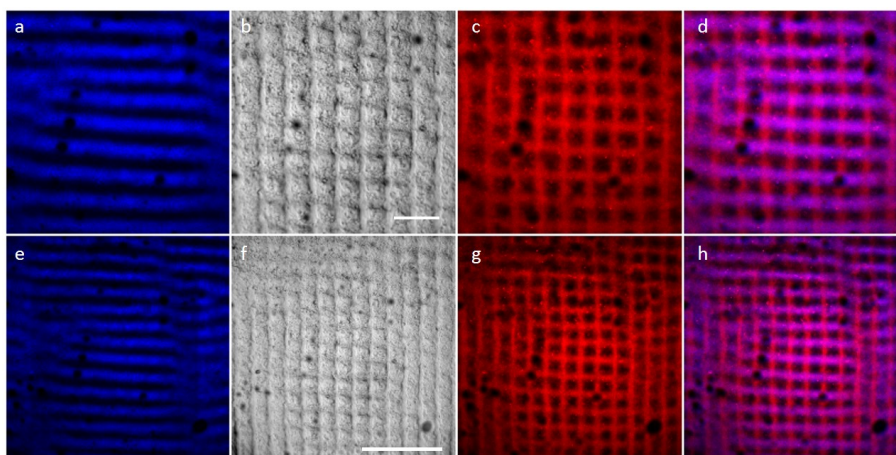


Figure 5.19: Orthogonally patterned 2 layer stack with Hoechst dye loaded into layer 1 and rhodamine dye into layer 2. The overlaying of the two layers has produced a very well defined cross hatch pattern. The different colours show the location of the fluorescently tagged enzymes a&e) dylight-HRP b&f) brightfield c&g) RITC-GOx and d&h) overlaid fluorescence channels. While the Hoechst has remained within the original layer of patterning, the rhodamine has moved into both layers. Scale bar 500 μm

As previously, to investigate the behaviour and architectures of these structures, fluorescent dyes were introduced into each layer. Again the movement of dyes between different layers persisted as a problem, however Hoechst dye now appeared to remain within the specific layer it was patterned into originally due to the different transformation with constrained fibrils. Samples imaged in the same areas after several days did not show any signs of further movement between the layers, with Hoechst remaining in one direction and the rhodamine having permeated into both (Figure 5.19).

Similarly to the previous thin film results, enzymes loaded into different layers did not remain distinctly within their layer (Figure 5.20). They were sequestered within the droplets and were found to have moved entirely into all gelled features regardless of their initial location within the layers. As such, again the spatially distinct layered cascade could not be investigated (Figure 5.11).

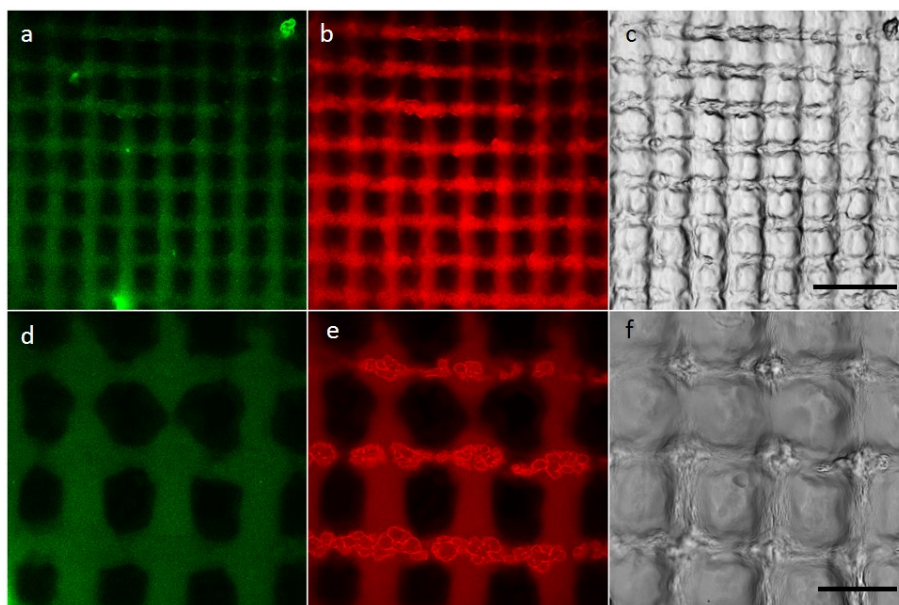


Figure 5.20: Orthogonally patterned two layer enzymatically gelled thin film stack loaded with enzymes in both layers. Layer 1 was patterned in 1D with fluorescein isothiocyanate (FITC) tagged GOx and layer 2 with RITC-GOx. While the cross hatch pattern has been produced by the two orthogonally patterned coacervate populations, there has been movement of the tagged enzymes into both layers of the stack. Scale bars a-c) 250 μm d-f) 100 μm

Consequently the layer specificity of guest molecules within their specific layer in a 2 layer thin film stack of some different guest molecules was investigated. To document the movement of the guest molecules between layers, 2 layer gels were produced with a guest loaded into either layer 1 or layer 2 and the other layer patterned without any guest molecules. Any fluorescence observed in the layer that was 'empty' would reveal the inter-layer movement of the guest molecule. From the selection of guest molecules investigated (a variety of dyes and tagged biomolecules) Hoechst was chosen as the best option to investigate higher stacked thin films, as it remained within the specific layer it was loaded into, due to the strong interactions with the fibril structures which were now constrained on the droplet interiors and transforming into the continuous tube-like features.

5.2.4.4 Higher layering

Finally, Hoechst was used to investigate stacking beyond 2 layers. Following the enzymatic thin film protocol as before with each layer patterned orthogonally to the one below, 3 layers of thin film were produced (Section 2.2.4.6). Both the top and bottom layers were loaded with Hoechst, and were parallel to each other, with an orthogonally patterned middle layer produced without any fluorescent guest molecules added. The 3D reconstruction of the gel revealed hollow areas where the layer 2 gel was located due to the lack of movement of the Hoechst into this layer (Figure 5.21a). This was the strongest evidence yet that the other layers were forming around other patterned gel structures. While this construct only extended to $\approx 40 \mu\text{m}$, so there was no height increase compared to the other thin film structures, it demonstrated the potential for building more complex structures with layer specific guest molecules. (Figure 5.21).

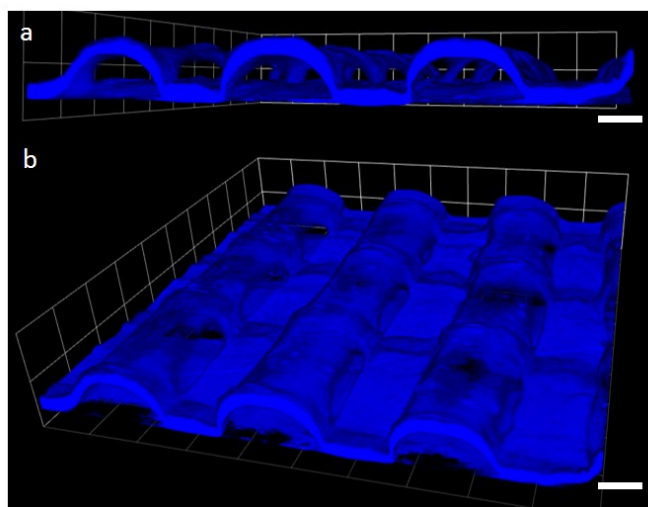


Figure 5.21: Triple layered enzymatically hydrogelated thin film construct. Hoechst dye was loaded into layer 1 and 3, while layer 2 was left without any guest molecules. a) an x-z plane view of the hollow cavity, due to the middle layer which was left without any guest molecules added, which the Hoechst layers have formed around b) a top down view of the sample. Scale bars $40 \mu\text{m}$

5.2.5 2D patterned thin films

Similar investigations with acoustically micropatterned thin films were also performed in a 2D ($6.7 \times 6.69 \text{ MHz}$) applied acoustic field. Investigations regarding the behaviour of the preformed FMOC-

AA/PDDA coacervate droplets, at a 3:7 molar ratio 400-500 Mw PDDA, left to trap and coalesce in the presence of the acoustic field resulted in 1 large droplet per node (Figure 5.22).

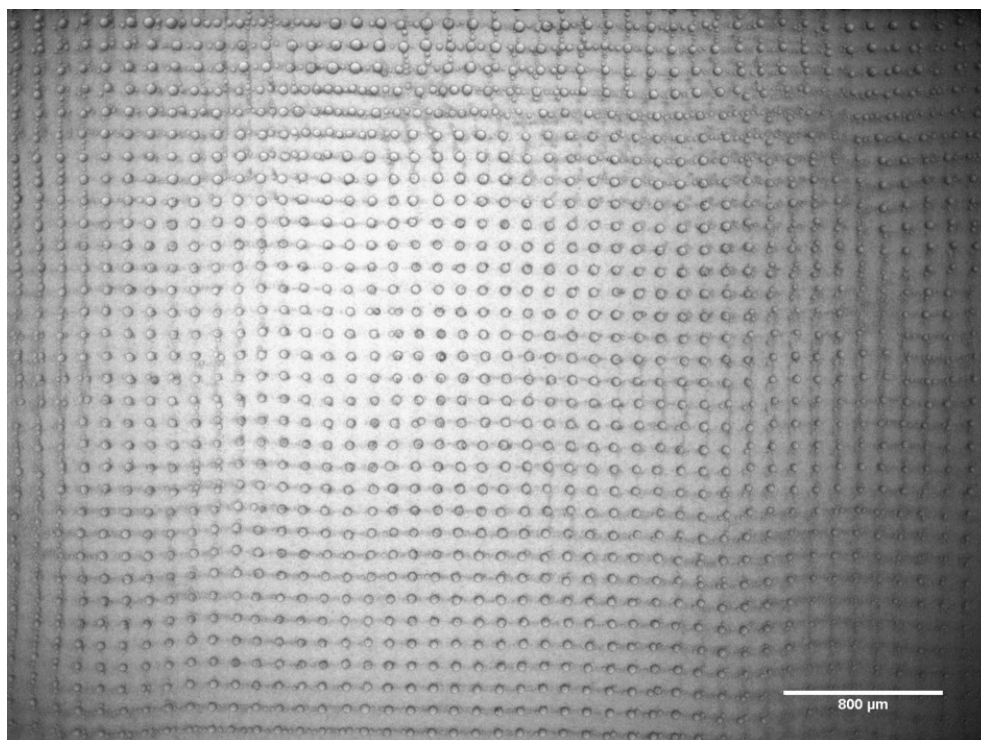


Figure 5.22: Gridded array of preformed coacervate droplets at 3:7 Fmoc-AA:PDDA ratio with 400-500 kDa PDDA trapped in a 2D (6.7 x 6.69 MHz) acoustic field for 30 minutes. Scale bar 800 μm

These 400-500 kDa droplets measured on average $42.8 \pm 3.3 \mu\text{m}$ in diameter compared to $2.5 \pm 1.2 \mu\text{m}$ when preformed and left in free solution. The improved spatial isolation from forming droplets with this higher Mw PDDA was observed over a much larger area of the trapping device than previously seen. These larger droplets also had sufficient surface interaction with the glass slide to remain at their trapped locations throughout supernatant removal with a paper towel and successfully transformed into 2D patterned thin films upon the addition of GDL solution.

5.2.5.1 2D two-step enzymatic cascade reaction

Micropatterned 2D (6.7 x 6.69 MHz) thin films were also prepared with sequestered enzymes (RITC-GOx and Dylight-HRP) to observe the propagation of the enzymatic cascade reaction across the spatially isolated array of hydrogelled compartments (Figure 5.23).

Similar observations were made for the coupled reaction within the 2D thin film as in the 1D thin film. The reaction front was seen by the different fluorescence intensity increase for the neighbouring droplets across a row due to the diffusion of the substrate across the thin film (Figure 5.23c). The arrow shows the direction of increasing time. At the last displayed time point, the fluorescence intensity is highest for the droplet in position 1 compared with position 6. In a larger field of view, this propagation would be more observable. The gelled droplets were also entirely spatially distinct from each other, so this further evidenced the constraint of the reaction within the droplets and that the diffusion of the substrates and the o-PD occurred across the thin film. Again the products remained preferentially on the droplet interior and did not move outside of the gelled features.

No fluorescence developed outside of the hydrogelled features within the 2D thin film as the enzyme reactions progressed, providing strong evidence that the tagged enzymes and their reaction products remain preferentially within the gelled coacervate features throughout the course of the reaction. The evolution of the reaction product within these regions further demonstrates the localisation of the reaction within the transformed droplets, meaning that the hydrogelled droplet cores can act as reaction centres in a 2D spatially distinct grid of isolated compartments enabling reaction propagation studies within an x-y plane.

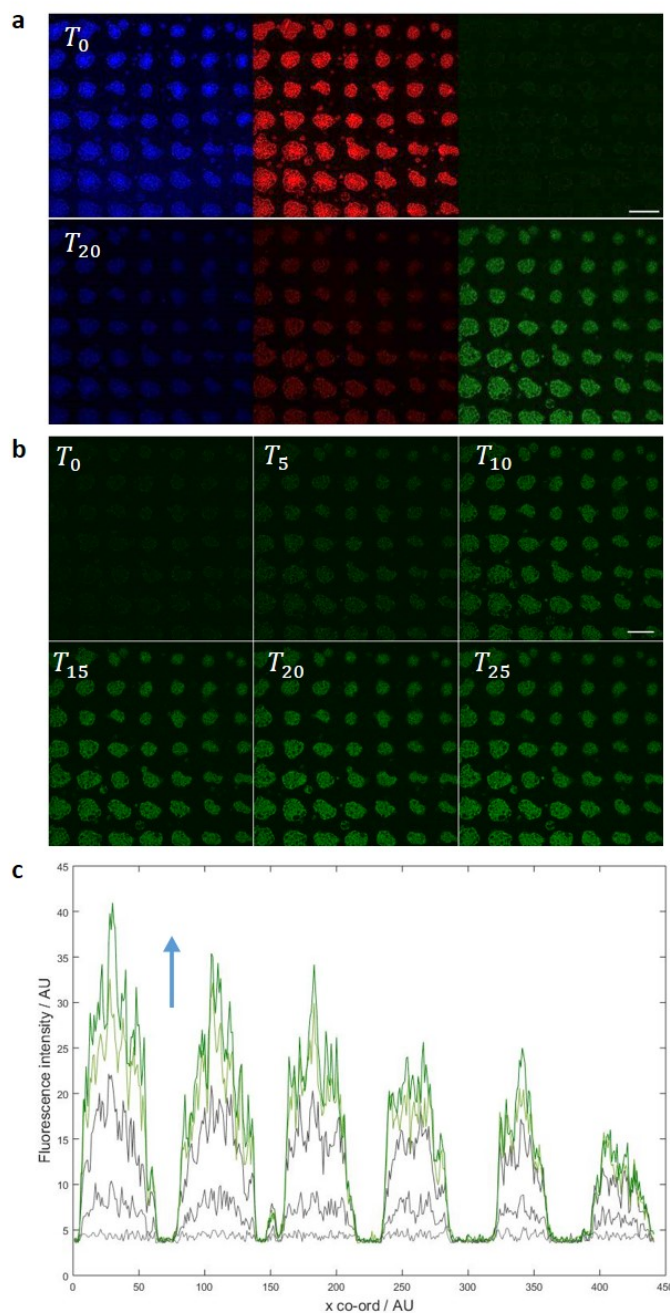


Figure 5.23: Evolution of 2,3-DAP observed in green fluorescence channel as coupled enzymatic reaction occurs in a 2D patterned gelatinous thin film. Time is given in minutes following addition of the reaction mixture of o-PD and glucose to the thin film. a) The blue and red channels in the images show the location of the fluorescently tagged enzymes dylightHRP and RITC-GOx respectively. The green channel shows the evolution of fluorescence as the o-PD is converted to 2,3-DAP. b) finer time scale of the green channel c) fluorescence intensity profile in the green channel across a row of 6 droplets. The arrow shows the direction of increasing time. Different colours show different time points. Scale bar $100 \mu m$

5.2.5.2 Effect of enzymes on droplet coalescence in a 2D acoustic field

In these samples the presence of multiple voids within the transformed gel at each trapping point implied the presence of several droplets rather than one, which was contrary to what had been demonstrated for coacervate droplets trapped in a 2D acoustic field previously (Figure 5.22). As such the behaviour of the coacervate phase in the 2D field when loaded with the guest molecules RITC-GOx and dylight-HRP was further observed. It seemed that the presence of these guest molecules inhibited the coalescence so that the coacervates clustered in groups at the nodal points, rather than coalesced into 1 large droplet (Figure 5.24).

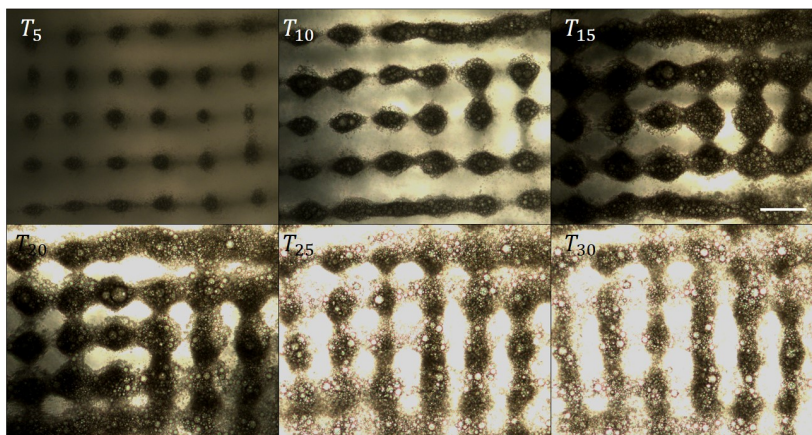


Figure 5.24: Time-lapse series to show the trapping behaviours of preformed 400-500 kDa PDDA coacervates (3:7 Fmoc-AA:PDDA) loaded with tagged enzymes (RITC-GOx and dylight-HRP) in a 2D (6.7x6.69 MHz) field with time given in minutes. Scale bar 100 μm

Over the course of 1 hour, the nodal point distinction was lost as coacervate droplets migrated to the trapping points but were hindered on reaching them due to the presence of other droplets already there which they did not coalesce with. They settled where they could resulting in a loss of definition of the nodal point. In some cases the position of the settled droplets were unstable as there were still forces acting to move them towards the pressure minima. As the other droplets moved about, these unstable droplets would then move again. They may also have blocked the pathway of other droplets moving through the cavity towards trapping points elsewhere, particularly in a 2D field.

Comparing the first and last image in the time-lapse, it can be seen that what started out as 2D now looked 1D with some larger droplets periodically along the line (Figure 5.24). Due to these droplet behaviours over the course of the reaction, at this stage initiation of hydrogelation will not

necessarily impart clearly ordered one droplet per node features into the thin film as it would have done previously in samples without the guest molecules, leading to the multiple voids within the nodal points of the thin film.

5.2.5.3 2D enzymatically hydrogelated films

As before, the gluconic acid product in the conversion of glucose by glucose oxidase was used to hydrogelate the coacervate droplets. For 2D patterned thin films, there were spatially isolated single droplets per node with fibril structures emanating out between the droplets immobilised within the hydrogel (Figure 5.25).

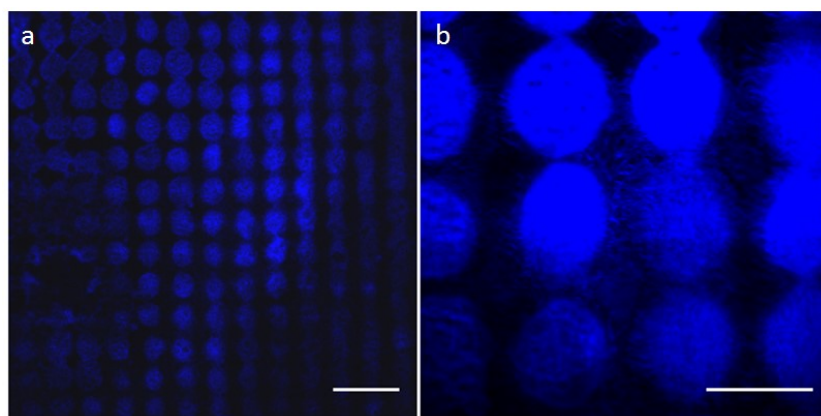


Figure 5.25: Enzymatically hydrogelated thin films loaded with Hoechst dye. a) & b) both show the spatially isolated gelated coacervate droplets patterned at the nodal points of the 2D (6.7 x 6.69 MHz) field. Scale bars a) 200 μm and b) 100 μm

5.3 Conclusions and Future Work

The ordered hydrogel fabrication process was adapted to produce gelatinous thin films so that only the ordered features would be accessible for further studies. Removal of the supernatant phase, after 1 hour of trapping, prior to initiating the gelation resulted in fully transformed bulk material on the surface of the glass slide without any higher extending unordered hydrogel material present and addressing some of the diffusion limitations. While these thin films were too thin for rheological investigations, the presence of fibril structures confirmed the hydrogelation transformation of the coacervate droplets. The sequestration properties of the coacervate droplets were again used in thin

film enzymatic cascade studies with both single and dual coupled reactions observed. The spatially isolated, periodically arranged reaction compartments, within a hydrogel matrix would serve as a route for understanding the diffusion through a hydrogel network and they could also be used in micro-array technologies.

The GOx/HRP enzymatic cascade produces a product of gluconic acid. This was exploited as an alternative route to lower the pH and initiate hydrogelation within the trapped pH-responsive coacervate samples. Maximal loading of GOx for the majority to remain within the bulk phase rather than the supernatant was found and then used in lowering the pH as the enzyme evolved the acidic product. With sufficient glucose substrate added, the pH reduction was sufficient and slow enough to homogeneously lower the pH and hydrogelate the thin films.

The capacity of stacking these thin films on top of each other in pursuit of higher ordered gel structures was explored. Here the two pairs of transducers oriented orthogonally to each other were utilised in preparing stacked thin films with orthogonally patterned lines to ascertain the different layers via both the GDL and enzymatic hydrogelation routes. Unfortunately the equilibrium sequestration nature of the coacervate droplets resulted in movement of different guest molecules between the two layers of the films and no layer specific retention of guest molecules. However the enzymatically hydrogelated films exhibited different morphologies which enabled layer specific isolation of some guest molecules. These more clearly distinct patterned features also extended over much larger areas than previously observed with the GDL hydrogelation route.

These enzymatically hydrogelated films were utilised in attempting to build higher layered structures. The resulting connected features formed via this route enabled better resolution of the different layers comprising a stack. The most promising results for stacking higher came for a triple layered film using Hoechst in layers 1 and 3 and an 'empty' middle layer. Here hollow features surrounded by Hoechst dye could be elucidated which provided evidence that the layers had formed around each other. The hollow regions demonstrated within the triple layer gel present the best evidence of the potential for layering the thin film structures. Future investigations should focus on steps to maintain layer specificity of different guest molecules. Perhaps through utilising different protocells, such as colloidosomes, which have very small pores and would limit the diffusion of the larger guest molecules or through using coacervate droplets with additional membranes to limit

the movement of the loaded guest molecules. [184, 232] In this way, the different layers could be better resolved to properly investigate what is happening in the stacking and aid in keeping different guest molecules separated. This would enable investigations into communication between different distinct populations, as initially proposed with the cross hatched structures.

Single layered 2D enzymatically hydrogelated films present spatially isolated features which could be utilised in biosensing applications and to monitor dosage or reaction gradients across a film. Further complexity could be introduced into these stacked structures by varying the trapping pattern within each layer. Due to the two pairs of transducers within the trapping devices, there are two patterning options; lines and a grid-like array. These could be combined in several different ways to produce layered features atop of each other. The cross hatched overlaid layers of orthogonal 1D patterning were the easiest to observe but it would also be possible to pattern 1D then 2D. Then the 1D patterned layer could potentially act as a diffusion pathway to guide molecules to the 2D spheres spaced along them.

Alternative guest molecules such as solid particles could be patterned alongside the coacervate droplets in composite materials. These could aid in directional reinforcement and be patterned within the gels at different heights by loading into different layers. The sequestration property of the coacervate droplets also presents the possibility of loading particles into the droplets that would otherwise be too small for acoustic patterning, for positioning within a gel matrix.

The morphologies within enzymatically hydrogelated films appear to be sufficient to keep very distinct, narrow lines of transformed material leaving enough space between each gelled line for neighbouring material. Within the thin films themselves, using the acoustic manipulation capability of the device, different populations of material could be ordered side by side, without touching each other, offering different setups to monitor chemical communication.

Preliminary results where a layer of agarose was added on top of a thin film demonstrated that the patterned features could be embedded into it and removed from the surface of the glass (Figure 5.26). Hence these more neatly patterned cohesive structure can now be moved into different environments. Through this embedding route, stacking of patterned structures could be integrated within other gel matrices, extending the complexity of the layered gels that could be formed and perhaps aiding in keeping different guest molecule populations spatially discrete.

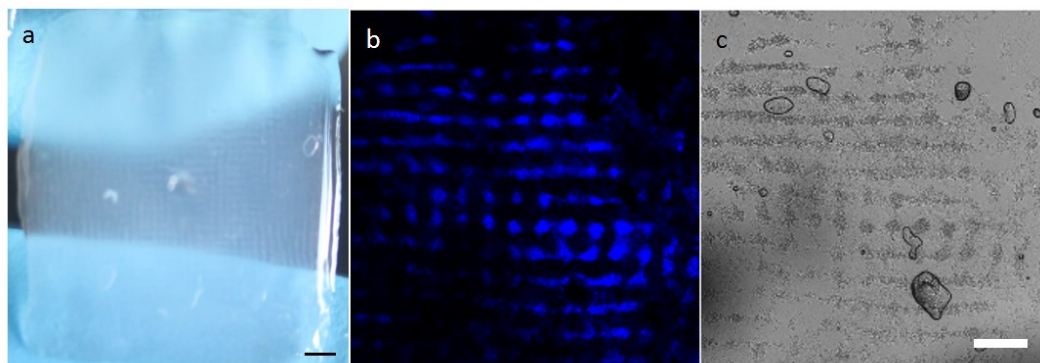


Figure 5.26: Agarose hydrogel embedded with a micropatterned thin film a) photograph of a 2D (2.15 x 2.14 MHz) patterned thin film embedded into agarose b) fluorescence image of 2D (6.7 x 6.69 MHz) micropatterned coacervate droplets embedded into the agarose c) corresponding bright field image Scale bars top 2 mm and bottom 200 μm

5.3.1 Towards enzymatically controllable structures

Another enzymatic reaction is that of urease which will convert urea into ammonia and carbon dioxide (Figure 5.27). It was shown that submersion of a gelled sample in high pH buffer, yielded disruption of the gel network and recovery of coacervate droplets. Ammonia would serve to increase the pH of solution. If urease was loaded into the coacervate droplets alongside GOx, prior to patterning, this could provide a route towards on and off switching between hydrogels and coacervate droplets in an enzymatically hydrogelled thin film (Figure 5.28). Further upon recovering the droplets, different patterns could then be fixed upon hydrogelation of the sample for a second time enabling rearrangement of the ordered network.

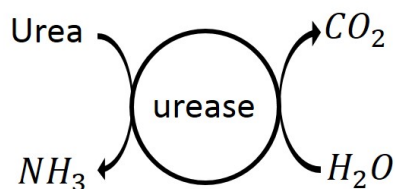


Figure 5.27: Urease enzyme reaction scheme. Upon addition of substrate urea, this is converted into ammonia and carbon dioxide which raises the overall pH of the solution

Addition of glucose would initiate the GOx reaction whereby the pH would be lowered and induce hydrogelation. Then addition of urea would initiate the urease reaction and increase the pH disrupting

the gelled network. When droplets are recovered the orientation of the trapping could then be altered from 1D vertical to 1D horizontal or from 1D to 2D and vice versa. The improved hydrogel features exhibited through the enzymatic gelation due to the localised reaction and pH decrease, could result in better droplet recovery upon pH increase in a similar constrained location on droplet or gelled droplet interiors.

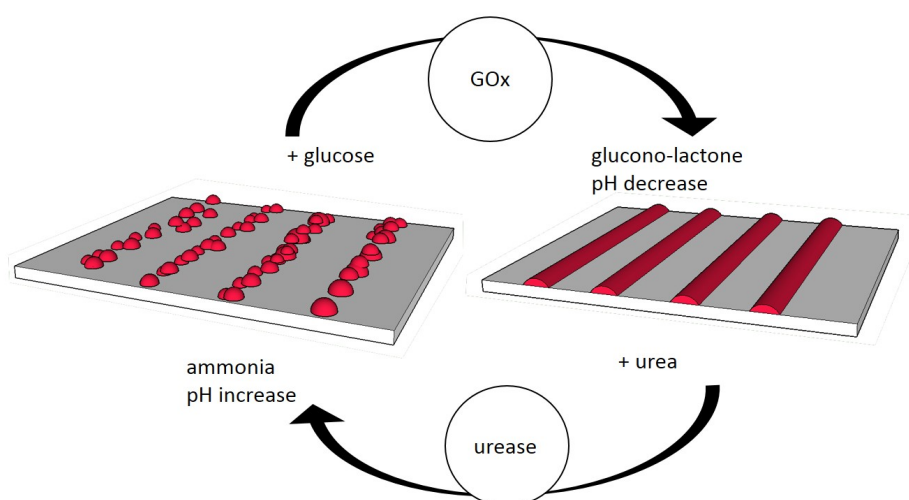


Figure 5.28: Switching schematic for an on-off enzyme switch. Utilising the pH decrease from the enzymatic reaction of GOx with glucose, the coacervate droplets undergo hydrogelation and transform into a hydrogel. For samples also prepared with urease enzyme, addition of the substrate urea would result in an increase of the pH, disruption of the hydrogel network and recovery of the droplet phase. In this way, the sample could oscillate between the droplet and hydrogel phases

Some preliminary experiments with thin films produced via enzymatic gelation loaded with GOx and urease were produced. Upon addition of the urea in specific locations, pH increase was sufficient to recover droplets in those regions (Figure 5.29a). Outside of these areas, the gelled structures remained intact (Figure 5.29b). When samples were completely immersed in urea for the course of a day, upon removal and drying some remnants of the ordered structures still remained on the surface of the glass. This would perturb or obscure the patterning within the second rearrangement and hydrogelation of the sample.

These proof of concept experiments demonstrate the potential for dynamic rearrangement of the gel structures through enzymatic reactions by oscillating between the droplet and hydrogel states which could be useful for real time rearrangement of the ordered features. While this process is currently

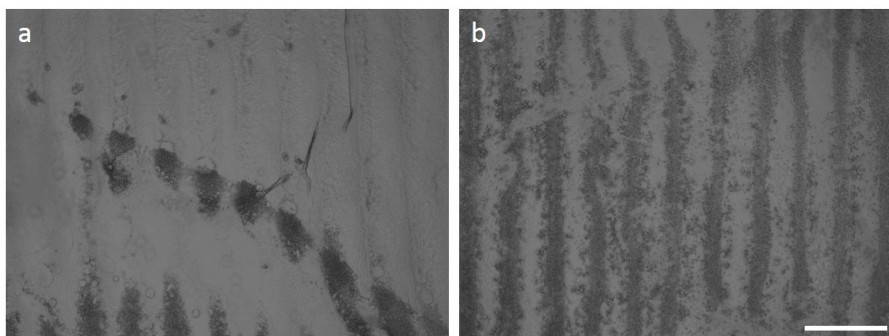


Figure 5.29: Disruption of a thin film loaded with urease. Upon addition of substrate urea, this is converted into ammonia and carbon dioxide which raises the overall pH of the solution and disrupts the hydrogel film a) the edge of the urea droplet can be seen arching across the centre, above the edge gelled material remains and below it droplets have been recovered b) an area of sample inside the area of the urea droplet which has recovered to the coacervate phase. Scale bar 200 μm

limited by the lack of complete disruption of the ordered coacervate material, steps could be taken to completely remove any patterning on the glass surface ahead of re-patterning and fixing the hydrogel, such as different surface treatments of the glass slide.

5.3.2 Towards biological relevance

The integration of these ordered features within the field of tissue engineering would be a step towards maintaining cell patterning arrangements without continued exposure to the acoustic field, acting to obstruct cellular migration with hydrogel barriers. [259]

The stability of the ordered hydrogel structures in the presence of cell media was investigated. A patterned thin film was submerged in cell culture media and the structures were monitored over the course of 24 hours. After this time, the structures had been disrupted due to the effect of the salts in the media solution disrupting the hydrogel network and coacervate droplets. The salt stability of the coacervate droplets and transformed hydrogel system should be more fully explored. However alongside the instability of the material within the salt solutions, both the gelation routes presented here, require reduction in pH of the environment which is unfavourable for tissue engineering applications as this is not a hospitable environment for a cell. With biological applications in mind, an alternative coacervate-based hydrogel system should be developed.

CHAPTER

6

**DEVELOPMENT OF ACOUSTICALLY MICROPATTERNED
POLYPEPTIDE/NUCLEOTIDE COACERVATE BASED HYDROGELS**

Chapter overview

In this chapter, work underlying the development of a coacervate-based hydrogel system comprising poly-L-lysine (PLys) and adenosine-5'-monophosphate (AMP) is presented. The droplet properties were investigated in order to facilitate the acoustic trapping of this system. The aim in using these components, was to fabricate ordered hydrogels under more physiological conditions so that the hydrogel constructs would have more biological relevance.

6.1 Introduction

In fields such as regenerative medicine, drug delivery or tissue engineering, the integration and emulation of biological processes is of great importance. [124, 138, 139, 260–263] To facilitate in this process biomolecules are often used. Materials that are sensitive to minute environmental changes, have been shown to exhibit stimuli-responsive swelling. Enzymes can be loaded within a hydrogel network and upon pH changes water will be absorbed or desorbed. [123, 264]. Cellular interaction can be improved by introducing additional functionality to hydrogel materials, such as cell adhesive ligands. [247, 265] In drug delivery, using specific cell markers for targeting has resulted in successful uptake of different drugs through particular pathways. [266–268] When introducing biomolecules into materials, they need to be understood from the bottom up.

6.1.1 Biologically relevant building blocks

Perhaps the most biologically relevant building blocks are those found in our DNA; nucleotides. Nucleotides are the 'building blocks' of nucleic acids which, in turn, are the monomer units for the polynucleotides; DNA and RNA. Both of which are essential biomolecules, containing the genetic codes for living organisms. [65, 66, 269]

A nucleotide comprises 3 parts:

- A nucleobase of adenine, uracil, guanine, thymine or cytosine
- A sugar of ribose or deoxyribose
- One or more phosphate groups

A nucleobase attached to a sugar is known as a nucleoside. Nomenclature of nucleotides consists of the nucleoside (adenosine, guanosine etc) followed by the number of phosphate groups present (mono-, di-, tri-phosphate) (Figure 6.1). A phosphate group consists of one central phosphorus atom surrounded by four oxygens.

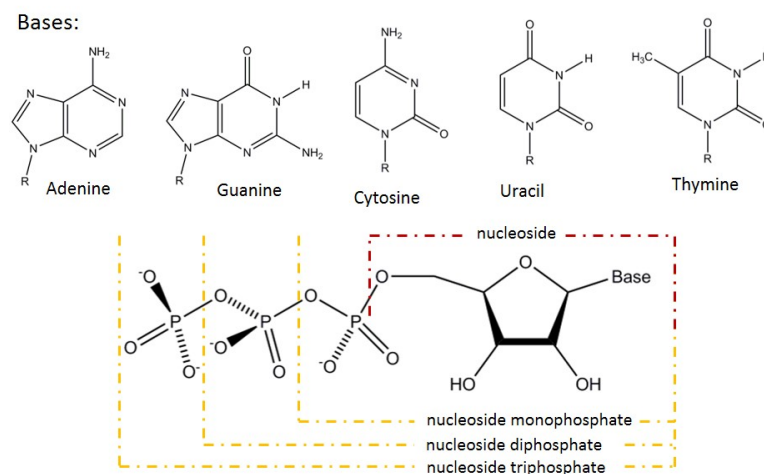


Figure 6.1: Naming conventions and structures of the different nucleotides. The different bases are shown across the top of the figure. When any of these bases are connected to the sugar, pentose, they will form a nucleoside. Nucleotides are the nucleoside connected to a number of phosphate groups. Reproduced from [270]

The five natural nucleobases are the building blocks of DNA which carries huge amounts of information. They are very relevant in the design of biological materials since they can be used in self recognition, as supramolecular synthons and for targeting functional groups. [271–273]

6.1.2 Biologically relevant materials design

The biological process of self-assembly serves as inspiration for the fabrication of novel structures. [274, 275] These supramolecular structures will form in particular environmental conditions without human intervention. The self-assembling nature and high water content of molecular hydrogels, alongside the variety of different biologically relevant molecules they can be made from, particularly protected amino acids and peptides, makes them attractive for designing biological materials. [276–279]

Recently, metal coordination chemistry has been used as a design route towards self-assembled gels with functional properties, known as metallo-hydrogels. [280–282] The reversible bonds are based on metal-ligand coordination. [283] A gelator molecule has many ligands which are not part of the self-assembly process, however through binding a metal ion to them the self-assembly behaviour can be modified. [284, 285]

6.1.2.1 Metal coordination

A coordination complex refers to a central atom surrounded by bound molecules or ions. The central atom is referred to as the coordination centre and the surrounding ions or molecules are known as ligands. The coordination term refers to the nature of the covalent bonds where both electrons come from one atom. These electrons are contributed by a donor, also known as a lewis base or ligand, to an acceptor, known as a lewis acid.

In a metal coordination complex, the metal ion centre is the lewis acid and the surrounding ligands act as the donors. Binding of a metal ion to a gelator molecule containing an appended ligand site can affect the self-aggregation modes enabling tuning of the gelation ability. [285, 286]

Metal coordination can cross-link molecules into supramolecular gels. [287] Few reports document gelation with ligands already present on small molecules so ligands must often be designed specifically for purpose so that the metal salts will trap solvent and cross-link the molecules. [288, 289] However some nucleotides and their derivatives, particularly guanine, can assemble into hydrogels. The chemistry of guanosine and some derivatives, enables a hydrogel transition. Under certain conditions, with self-complementary hydrogen bonding edges, aromatic surfaces and a strong dipole, the molecules promote self-association into highly ordered cyclic tetramers known as G-quartets (Figure 6.2a & b). [290] The quartets are linked together by hydrogen bonds and are stabilized by metal cations (K^+ , Na^+). [292] These quartets can helically stack and are held together by different interactions (Figure 6.2c). [293] Dash *et al.* have produced supramolecular hydrogels from the chelation of Ag^+ ions with GMP with the filaments comprising arrays of helically stacked, chiral dimers of Ag-GMP. [294] Of particular note for the work presented in this chapter is the metal coordination of AMP with Zn^{2+} and self-assembly into a hydrogel (Figure 6.2d). [295]

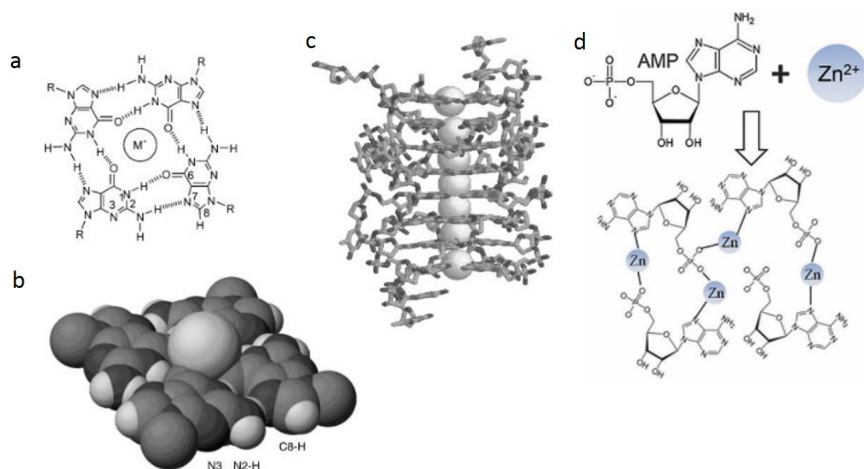


Figure 6.2: Nucleotide structures a) a G-quartet b) space-filling model of a G-Quartet with a metal ion bound above the planar assembly c) crystal structure of stacked G-Quartets d) metal coordination of AMP with $ZnCl_2$. Reproduced from references [290, 291]

6.1.2.2 A polypeptide/nucleotide coacervate based hydrogel

The cell-like characteristics of coacervates and their versatility in composition from many different molecules make them attractive options in the design of biologically relevant systems (Section 1.4.6.2). Recently the coacervation of nucleotides, such as nucleoside triphosphates, adenosine-5'-diphosphate (ADP) and monophosphate (AMP), with an oppositely charged polypeptide, poly-L-lysine (PLys) of varying length, was demonstrated. [296]

AMP has also been shown to self-assemble into a hydrogel, via metal coordination with zinc ions, Zn^{2+} . [295] Zn^{2+} acts as a Lewis acid and can be coordinated by many ligands. Since AMP has also been shown to coacervate with PLys, this provided a conceivable route towards the design of responsive coacervate droplets that would undergo structural transformation into a hydrogel via metal coordination.

The cationic PLys is widely used at a low concentration as a surface coating to improve cell adhesion due to electrostatic charge interactions with the cell membrane. [297] Lysine is also known to interact strongly with nucleotides, with lysine residues an important part of nucleic-acid protein assembly. [298–301] AMP is used in cellular metabolism processes, interconverting between adenosine di- or tri-phosphate (ADP and ATP respectively). [302] Thus, both the different chemical species used in this

coacervate system would be biologically relevant. Further, the Zn^{2+} ions required for hydrogelation and introduced through the salt $ZnCl_2$ have been reported as non-toxic at the concentrations used here.

Integrated with the technique of acoustic trapping, these PLys/AMP nucleotide coacervate droplets, comprised of more biologically relevant components than the previously presented polymer/dipeptide coacervate system and capable of a hydrogelation transformation through metal coordination with Zn^{2+} , provided a plausible route for fabrication of biocompatible acoustically patterned hydrogels. This chapter presents the development and optimisation of this coacervate system for successful acoustic trapping. Further the gelation transformation through metal coordination of the AMP component is extended from the methodology provided by Liang *et al.* to transform the trapped coacervates into a patterned hydrogel. [291]

6.2 Results and Discussion

The coacervate system based on the polymer, poly-L-lysine (PLys) with nucleotide adenosine-5'-monophosphate (AMP) had already been documented. [103] The process of nucleotide gelation via metal coordination of zinc chloride ($ZnCl_2$) with AMP had also been performed. [291] To ascertain the viability of gelation of AMP within a coacervate droplet state with PLys, investigations were first begun into adapting the gelation protocol for the AMP. Following this, the gelation of coacervated AMP with PLys was explored and then the system was acoustically patterned and transformed to produce ordered hydrogels.

6.2.1 AMP gelation

The metal coordination based gelation of AMP was reported through a method involving centrifugation. For the acoustic trapping of any system, the centrifugation step would not be a plausible route. With acoustic trapping in mind, AMP solutions would be required to gelate entirely through mixing. As such early investigations focused on achieving bulk gelation of AMP solutions via metal coordination through mixing only. Gelation was verified by the vial inversion test.

As shown previously, upon the addition of $ZnCl_2$ to AMP solutions, nanofibers form and under

centrifugation (9000 rpm for 5 minutes) the gel will separate out from the water phase. [291] To avoid the centrifugation step, higher concentrations of both AMP and ZnCl_2 were used. Firstly, 100 μL volumes of AMP at different concentrations (serial titration from 50 to 3.125 mM) were mixed with 50 μL 50 mM ZnCl_2 and left overnight to gelate. Upon inverting the vial, no flowing was observed demonstrating a gel had been formed. The entire volume had transformed apart from the 6.25 and 3.125 mM solutions which exhibited partial transformation with some gel-like features on the edge of the inverted vials (Figure 6.3).

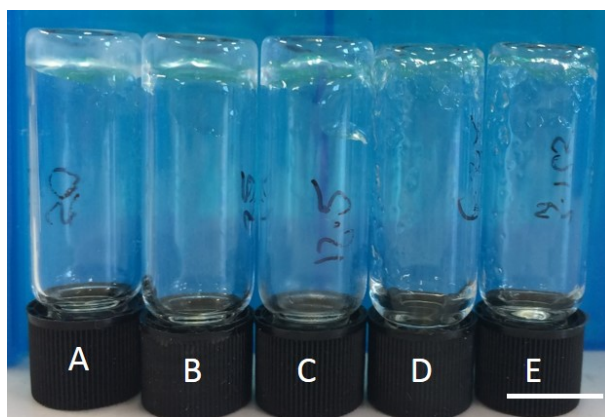


Figure 6.3: Bulk gelation of 100 μL different concentration AMP with fixed ZnCl_2 (50 μL 50 mM) A 50 mM B 25 mM C 12.5 mM D 6.25 mM E 3.125 mM Scale bar 10 mm

The mixing of ZnCl_2 (50 μL , 50mM) with AMP directly at 100 μL volume and varying concentrations was sufficient to transform the solution without any centrifugation. To ascertain whether scale up of the volume was possible, towards 1 mL for the volume of the acoustic trapping device, a fixed concentration of AMP (50 and 5 mM), was mixed at different volumes with ZnCl_2 (50 μL , 50 mM) and left to gelate overnight.

The larger volumes of AMP solution were diluting the ZnCl_2 present in the total volume such that less of the total volume was transforming into a hydrogel. Equal volumes transformed the entire solution into a hydrogel (Figure 6.4A) and increasing the volume of AMP resulted in less material transforming with the least gel present in the vial for 250 μL AMP. Increasing the volume of ZnCl_2 added would increase the overall concentration of the ZnCl_2 and increase the volume of gelled solution however this would also dilute the AMP. Addition of increased concentration of ZnCl_2 (100 mM) resulted in localised gelation at the site of addition rather than after diffusion across the whole solution so the

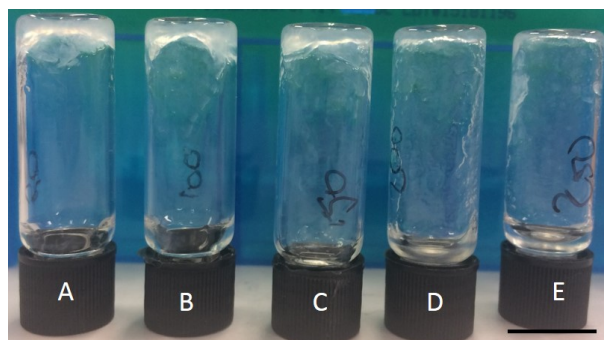


Figure 6.4: Bulk gelation of different volumes of 50 mM AMP with ZnCl_2 (50 μL , 50 mM) A 50 μL B 100 μL C 150 μL D 200 μL E 250 μL Scale bar 10 mm

concentration was kept at 50 mM.

Another factor involved with the gelation process is the time following mixing, since the ZnCl_2 must diffuse throughout the whole volume to complex with the AMP for full complexation of the whole solution. When 50 μL 50 mM ZnCl_2 was mixed with 100 μL 50 mM AMP, the solution fully transformed within 30 minutes of mixing (Figure 6.5).

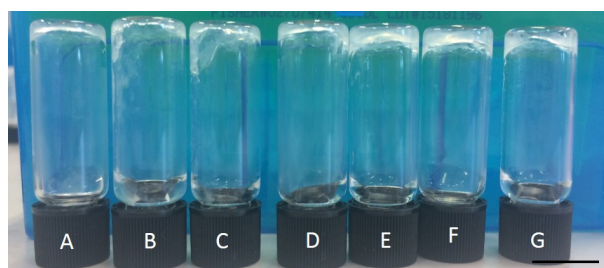


Figure 6.5: Gelation of 100 μL 50 mM AMP mixed with 50 μL 50 mM ZnCl_2 . Vials were inverted at different times following mixing; A 1 min B 2 mins C 5 mins D 10 E 15 F 30 G overnight Scale bar 10 mm

Further investigations revealed that to transform 1 mL of 50 mM or 5 mM AMP required 400 μL 50 mM ZnCl_2 and leaving the solution for 30 minutes or overnight respectively. At these concentrations the gelation transformation was at a rate that led towards homogeneous gelation. The gelation transformation did not happen instantaneously upon mixing, tending to transform the entire volume over a longer timeframe. This slower homogeneous transformation would be a beneficial property in the preservation and recovery of ordering in the acoustic trapping device following mixing, before immobilization of the ordered features within the hydrogel network.

These promising developments regarding the gelation of the AMP component of the system validated investigating gelation of the coacervate system .

6.2.2 PLys/AMP coacervation

Previous work reported the coacervation of PLys with AMP mixed at an equimolar 4 mM ratio at pH 8. [296] However these concentrations would result in too few and potentially too small coacervate droplets for trapping to be resolved.

From the previous chapters presenting acoustic trapping of coacervate droplets, it is known that there are some system criteria:

- The number density of droplets in solution needs to be high enough for any patterning to be resolved.
- Droplets must be in the right size regime (> 500 nm) to experience the acoustic force.
- Enough of the gelating component must be present within the droplets and solution for hydrogel transformation

Therefore concentrations far exceeding the 4 mM reported were of most interest as there would be more droplets formed upon coacervation and due to these increased numbers they should coalesce to large enough sizes for acoustic trapping. Gelation of AMP at various concentrations was possible and had been demonstrated. As such coacervate droplets were made at higher concentrations and their properties tailored for acoustic trapping.

6.2.2.1 Tailoring coacervate droplet sizes for acoustic trapping

Upon mixing PLys with AMP at 50 mM in an equimolar ratio the solution turned visibly turbid and microscopy observations confirmed the presence of spherical micro-droplets in solution. With the trapping caveats in mind, coacervate droplets were formed at different ratios to see the effect on the droplet size. The dynamic light scattering (DLS) measurements of the size of droplets from different ratios of mixing PLys:AMP are shown in Table 6.1.

PLys:AMP molar ratio	Size / nm
2:1	100-200
1:1	≈ 100
1:2	≈ 500
1:4	≈ 1000-2000

Table 6.1: Dynamic light scattering size range measurements of coacervate droplets mixed at different volume ratios from stock solutions of PLys and AMP at 50 mM

The equimolar coacervate droplets were the smallest with size increasing to μm range with more AMP present during coacervation. The more AMP present the better for the gelation transformation. It was observed that upon mixing at 1:1 ratio this coacervate solution went turbid but after measurement it had become clear implying that the droplets had disrupted in solution and were unstable. The ratios with more AMP than PLys were used due to their increased size suitability and that they remained turbid following size measurement implying that they were more stable in solution.

Within the literature it is documented that PLys is utilised in surface coatings to improve cell adhesion. [297] The concentrations used in these processes are low. It was also a concern that the rapid gelation following mixing might impede recovery of disrupted droplet trapping, from fluid mixing in the device, prior to immobilisation. Consequently, the coacervate solutions were mixed at 50 mM and then diluted so that the overall concentrations were reduced.

The initial formation of the droplets at higher concentration would favour the formation of enough droplets to elucidate trapping in an acoustic field and encourage coalescence towards sizes for the droplets to experience an acoustic force. Since the volume of the trapping device is $\approx 1 \text{ mL}$, solutions were diluted to 1 mL total volume. PLys and AMP were mixed at 50 mM concentration at the desired ratio to a small volume (200 μL total). Droplets were left for five minutes to form and coalesce, then the solution was diluted with HEPES buffer. The resulting sizes of the diluted solutions of coacervate droplets were then found using DLS. Droplets formed following this methodology, were still at sizes suitable for acoustic trapping (Table 6.2). In some cases, this process encouraged larger droplets than achieved previously at the same ratios from direct mixing, with droplets at a 1:2 ratio measuring an average of 4 μm compared to 0.5 μm .

The improved droplet sizing following the dilution method, made the coacervates more suitable in size for acoustic trapping.

PLys:AMP ratio	Size / nm
1:1	≈ 200
1:2	≈ 4000
1:4	≈ 3000
1:9	≈ 1500
1:19	≈ 1500

Table 6.2: Dynamic light scattering size range measurements of coacervate droplets formed at different volume ratios from stock solutions of PLys and AMP at 50 mM

6.2.3 PLys/AMP coacervate gelation

Bringing the two threads of investigation together, a sample of 1:2 (PLys:AMP made at 50 mM to 200 μ L and then diluted with 800 μ L HEPES) ratio coacervate droplets was gelled alongside a control 5 mM AMP (1 mL total) only solution. The AMP solution was colourless prior to mixing with $ZnCl_2$. Upon transformation into a hydrogel network, the AMP hydrogel went turbid implying the formation of fibrillar structures. Upon comparison of the resulting gels, there were some noticeably different morphologies with spherical droplets embedded into the coacervate based hydrogel sample (Figure 6.6a) compared with the AMP only gel (Figure 6.6b).

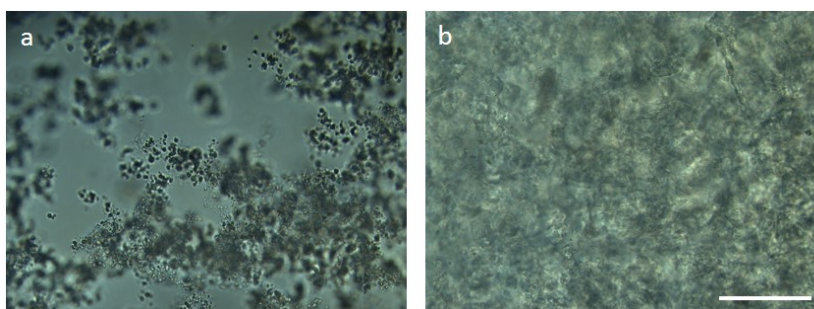


Figure 6.6: Comparison of a hydrogelated coacervate solution with a nucleotide hydrogel a) 1:1 PLys:AMP 50 mM gelled coacervate morphology b) 5 mM AMP only gel morphology. Scale bar 50 μ m

The presence of spherical coacervate droplets within the transformed hydrogel network was again encouraging for introducing ordered features into the hydrogel network through acoustic trapping. The intact spherical structures were also important for guest molecule localisation within the network.

6.2.4 PLYs AMP hydrogel characterisation

The mechanical properties of the AMP only and coacervate-based hydrogels were compared using rheological characterisation.

Samples were prepared at the ratio of investigation (1:2) following the coacervate preparation protocol (Section 2.2.5.1). Following dilution with HEPES to 1 mL, samples were then mixed with ZnCl_2 (400 μL , 50 mM). AMP only gels were formed at 50 mM and 5 mM concentrations. Following gelation they were loaded onto the baseplate of the geometry using a spatula. The coacervate gels were only explored at the 1:2 ratio because this was the sample with the most PLYs compared with AMP and as such believed to be the one that would deviate most from the AMP only behaviour.

Frequency sweeps were acquired on samples 1 day after mixing with ZnCl_2 (Figure 6.7). 50 mM AMP samples exhibited too much slip on the baseplate for data to be acquired. Both the AMP hydrogel at 5 mM concentration (yellow) and the 1:2 coacervate hydrogel (green) exhibited expected hydrogel behaviours from 0.1 - 10 Hz exhibiting moduli independent of the strain applied with an elastic modulus (hollow symbols) higher than the viscous (filled symbols) modulus over the entire range. Interestingly the moduli are higher for the coacervate hydrogel sample compared to the nucleotide only hydrogel. This is due to the fact that the concentration of AMP in solution is practically the same but the entanglement and interactions with the PLYs are increasing the strength of the coacervate hydrogel under shear.

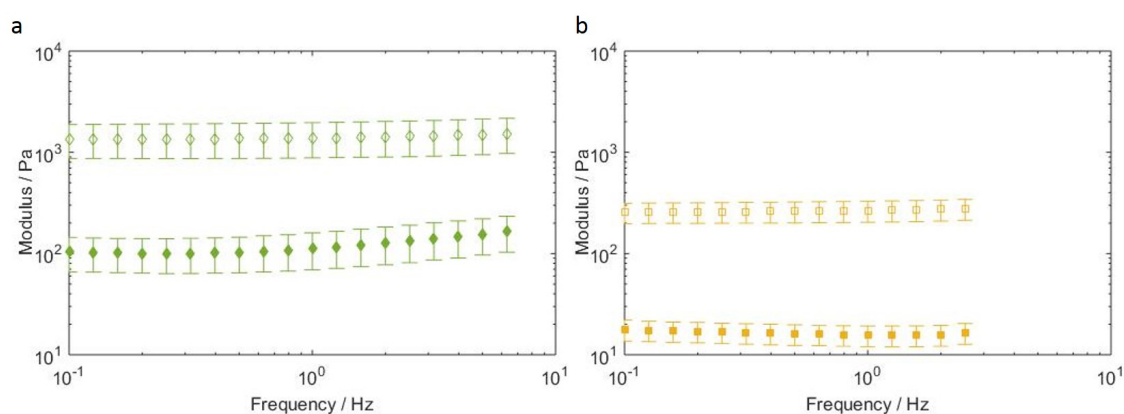


Figure 6.7: Rheology frequency sweep data for nucleotide and coacervate hydrogels a) 1:2 coacervates b) 5 mM AMP hydrogel

Strain sweep measurements were acquired 3 hours after mixing all solutions with ZnCl_2 . All 3 samples

exhibited the expected strain behaviour of a viscoelastic material with a linear viscoelastic (LVE) region followed by a crossover point where viscous behaviour dominated over elastic (Figure 6.8a). The higher concentration AMP gel (blue) suffered from slipping on the baseplate at strains above 10%, but both other gels (5 mM and 1:2 coac) did not slip. The rheology profiles for 5 mM AMP (yellow) and 1:2 coacervate gel (green) are very similar with the coacervate gel at a slightly lower modulus and cross over point.

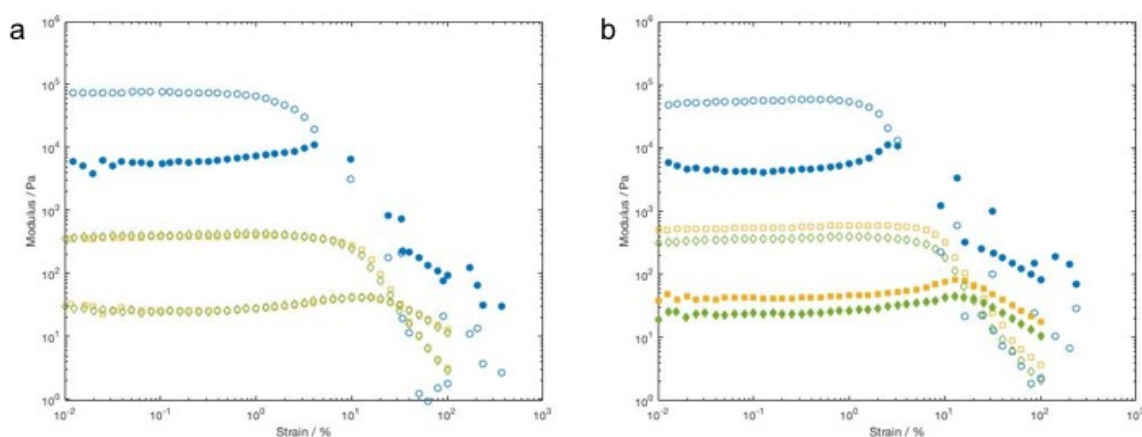


Figure 6.8: Rheology strain sweep data for nucleotide hydrogels at different concentrations and a coacervate hydrogel. Blue 50 mM yellow 5 mM AMP and green 1:2 coacervates a) measurements acquired 3 hours after mixing b) measurements acquired 24 hours after mixing

Rheological data was also acquired with samples left for one day after mixing with ZnCl_2 (Figure 6.8b). Largely the same trends were observed as with the results acquired a few hours after gelation, but now the 5 mM AMP only and 1:2 coacervate hydrogel samples had identical moduli, implying that leaving the solution longer enabled full transformation into a hydrogel.

6.2.4.1 Rheological quantification of gelation time

Attempts to quantify the gelation time for the coacervate based hydrogel were performed by acquiring viscolastic measurements every 10 minutes overnight (Figure 6.9a). Solutions were added directly onto the test bed following mixing with ZnCl_2 , and data acquisition started.

As the system undergoes hydrogel transformation the different elastic and viscous moduli should tend towards that of a viscoelastic hydrogel material. Throughout the experiment water will evaporate off, but this water loss was limited as much as possible by providing small water containers within

the temperature controlled covering to assist in maintaining a humid environment and to avoid complete dehydration of the sample. Since the centrifugation step assisted in gelation within the work by Liang *et al.* demonstrating the gelation of AMP, the shear forces exerted on the gel from the geometry might have influenced the gelation and thus may not give an entirely accurate depiction of the gelation transformation. [291] In order to investigate this effect, a control sample was formed in a vial under the same conditions as the sample on the rheometer (Figure 6.9b).

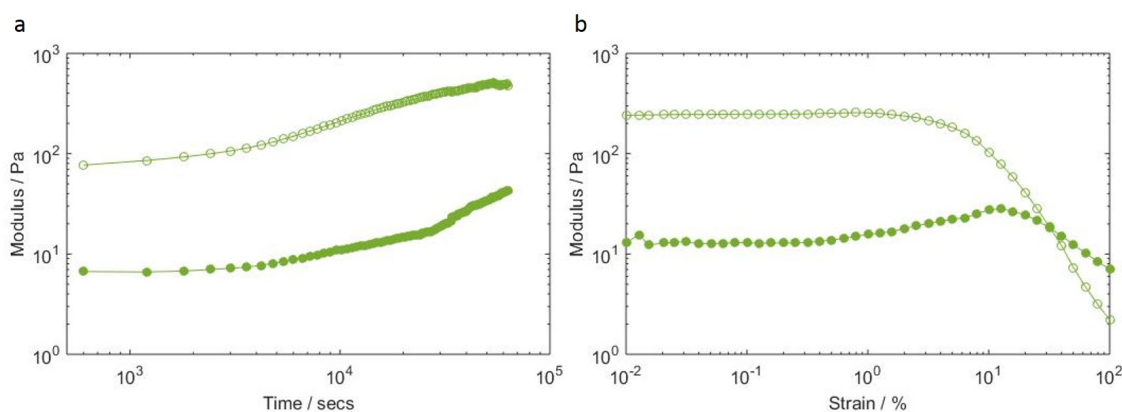


Figure 6.9: Rheological measurements of viscoelastic properties of a sample of coacervates (1:2 PLYs:AMP ratio at 50 mM concentration) a) undergoing the hydrogel transformation on the rheometer with measurements acquired every 10 minutes overnight b) strain sweep of an identical sample left to gelate in a vial. The viscous and elastic moduli are the same order of magnitude at 1 Hz and 1% strain.

The sample shows an increase in both elastic and viscous moduli with time, beginning initially with gel-like characteristics as the elastic modulus (77 Pa) is higher than the viscous modulus (7 Pa) (Figure 6.9a). This implies that upon mixing some complexation occurs to transform the solution into a hydrogel instantaneously. An increase in the moduli implies the formation of an extended cross-linked network within the sample as the elastic and viscous moduli increase to 500 and 42 Pa respectively overnight.

The sample formed under the same conditions but within a vial was tested with a strain sweep after being left to gelate overnight (Figure 6.9b). The elastic and viscous moduli are at different values, 240 and 12 Pa, compared with the final data points of the time sweep, 500 and 42 Pa. These differences are believed to have arisen due to differential sample hydration over the course of the experiment and the absence of force applied from the test geometry.

6.2.4.2 Differential Scanning Calorimetry

Differential scanning calorimetry (DSC) runs were performed in triplicate for both AMP hydrogels at 5 and 50 mM concentration and 1:2 coacervate hydrogels (Figure 6.10). They all exhibit an endothermic peak between 30-70 °C indicative of a sol-gel transformation.

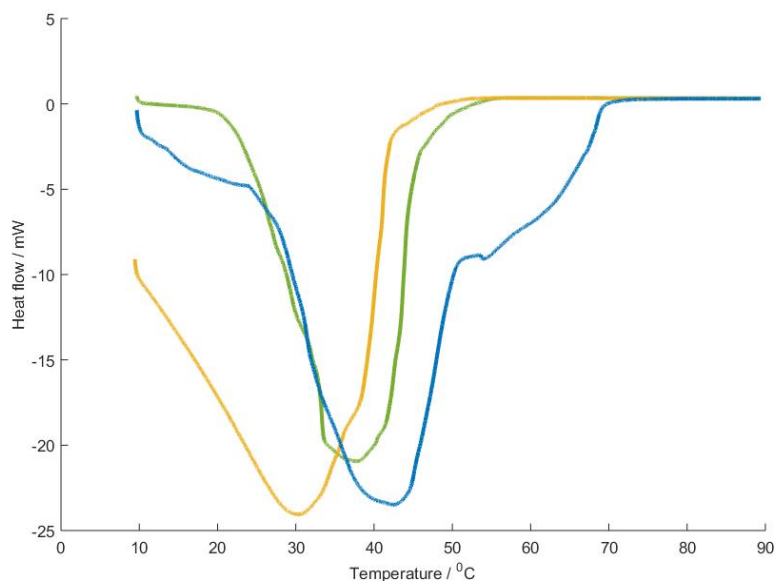


Figure 6.10: Differential scanning calorimetry for 50 and 5 mM AMP hydrogels, blue and yellow curves respectively and 1:2 PLys:AMP coacervate based hydrogel shown by the green curve

The 50 mM AMP hydrogel (blue curve) has the highest temperature transition at 45 °C, while the 5 mM (yellow curve) shows the lowest temperature transition at 30 °C. Despite the difference in temperature, it requires the same heat flow to transition between states. The 1:2 coacervate hydrogel requires slightly less heat, with a peak at 38 °C, presumably due to the slight disruption of coordination between AMP molecules within the hydrogel network due to the presence of the PLys.

6.2.5 Acoustic patterning of PLys/AMP coacervates in a 2D acoustic field

As previously shown for the polymer/dipeptide coacervate system, coacervate droplets at different ratios will have different coalescence behaviours in an applied acoustic field. The trapping of the PLys/AMP droplets was observed in a 2D field at various ratios.

Coacervate droplets were formed at the desired ratios using stock solutions at 50 mM concentration

to 200 μL and then diluted with 800 μL HEPES. The diluted coacervate solutions were then added directly into the trapping device under a 2D (6.7 x 6.69 MHz) applied acoustic field. After 5 minutes, patterns could be resolved.

The different ratios displayed different nodal point behaviours. Despite the encouraging trapping size of the droplets in solution from DLS measurements, samples at the 1:2 ratio did not exhibit clear patterning when left in the acoustic field. Coacervate solutions prepared at 1:4 and 1:10 ratios did pattern in the field, over large areas, with clearly distinct nodal points where the droplets had migrated to (Figure 6.11).

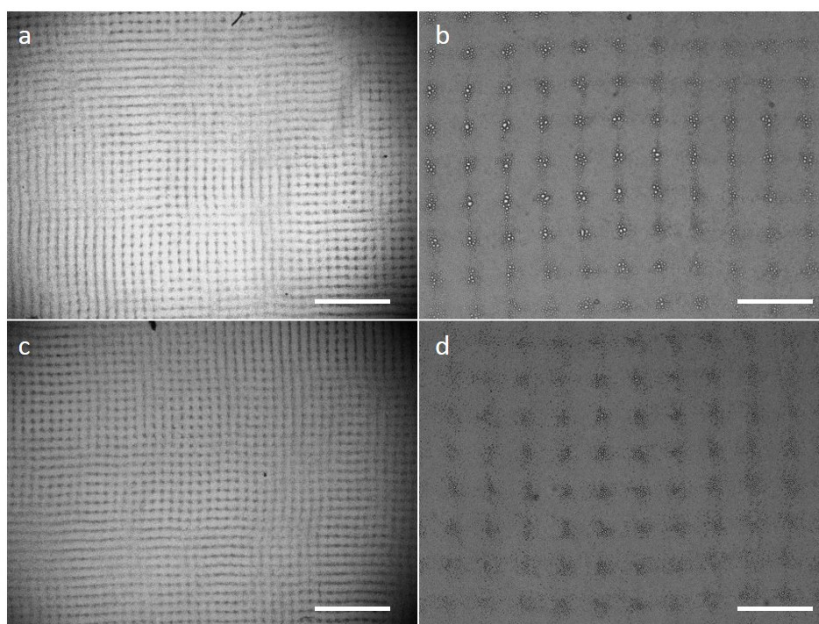


Figure 6.11: 2D (6.7 x 6.69 MHz) patterned coacervate solutions after 30 minutes in the applied field at a) and b) 1:4 and c) and d) 1:10 ratio (PLys:AMP). Scale bar 500 and 200 μm

However none of the ratios displayed the same coalescence, as with the FMOC-AA/PDDA coacervates, with no large droplets in the trapping points even when left to trap for 30 minutes or longer. From the previous investigations (Section 4.2.4.2), samples were left to experience the acoustic force for up to 1 hour in attempts to achieve large droplets in the nodal points. After this time, there was little coalescence of the droplets to larger sizes and instead they remained within the nodal points as clusters of droplets. However size measurements of the trapped droplets, taken from microscopy images, show that the largest droplets in the trapping points at 1:4 (PLys:AMP) ratio were 6.0 ± 1.7

μm in size compared to $3.3 \pm 1.1 \mu\text{m}$ in free solution and at 1:10 (PLys:AMP) ratio $5.3 \pm 1.2 \mu\text{m}$ in size compared to $2.6 \pm 0.7 \mu\text{m}$ in free solution, so there was some coalescence in the trapping points.

6.2.6 Hydrogelation of PLys/AMP coacervate droplets in an acoustic field

Gelation required the addition of ZnCl_2 into the sample cavity. Due to the limited coalescence of the coacervate droplets in the acoustic field, it was believed that they would not be large enough to have sufficient surface interaction with the glass slide to remain at their trapped position if the fluid was perturbed. However this was not the case. Upon addition of ZnCl_2 ($400 \mu\text{L}$, 50 mM) into the sample cavity of a sample of coacervate droplets (1:4 PLys:AMP molar ratio) trapped for 1 hour, to mix directly with the coacervate solution already present in the trapping device, the majority of droplets remained at their trapping points and spherical features were immobilized into the resulting hydrogel network (Figure 6.12). The gel-like rheological properties (Section 6.2.4.1) of the sample minutes after mixing imply an instantaneous immobilisation of the coacervate droplets within the network and this is why the patterning was retained upon mixing ZnCl_2 into the coacervate solution.

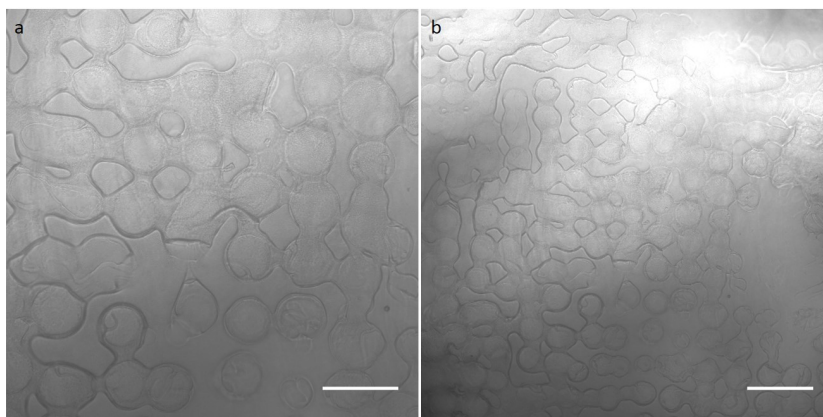


Figure 6.12: 2D patterned (6.7×6.69) MHz 1:4 ratio (PLys:AMP) monolith hydrogel a) connected circular features at the expected spacing are observed b) these features extend over a large area of the sample. Scale bar a) $150 \mu\text{m}$ b) $250 \mu\text{m}$

For the 2D hydrogel, it appears that the clusters of droplets at the nodal points may have coalesced upon their transformation into one large spherical shape. Again no coacervate droplet features appear retained within the patterned gel compared to the droplets still present in the unordered transformed coacervate hydrogel (Figure 6.6a) but the morphology differs from the AMP only hydrogel (Figure

6.6b). However these roughly spherical regions of material appear in a regular gridded arrangement across a large area of the hydrogel, and so were attributed to the acoustic field. In some areas the nodal features have merged with each other so that the distinction is lost.

6.2.6.1 Hydrogelation of coacervate droplets in a 1D acoustic field

Coacervate droplets were also trapped in a 1D acoustic field and then transformed into a hydrogel through addition of ZnCl_2 (Figure 6.13). The morphologies observed in the 1D patterned coacervate hydrogel are very different from those in the unordered coacervate hydrogel and the 2D patterned hydrogel (Figure 6.12). There are ordered lines across the base, with roughly spherical features and no clearly defined droplet structures remaining. These are obscured from view by higher layer material which is unordered but has also gelled (Figure 6.13a). Mixing fronts appear to have been preserved within the gel structure, appearing as ripples.

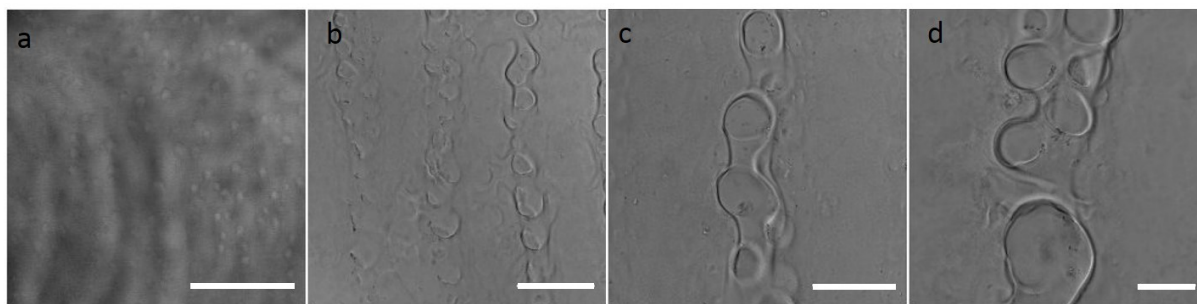


Figure 6.13: [1D (6.7 MHz) micropatterned coacervate hydrogel formed at a 1:4 PLYS:AMP ratio a) low magnification view with fluid movements imparted into the network b) lines of transformed droplets c) & d) individual lines of transformed droplets Scale bars a) 500 b) 100 c) 50 and d) 25 μm

As with the FMOC-AA/PDDA coacervate system, this protocol produced a full transformation of the entire solution into hydrogel monoliths. However on the macroscale within the acoustic trapping device, there was not full gelation across the whole volume, indicating that there was insufficient mixing of the ZnCl_2 throughout the entire solution which resulted in some areas fully transforming and others not. Repeating these experiments varying the concentration and volumes of ZnCl_2 added did not result in entire transformation across the trapping device.

6.2.6.2 Micropatterned thin films

In light of only partial gelation of the volume of solution within the trapping device, experiments were repeated following the supernatant removal protocol adopted for the thin films with the Fmoc-AA/PDDA system (Section 2.2.4.1). After 1 hour the supernatant was wicked off from the cavity, using a paper towel, and there was no disruption of the patterning across the cavity comparing the before and after supernatant removal images (Figure 6.14).

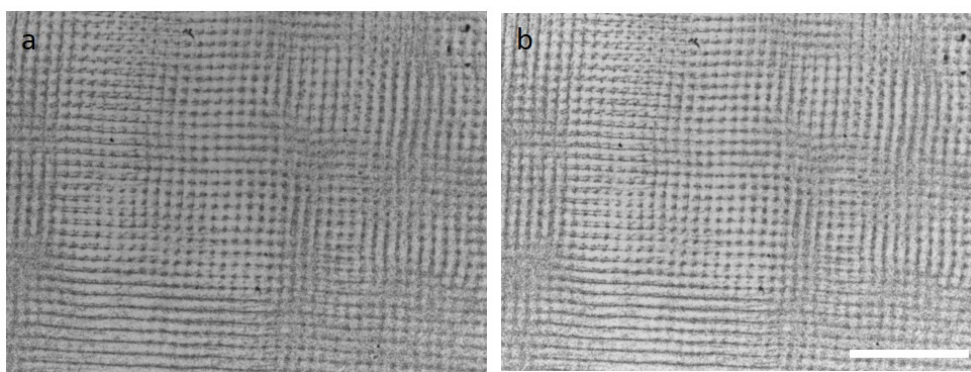


Figure 6.14: 2D patterned 1:4 ratio coacervate droplets a) trapped for 1 hour and then b) following supernatant removal with a paper towel. Patterning has not been disrupted despite limited coalescence of the droplets. Scale bar 800 μm

The extracted volume was then replaced with an equal volume of ZnCl_2 (1 mL, 50 mM). This method provided a route that better preserved the ordering of the droplets within the transformed hydrogel thin films compared to the monolith counterparts. The entire immersion of the sample within ZnCl_2 , removed any diffusion limited effects that were inhibiting gelation of the whole volume of solution in the acoustic device and enabled transformation over the whole area of the sample simultaneously. Upon addition, trapped coacervate material instantly transformed to leave behind ordered features on the glass of noticeably different morphology to those observed previously.

In the 2D patterned films, it appears that there was transformation into spherical ring structures surrounding whatever droplets that were present at the nodal point and so must have been rapidly transforming the AMP present (Figure 6.15). The transformed material was spatially distinct and remained of a similar size to the droplets trapped at that point, contrasting with the equivalent monolith sample where much larger spherical features were observed (Figure 6.12).

In samples prepared the same way but with 1D (6.7 MHz) trapping, again there were spherical

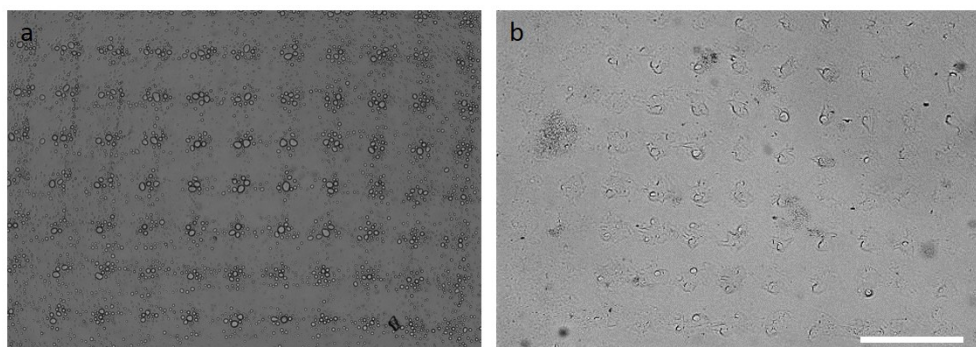


Figure 6.15: 2D (6.7 x 6.69 MHz) patterned 1:4 ratio coacervate droplets a) droplets remain at the nodal points following supernatant removal with a paper towel b) following addition of 1 mL of ZnCl_2 the droplets rapidly transform leaving behind spherical gelled structures at the nodal point. Scale bar 200 μm

ring structures remaining on the glass where droplets once were (Figure 6.16d). Again the different neighbouring droplets in the same trapping point have interconnected during their transformation. Compared with the features in the equivalent monolith sample (Figure 6.13), both structures appear quite similar.

The rapid transformation into a thin film occurs without the supernatant present to dilute the ZnCl_2 , must be rapidly transforming the AMP present within the droplets entirely. Due to the spatial organisation, the neighbouring droplets are the only surrounding material to interconnect and form the fibril network. The transformation leaves behind organised fibrils on the surface of the glass but no intact spherical coacervate droplets, as they are too small so must transform entirely rather than leaving a contracted core in the nodal point.

6.2.6.3 Guest molecules

As with all coacervate systems, the sequestration properties of the droplets can be used in exploring the droplet behaviour by addition of guest molecules. However, the sequestration of some guest molecules is also possible within the AMP only hydrogel. [303] The benefit of loading the guest molecules within the coacervate droplets would enable localisation of them at particular locations within the droplets in solution as opposed to being dispersed throughout it.

As with the Fmoc-AA/PDDA system, guest molecules were added into the PLYs prior to the addition of AMP so that they were present during coacervation. The sequestration properties of the droplets

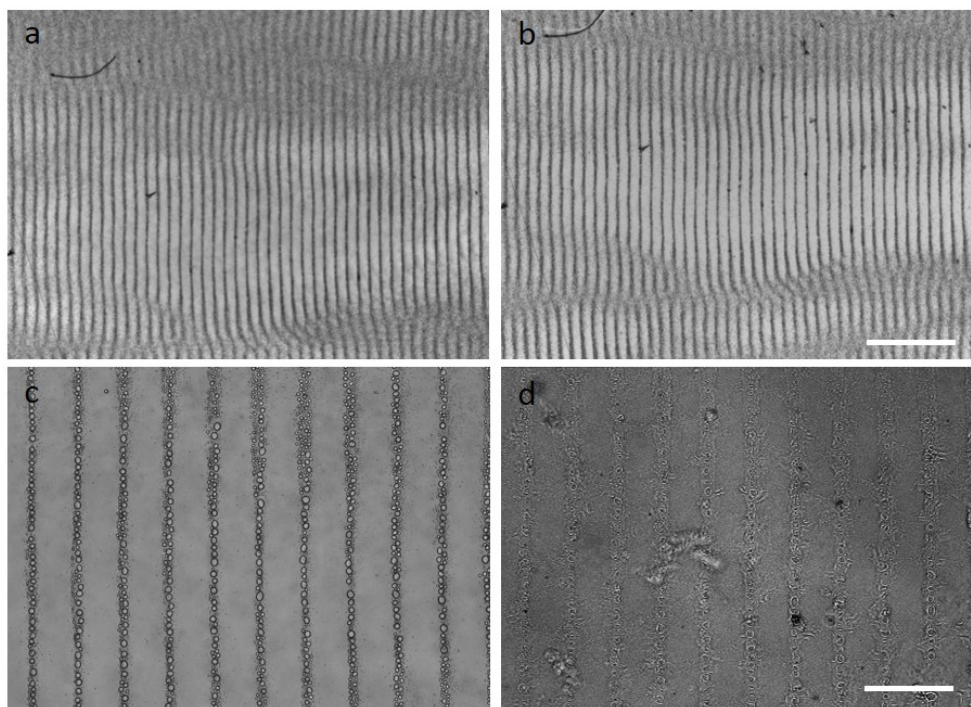


Figure 6.16: 1D (6.7 MHz) 1:4 ratio coacervate thin film patterning procedure a) & b) coacervate droplets trapped for 30 minutes in the applied field c) droplets remain trapped following supernatant removal with a paper towel d) following addition of $ZnCl_2$ the droplets rapidly transform at their trapped locations Scale bars a) & b) 800 c) & d) 200 μm

were again investigated using fluorescence microscopy and fluorescently tagged guest molecules. Again Hoechst, tagged GOx and single-stranded DNA were added to serve as examples of the different types of molecules (dyes, enzymes and biomolecules respectively) that could be loaded into the droplets and hydrogel network.

As expected, the guest molecules located preferentially inside the droplets, even when the droplets were formed at different ratios. Hoechst dye is shown as a representative example, of the droplet loading at 1:2 and 1:10 ratio (PLys:AMP) in Figure 6.17 a and b respectively.

Following the hydrogel transformation, both the enzyme, fluorescein isothiocyanate tagged glucose oxidase (FITC-GOx) and Cy5 tagged single-stranded DNA (Cy5-ss-DNA) remained predominantly within the areas of hydrogel where droplets had transformed (Figure 6.18). The droplets had transformed entirely so that their payload of the guest molecule was released at that location but contained within the dense region of fibrils. The guest molecules were immobilized within the gel network at those locations. This was in keeping with the observations and loading of enzymes and GFP into

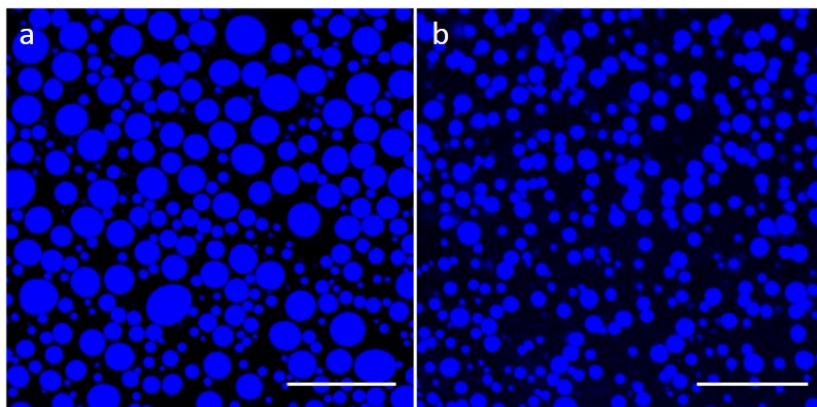


Figure 6.17: Sequestration of Hoechst dye into PLys:AMP coacervate droplets formed at different volume ratios a) 1:2 b) 1:10 Scale bars 50 μm

the AMP only hydrogels, where it is believed that proteins and biomolecules interact more strongly within the neutral Zn/AMP hydrogel. [303]

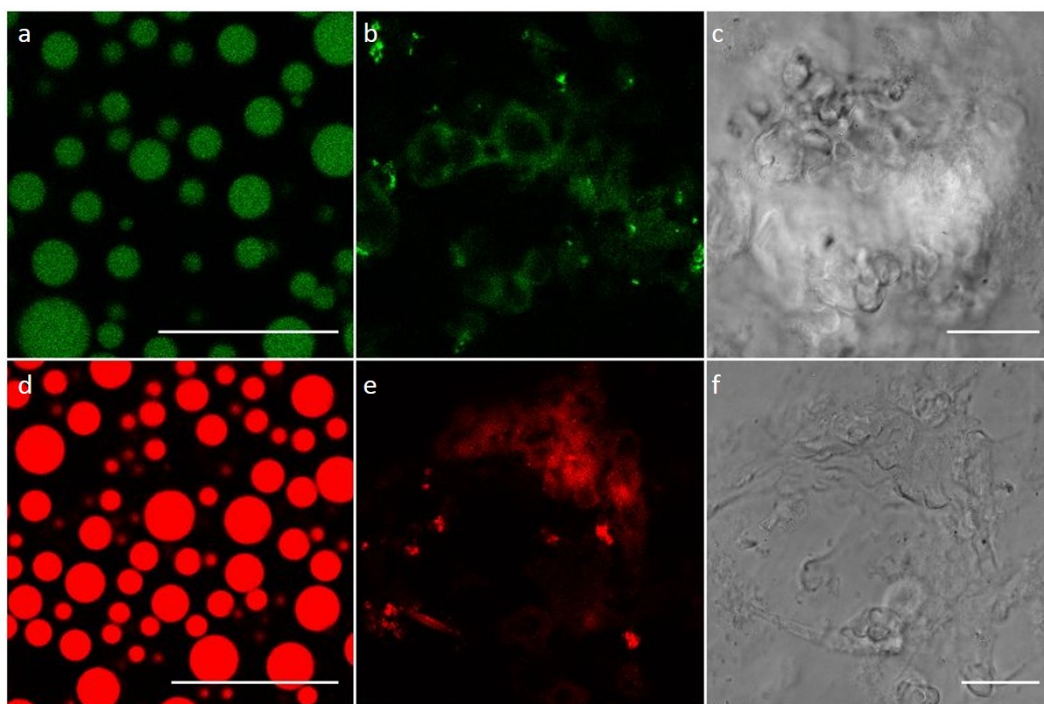


Figure 6.18: Sequestration of FITC-Gox and Cy5-ss-DNA within unordered transformed 1:2 PLys:AMP thin film hydrogels. a-c) FITC-Gox a) droplets free in solution b) transformed hydrogel fluorescent channel c) corresponding brightfield image of b). d-f) Cy5-ss-DNA d) droplets free in solution e) transformed hydrogel fluorescent channel f) corresponding brightfield image of e). Scale bars 25 μm

Hoechst dye, despite clearly elucidating the fibril network in the FMOC-AA/PDDA hydrogels, was

hard to resolve in transformed PLys/AMP hydrogels (Figure 6.19a & b). In densely packed regions of fibrils which could be resolved in bright field microscopy more clearly, there was some corresponding fluorescence signal. Increasing the concentration of the dye did not improve fluorescent imaging after hydrogel transformation.

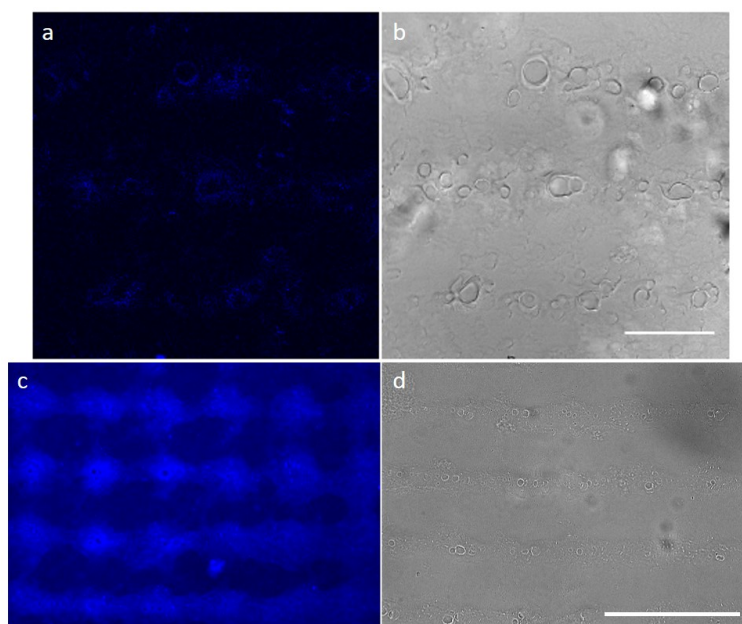


Figure 6.19: Sequestration of Hoechst within a transformed thin film hydrogel. a & b) fluorescence and corresponding bright field image of Hoechst dye within a transformed thin film that was added during coacervation. c & d) fluorescence and corresponding bright field image of Hoechst dye within a transformed thin film that was added after gelation. Scale bar a & b 100 μm c & d 200 μm

However if Hoechst was added to the samples after they had gelled, the different gelled features were resolvable in fluorescence mode (Figure 6.19c & d).

It is believed that the Hoechst dye is released into the hydrogel network upon hydrogelation of the droplets into fibrils. It can be used in elucidating the gelled features, as demonstrated by adding it to gelled samples after hydrogelation, however, it doesn't interact as strongly with the hydrogel compared with the other tagged guest molecules.

6.3 Conclusions and Future Work

These preliminary investigations serve to demonstrate that another coacervate system, comprising a nucleotide and polypeptide, can be transformed into a hydrogel network via metal coordination. Further, the acoustic trapping and subsequent gelation of the coacervate system within an acoustic field produced hydrogels and gelatinous thin films with ordered features in both 1D and 2D.

This system serves as one other example of a coacervate-based hydrogel system that can be acoustically patterned and transformed into an ordered hydrogel network. It demonstrates the versatility of the acoustic patterning technique for use with other coacervate-based hydrogel systems. Through careful selection of different components with added functionality and biological compatibility, systems could be designed and optimised for specific applications such as tissue culture.

This system requires further investigation to optimise the resulting hydrogels. While rheology and DSC results characterise the properties of a hydrogel, the gelation within the acoustic trapping device was assumed due to the variation in sample morphology from that of the trapped droplets. Presently, there are varying morphologies achieved within the transformation process with ordered coacervate droplets. The differing results acquired in these investigations show that the nature of the formation of the gel network is still largely unknown. Are the coacervate droplets merely embedded into a gelled supernatant as free AMP transforms or do the droplets themselves comprise the hydrogel? There is evidence to suggest that the transformation occurs without the supernatant present, due to the hydrogelated thin film constructs. However fibrillar structures were not resolved throughout the transformation. Manipulating the concentrations to slow down the transformation so it could be observed throughout via microscopy could reveal the processes underlying the different morphologies achieved. Tagging the different components with fluorescent molecules could be enlightening into the behaviour of the coacervated polypeptide and nucleotide during metal coordination as the movement of the different components during the transformation could be tracked.

The integration of this more biologically relevant system, with living cells should be further explored. Firstly with investigations into the salt and pH stability of the coacervate droplets formed at trapping appropriate ratios. This could be specifically implemented with cell media solutions or directly through the addition of sodium chloride salt into the coacervate precursor solutions. Coacervate

stability in salt is a well-documented investigation where turbidity of coacervate solutions is observed in the presence of differing salt concentrations. Turbidity of solution implies the onset of droplet formation due to the scattering of the light and so UV Vis can be used to monitor this easily. Similarly for pH stability, the turbidity of coacervate droplets formed within different pH solutions through the use of buffers is monitored. Secondly the stability of the hydrogels formed when immersed in different salt and pH solutions would also need to be found. Here perhaps the exploration of coacervate systems comprising other nucleotides and hydrogelation through coordination with different metal salts may result in more stable hydrogels.

These coacervate droplets could be utilised as a route for 'anchoring' cells onto the surface of the glass, due to the rapid transformation of the droplets combined with the attraction between PLys and cell membranes. Cells can be acoustically patterned however once the acoustic field is removed they move of their own accord out of the patterned arrangement. With gelled coacervate material to anchor sections of the cell membrane this could limit their migration away from those desired positions and enable their encapsulation within a hydrogel network. Further the PLys cell adhesion benefit, could enable these coacervates to be used as an option for storing cells by encapsulating them in a hydrogel membrane. [150] Mixing the cells with Plys would result in charge attraction of the polymer on the cell membrane. Addition of the AMP would then result in coacervates forming on the surface of the cell. Subsequent hydrogelation could result in additional coacervate gel membranes over the surface of the cells which could make them more resilient to longer exposure to an acoustic field or again aid in the anchoring of the cells within an acoustic field.

The full transformation of the coacervate droplets into the hydrogel limits the site specific isolation of guest molecules within spatially organised reaction compartments within the ordered hydrogels. However better understanding and control over the transformation process and coalescence to larger droplet sizes may result in retention of the coacervate structure within micropatterned hydrogels.

CHAPTER



GENERAL CONCLUSIONS

The research presented in this thesis explores the acoustic trapping of coacervate systems, which will undergo structural reconfiguration into hydrogels, as a route for fabrication of micropatterned soft, viscoelastic materials. Due to a difference in acoustic properties, such as density and compressibility of the bulk droplet phase compared with the surrounding aqueous supernatant phase, coacervate systems are suitable for acoustic trapping.

A standing wave acoustic manipulation device was adapted for greater compatibility with chemical systems. The trapping within these devices formed patterns in an x-y plane towards the bottom of the device. This device comprised four orthogonally arranged transducers surrounding a square sample cavity with a 2 mm acrylic periphery separating the transducers from it. The implications on the acoustic behaviours, due to these adaptations, are not fully understood however the successful patterning within these devices fell within expected behaviours and so was not investigated, but in future investigations it may become more critical. Oppositely sited transducers comprised a counter-propagating standing wave pair, such that trapping in both 1D or 2D in an x-y plane was possible through driving one or both pairs respectively. The migration of micron-sized coacervate droplets to the half-wavelength spaced pressure nodes of an applied acoustic field, due to the acoustic force, was observed. When both pairs of transducers were driven for 2D trapping, a 10 kHz difference in driving frequency between each pair was introduced to ensure that the acoustic fields were temporally uncorrelated. The patterns formed within the trapping devices were in best agreement with modelling using a Huygen's approximation, which accounts for the size of the transducer with respect to the cavity. Results implied that matching the resonance behaviour, through impedance analysis of the transducers at a particular driving frequency, within a counter-propagating pair is very important for the most extensive trapping across the entire device cavity. While trapping was observed for randomly allocated transducer pairings, the area that was patterned within the entire 20 mm cavity was not as large as when the transducers were matched.

Polymer/dipeptide coacervate droplets were formed in situ in the presence of an acoustic standing wave field. Upon the mixing of deprotonated N-(fluorenyl-9-methoxy-carbonyl)di-alanine (FMOC-AA) with the cationic polymer poly (diallyldimethylammonium) chloride (PDDA) coacervate droplets were formed within the sample cavity of the trapping device. These coacervate droplets then migrated to the pressure nodes of both 1D and 2D applied acoustic fields, to form lines or gridded arrays

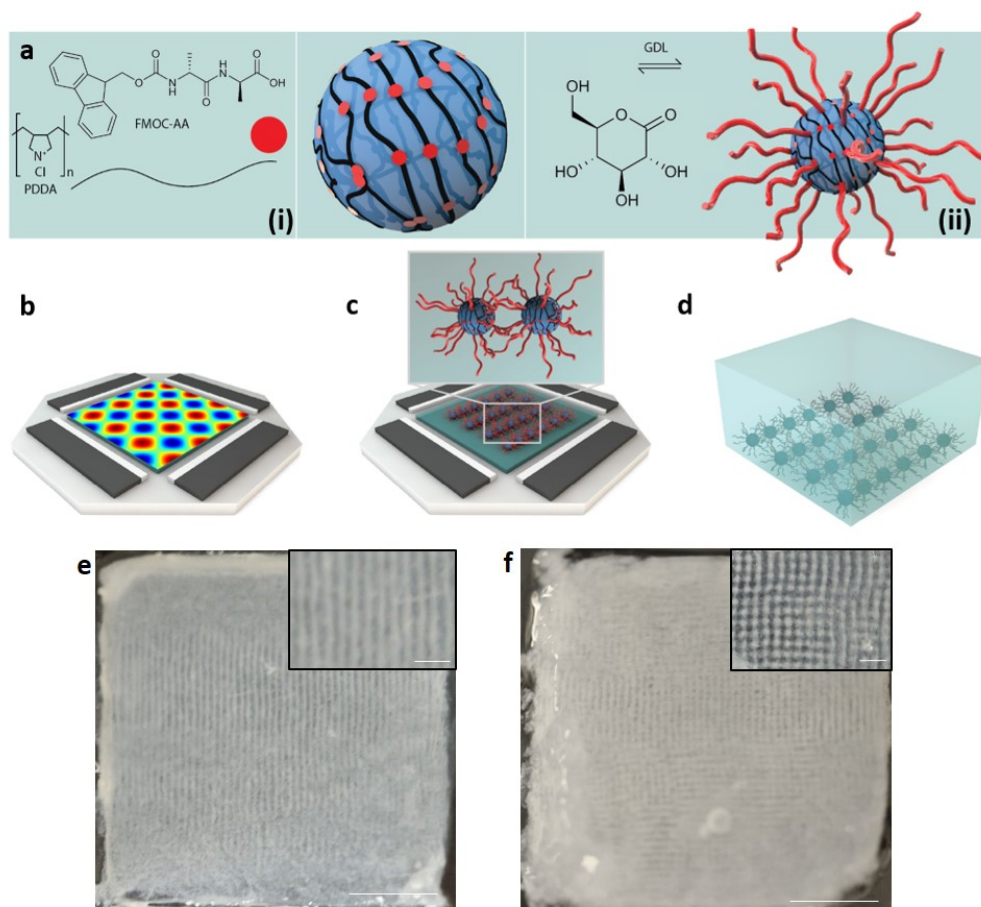


Figure 7.1: Micropatterned hydrogel summary a-e) shows the different steps in the acoustic micropatterning procedure to fabricate micropatterned hydrogels e) 1D patterned hydrogel at 2.15 MHz f) 2D patterned hydrogel at 2.15 MHz. Scale bars 5 mm insets 1mm. All images reproduced from Chapter 4.

respectively, over the course of one minute. When left for some time, the acoustic field induced coalescence of the droplets to much greater sizes than in free solution. For the case of 2D trapping, when the ratio of mixing of the Fmoc-AA:PDDA was optimised to 3:7, one large droplet per trapping point was observed. The periodicity of these patterns was controlled by the different driving frequencies of the transducers, identified through impedance analysis. The hydrogel transformation was initiated by pH reduction, through mixing in glucono- δ -lactone (GDL) powders, such that the Fmoc-AA became protonated initiating supramolecular self-assembly with the alanine and fluorenyl residues stacking into fibril structures which entangled into a hydrogel network. Within the trapping device, addition of GDL powders carefully into the sample cavity lowered the pH slowly and transformed the

system in the presence of an acoustic field. The coacervates transformed at their trapped positions to produce micropatterned hydrogels (Figure 7.1 a-d). Following removal of the acoustic field, the ordered features remained within the hydrogel network with contracted droplet cores present periodically throughout. The well-documented sequestration behaviours of coacervate droplets were exploited to load a variety of different guest molecules into the hydrogel network forming a hydrogel material with periodically arranged, isolated dyes, proteins or biomolecules.

Interestingly, rheological characterisation of the hydrogels revealed no mechanical differences between the 20 mm square unordered, 1D or 2D patterned hydrogels. This was later accounted for by the limited vertical extent of the patterning through the hydrogels extending to $\approx 70 \mu\text{m}$, elucidated through exploiting the sequestration of fluorescent dyes on the droplet interiors. Consequently a protocol was developed to produce gelatinous thin films, removing the bulk of unordered material so that only the patterned bulk phase remained to be gelled. Loading the droplets with different enzymes prior to patterning, enabled the study of one and two step enzymatic cascades of horseradish peroxidase and glucose oxidase/horseradish peroxidase across the micropatterned films. The reaction could be monitored using fluorescence microscopy through the transformation of a non-fluorescent substrate to a fluorescent product (Figure 7.2a).

Another product of the enzymatic cascade of glucose oxidase from the glucose substrate was gluconic acid. This was found to be successful in lowering the pH of solution to initiate the hydrogelation process. This enzymatic gelation route produced thin films with different morphologies, most noticeably with the 1D patterned hydrogels, due to the localised pH reduction within the droplets. These more cohesive connected structures enabled investigations into stacking the thin films layer by layer towards higher patterned structures and more complex ordered hydrogel features, such as the cross-hatch patterns formed by sequential orthogonally patterned layers (Figure 7.2b). Unfortunately the dynamic movement of different guest molecules between sequentially patterned layers inhibited studies of reactions originating at intersections where different molecules would be in close proximity to interact. However the stacking investigations revealed some intriguing structures, such as those displayed within a 3 layer stacked construct, which warrant some further investigation (Figure 7.2c). Further to this, the embedding of thin films within other gel matrices could be incorporated for use in investigating diffusion within other hydrogel matrices or to aid in keeping the guest molecules

within different coacervate based thin films isolated.

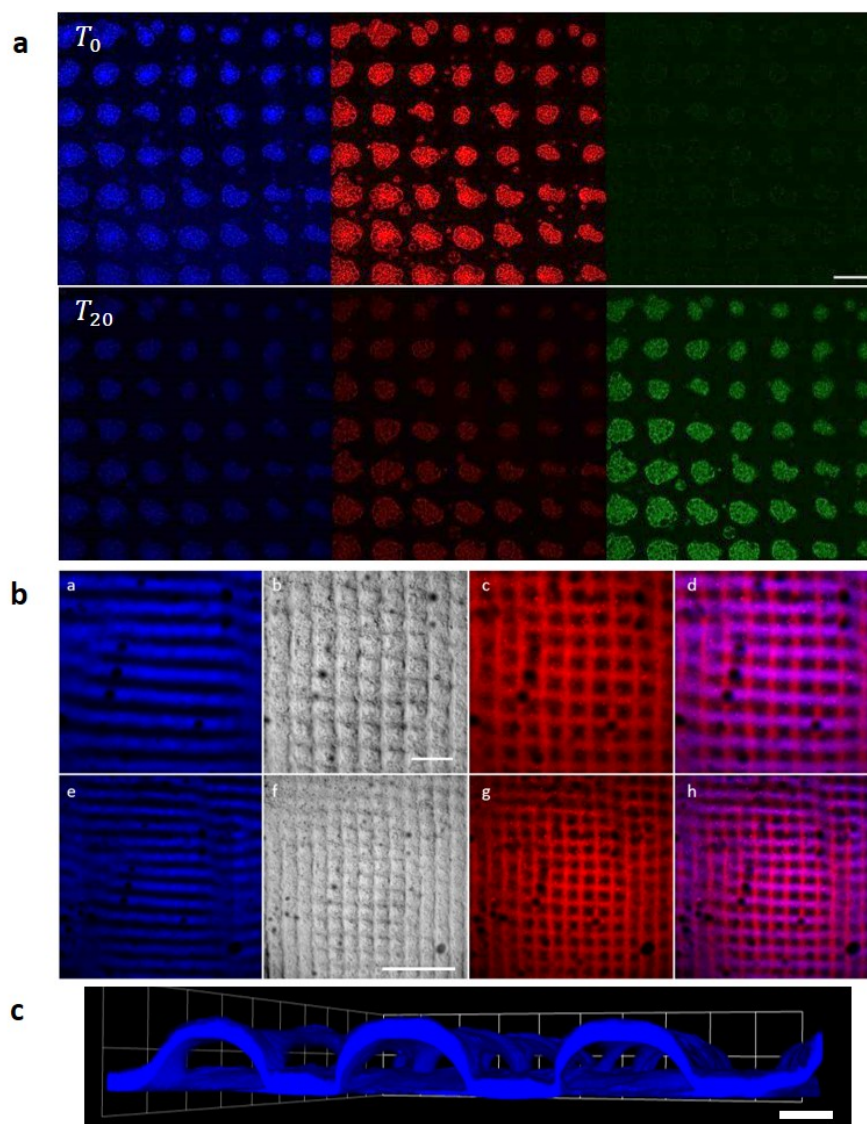


Figure 7.2: Micropatterned gelatinous thin film summary a) shows the three different fluorescent channels used in the observation of the coupled glucose oxidase (GOx) and horseradish peroxidase (HRP) enzyme cascade. Fluorescently tagged GOx and HRP are shown in the red and blue channels respectively and the evolution of the fluorescent product is shown in the green channel. b) 2 layer orthogonally patterned enzymatically hydrogelated thin film stack elucidated with a different dye loaded into each layer. Here Hoechst (blue) in layer 1 and rhodamine (red) in layer 2. c) 3 layer orthogonally patterned enzymatically hydrogelated thin film stack elucidated with Hoechst dye loaded into layer 1 and 3. Scale bars a) 100 b) 500 c) 40 μm . All images reproduced from Chapter 5.

With these promising micropatterned hydrogel constructs and architectures being applicable within biological fields, a more biologically relevant polypeptide/nucleotide coacervate system was se-

lected. The cationic polypeptide poly-L-lysine (PLys) undergoes coacervation upon mixing with the nucleotide adenosine-5'-monophosphate (AMP). This system was extended to that of a hydrogel through investigations where AMP was shown to gelate through metal coordination with zinc chloride (ZnCl_2). Thus, in a similar fashion to the combination of one low molecular weight dipeptide based gelator with a polymer to produce the polymer/dipeptide reconfigurable system, another coacervate based hydrogel system was developed. The rheological properties of the coacervate hydrogel were compared with the nucleotide hydrogel, with slight differences in viscoelastic behaviours found for similar concentrations of nucleotide in each.

The system properties, such as charge, composition and size, were then adjusted to suitable parameters for acoustic patterning so that in an applied acoustic field they would migrate to the trapping points (Figure 7.3). Despite limited coalescence within the trapping points, ordered hydrogels were still formed from different molar ratios of PLys:AMP. Coacervate droplets were left to trap in the acoustic field and following the addition of ZnCl_2 into the sample cavity, the samples transformed into ordered hydrogel constructs. Both thin films and monolith hydrogels were formed. As before, the droplets were loaded with guest molecules but upon transformation of this system guest molecules were immobilized in dense fibril regions. The disruption of spherical droplet structures was due to the rapid and full transformation of the AMP into a hydrogel.

In summary, it has been demonstrated that standing wave acoustic trapping devices can be used for the generation of spatially organised 1D lines or 2D gridded arrays of coacervate droplets. Both polymer/dipeptide and polypeptide/nucleotide coacervate systems were transformed into hydrogels in the presence of the acoustic field through initiation of the supramolecular self-assembly by pH reduction and metal coordination respectively. Stacking and entanglements of the nanofilaments from the coacervate droplets immobilized in an applied acoustic field resulted in the formation of 1D or 2D patterned hydrogel constructs. Droplet features were retained within the networks of both gelatinous thin films and thicker monolith hydrogel constructs, facilitating the spatial isolation of guest molecules inside the droplets and consequently within the hydrogel matrix. Subsequently, enzymatic cascades could be initiated in specific regions of micropatterned hydrogels and even act to lower the pH for hydrogelation of the dipeptide system. Enzymatically hydrogelated thin film constructs were stacked layer by layer to obtain more complex networks and higher extending

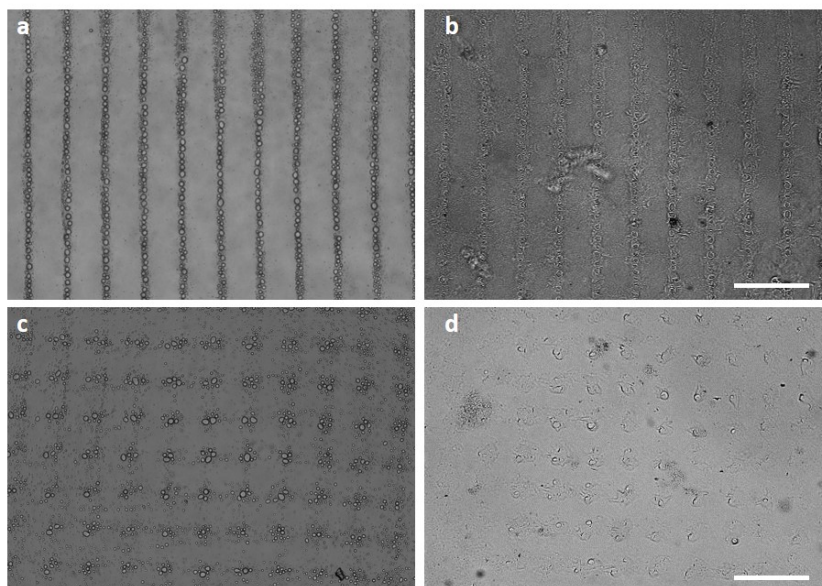


Figure 7.3: Micropatterned polypeptide/nucleotide coacervate hydrogel summary a) 1D (6.7 MHz) patterned 1:4 PLys:AMP ratio coacervate droplets after 30 minutes in the acoustic field b) the same sample following thin film hydrogelation with addition of ZnCl₂ c) 2D (6.7 x 6.69 MHz) patterned 1:4 PLys:AMP ratio coacervate droplets after 1 hour in the acoustic field b) the same sample following thin film hydrogelation with addition of ZnCl₂ Scale bars 200 μm . All images reproduced from Chapter 6.

patterned features. These results suggest that the technique of standing wave acoustic trapping is a powerful tool in the construction of micropatterned soft viscoelastic materials with particular relevance to tissue engineering, cell studies and microarray technologies.

BIBLIOGRAPHY

- [1] T. C. Kriss and V. M. Kriss, "History of the Operating Microscope: From Magnifying Glass to Microneurosurgery," *Neurosurgery*, vol. 42, no. 4, pp. 889–907, 1998.
- [2] Gordon E. Moore, "Progress In Digital Integrated Electronics," *IEDM Tech. Digest*, pp. 11–13, 1975.
- [3] C. Disco and B. van der Meulen, *Getting New Technologies Together*. Walter de Gruyter, 1998.
- [4] D. Mijatovic, J. C. Eijkel, and A. Van Den Berg, "Technologies for nanofluidic systems: Top-down vs. bottom-up - A review," *Lab on a Chip*, vol. 5, no. 5, pp. 492–500, 2005.
- [5] H. Jansen, N. Tas, and J. Berenschot, "MEMS-Based Nanotechnology," 2004.
- [6] D. B. Weibel, W. R. DiLuzio, and G. M. Whitesides, "Microfabrication meets microbiology," *Nature Reviews Microbiology*, vol. 5, no. 3, pp. 209–218, 2007.
- [7] B. Wu and A. Kumar, "Extreme ultraviolet lithography: A review," *Journal of Vacuum Science & Technology B: Microelectronics and Nanometer Structures*, vol. 25, no. 6, p. 1743, 2007.
- [8] A. A. Tseng, "Recent developments in micromilling using focused ion beam technology," *Journal of Micromechanics and Microengineering*, vol. 14, no. 4, 2004.
- [9] Y. Chen, "Nanofabrication by electron beam lithography and its applications: A review," *Microelectronic Engineering*, vol. 135, pp. 57–72, 2015.
- [10] Y. N. Xia and G. M. Whitesides, "Soft lithography," *Annual Review Of Materials Science*, vol. 37, no. 5, pp. 551–575, 1998.
- [11] D. Qin, Y. Xia, and G. M. Whitesides, "Soft lithography for micro- and nanoscale patterning," *Nature Protocols*, vol. 5, no. 3, pp. 491–502, 2010.
- [12] J. C. McDonald, D. C. Duffy, J. R. Anderson, D. T. Chiu, H. Wu, O. J. Schueller, and G. M. Whitesides, "Fabrication of microfluidic systems in poly(dimethylsiloxane).," *Electrophoresis*, vol. 21, no. 1, pp. 27–40, 2000.

- [13] B. C. Gross, J. L. Erkal, S. Y. Lockwood, C. Chen, and D. M. Spence, "Evaluation of 3D printing and its potential impact on biotechnology and the chemical sciences," *Analytical Chemistry*, vol. 86, no. 7, pp. 3240–3253, 2014.
- [14] C. Schubert, M. C. Van Langeveld, and L. A. Donoso, "Innovations in 3D printing: A 3D overview from optics to organs," *British Journal of Ophthalmology*, vol. 98, no. 2, pp. 159–161, 2014.
- [15] F. Rengier, A. Mehndiratta, H. Von Tengg-Kobligk, C. M. Zechmann, R. Unterhinninghofen, H. U. Kauczor, and F. L. Giesel, "3D printing based on imaging data: Review of medical applications," *International Journal of Computer Assisted Radiology and Surgery*, vol. 5, no. 4, pp. 335–341, 2010.
- [16] W. Wu, A. Deconinck, and J. A. Lewis, "Omnidirectional printing of 3D microvascular networks," *Advanced Materials*, vol. 23, no. 24, pp. 178–183, 2011.
- [17] C. L. Ventola, "Medical Applications for 3D Printing: Current and Projected Uses.," *P & T*, vol. 39, no. 10, pp. 704–711, 2014.
- [18] B. Leukers, H. Gülkan, S. H. Irsen, S. Milz, C. Tille, M. Schieker, and H. Seitz, "Hydroxyapatite scaffolds for bone tissue engineering made by 3D printing," *Journal of Materials Science: Materials in Medicine*, vol. 16, no. 12, pp. 1121–1124, 2005.
- [19] A. Murphy, S V, Atala, "3D bioprinting of tissues and organs," *Nat biotechnology*, vol. 32, no. 8, pp. 773–785, 2014.
- [20] C. X. Lam, X. M. Mo, S. H. Teoh, and D. W. Hutmacher, "Scaffold development using 3D printing with a starch-based polymer," *Materials Science and Engineering C*, vol. 20, no. 1-2, pp. 49–56, 2002.
- [21] G. Villar, A. D. Graham, and H. Bayley, "A tissue-like printed material.," *Science (New York, N.Y.)*, vol. 340, no. 6128, pp. 48–52, 2013.
- [22] M. M. Stanton, J. Samitier, and S. Sánchez, "Bioprinting of 3D hydrogels," *Lab on a Chip*, vol. 15, no. 15, pp. 3111–3115, 2015.
- [23] J. Goole and K. Amighi, "3D printing in pharmaceuticals: A new tool for designing customized drug delivery systems," *International Journal of Pharmaceutics*, vol. 499, no. 1-2, pp. 376–394, 2016.
- [24] V. Mironov, T. Boland, T. Trusk, G. Forgacs, and R. R. Markwald, "Organ printing: Computer-aided jet-based 3D tissue engineering," *Trends in Biotechnology*, vol. 21, no. 4, pp. 157–161, 2003.
- [25] N. Pamme, "Magnetism and microfluidics," *Lab on a Chip*, vol. 6, no. 1, pp. 24–38, 2006.

- [26] A. Aki, O. Ito, H. Morimoto, Y. Nagaoka, Y. Nakajima, T. Mizuki, T. Hanajiri, R. Usami, and T. Maekawa, "Capture of nonmagnetic particles and living cells using a microelectromagnetic system," *Journal of Applied Physics*, vol. 104, no. 9, 2008.
- [27] S. Hutzler, D. Weaire, F. Eliás, and E. Janiaud, "Juggling with bubbles in cylindrical ferrofluid foams," *Philosophical Magazine Letters*, vol. 82, no. 5, pp. 297–301, 2002.
- [28] M. D. Simon and A. K. Geim, "Diamagnetic levitation: Flying frogs and floating magnets (invited)," *Journal of Applied Physics*, vol. 87, no. 9, pp. 6200–6204, 2000.
- [29] B. R. Whatley, X. Li, N. Zhang, and X. Wen, "Magnetic-directed patterning of cell spheroids," *Journal of Biomedical Materials Research - Part A*, vol. 102, no. 5, pp. 1537–1547, 2014.
- [30] S. J. Lighthill, "Acoustic streaming," *Journal of Sound and Vibration*, vol. 61, no. 3, pp. 391–418, 1978.
- [31] A. Rosenthal and J. Voldman, "Dielectrophoretic traps for single-particle patterning," *Biophysical Journal*, vol. 88, no. 3, pp. 2193–2205, 2005.
- [32] M. Ozkan, T. Pisanic, J. Scheel, C. Barlow, S. Esener, and S. N. Bhatia, "Electro-optical platform for the manipulation of live cells," *Langmuir*, vol. 19, no. 5, pp. 1532–1538, 2003.
- [33] M. Evander and J. Nilsson, "Acoustofluidics 20: Applications in acoustic trapping," *Lab on a Chip*, vol. 12, pp. 4667–4676, 2012.
- [34] E. H. Brandt, "Suspended by sound," *Nature*, vol. 413, no. 6855, pp. 474–475, 2001.
- [35] F. Petersson, A. Nilsson, C. Holm, H. Jönsson, and T. Laurell, "Separation of lipids from blood utilizing ultrasonic standing waves in microfluidic channels," *Analyst*, vol. 129, no. 10, pp. 938–943, 2004.
- [36] A. E. Christakou, M. Ohlin, M. a. Khorshidi, T. Frisk, B. Vanherberghen, B. Önfelt, and M. Wiklund, "Aggregation and Long-Term Positioning of Cells By Ultrasound in a Multi-Well Microchip for High-Resolution Imaging of the Natural Killer Cell Immune Synapse," *Life Sciences*, pp. 329–331, 2011.
- [37] B. Hammarström, B. Nilson, T. Laurell, J. Nilsson, and S. Ekström, "Acoustic trapping for bacteria identification in positive blood cultures with MALDI-TOF MS," *Analytical Chemistry*, vol. 86, no. 21, pp. 10560–10567, 2014.
- [38] B. Hammarström, T. Laurell, and J. Nilsson, "Acoustic Trapping of Bacteria and Nanoparticles in Disposable Glass Capillaries Using Seed Particles," *Proc. Micro Total Analysis Systems Conferences*, pp. 1707–1709, 2011.

- [39] Y. Chen, S. Li, Y. Gu, P. Li, X. Ding, L. Wang, J. P. McCoy, S. J. Levine, and T. J. Huang, "Continuous enrichment of low-abundance cell samples using standing surface acoustic waves (SSAW)," *Lab on a Chip*, vol. 14, no. 5, pp. 924–930, 2014.
- [40] J. Shi, D. Ahmed, X. Mao, S. C. S. Lin, A. Lawit, and T. J. Huang, "Acoustic tweezers: Patterning cells and microparticles using standing surface acoustic waves (SSAW)," *Lab on a Chip*, vol. 9, no. 20, pp. 2890–2895, 2009.
- [41] F. Gesellchen, A. L. Bernassau, T. Déjardin, D. R. Cumming, and M. O. Riehle, "Cell patterning with a heptagon acoustic tweezer-application in neurite guidance," *Lab on a Chip - Miniaturisation for Chemistry and Biology*, vol. 14, no. 13, pp. 2266–2275, 2014.
- [42] A. Grinenko, C. K. Ong, C. R. P. Courtney, P. D. Wilcox, and B. W. Drinkwater, "Efficient counter-propagating wave acoustic micro-particle manipulation," *Applied Physics Letters*, vol. 101, no. 23, 2012.
- [43] C. Courtney, C. Ong, B. Drinkwater, A. Bernassau, P. Wilcox, and D. Cumming, "Manipulation of particles in two dimensions using phase controllable ultrasonic standing waves," *Proceedings of the Royal Society A*, no. September 2011, pp. 337–360, 2012.
- [44] D. J. Collins, B. Morahan, J. Garcia-Bustos, C. Doerig, M. Plebanski, and A. Neild, "Two-dimensional single-cell patterning with one cell per well driven by surface acoustic waves," *Nature Communications*, vol. 6, pp. 1–11, 2015.
- [45] R. R. Collino, T. R. Ray, R. C. Fleming, C. H. Sasaki, H. Haj-Hariri, and M. R. Begley, "Acoustic field controlled patterning and assembly of anisotropic particles," *Extreme Mechanics Letters*, vol. 5, pp. 37–46, 2015.
- [46] M.-S. Scholz, B. W. Drinkwater, T. M. Llewellyn-Jones, and R. S. Trask, "Counterpropagating Wave Acoustic Particle Manipulation Device for the Effective Manufacture of Composite Materials," *IEEE Transactions on Ultrasonics, Ferroelectrics and Frequency Control*, vol. 62, no. 10, pp. 1845–1855, 2015.
- [47] M. Saito, K. Itagaki, K. Hayashi, and K. Tsubata, "Composite materials with ultrasonically induced layer or lattice structure," *Japanese Journal of Applied Physics, Part 1: Regular Papers and Short Notes and Review Papers*, vol. 38, no. 5 B, pp. 3028–3031, 1999.
- [48] T. M. Llewellyn-Jones, B. W. Drinkwater, and R. S. Trask, "3D printed components with ultrasonically arranged microscale structure," *Smart Materials and Structures*, vol. 25, no. 2, p. 02LT01, 2016.
- [49] L. Cox, A. Croxford, B. W. Drinkwater, and A. Marzo, "Acoustic Lock: Position and orientation trapping of non-spherical sub-wavelength particles in mid-air using a single-axis acoustic levitator," *Applied Physics Letters*, vol. 113, no. 5, p. 054101, 2018.

- [50] D. Foresti, M. Nabavi, M. Klingauf, A. Ferrari, and D. Poulikakos, "Acoustophoretic contactless transport and handling of matter in air," *Proceedings of the National Academy of Sciences*, vol. 110, no. 31, pp. 12549–12554, 2013.
- [51] D. Wichterle, O. Lim, "Hydrophilic gels for biological use," *Nature*, vol. 185, no. 4706, pp. 117–118, 1960.
- [52] P. J. Flory, "Introductory lecture," *Faraday Discussion*, vol. 57, pp. 7–18, 1974.
- [53] M. C. Koetting, J. T. Peters, S. D. Steichen, and N. A. Peppas, "Stimulus-responsive hydrogels: Theory, modern advances, and applications," *Materials Science and Engineering R: Reports*, vol. 93, pp. 1–49, 2015.
- [54] S. J. Buwalda, K. W. M. Boere, P. J. Dijkstra, J. Feijen, T. Vermonden, and W. E. Hennink, "Hydrogels in a historical perspective : From simple networks to smart materials," *Journal of Controlled Release*, vol. 190, pp. 254–273, 2014.
- [55] J. M. Zuidema, C. J. Rivet, R. J. Gilbert, and F. a. Morrison, "A protocol for rheological characterization of hydrogels for tissue engineering strategies," *Journal of Biomedical Materials Research - Part B Applied Biomaterials*, vol. 102, pp. 1063–1073, 2014.
- [56] S. R. Raghavan and J. F. Douglas, "The conundrum of gel formation by molecular nanofibers, wormlike micelles, and filamentous proteins: Gelation without cross-links?," *Soft Matter*, vol. 8, no. 33, pp. 8539–8546, 2012.
- [57] F. A. Morrison, *Understanding Rheology*. Oxford University Press, 2001.
- [58] P. Atkins, "Chapter 8 Consequences of equilibrium," in *The Elements of Physical Chemistry*, pp. 167–182, Oxford University Press, 2003.
- [59] K. J. Bishop, C. E. Wilmer, S. Soh, and B. A. Grzybowski, "Nanoscale forces and their uses in self-assembly," *Small*, vol. 5, no. 14, pp. 1600–1630, 2009.
- [60] P. Atkins, "Chapter 14 The chemical bond," in *The Elements of Physical Chemistry*, pp. 325–349, Oxford University Press, 2003.
- [61] P. Atkins, "Chapter 16 Molecular substances," in *The Elements of Physical Chemistry*, pp. 381–391, Oxford University Press, 2003.
- [62] J. N. Israelachvili, *Intermolecular and Surface Forces*. Elsevier Inc., 2011.
- [63] J. F. Wilkinson, "The extracellular polysaccharides of bacteria," *Bacteriological reviews*, vol. 22, no. 1, pp. 46–73, 1958.

- [64] R. D. Preston, "Polysaccharide Conformation and Cell Wall Function," *Annual Review of Plant Physiology*, vol. 30, no. 1, pp. 55–78, 1979.
- [65] A. Eschenmoser, "Towards a Chemical Etiology of Nucleic Acid Structure," *Origins Life Evol. Biospheres*, vol. 27, no. June, p. 535, 1997.
- [66] P. Hobza and J. Šponer, "Structure, Energetics, and Dynamics of the Nucleic Acid Base Pairs: Nonempirical *Ab Initio* Calculations," *Chemical Reviews*, vol. 99, no. 11, pp. 3247–3276, 1999.
- [67] D. Voet and J. Voet, "Chapter 6," in *Biochemistry*, pp. 124–160, Wiley NY, 3rd ed., 2004.
- [68] P. Terech and R. G. Weiss, "Low Molecular Mass Gelators of Organic Liquids and the Properties of Their Gels," *Chemical Reviews*, vol. 97, no. 8, pp. 3133–3160, 1997.
- [69] L. A. Estroff and A. D. Hamilton, "Water gelation by small organic molecules," *Chemical Reviews*, vol. 104, no. 3, pp. 1201–1217, 2004.
- [70] M. De Loos, B. L. Feringa, and J. H. Van Esch, "Design and application of self-assembled low molecular weight hydrogels," *European Journal of Organic Chemistry*, no. 17, pp. 3615–3631, 2005.
- [71] G. M. Whitesides, J. P. Mathias, and C. T. Seto, "Molecular Self-Assembly and Nanochemistry : A Chemical Strategy for the Synthesis of Nanostructures," *Science*, vol. 254, no. 5036, pp. 1312–1319, 1991.
- [72] A. Z. Cardoso, A. E. Alvarez, B. N. Cattoz, C. Gri, S. M. King, W. J. Frith, and D. J. Adams, "The influence of the kinetics of self-assembly on the properties of dipeptide hydrogels," *Faraday Discussions*, vol. 166, pp. 101–116, 2013.
- [73] R. Weiss and P. Terech, *Molecular Gels*. Springer Netherlands Dordrecht, 2006.
- [74] C. Tomasini and N. Castellucci, "Peptides and peptidomimetics that behave as low molecular weight gelators," *Chemical Society Reviews*, vol. 42, no. 1, pp. 156–172, 2013.
- [75] J. Raeburn, A. Zamith Cardoso, and D. J. Adams, "The importance of the self-assembly process to control mechanical properties of low molecular weight hydrogels.," *Chemical Society reviews*, vol. 42, no. 12, pp. 5143–56, 2013.
- [76] M. Mulvee, N. Vasiljevic, S. Mann, and A. J. Patil, "Construction of supramolecular hydrogels using photo-generated nitric oxide radicals," *Soft Matter*, vol. 14, no. 29, pp. 5950–5954, 2018.

- [77] E. R. Draper, K. L. Morris, M. A. Little, J. Raeburn, C. Colquhoun, E. R. Cross, T. O. McDonald, L. C. Serpell, and D. J. Adams, "Hydrogels formed from Fmoc amino acids," *CrystEngComm*, vol. 17, no. 42, pp. 8047–8057, 2015.
- [78] J. Raeburn, G. Pont, L. Chen, Y. Cesbron, R. Levy, and D. J. Adams, "Fmoc-diphenylalanine hydrogels : understanding the variability in reported mechanical properties," *Soft Matter*, vol. 8, pp. 1168–1174, 2012.
- [79] F. J. M. Hoeben, P. Jonkheijm, E. W. Meijer, and A. P. H. J. Schenning, "About Supramolecular Assemblies of π -Conjugated Systems," *Chemical Reviews*, vol. 105, no. 4, pp. 1491–1546, 2005.
- [80] C. A. Hunter and J. K. Sanders, "The Nature of π - π Interactions," *Journal of the American Chemical Society*, vol. 112, no. 14, pp. 5525–5534, 1990.
- [81] F. Zhao, Y. Gao, J. Shi, H. M. Browdy, and B. Xu, "Novel anisotropic supramolecular hydrogel with high stability over a wide pH range," *Langmuir*, vol. 27, no. 4, pp. 1510–1512, 2011.
- [82] A. Aggeli, I. A. Nyrkova, M. Bell, R. Harding, L. Carrick, T. C. B. McLeish, A. N. Semenov, and N. Boden, "Hierarchical self-assembly of chiral rod-like molecules as a model for peptide -sheet tapes, ribbons, fibrils, and fibers," *Proceedings of the National Academy of Sciences*, vol. 98, no. 21, pp. 11857–11862, 2001.
- [83] H. R. Bungenberg de Jong, H. G., Kruyt, "Coacervation. (Partial miscibility in colloid systems). (Preliminary Communication)," vol. 131, 1929.
- [84] K. Kaibara, T. Okazaki, H. B. Bohidar, and P. Dubin, "pH-induced coacervation in complexes of bovine serum albumin and cationic polyelectrolytes," *Biomacromolecules*, vol. 1, pp. 100–107, 2000.
- [85] C. van Oss, "Coacervation, Complex-Coacervation and Flocculation," *Journal of Dispersion Science and Technology*, vol. 9, no. 5, pp. 561–573, 1988.
- [86] A. Gupta and H. B. Bohidar, "Kinetics of phase separation in systems exhibiting simple coacervation," *Physical Review E - Statistical, Nonlinear, and Soft Matter Physics*, vol. 72, no. February, pp. 1–9, 2005.
- [87] C. G. D. Kruif, F. Weinbreck, and R. D. Vries, "Complex coacervation of proteins and anionic polysaccharides," *Current opinion in Colloid and Interface Science*, vol. 9, pp. 340–349, 2004.
- [88] D. S. Williams, S. Koga, C. R. C. Hak, A. Majrekar, A. J. Patil, A. W. Perriman, and S. Mann, "Polymer/nucleotide droplets as bio-inspired functional micro-compartments," *Soft Matter*, vol. 8, p. 6004, 2012.

- [89] B. Mohanty and H. B. Bohidar, "Systematic of alcohol-induced simple coacervation in aqueous gelatin solutions," *Biomacromolecules*, vol. 4, no. 4, pp. 1080–1086, 2003.
- [90] S. S. Singh, A. K. Siddhanta, R. Meena, K. Prasad, S. Bandyopadhyay, and H. B. Bohidar, "Inter-molecular complexation and phase separation in aqueous solutions of oppositely charged biopolymers," *International Journal of Biological Macromolecules*, vol. 41, no. 2, pp. 185–192, 2007.
- [91] S. Turgeon, C. Schmitt, and C. Sanchez, "Protein-polysaccharide complexes and coacervates," *Current opinion in Colloid and Interface Science*, vol. 12, pp. 166–178, 2007.
- [92] A. Prokop, D. Hunkeler, S. DiMari, M. A. Haralson, and T. G. Wang, "Water Soluble Polymers for Immunoisolation I: Complex Coacervation and Cytotoxicity," *Advances in Polymer Science*, vol. 136, pp. 1–51, 1998.
- [93] C. Schmitt, L. Aberkane, and C. Sanchez, "Protein-polysaccharide complexes and coacervates," *Handbook of Hydrocolloids: Second Edition*, vol. 167, no. 1-2, pp. 420–476, 2009.
- [94] Y. Yeo, E. Bellas, W. Firestone, R. Langer, and D. S. Kohane, "Complex coacervates for thermally sensitive controlled release of flavor compounds," *Journal of Agricultural and Food Chemistry*, vol. 53, no. 19, pp. 7518–7525, 2005.
- [95] C. Peniche, I. Howland, O. Carrillo, C. Zaldívar, and W. Argüelles-Monal, "Formation and stability of shark liver oil loaded chitosan/calcium alginate capsules," *Food Hydrocolloids*, vol. 18, no. 5, pp. 865–871, 2004.
- [96] H. Zhao, C. Sun, R. J. Stewart, and J. H. Waite, "Cement proteins of the tube-building polychaete *Phragmatopoma californica*," *Journal of Biological Chemistry*, vol. 280, no. 52, pp. 42938–42944, 2005.
- [97] C. P. Brangwynne, "Soft active aggregates: Mechanics, dynamics and self-assembly of liquid-like intracellular protein bodies," *Soft Matter*, vol. 7, no. 7, pp. 3052–3059, 2011.
- [98] A. J. Oparin, *Origin of Life*. Dover Publications, 2003.
- [99] S. Mann, "Systems of Creation: The Emergence of Life from Nonliving Matter," *Accounts of chemical research*, vol. 45, no. 12, pp. 2131–2141, 2012.
- [100] A. J. Dzieciol and S. Mann, "Designs for life: protocell models in the laboratory," *Chemical Society Reviews*, vol. 41, no. 1, pp. 79–85, 2012.
- [101] A. P. Minton, "How can biochemical reactions within cells differ from those in test tubes?," *Journal of Cell Science*, vol. 119, pp. 2063–2869, 2006.

- [102] T. Y. D. Tang, M. Antognozzi, J. A. Vicary, A. W. Perriman, and S. Mann, "Small-molecule uptake in membrane-free peptide/nucleotide protocells," *Soft Matter*, vol. 9, no. 31, pp. 7647–7656, 2013.
- [103] S. Koga, D. S. Williams, A. W. Perriman, and S. Mann, "Peptide-nucleotide microdroplets as a step towards a membrane-free protocell model," *Nature chemistry*, vol. 3, no. 9, pp. 720–724, 2011.
- [104] J. Crosby, T. Treadwell, M. Hammerton, K. Vasilakis, M. P. Crump, D. S. Williams, and S. Mann, "Stabilization and enhanced reactivity of actinorhodin polyketide synthase minimal complex in polymer-nucleotide coacervate droplets," *Chemical Communications*, vol. 48, no. 97, pp. 11832–11834, 2012.
- [105] K. Lv, A. W. Perriman, and S. Mann, "Photocatalytic multiphase micro-droplet reactors based on complex coacervation," *Chemical Communications*, vol. 51, no. 41, pp. 8600–8602, 2015.
- [106] E. Sokolova, E. Spruijt, M. M. K. Hansen, E. Dubuc, J. Groen, V. Chokkalingam, A. Piruska, H. A. Heus, and W. T. S. Huck, "Enhanced transcription rates in membrane-free protocells formed by coacervation of cell lysate," *Proceedings of the National Academy of Sciences*, vol. 110, no. 29, pp. 11692–11697, 2013.
- [107] T. Y. Dora. Tang, D. Van Swaay, A. DeMello, J. L. Ross Anderson, and S. Mann, "In vitro gene expression within membrane-free coacervate protocells," *Chemical Communications*, vol. 51, no. 57, pp. 11429–11432, 2015.
- [108] H. B. Bohidar, "Coacervates : A novel state of soft matter - An overview," *Journal of Surface Science and Technology*, vol. 24, no. 3, pp. 105–124, 2008.
- [109] E. Kokufuta, "Functional immobilized biocatalysts," *Progress in Polymer Science*, vol. 17, no. 4, pp. 647–697, 1992.
- [110] J. Xia, K. Mattison, V. Romano, P. L. Dubin, and B. B. Muhoberac, "Complexation of trypsin and alcohol dehydrogenase with poly(diallyldimethylammonium chloride)," *Biopolymers*, vol. 41, no. 4, pp. 359–365, 1997.
- [111] S. Lim, Y. S. Choi, D. G. Kang, Y. H. Song, and H. J. Cha, "The adhesive properties of coacervated recombinant hybrid mussel adhesive proteins," *Biomaterials*, vol. 31, no. 13, pp. 3715–3722, 2010.
- [112] N. R. Johnson and Y. Wang, "Coacervate delivery systems for proteins and small molecule drugs," *Expert Opinion on Drug Delivery*, vol. 11, no. 12, pp. 1829–1832, 2014.
- [113] S. R. Macewan and A. Chilkoti, "Applications of elastin-like polypeptides in drug delivery," *Journal of Controlled Release*, vol. 190, pp. 314–330, 2014.

- [114] A. Grinthal and J. Aizenberg, "Adaptive all the way down: Building responsive materials from hierarchies of chemomechanical feedback," *Chemical Society Reviews*, vol. 42, no. 17, pp. 7072–7085, 2013.
- [115] T. Aida, E. W. Meijer, and S. I. Stupp, "Functional supramolecular polymers," *Science*, vol. 335, no. 6070, pp. 813–817, 2012.
- [116] J. Thiele, Y. Ma, S. M. Bruekers, S. Ma, and W. T. Huck, "25th anniversary article: Designer hydrogels for cell cultures: A materials selection guide," *Advanced Materials*, vol. 26, no. 1, pp. 125–148, 2014.
- [117] R. K. Kumar, M. Li, S. N. Olof, A. J. Patil, and S. Mann, "Artificial cytoskeletal structures within enzymatically active bio-inorganic protocells," *Small*, vol. 9, no. 3, pp. 357–362, 2013.
- [118] R. K. Kumar, R. Harniman, A. J. Patil, and S. Mann, "Self-transformation and structural re-configuration in coacervate-based protocells," *Chemical Science*, vol. 7, pp. 5879–5887, 2016.
- [119] I. Chen, "The emergence of cells during the origin of life," *Science*, vol. 314, pp. 1558–1559, 2006.
- [120] M. R. Guilherme, F. A. Aouada, A. R. Fajardo, A. F. Martins, A. T. Paulino, M. F. Davi, A. F. Rubira, and E. C. Muniz, "Superabsorbent hydrogels based on polysaccharides for application in agriculture as soil conditioner and nutrient carrier: A review," *European Polymer Journal*, vol. 72, pp. 365–385, 2015.
- [121] E. M. Ahmed, "Hydrogel: Preparation, characterization, and applications: A review," *Journal of Advanced Research*, vol. 6, no. 2, pp. 105–121, 2015.
- [122] P. Calvert, "Hydrogels for soft machines," *Advanced Materials*, vol. 21, pp. 743–756, 2009.
- [123] Y. Qiu and K. Park, "Environment-sensitive hydrogels for drug delivery," *Advanced Drug Delivery Reviews*, vol. 64, no. SUPPL., pp. 49–60, 2012.
- [124] P. D. Thornton, R. J. Mart, and R. V. Ulijn, "Enzyme-responsive polymer hydrogel particles for controlled release," *Advanced Materials*, vol. 19, no. 9, pp. 1252–1256, 2007.
- [125] C. V. Taylor, "The contractile vacuole in Euplotes: An example of the sol-gel reversibility of cytoplasm," *Journal of Experimental Zoology*, vol. 37, no. 3, pp. 259–289, 1923.
- [126] M. Suzuki, "An artificial muscle by PVA hydrogel can generate high power close to living skeletal muscles," in *Proceedings of the Annual International Conference of the IEEE Engineering in Medicine and Biology Society*, 1989.

- [127] R. Geryak and V. V. Tsukruk, "Reconfigurable and actuating structures from soft materials.," *Soft matter*, vol. 10, no. 9, pp. 1246–63, 2014.
- [128] D. G. Wallace and J. Rosenblatt, "Collagen gel systems for sustained delivery and tissue engineering," vol. 55, pp. 1631–1649, 2003.
- [129] Y.-M. Kwon, Z. Xia, S. Glyn-Jones, D. Beard, H. S. Gill, and D. W. Murray, "Dose-dependent cytotoxicity of clinically relevant cobalt nanoparticles and ions on macrophages in vitro.," *Biomedical materials (Bristol, England)*, vol. 4, p. 025018, 2009.
- [130] M.-C. Chen, H.-W. Tsai, C.-T. Liu, S.-F. Peng, W.-Y. Lai, S.-J. Chen, Y. Chang, and H.-W. Sung, "A nanoscale drug-entrapment strategy for hydrogel-based systems for the delivery of poorly soluble drugs," *Biomaterials*, vol. 30, pp. 2102–2111, apr 2009.
- [131] P. Gupta, K. Vermani, and S. Garg, "Hydrogels : from controlled release to pH-responsive drug delivery," *Drug Discovery Today*, vol. 7, no. 10, pp. 569–579, 2002.
- [132] Y. J. Chuah, Y. Peck, J. E. J. Lau, H. T. Hee, and D. A. Wang, "Hydrogel based cartilaginous tissue regeneration: Recent insights and technologies," *Biomaterials Science*, vol. 5, no. 4, pp. 613–631, 2017.
- [133] R. A. Stile and K. E. Healy, "Thermo-responsive peptide-modified hydrogels for tissue regeneration," *Biomacromolecules*, vol. 2, no. 1, pp. 185–194, 2001.
- [134] J. N. Hunt, K. E. Feldman, N. a. Lynd, J. Deek, L. M. Campos, J. M. Spruell, B. M. Hernandez, E. J. Kramer, and C. J. Hawker, "Tunable, high modulus hydrogels driven by ionic coacervation," *Advanced Materials*, vol. 23, pp. 2327–2331, 2011.
- [135] S. V. Vlierberghe, P. Dubruel, and E. Schacht, "Biopolymer-Based Hydrogels As Scaffolds for Tissue Engineering Applications : A Review," *ACS Biomacromolecules*, vol. 12, pp. 1387–1408, 2011.
- [136] K. Y. Lee and D. J. Mooney, "Hydrogels for tissue engineering," *Chemical Reviews*, vol. 101, no. 7, pp. 1869–1879, 2001.
- [137] A. Khademhosseini and R. Langer, "Microengineered hydrogels for tissue engineering," *Biomaterials*, vol. 28, no. 34, pp. 5087–5092, 2007.
- [138] B. V. Slaughter, S. S. Khurshid, O. Z. Fisher, A. Khademhosseini, and N. A. Peppas, "Hydrogels in Regenerative Medicine," *Advanced Materials*, vol. 21, pp. 3307–3329, 2009.
- [139] J. L. Drury and D. J. Mooney, "Hydrogels for tissue engineering: scaffold design variables and applications," *Biomaterials*, vol. 24, pp. 4337–4351, 2003.

- [140] H. Tanaka, M. Matsumura, and I. A. Veliky, "Diffusion characteristics of substrates in Calcium alginate gel beads," *Biotechnology and Bioengineering*, vol. 26, no. 1, pp. 53–58, 1984.
- [141] R. Bashir, J. Z. Hilt, O. Elibol, A. Gupta, and N. A. Peppas, "Micromechanical cantilever as an ultrasensitive pH microsensor," *Applied Physics Letters*, vol. 81, pp. 3091–3093, oct 2002.
- [142] A. Richter, G. Paschew, S. Klatt, J. Lienig, K. F. Arndt, and H. J. P. Adler, "Review on hydrogel-based pH sensors and microsensors," *Sensors*, vol. 8, no. 1, pp. 561–581, 2008.
- [143] N. A. Peppas, "Physiologically Responsive Hydrogels," *Journal of Bioactive and Compatible Polymers*, vol. 6, no. 3, 1991.
- [144] F. A. H. Maruyama, H. Matsumoto, T. Fukuda, "Functionalized hydrogel surface patterned in a chip for local pH sensing," in *IEEE 21st International Conference on Microelectromechanical Systems*, 2008.
- [145] S. J. Bryant, T. T. Chowdhury, D. A. Lee, D. L. Bader, and K. S. Anseth, "Crosslinking density influences chondrocyte metabolism in dynamically loaded photocrosslinked poly(ethylene glycol) hydrogels," *Annals of Biomedical Engineering*, vol. 32, no. 3, pp. 407–417, 2004.
- [146] L. M. Weber, C. G. Lopez, and K. S. Anseth, "Effects of PEG hydrogel crosslinking density on protein diffusion and encapsulated islet survival and function.," *Journal of biomedical materials research. Part A*, vol. 90, no. 3, pp. 720–729, 2009.
- [147] K. V. Ranga Rao and K. Padmalatha Devi, "Swelling controlled-release systems: recent developments and applications," *International Journal of Pharmaceutics*, vol. 48, no. 1-3, pp. 1–13, 1988.
- [148] T. Miyata, T. Uragami, and K. Nakamae, "Biomolecule-sensitive hydrogels," *Advanced Drug Delivery Reviews*, vol. 54, no. 1, pp. 79–98, 2002.
- [149] T. Okano, Y. H. Bae, H. Jacobs, and S. W. Kim, "Thermally on-off switching polymers for drug permeation and release," *Journal of Controlled Release*, vol. 11, no. 1-3, pp. 255–265, 1990.
- [150] N. C. Hunt and L. M. Grover, "Cell encapsulation using biopolymer gels for regenerative medicine," pp. 733–742, 2010.
- [151] X. Zhao, A. Papadopoulos, S. Ibusuki, D. A. Bichara, D. B. Saris, J. Malda, K. S. Anseth, T. J. Gill, and M. A. Randolph, "Articular cartilage generation applying PEG-LA-DM/PEGDM copolymer hydrogels," *BMC Musculoskeletal Disorders*, vol. 17, no. 1, pp. 1–10, 2016.
- [152] C. Y. Ko, C. Y. Yang, S. R. Yang, K. L. Ku, C. K. Tsao, D. Chwei-Chin Chuang, I. M. Chu, and M. H. Cheng, "Cartilage formation through alterations of amphiphilicity of poly(ethylene glycol)-poly(caprolactone) copolymer hydrogels," *RSC Advances*, vol. 3, no. 48, pp. 25769–25779, 2013.

- [153] J.-Y. Sun, X. Zhao, W. R. K. Illeperuma, O. Chaudhuri, K. H. Oh, D. J. Mooney, J. J. Vlassak, and Z. Suo, "Highly stretchable and tough hydrogels," *Nature*, vol. 489, no. 7414, pp. 133–136, 2012.
- [154] S. Lin, H. Yuk, T. Zhang, G. A. Parada, H. Koo, C. Yu, and X. Zhao, "Stretchable Hydrogel Electronics and Devices," *Advanced Materials*, pp. 1–9, 2015.
- [155] K. Yasuda, J. P. Gong, Y. Katsuyama, A. Nakayama, Y. Tanabe, E. Kondo, M. Ueno, and Y. Osada, "Biomechanical properties of high-toughness double network hydrogels," *Biomaterials*, vol. 26, pp. 4468–4475, 2005.
- [156] J. P. Gong, Y. Katsuyama, T. Kurokawa, and Y. Osada, "Double-network hydrogels with extremely high mechanical strength," *Advanced Materials*, vol. 15, no. 14, pp. 1155–1158, 2003.
- [157] A. S. Hoffman, "Hydrogels for biomedical applications," *Advanced Drug Delivery Reviews*, vol. 64, pp. 18–23, dec 2012.
- [158] M. S. Hahn, L. J. Taite, J. J. Moon, M. C. Rowland, K. A. Ruffino, and J. L. West, "Photolithographic patterning of polyethylene glycol hydrogels," *Biomaterials*, vol. 27, no. 12, pp. 2519–2524, 2006.
- [159] M. B. Applegate, J. Coburn, B. P. Partlow, J. E. Moreau, J. P. Mondia, B. Marelli, D. L. Kaplan, and F. G. Omenetto, "Laser-based three-dimensional multiscale micropatterning of biocompatible hydrogels for customized tissue engineering scaffolds," *Proceedings of the National Academy of Sciences*, vol. 112, no. 39, pp. 12052–12057, 2015.
- [160] Z. J. Wang, C. N. Zhu, W. Hong, Z. Liang Wu, and Q. Zheng, "Cooperative deformations of periodically patterned hydrogels," *Science Advances*, vol. 3, no. 9, pp. 1–9, 2017.
- [161] M. Guvendiren, S. Yang, and J. A. Burdick, "Swelling-Induced surface patterns in hydrogels with gradient crosslinking density," *Advanced Functional Materials*, vol. 19, no. 19, pp. 3038–3045, 2009.
- [162] D. M. Kirchmayer, R. Gorkin, and M. In Het Panhuis, "An overview of the suitability of hydrogel-forming polymers for extrusion-based 3D-printing," *Journal of Materials Chemistry B*, vol. 3, no. 20, pp. 4105–4117, 2015.
- [163] J. P. Armstrong, M. Burke, B. M. Carter, S. A. Davis, and A. W. Perriman, "3D Bioprinting Using a Templated Porous Bioink," *Advanced Healthcare Materials*, vol. 5, no. 14, pp. 1724–1730, 2016.
- [164] L. E. Bertassoni, M. Cecconi, V. Manoharan, M. Nikkhah, J. Hjortnaes, A. L. Cristino, G. Barabaschi, D. Demarchi, M. R. Dokmeci, Y. Yang, and A. Khademhosseini, "Hydrogel bioprinted microchannel networks for vascularization of tissue engineering constructs," *Lab on a Chip*, vol. 14, no. 13, pp. 2202–2211, 2014.

- [165] A. N. Stachowiak, A. Bershteyn, E. Tzatzalos, and D. J. Irvine, "Bioactive hydrogels with an ordered cellular structure combine interconnected macroporosity and robust mechanical properties," *Advanced Materials*, vol. 17, no. 4, pp. 399–403, 2005.
- [166] E. Palleau, D. Morales, M. D. Dickey, and O. D. Velev, "Reversible patterning and actuation of hydrogels by electrically assisted ionoprinting," *Nature Communications*, vol. 4, pp. 1–7, 2013.
- [167] T.-Y. Liu, S.-H. Hu, T.-Y. Liu, D.-M. Liu, and S.-Y. Chen, "Magnetic-sensitive behavior of intelligent ferrogels for controlled release of drug," *Langmuir*, vol. 22, pp. 5974–5978, 2006.
- [168] M. T. Lopez-lopez, G. Scionti, A. C. Oliveira, J. D. G. Duran, A. Campos, M. Alaminos, and I. A. Rodriguez, "Generation and Characterization of Novel Magnetic Field-Responsive Biomaterials," *PLoS ONE*, pp. 1–17, 2015.
- [169] J. A. Burdick, A. Khademhosseini, and R. Langer, "Fabrication of gradient hydrogels using a microfluidics/photopolymerization process," *Langmuir*, vol. 20, no. 13, pp. 5153–5156, 2004.
- [170] R. G. Kirste, W. A. Kruse, and K. Ibel, "Determination of the conformation of polymers in the amorphous solid state and in concentrated solution by neutron diffraction," *Polymer*, vol. 16, no. 2, pp. 120–124, 1975.
- [171] D. Huh, K. L. Mills, X. Zhu, M. A. Burns, M. D. Thouless, and S. Takayama, "Tuneable elastomeric nanochannels for nanofluidic manipulation," *Nature Materials*, vol. 6, no. 6, pp. 424–428, 2007.
- [172] M.-y. Chiang, Y.-w. Hsu, H.-y. Hsieh, S.-y. Chen, and S.-k. Fan, "Constructing 3D heterogeneous hydrogels from electrically manipulated prepolymer droplets and crosslinked microgels," no. October, pp. 1–9, 2016.
- [173] A. Pich, S. Bhattacharya, Y. Lu, V. Boyko, and H. J. P. Adler, "Temperature-sensitive hybrid microgels with magnetic properties," *Langmuir*, vol. 20, no. 24, pp. 10706–10711, 2004.
- [174] J. K. Oh, R. Drumright, D. J. Siegwart, and K. Matyjaszewski, "The development of microgels/nanogels for drug delivery applications," *Progress in Polymer Science (Oxford)*, vol. 33, no. 4, pp. 448–477, 2008.
- [175] A. K. Gaharwar, N. A. Peppas, and A. Khademhosseini, "Nanocomposite hydrogels for biomedical applications," *Biotechnology and Bioengineering*, vol. 111, no. 3, pp. 441–453, 2014.
- [176] L. Bonanno and E. Segal, "Nanostructured porous silicon-polymer based hybrids: from biosensing to drug delivery," *Nanomedicine*, vol. 6, no. 10, 2011.

- [177] H. Dehne, F. M. Hecht, and A. R. Bausch, "The mechanical properties of polymer-colloid hybrid hydrogels," *Soft Matter*, vol. 13, no. 27, pp. 4786–4790, 2017.
- [178] K. A. Garvin, D. C. Hocking, and D. Dalecki, "Controlling the spatial organization of cells and extracellular matrix proteins in engineered tissues using ultrasound standing wave fields," *Ultrasound in Medicine and Biology*, vol. 36, no. 11, pp. 1919–1932, 2010.
- [179] L. Gherardini, C. M. Cousins, J. J. Hawkes, J. Spengler, S. Radel, H. Lawler, B. Devcic-Kuhar, M. Gröschl, W. T. Coakley, and A. J. McLoughlin, "A new immobilisation method to arrange particles in a gel matrix by ultrasound standing waves," *Ultrasound in Medicine and Biology*, vol. 31, no. 2, pp. 261–272, 2005.
- [180] K. A. Garvin, J. VanderBurgh, D. C. Hocking, and D. Dalecki, "Controlling collagen fiber microstructure in three-dimensional hydrogels using ultrasound," *The Journal of the Acoustical Society of America*, vol. 134, no. 2, pp. 1491–1502, 2013.
- [181] M. Li, X. Huang, T.-Y. D. Tang, and S. Mann, "Synthetic cellularity based on non-lipid microcompartments and protocell models," *Current Opinion in Chemical Biology*, vol. 22, pp. 1–11, 2014.
- [182] X. Huang and B. Voit, "Progress on multi-compartment polymeric capsules," *Polymer Chemistry*, vol. 4, no. 3, pp. 435–443, 2013.
- [183] X. Huang, M. Li, D. C. Green, D. S. Williams, A. J. Patil, and S. Mann, "Interfacial assembly of protein-polymer nano-conjugates into stimulus-responsive biomimetic protocells," *Nature Communications*, vol. 4, no. May, pp. 1–9, 2013.
- [184] A. D. Dinsmore, M. F. Hsu, M. G. Nikolaidis, M. Marquez, A. R. Bausch, and D. A. Weitz, "Colloidosomes: Selectively permeable capsules composed of colloidal particles," *Science*, vol. 298, no. November, pp. 1006–1009, 2002.
- [185] L. Tian, N. Martin, P. G. Bassindale, A. J. Patil, M. Li, A. Barnes, B. W. Drinkwater, and S. Mann, "Spontaneous assembly of chemically encoded two-dimensional coacervate droplet arrays by acoustic wave patterning," *Nature Communications*, vol. 7, no. May, pp. 1–10, 2016.
- [186] Leica Microsystems, "Step by Step Guide to Fluorescence microscopy."
- [187] Horiba Scientific, "Dynamic Light Scattering Technology."
- [188] Malvern Instruments Ltd, "What is the Zetasizer Nano?," in *Zetasizer Nano Series User Manual*, p. 2.2, Malvern Instruments Ltd., 2004.
- [189] JEOL, "Scanning Electron Microscope A To Z," *Serving Advanced Technology*, p. 32, 2006.

- [190] H. A. Barnes, J. Hutton, and K. Walters, *An introduction to Rheology*. London:Elsevier, 1989.
- [191] H. Förster, “UV/Vis Spectroscopy,” in *Characterization I. Molecular Sieves – Science and Technology*, p. 339, Springer, Berlin, Heidelberg, 2004.
- [192] Malvern Panalytical, “Differential Scanning Calorimetry.”
- [193] M. Faraday, “On a peculiar class of acoustical figures; and on certain forms assumed by groups of particles upon vibrating elastic surfaces,” *Philosophical transactions of the Royal Society of London*, vol. 121, pp. 299–340, 1831.
- [194] A. Kundt, “Acoustic experiments,” *The London, Edinburgh, and Dublin Philosophical Magazine and Journal of Science*, vol. 35, no. 234, pp. 41–48, 1868.
- [195] A. Kundt, ““Über eine neue art akustischer staubfiguren und uber die anwendung derselben zur bestimmung der schallgeschwindigkeit in festen korpern und gasen,” *Annalen der Physik*, vol. 203, no. 4, pp. 497–523, 1866.
- [196] L. V. L. King, “On the acoustic radiation pressure on spheres,” *Proceedings of the Royal Society of London. Series A - Mathematical and Physical Sciences*, vol. 147, no. 861, pp. 212–240, 1934.
- [197] K. Yosioka and Y. Kawasima, “Acoustic radiation pressure on a compressible sphere,” *Acustica*, vol. 5, no. 3, pp. 167–173, 1955.
- [198] L. P. Gorkov, “On the forces acting on a small particle in an acoustical field in an ideal fluid,” *Soviet Physics Doklady*, vol. 6, no. 9, pp. 773–775, 1962.
- [199] A. Lenshof, C. Magnusson, and T. Laurell, “Acoustofluidics 8: Applications of acoustophoresis in continuous flow microsystems,” *Lab on a Chip*, vol. 12, no. 7, pp. 1210–1223, 2012.
- [200] H. Bruus, “Acoustofluidics 7: The acoustic radiation force on small particles,” 2012.
- [201] E. A. Weiser, M. A. H.; Apfel, R. E.; Neppiras, “Interparticle Forces on Red Cells in a Standing Wave Field,” *Acustica*, vol. 56, no. 1984, pp. 114–119.
- [202] G. Memoli, C. R. Fury, K. O. Baxter, P. N. Gélat, and P. H. Jones, “Acoustic force measurements on polymer-coated microbubbles in a microfluidic device,” *The Journal of the Acoustical Society of America*, vol. 141, no. 5, pp. 3364–3378, 2017.
- [203] B. Drinkwater, “Dynamic-field devices for the ultrasonic manipulation of microparticles,” *Lab on a Chip*, 2016.

- [204] O. Manneberg, J. Svennebring, H. M. Hertz, and M. Wiklund, "Wedge transducer design for two-dimensional ultrasonic manipulation in a microfluidic chip," *Journal of Micromechanics and Microengineering*, vol. 18, no. 9, 2008.
- [205] I. Leibacher, P. Reichert, and J. Dual, "Microfluidic droplet handling by bulk acoustic wave (BAW) acoustophoresis," *Lab on a Chip*, vol. 15, no. 13, pp. 2896–2905, 2015.
- [206] S. C. S. Lin, X. Mao, and T. J. Huang, "Surface acoustic wave (SAW) acoustophoresis: Now and beyond," *Lab on a Chip*, vol. 12, no. 16, pp. 2766–2770, 2012.
- [207] G. Destgeer and H. J. Sung, "Recent advances in microfluidic actuation and micro-object manipulation via surface acoustic waves," *Lab on a Chip*, vol. 15, no. 13, pp. 2722–2738, 2015.
- [208] J. Lee, S. Y. Teh, A. Lee, H. H. Kim, C. Lee, and K. K. Shung, "Single beam acoustic trapping," *Applied Physics Letters*, vol. 95, no. 7, 2009.
- [209] J. Lee, C. Lee, and K. K. Shung, "Calibration of sound forces in acoustic traps," *IEEE Transactions on Ultrasonics, Ferroelectrics, and Frequency Control*, vol. 57, no. 10, pp. 2305–2310, 2010.
- [210] P. Glynne-Jones, C. E. Démoré, C. Ye, Y. Qiu, S. Cochran, and M. Hill, "Array-controlled ultrasonic manipulation of particles in planar acoustic resonator," *IEEE Transactions on Ultrasonics, Ferroelectrics, and Frequency Control*, vol. 59, no. 6, pp. 1258–1266, 2012.
- [211] P. Glynne-Jones, R. J. Boltryk, and M. Hill, "Acoustofluidics 9: Modelling and applications of planar resonant devices for acoustic particle manipulation," *Lab on a Chip*, vol. 12, pp. 1417–1426, 2012.
- [212] C. R. Courtney, C. K. Ong, B. W. Drinkwater, P. D. Wilcox, C. Demore, S. Cochran, P. Glynne-Jones, and M. Hill, "Manipulation of microparticles using phase-controllable ultrasonic standing waves," *Journal of the Acoustic Society of America*, vol. 128, no. 4, 2010.
- [213] P. Bhaskar, *The Development of an Acousto-Optical Trapping System*. PhD thesis, 2018.
- [214] P. Atkins, T. Overton, J. Rourke, M. Weller, and F. Armstrong, *Inorganic Chemistry*. Oxford University Press, 2006.
- [215] "COMSOL Multiphysics Cyclopedia."
- [216] T. Gomez, "Acoustic Impedance Matching of Piezoelectric," *IEEE Transactions on Ultrasonics, Ferroelectrics and Frequency Control*, vol. 51, no. 5, pp. 624–633, 2004.
- [217] M. Wiklund, R. Green, and M. Ohlin, "Acoustofluidics 14: Applications of acoustic streaming in microfluidic devices," *Lab on a Chip*, vol. 12, no. 14, p. 2438, 2012.

- [218] J. F. Spengler and W. T. Coakley, "Ultrasonic trap to monitor morphology and stability of developing microparticle aggregates," *Langmuir*, vol. 19, no. 9, pp. 3635–3642, 2003.
- [219] L. a. Kuznetsova and W. T. Coakley, "Microparticle concentration in short path length ultrasonic resonators: Roles of radiation pressure and acoustic streaming," *The Journal of the Acoustical Society of America*, vol. 116, no. October 2004, p. 1956, 2004.
- [220] P. G. Bassindale, D. B. Phillips, A. C. Barnes, and B. W. Drinkwater, "Measurements of the force fields within an acoustic standing wave using holographic optical tweezers," *Applied Physics Letters*, vol. 104, no. 16, 2014.
- [221] M. Wiklund and H. M. Hertz, "Ultrasonic enhancement of bead-based bioaffinity assays," *Lab on a Chip*, vol. 6, no. 10, pp. 1279–1292, 2006.
- [222] M. Bengtsson and T. Laurell, "Ultrasonic agitation in microchannels," *Analytical and Bioanalytical Chemistry*, vol. 378, no. 7, pp. 1716–1721, 2004.
- [223] J. A. Frangos, L. V. McIntire, and S. G. Eskin, "Shear stress induced stimulation of mammalian cell metabolism," *Biotechnology and Bioengineering*, vol. 32, no. 8, pp. 1053–1060, 1988.
- [224] D. L. Miller and J. Quddus, "Sonoporation of monolayer cells by diagnostic ultrasound activation of contrast-agent gas bodies," *Ultrasound in Medicine and Biology*, vol. 26, no. 4, pp. 661–667, 2000.
- [225] M. Caleap and B. W. Drinkwater, "Acoustically trapped colloidal crystals that are reconfigurable in real time," vol. 111, no. 17, pp. 6226–6230, 2014.
- [226] N. Huebsch, C. J. Kearney, X. Zhao, J. Kim, C. A. Cezar, Z. Suo, and D. J. Mooney, "Ultrasound-triggered disruption and self-healing of reversibly cross-linked hydrogels for drug delivery and enhanced chemotherapy," *Proceedings of the National Academy of Sciences*, vol. 111, no. 27, pp. 9762–9767, 2014.
- [227] D. J. Adams, M. F. Butler, W. J. Frith, M. Kirkland, L. Mullen, and P. Sanderson, "A new method for maintaining homogeneity during liquid–hydrogel transitions using low molecular weight hydrogelators," *Soft Matter*, vol. 5, no. 9, p. 1856, 2009.
- [228] G. Memoli, K. O. Baxter, H. G. Jones, K. P. Mingard, and B. Zeqiri, "Acoustofluidic measurements on polymer-coated microbubbles: Primary and secondary Bjerknes forces," *Micromachines*, vol. 9, no. 8, 2018.
- [229] N. Martin, M. Li, and S. Mann, "Selective Uptake and Refolding of Globular Proteins in Coacervate Microdroplets," *Langmuir*, vol. 32, no. 23, pp. 5881–5889, 2016.

- [230] J. P. Armstrong, S. N. Olof, M. D. Jakimowicz, A. P. Hollander, S. Mann, S. A. Davis, M. J. Miles, A. J. Patil, and A. W. Perriman, "Cell paintballing using optically targeted coacervate microdroplets," *Chemical Science*, vol. 6, no. 11, pp. 6106–6111, 2015.
- [231] D. Garenne, L. Beven, L. Navailles, F. Nallet, E. J. Dufourc, and J. P. Douliez, "Sequestration of Proteins by Fatty Acid Coacervates for Their Encapsulation within Vesicles," *Angewandte Chemie - International Edition*, vol. 55, no. 43, pp. 13475–13479, 2016.
- [232] D. S. Williams, A. J. Patil, and S. Mann, "Spontaneous structuration in coacervate-based protocells by polyoxometalate-mediated membrane assembly," *Small (Weinheim an der Bergstrasse, Germany)*, vol. 10, no. 9, pp. 1830–40, 2014.
- [233] R. Chollakup, J. B. Beck, K. Dirnberger, M. Tirrell, and C. D. Eisenbach, "Polyelectrolyte molecular weight and salt effects on the phase behavior and coacervation of aqueous solutions of poly(acrylic acid) sodium salt and poly(allylamine) hydrochloride," *Macromolecules*, vol. 46, no. 6, pp. 2376–2390, 2013.
- [234] S. L. Perry, Y. Li, D. Priftis, L. Leon, and M. Tirrell, "The effect of salt on the complex coacervation of vinyl polyelectrolytes," *Polymers*, vol. 6, no. 6, pp. 1756–1772, 2014.
- [235] Y. Wang, K. Kimura, P. L. Dubin, and W. Jaeger, "Polyelectrolyte-micelle coacervation: Effects of micelle surface charge density, polymer molecular weight, and polymer/surfactant ratio," *Macromolecules*, vol. 33, no. 9, pp. 3324–3331, 2000.
- [236] M. Li, D. C. Green, J. L. R. Anderson, B. P. Binks, and S. Mann, "In vitro gene expression and enzyme catalysis in bio-inorganic protocells," *Chemical Science*, vol. 2, no. 9, p. 1739, 2011.
- [237] M. P. Lutolf, "Integration column: Artificial ECM: Expanding the cell biology toolbox in 3D," *Integrative Biology*, vol. 1, no. 3, pp. 235–241, 2009.
- [238] S. P. Zustiak and J. B. Leach, "Hydrolytically degradable poly(ethylene glycol) hydrogel scaffolds with tunable degradation and mechanical properties," *Biomacromolecules*, vol. 11, no. 5, pp. 1348–1357, 2010.
- [239] N. E. Fedorovich, J. Alblas, J. R. de Wijn, W. E. Hennink, A. J. Verbout, and W. J. Dhert, "Hydrogels as Extracellular Matrices for Skeletal Tissue Engineering: State-of-the-Art and Novel Application in Organ Printing," *Tissue Engineering*, vol. 13, no. 8, pp. 1905–1925, 2007.
- [240] P. Krsko and M. Libera, "Biointeractive hydrogels," *Materials Today*, vol. 8, no. 12, pp. 36–44, 2005.
- [241] S. H. Lee, J. S. Miller, J. J. Moon, and J. L. West, "Proteolytically degradable hydrogels with a fluorogenic substrate for studies of cellular proteolytic activity and migration," *Biotechnology Progress*, vol. 21, no. 6, pp. 1736–1741, 2005.

- [242] D. Gao, X. Hao, M. A. Philbert, and R. Kopelman, "Bioeliminable nanohydrogels for drug delivery," *Nano Letters*, vol. 8, no. 10, pp. 3320–3324, 2008.
- [243] J. D. Kretlow, L. Klouda, and A. G. Mikos, "Injectable matrices and scaffolds for drug delivery in tissue engineering," *Advanced Drug Delivery Reviews*, vol. 59, no. 4-5, pp. 263–273, 2007.
- [244] J. P. Vacanti and R. Langer, "Tissue engineering: the design and fabrication of living replacement devices for surgical reconstruction and transplantation," *The Lancet*, vol. 354, pp. S32–S34, 1999.
- [245] T. R. Hoare and D. S. Kohane, "Hydrogels in drug delivery: Progress and challenges," *Polymer*, vol. 49, no. 8, pp. 1993–2007, 2008.
- [246] J. Jagur-Grodzinski, "Polymeric gels and hydrogels for biomedical and pharmaceutical applications," *Polymers for Advanced Technologies*, vol. 21, no. 1, pp. 27–47, 2010.
- [247] S. Khetan and J. A. Burdick, "Patterning hydrogels in three dimensions towards controlling cellular interactions," *Soft Matter*, vol. 7, p. 830, 2011.
- [248] W. Lee, V. Lee, S. Polio, P. Keegan, J. H. Lee, K. Fischer, J. K. Park, and S. S. Yoo, "On-demand three-dimensional freeform fabrication of multi-layered hydrogel scaffold with fluidic channels," *Biotechnology and Bioengineering*, vol. 105, no. 6, pp. 1178–1186, 2010.
- [249] S. Hong, D. Sycks, H. F. ai Chan, S. Lin, G. P. Lopez, F. Guilak, K. W. Leong, and X. Zhao, "3D Printing: 3D Printing of Highly Stretchable and Tough Hydrogels into Complex, Cellularized Structures," *Advanced materials (Deerfield Beach, Fla.)*, vol. 27, no. 27, p. 4034, 2015.
- [250] I. Tokarev and S. Minko, "Stimuli-responsive hydrogel thin films," *Soft Matter*, vol. 5, no. 3, pp. 511–524, 2009.
- [251] Y. Xu, Z. Lin, X. Huang, Y. Liu, Y. Huang, and X. Duan, "Flexible solid-state supercapacitors based on three-dimensional graphene hydrogel films," *ACS Nano*, vol. 7, no. 5, pp. 4042–4049, 2013.
- [252] J. T. Suri, D. B. Cordes, F. E. Cappuccio, R. A. Wessling, and B. Singaram, "Continuous Glucose Sensing with a Fluorescent Thin-Film Hydrogel," *Angewandte Chemie - International Edition*, vol. 42, no. 47, pp. 5857–5859, 2003.
- [253] S. R. Caliali and J. A. Burdick, "A practical guide to hydrogels for cell culture," *Nature methods*, vol. 13, no. 5, pp. 405–414, 2016.
- [254] D. Buenger, F. Topuz, and J. Groll, "Hydrogels in sensing applications," *Progress in Polymer Science*, vol. 37, no. 12, pp. 1678–1719, 2012.

- [255] M. Nakahata, E. Gantumur, K. Furuno, S. Sakai, and M. Taya, "Versatility of hydrogelation by dual-enzymatic reactions with oxidases and peroxidase," *Biochemical Engineering Journal*, vol. 131, pp. 1–8, 2018.
- [256] S. F. M. Van Dongen, M. Nallani, J. J. L. M. Cornelissen, R. J. M. Nolte, and J. C. M. Van Hest, "A three-enzyme cascade reaction through positional assembly of enzymes in a polymersome nanoreactor," *Chemistry - A European Journal*, vol. 15, no. 5, pp. 1107–1114, 2009.
- [257] V. Linko, M. Eerikäinen, and M. A. Kostianen, "A modular DNA origami-based enzyme cascade nanoreactor," *Chemical Communications*, vol. 51, no. 25, pp. 5351–5354, 2015.
- [258] J. Crosby, T. Treadwell, M. Hammerton, K. Vasilakis, M. P. Crump, D. S. Williams, and S. Mann, "Stabilization and enhanced reactivity of actinorhodin polyketide synthase minimal complex in polymer–nucleotide coacervate droplets," 2012.
- [259] T. M. Valentin, S. E. Leggett, P.-Y. Chen, J. K. Sodhi, L. H. Stephens, H. D. McClintock, J. Y. Sim, and I. Y. Wong, "Stereolithographic Printing of Ionically-Crosslinked Alginate Hydrogels for Degradable Biomaterials and Microfluidics," *Lab Chip*, vol. 17, pp. 3474–3488, 2017.
- [260] E. Jabbarzadeh, T. Starnes, Y. M. Khan, T. Jiang, A. J. Wirtel, M. Deng, Q. Lv, L. S. Nair, S. B. Doty, and C. T. Laurencin, "Induction of angiogenesis in tissue-engineered scaffolds designed for bone repair: a combined gene therapy-cell transplantation approach.," *Proceedings of the National Academy of Sciences of the United States of America*, vol. 105, no. 32, pp. 11099–11104, 2008.
- [261] N. A. Peppas, J. Z. Hilt, A. Khademhosseini, and R. Langer, "Hydrogels in biology and medicine: From molecular principles to bionanotechnology," *Advanced Materials*, vol. 18, no. 11, pp. 1345–1360, 2006.
- [262] V. L. Tsang, A. A. Chen, L. M. Cho, K. D. Jadin, R. L. Sah, S. DeLong, J. L. West, and S. N. Bhatia, "Fabrication of 3D hepatic tissues by additive photopatterning of cellular hydrogels," *The FASEB Journal*, vol. 21, no. 3, pp. 790–801, 2007.
- [263] M. W. Tibbitt and K. S. Anseth, "Hydrogels as extracellular matrix mimics for 3D cell culture," *Biotechnology and Bioengineering*, vol. 103, no. 4, pp. 655–663, 2009.
- [264] I. M. El-Sherbiny, E. M. Abdel-Bary, and D. R. K. Harding, "Swelling characteristics and in vitro drug release study with pH- and thermally sensitive hydrogels based on modified chitosan," *Journal of Applied Polymer Science*, vol. 102, no. 2, pp. 977–985, 2006.
- [265] E. Rouslahti and M. D. Pierschbacher, "New Perspectives in Cell Adhesion: RGD and Integrins," *Science*, vol. 238, pp. 491–497, 1987.

- [266] T. M. Allen, "Ligand-targeted therapeutics in anticancer therapy," *Nature Reviews Cancer*, vol. 2, no. 10, pp. 750–763, 2002.
- [267] T. Lammers, W. E. Hennink, and G. Storm, "Tumour-targeted nanomedicines: Principles and practice," *British Journal of Cancer*, vol. 99, no. 3, pp. 392–397, 2008.
- [268] L. M. Bareford and P. W. Swaan, "Endocytic mechanisms for targeted drug delivery," *Advanced Drug Delivery Reviews*, vol. 59, no. 8, pp. 748–758, 2007.
- [269] R. R. Breaker, "Natural and engineered nucleic acids as tools to explore biology," *Nature*, vol. 432, no. 7019, pp. 838–845, 2004.
- [270] Bello Lectures, "Nucleotides," 2009.
- [271] M. R. Jones, N. C. Seeman, and C. A. Mirkin, "Programmable materials and the nature of the DNA bond," *Science*, vol. 347, no. 6224, 2015.
- [272] F. A. Aldaye, A. L. Palmer, and H. F. Sleiman, "Assembling Materials with DNA as the Guide," *Science*, vol. 321, no. September, pp. 1795–1799, 2008.
- [273] M. A. Clark, R. A. Acharya, C. C. Arico-Muendel, S. L. Belyanskaya, D. R. Benjamin, N. R. Carlson, P. A. Centrella, C. H. Chiu, S. P. Creaser, J. W. Cuzzo, C. P. Davie, Y. Ding, G. J. Franklin, K. D. Franzen, M. L. Gefter, S. P. Hale, N. J. Hansen, D. I. Israel, J. Jiang, M. J. Kavarana, M. S. Kelley, C. S. Kollmann, F. Li, K. Lind, S. Mataruse, P. F. Medeiros, J. A. Messer, P. Myers, H. O'Keefe, M. C. Oliff, C. E. Rise, A. L. Satz, S. R. Skinner, J. L. Svendsen, L. Tang, K. Van Vloten, R. W. Wagner, G. Yao, B. Zhao, and B. A. Morgan, "Design, synthesis and selection of DNA-encoded small-molecule libraries," *Nature Chemical Biology*, vol. 5, no. 9, pp. 647–654, 2009.
- [274] G. M. Whitesides and B. Grzybowski, "Self-assembly at all scales," *Science (New York, N.Y.)*, vol. 295, no. 5564, pp. 2418–2421, 2002.
- [275] J.-M. Lehn, "Toward Self-Organization and Complex Matter," vol. 295, no. March, pp. 2400–2404, 2002.
- [276] S. Fleming and R. V. Ulijn, "Design of nanostructures based on aromatic peptide amphiphiles," *Chemical Society Reviews*, vol. 43, no. 23, pp. 8150–8177, 2014.
- [277] T. Liebmann, S. Rydholm, V. Akpe, and H. Brismar, "Self-assembling Fmoc dipeptide hydrogel for in situ 3D cell culturing," *BMC Biotechnology*, vol. 7, pp. 1–11, 2007.
- [278] V. Jayawarna, M. Ali, T. A. Jowitt, A. F. Miller, A. Saiani, J. E. Gough, and R. V. Ulijn, "Nanostructured hydrogels for three-dimensional cell culture through self-assembly of fluorenylmethoxycarbonyl-dipeptides," *Advanced Materials*, vol. 18, no. 5, pp. 611–614, 2006.

- [279] V. Jayawarna, A. Smith, J. E. Gough, and R. V. Ulijn, "Three-dimensional cell culture of chondrocytes on modified di-phenylalanine scaffolds," *Biochemical Society transactions*, vol. 35, no. Pt 3, pp. 535–7, 2007.
- [280] G. L. Fiore, J. L. Klinkenberg, A. Pfister, and C. L. Fraser, "Iron tris(bipyridine) PEG hydrogels with covalent and metal coordinate cross-links," *Biomacromolecules*, vol. 10, no. 1, pp. 128–133, 2009.
- [281] S. J. Buwalda, P. J. Dijkstra, and J. Feijen, "Poly(ethylene glycol)-poly(L -lactide) star block copolymer hydrogels crosslinked by metal-ligand coordination," *Journal of Polymer Science, Part A: Polymer Chemistry*, vol. 50, no. 9, pp. 1783–1791, 2012.
- [282] D. E. Fullenkamp, L. He, D. G. Barrett, W. R. Burghardt, and P. B. Messersmith, "Mussel-inspired histidine-based transient network metal coordination hydrogels," *Macromolecules*, vol. 46, no. 3, pp. 1167–1174, 2013.
- [283] E. A. Appel, J. del Barrio, X. J. Loh, and O. A. Scherman, "Supramolecular polymeric hydrogels," *Chemical Society Reviews*, vol. 41, p. 6195, 2012.
- [284] F. Fages, "Metal coordination to assist molecular gelation," *Angewandte Chemie - International Edition*, vol. 45, no. 11, pp. 1680–1682, 2006.
- [285] S. Basak, J. Nanda, and A. Banerjee, "Multi-stimuli responsive self-healing metallo-hydrogels: Tuning of the gel recovery property," *Chemical Communications*, vol. 50, no. 18, pp. 2356–2359, 2014.
- [286] G. O. Lloyd and J. W. Steed, "Anion-tuning of supramolecular gel properties," *Nature Chemistry*, vol. 1, no. 6, pp. 437–442, 2009.
- [287] J. A. Foster and J. W. Steed, "Exploiting cavities in supramolecular gels," *Angewandte Chemie - International Edition*, vol. 49, no. 38, pp. 6718–6724, 2010.
- [288] J. Della Rocca, D. Liu, and W. Lin, "Nanoscale metal-organic frameworks for biomedical imaging and drug delivery," *Accounts of Chemical Research*, vol. 44, no. 10, pp. 957–968, 2011.
- [289] F. R. Kersey, D. M. Loveless, and S. L. Craig, "A hybrid polymer gel with controlled rates of cross-link rupture and self-repair," *Journal of the Royal Society Interface*, vol. 4, no. 13, pp. 373–380, 2007.
- [290] J. T. Davis, "G-Quartets 40 Years Later: From 5-GMP to Molecular Biology and Supramolecular Chemistry," *Angewandte Chemie - International Edition*, vol. 43, no. 6, pp. 668–698, 2004.
- [291] H. Liang, Z. Zhang, Q. Yuan, and J. Liu, "SI Self-healing metal-coordinated hydrogels using nucleotide ligands," *Chem. Commun.*, vol. 51, no. 82, pp. 15196–15199, 2015.

- [292] R. N. Das, Y. P. Kumar, S. Pagoti, A. J. Patil, and J. Dash, "Diffusion and birefringence of bioactive dyes in a supramolecular guanosine hydrogel," *Chemistry - A European Journal*, vol. 18, no. 19, pp. 6008–6014, 2012.
- [293] L. E. Buerkle, Z. Li, A. M. Jamieson, and S. J. Rowan, "Tailoring the properties of guanosine-based supramolecular hydrogels," *Langmuir*, vol. 25, no. 15, pp. 8833–8840, 2009.
- [294] M. Dash, F. Chiellini, R. M. Ottenbrite, and E. Chiellini, "Chitosan - A versatile semi-synthetic polymer in biomedical applications," *Progress in Polymer Science (Oxford)*, vol. 36, no. 8, pp. 981–1014, 2011.
- [295] H. Liang, Z. Zhang, Q. Yuan, and J. Liu, "Self-healing metal-coordinated hydrogels using nucleotide ligands," *Chem. Commun.*, vol. 51, no. 82, pp. 15196–15199, 2015.
- [296] D. S. Williams, *Designing Self-Assembled, Functional Mesocompartments Utilising Molecular Interactions*. PhD thesis, 2012.
- [297] D. Mazia, G. Schatten, and W. Sale, "Adhesion of Cells to Surfaces Coated with Polylysine," *Journal of Cell Biology*, vol. 66, no. 3, pp. 198–200, 1975.
- [298] M. Leng and G. Felsenfeld, "The preferential interactions of polylysine and polyarginine with specific base sequences in DNA," *Proceedings of the National Academy of Sciences*, vol. 56, no. 4, pp. 1325–1332, 1966.
- [299] E. N. Granados and J. Bello, "Interactions of poly (N epsilon , N epsilon , N epsilon , -trimethyllysine) and poly(lysine) with polynucleotides: circular dichroism and A-T sequence selectivity 253," *Biochemistry*, vol. 20, no. 1979, pp. 4761–4765, 1981.
- [300] G. Liu, M. Molas, G. A. Grossmann, M. Pasumarthy, J. C. Perales, M. J. Cooper, and R. W. Hanson, "Biological Properties of Poly-L-lysine-DNA Complexes Generated by Cooperative Binding of the Polycation," *Journal of Biological Chemistry*, vol. 276, no. 37, pp. 34379–34387, 2001.
- [301] N. A. Kas'yanenko and B. A. Dribinskii, "DNA packaging in water solutions induced by polylysine and spermidine," *Journal of Structural Chemistry*, vol. 48, no. 4, pp. 729–733, 2007.
- [302] B. B. Kahn, T. Alquier, D. Carling, and D. G. Hardie, "AMP-activated protein kinase: Ancient energy gauge provides clues to modern understanding of metabolism," *Cell Metabolism*, vol. 1, no. 1, pp. 15–25, 2005.
- [303] H. Liang, S. Jiang, Q. Yuan, G. Li, F. Wang, Z. Zhang, and J. Liu, "Co-immobilization of multiple enzymes by metal coordinated nucleotide hydrogel nanofibers: Improved stability and an enzyme cascade for glucose detection," *Nanoscale*, vol. 8, no. 11, pp. 6071–6078, 2016.